Single-Atom Magnetism Mapped by Spin-Polarized Scanning Tunneling Microscopy

Dissertation
zur Erlangung des Doktorgrades
im Department Physik
der Universität Hamburg

vorgelegt von
Lihui Zhou
aus Zhejiang, China

Hamburg
2010

Gutachter der Dissertation:
Prof. Dr. R. Wiesendanger
Prof. Dr. U. Merkt
Prof. Dr. P. M. Koenraad

Gutachter der Disputation:
Prof. Dr. R. Wiesendanger
Prof. Dr. H. P. Oepen

Datum der Disputation:
14.01.2011

Vorsitzender des Prüfungsausschusses:
Prof. Dr. A. Lichtenstein

Vorsitzender des Promotionsausschusses:
Prof. Dr. Jochen Bartels

Dekan der MIN-Fakultät:
Prof. Dr. Heinrich Graener

Abstract

Spin-polarized scanning tunneling spectroscopy is well suited to study the correlation between structural, electronic and magnetic properties with high spatial and energy resolution. This thesis reports on the first observation of magnetization curves of individual atoms by spin-polarized scanning tunneling spectroscopy (**single-atom magnetization curves**), which is used to investigate Co atoms adsorbed on Pt(1 1 1) and Fe atoms adsorbed on Cu(1 1 1).

A systematic study of different Co nanostructures on Pt(1 1 1) reveals an inversion of the spin polarization in the vacuum above individual Co atoms with respect to larger Co nanostructures, as *e.g.*, dimers and layers, which is attributed to the enhanced rotation symmetry of single atoms. This effect is believed to be general for single magnetic atoms adsorbed on surfaces.

The magnetization of the isolated Co atoms is found to be switching at 0.3 K, which is as yet too rapid to observe, and hence they behave paramagnetically. Fitting to a quasiclassical paramagnetic model, the magnetic moment is deduced to have a mean value of 3.5 μ_B with a wide spreading.

Co atoms located close to Co nanowires are proven to be stabilized due to the **Ruderman-Kittel-Kasuya-Yosida** (**RKKY**) coupling with the nanowires which is probably mediated by a surface resonance of Pt(1 1 1). As revealed by the investigation of Co pairs the RKKY coupling depends strongly on the distance and especially on the relative direction with respect to the substrate on the atomic scale, which is attributed to the non-spherical Fermi surface of the substrate. The measured pairwise RKKY coupling map is demonstrated to reliably predict the magnetism of more complex nanostructures built from a larger number of atoms. The same indirect exchange interaction between distant individual Co atoms forms a spatially inhomogeneous mean field, giving rise to the spreading in the magnetic moments.

A spin polarization above the Pt(1 1 1) surface in the vicinity of the Co nanowires is detected and found to be exponentially decaying in lateral distance from the interface with a long decay length of 1 nm.

The investigation of Fe atoms on Cu(1 1 1) also reveals paramagnetism with an out-of-plane easy axis and an RKKY mean field with a comparable strength as for Co adatoms on Pt(1 1 1).

Zusammenfassung

Spinpolarisierte Rastertunnelspektroskopie ist bestens geeignet zur Untersuchung der Korrelationen zwischen strukturellen, elektronischen und magnetischen Eigenschaften mit hoher Orts- und Energieauflösung. In dieser Arbeit werden die ersten Messungen von Magnetisierungskurven einzelner Atome mit Hilfe von spinpolarisierter Rastertunnelspektroskopie (**Einzelatom-Magnetisierungskurven**) vorgestellt, welche verwendet werden um Co Atome auf Pt(1 1 1) und Fe Atome auf Cu(1 1 1) zu untersuchen.

Eine systematische Untersuchung verschiedener Co Nanostrukturen auf Pt(1 1 1) zeigt eine Inversion der Spinpolarisierung im Vakuum über einzelnen Co Atomen gegenüber größeren Co Nanostrukturen, wie z.B. Dimeren und dünnen Schichten, was auf die höhere Rotationssymmetrie der Einzelatome zurückgeführt wird. Bei diesem Effekt handelt es sich vermutlich um eine allgemeine Eigenschaft einzelner auf Oberflächen adsorbierter magnetischer Atome.

Die Magnetisierungsrichtung einzelner Co Atome schaltet selbst bei 0.3 K mit einer Frequenz die Zeitauflösung des Experiments übersteigt. Daher wird ein paramagnetisches Verhalten der Atome beobachtet. Durch anfitten eines quasi-klassischen paramagnetischen Modells wird auf ein mittleres magnetisches Moment von 3.5 μ_B geschlossen, mit einer breiten Streuung der Messwerte um den Mittelwert.

Co Atome in der Nähe von Co Nanodrähten zeigen eine Stabilisierung ihrer Magnetisierungsrichtung durch die die **Rudermann-Kittel-Kasuya-Yosida (RKKY)**-Wechselwirkung mit den Nanodrähten, welche vermutlich über eine Oberflächenresonanz von Pt(1 1 1) vermittelt wird. Die Untersuchung von Co Paaren zeigt, dass die RKKY-Kopplung stark vom Abstand und insbesondere von der relativen Richtung, bezogen auf die atomare Oberflächenstruktur des Substrats, abhängt. Dieser Effekt wird der nichtsphärischen Fermi-Fläche des Substrats zugeschrieben. Es wird gezeigt, dass die gemessenen paarweisen RKKY-Kopplungsstärken zuverlässige Vorhersagen über die magnetischen Eigenschaften komplexerer Nanostrukturen welche aus einer größeren Anzahl von Atomen bestehen, erlauben. Eben diese indirekte Austauschwechselwirkung zwischen weit voneinander entfernten einzelnen Co Atomen erzeugt ein räumlich inhomogenes effektives Magnetfeld, welches für die breite Streuung der gemessenen magnetischen Momente verantwortlich ist.

Über der Pt(1 1 1) Oberfläche wurde in der Nähe von Co Nanodrähten eine Spinpolarisierung gemessen, welche lateral exponentiell mit einer größen Abklingbreite von 1 nm mit dem Abstand vom Nanodraht abn-

immt.

Die Untersuchung von Fe Atomen auf Cu(1 1 1) ergibt ebenfalls ein paramagnetisches Verhalten, mit der leichten Magnetisierungsrichtung senkrecht zur Oberfläche und einem effektiven RKKY Magnetfeld welches mit dem für Co Atome auf Pt(1 1 1) vergleichbar ist.

Contents

Chapter 1

Introduction

Being economical while living in the information age, there is ever growing interest over the recent decades in decreasing the size of magnetic data storage and spintronic devices. Currently, magnetic atoms adsorbed on non-magnetic substrates are of great interest and exploited as ideal model systems for the ultimate thinkable bit [1]. The magnetism of a single atom adsorbed on the surface of a crystal (adatom) is well-defined and controllable, and hence can be compared straight forwardly to density functional calculations. The fundamental understanding of adatom magnetism is a prerequisite towards the design of more complex and larger magnetic nanostructures built by ensembles of adatoms. The trend of miniaturization towards the limit of single atoms calls for appropriate tools to characterize their magnetic properties. A magnetization curve, *i.e.*, the measurement of the magnetization in response to an external static magnetic field, is the most direct experimental approach to study magnetic materials. It has been used since the early days of modern research in magnetism to deduce their basic properties. Various techniques, as *e.g.*, micro/nano superconducting quantum interference device (micro-/nano-SQUID) measurements [2, 3] and X-ray magnetic circular dichroism (XMCD) measurements [4], are able to measure magnetization curves of magnetic nanostructures, albeit limited to nanoparticles or large ensembles of adatoms. In this thesis, a new method to record the magnetization curve of one individual atom with a magnetic moment in the order of a Bohr magneton (μ_B) has been developed. The technique used is spin-polarized scanning tunneling spectroscopy (SP-STS). It can reveal the correlation between structural, electronic and magnetic properties in real space at the atomic level [5, 6]. Therefore, not only the role of the very local environment can be studied but also the electronic origin which determines the magnetic properties.

The figure of merit for the study of atomic magnetism using STS is $\mu_B B/k_B T$ where B is an external magnetic field, k_B is the Boltzmann constant and T is the temperature. In order to be sensitive enough to resolve the Zeeman splitting, the figure of merit has to be much larger than 1. Since furthermore interactions on the scale of tens of μeV are often dominating in atomic magnetism, the temperature needs to be smaller than 1K. Therefore, all the experiments are carried out in a scanning tunneling microscope (STM) operating at 0.3K and in a magnetic field up to 12 T, leading to a figure of merit of about 30. In order to obtain intrinsic properties of single magnetic adatoms, all the experiments are performed in ultra high vacuum (UHV) on atomically clean single crystal surfaces.

Two basic properties have to be considered while developing new magnetic materials for data storage: the magnetic moment and the magnetic anisotropy which forces the magnetic moment into a certain direction [1]. While a large magnetic moment can supply strong signal, the combination with a sufficiently large magnetic anisotropy can beat the superparamagnetic limit, making the magnetization stable and thus usable as a nonvolatile bit. This work is mainly performed on Co adatoms on the Pt(1 1 1) surface. This is a prototypical system where 3*d* magnetic atoms are adsorbed on a 5*d* nonmagnetic metallic substrate. Such a combination of different transition metals is of fundamental interest considering the following properties. 3*d* metals like Cr, Mn, Fe, Co and Ni are strong magnets and therefore can supply quite high magnetic moments. Transition metal substrates have a larger conduction electron density as compared to *sp*-metals like alkali metals, and, more importantly, their *d* states are partly occupied and cross the Fermi level (E_F). These electronic properties heavily affect their magnetic properties, as *e.g.*, the susceptibility. Moreover, *d* orbitals exhibit a strong anisotropy, and therefore the hybridization of 3*d* with 5*d* states may lead to unequal filling of the orbitals of distinct symmetry. This can result in a strong anisotropy of the orbital magnetization [7]. In addition Pt has a large Stoner enhancement factor and is highly polarizable ("nearly ferromagnetic"), and thus forms "giant moments" in contact to 3*d* impurities. Finally the typical Kondo temperature (T_K) for Co diluted in Pt bulk is 1 K [8]. Therefore T_K for Co on Pt(1 1 1) is at least < 0.1 K due to the reduced coordination [9, 10, 11, 12], that is the magnetic moment of Co adatoms is not screened by the Pt conduction electrons and it retains a magnetization. SP-STM is therefore applicable.

Co nanostructures grown on Pt(1 1 1) have been extensively studied in experiments [4, 13, 14, 15, 16, 17, 18, 19, 20, 21] and theory [22, 23, 24, 25, 26, 27, 28, 29, 30]. It was found by XMCD that the system of Co adatoms on Pt(1 1 1) has a spin moment m_S of 2.1 Bohr magnetons (μ_B) and an orbital

moment of 1.1 μ_B for the Co adatoms, while the induced magnetic moment of the Pt is 1.8 μ_B [4]. The spin and orbital moments of Co adatoms are significantly smaller as compared to the free atom due to the hybridization of the 3*d* states of Co with the 5*d* and 6*s* states of Pt, but substantially increased as compared to bulk Co due to the decrease in the coordination. The most striking property of this system is the large uniaxial magnetic anisotropy perpendicular to the Pt(1 1 1) surface (as also found by XMCD), with a magnetic anisotropy energy (MAE) of 9.3 meV/atom [4]. The origin for this high anisotropy is three-fold. First, the symmetry of Co adatoms is broken as compared to the free Co. Second, the coordination of Co adatoms is reduced leading to the localization of 3*d* electrons, which increases the local electronic density of states (LDOS) near E_F as well as m_S. Finally, there is an additional contribution to MAE from the strong spin-orbit coupling of the Pt 5*d* electrons. These properties makes it a promising system to study the fundamentals of magnetism of atoms in contact to a metallic substrate.

In this thesis the following basic issues with a view to the science of nanomagnetism and to the future potential application have been addressed:

1. The spin-resolved electronic structure is the key for a fundamental understanding of the magnetic properties of materials. In addition, the spin polarization of magnetic materials determines the quality of a magnetic device, as *e.g.*, the magnetoresistance of a magnetic tunneling junction. With SP-STM, the spin-resolved differential conductance is detectable which can easily be related to the spin-dependent LDOS. Chapter 5 will present the study of the spin-resolved spectroscopic properties of Co adatoms on Pt(1 1 1).

2. The stability of magnetization is crucial for building a nonvolatile memory. Its characterization is especially important for single magnetic adatoms where the superparamagnetic limit becomes even more critical. As demonstrated for more than a hundred year, magnetic stability and magnetic moments can be immediately revealed from magnetization curves. Chapter 6 will present the newly developed methodology of **single-atom magnetization curves**.

3. Magnetic interactions are the origin for (anti-)ferromagnetism in condensed matter. RKKY coupling is one of the three basic magnetic interactions existing in solids besides direct exchange and dipolar interaction. It describes the indirect exchange interaction between distantly separated magnetic ions mediated by the conduction electrons, and determines the magnetic properties in many conducting materials which contain a diluted amount of magnetic impurities. With the downscaling of the dimension of magnetic devices towards the atomic size, the separation between each bit

is also decreasing. Accordingly, their mutual interaction becomes prominent which could be either positive or negative to the performance of devices: (i) it could be exploited to mediate spin encoded information from one bit to another, which is the basis of a spin-based logic, or (ii) it could interfere the stored information. Therefore, a fundamental understanding of RKKY coupling at the atomic level is required. Chapter 7 will present how the surface RKKY interaction can be mapped on the atomic scale with the new technique. The sign, strength and directionality of the RKKY interaction between different Co adatom nanostructures is studied, which has a significant effect on the magnetic switching behavior of the adatoms.

4. RKKY coupling is mediated by the conduction electrons. Therefore, information on the electronic origin of RKKY coupling can be gathered from the investigation of the spin polarization induced by magnetic nanostructures. This can contribute to a detailed understanding of the substrate effect on the magnetic properties of adatoms. Moreover, it is also of importance to the understanding of magnetic properties of multilayers where the interface is known to play a key role but is not accessible. In Chapter 8 this issues is addressed in detail

5. In order to demonstrate that the new technique is applicable to different substrates, experiments are also performed on Fe adatoms on a Cu(1 1 1) surface which has a partially filled surface state and therefore is very different from the Pt(1 1 1) surface. The initial results on the preparation of the sample and the magnetic imaging of the magnetization of Fe adatoms will be presented in Chapter 9.

Finally, in order to achieve a complete insight into the single-atom magnetism, theoretical modeling is important. The first-principles calculations described in this thesis have been performed by Dr. Samir Lounis from the group of Prof. Dr. Stefan Blügel and Prof. Dr. Peter H. Dederichs at the Forschungszentrum Jülich, while the Monte-Carlo simulations have been carried out by Dr. Elena Vedmedenko in the Institute of Applied Physics of the University of Hamburg.

The thesis starts with an introduction to the basics of SP-STM (chapter 2) and to the experimental setup (chapter 3). Then, the preparation and spin-averaged electronic properties of the sample, and the preparation and calibration of the magnetic probe tip will be presented in Chapter 4.

Chapter 2

Scanning tunneling microscopy and spectroscopy

This chapter explains the basic principle of scanning tunneling microscopy (STM) and spectroscopy (STS). First it is briefly described how the STM works. Then quantum tunneling as the principle of STM is introduced within a one-dimensional model. In order to interpret the images that the STM obtains, the Tersoff-Hamann model is described, followed by the interpretation of the differential conductance. As the main technique the spin-polarized STM (SP-STM) as well as its spectroscopy mode is then described. Finally different modes of data acquisition are presented.

2.1 Scanning tunneling microscope

Figure 2.1 shows a schematic overview of the concept of the STM which basically contains a conductive sample, a conductive tip as the probe, and a feedback circuit. The sample and tip are separated by a vacuum gap of several Å leading to an overlap of the wave functions of the tip and sample. During STM operation, a bias voltage V_{stab} is applied to the sample so that a quantum tunneling current I starts to flow. The tunneling current is recorded by a preamplifier and used as an input to the feedback loop which regulates the vertical position z of the tip. This way, the tip can scan in the x-y plane across the sample surface, and z is recorded at each point (x, y) of the scanning area resulting in a real-space map of the surface topograph $z(x, y)$.

The vertical and lateral motions of the tip are accomplished by a piezoelectric element called tube scanner which allows for a tip movement with an accuracy better than 1 pm. In the constant current mode the detected

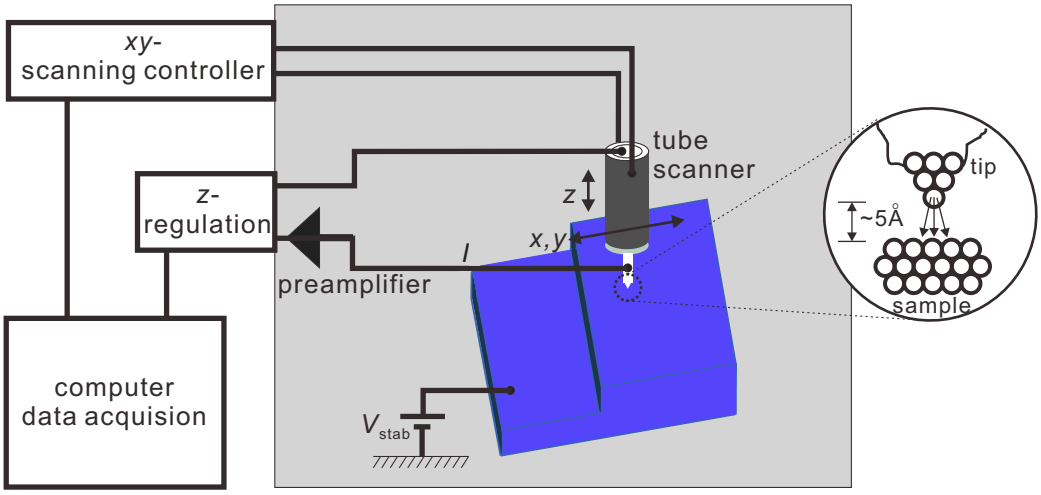

Figure 2.1: **Principle of an STM**. The tip mounted in a tube scanner and the sample are separated by a vacuum barrier of several Å in width. When a bias voltage V_{stab} is applied to the junction, a quantum tunneling current I can flow which is amplified by a pre-amplifier and recorded. While the gap spacing (z) of the two electrodes is kept regulated by a feedback loop using the tunneling current, the STM can scan line by line across the sample surface approximately following the topography of the surface.

tunneling current is compared to the setpoint current I_{stab} by the feedback loop, the deviation is amplified to apply a voltage to the z-electrode of the scanner tube until the difference vanishes. In order to let the tip move in a line-by-line fashion, a periodic sawtooth voltage and slope voltage is applied to the x- and y-electrode, respectively. A calibration allows the translation of the voltage values into real height and lateral displacement. The STM can work in spectroscopy mode as well, making the study of electronic structures in real space possible. Since the tunneling current exponentially depends on the separation as will be shown below, the STM has an extremely high spatial sensitivity and consequently a very high lateral resolution.

2.2 Quantum tunneling effect: Principle of STM

The basic mechanism of the STM is the quantum tunneling of electrons, which describes the motion of electrons through a potential barrier of finite height and width. In classical mechanics particles with an energy less than the barrier height are completely reflected from the barrier and

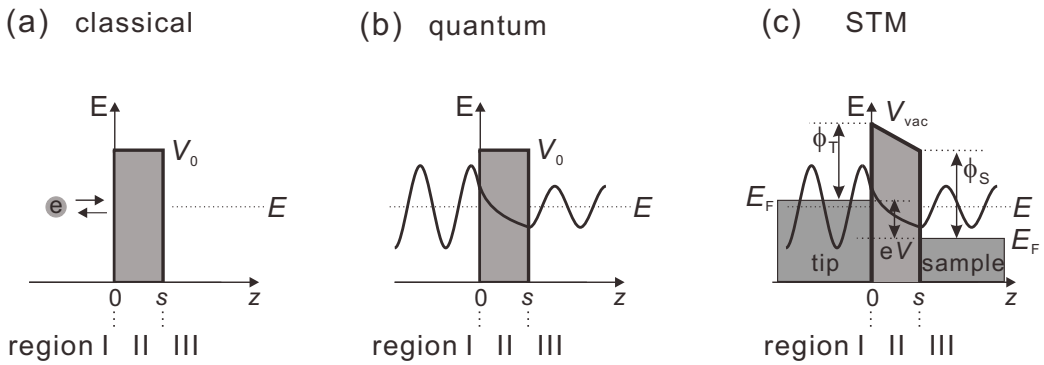

Figure 2.2: **Quantum tunneling of electrons in 1D**. **(a)** In classical mechanics an electron with an energy lower than the height of a potential barrier is forbidden to move across the barrier. **(b)** In quantum mechanics the electron has a certain probability to penetrate the barrier and tunnel through it. **(c)** In STM the work functions ϕ_T and ϕ_S of the tip and sample, and the bias voltage V determine the effective barrier.

forbidden to move across it (see Figure 2.2(a)); however, within quantum mechanics they can penetrate the barrier with non-zero probability. This effect can be illustrated with a one-dimensional quantum-mechanical model. We consider the elastic motion of an electron with an energy of E less than the height V_0 of a rectangular potential barrier with a width of s, as shown in Figure 2.2(b). This problem can be analytically solved using the time-independent Schrödinger equation in each region with respect to the barrier:

$$\left[-\frac{\hbar^2}{2m_e}\frac{d^2}{dz^2} + V(z)\right]\psi(z) = E\psi(z), \tag{2.1}$$

where $\hbar$ is the Plank constant divided by 2π, m_e is the free electron mass, and ψ is the electron wave function. The solution of the wave function in each region is given by:

$$\psi_I = A_1\exp(-ik_1z) + A_2\exp(ik_1z) \tag{2.2}$$

$$\psi_{II} = B_1\exp(-\kappa z) + B_2\exp(\kappa z) \tag{2.3}$$

$$\psi_{III} = C\exp(ik_2z). \tag{2.4}$$

Equation 2.2 describes a plane wave with incident and reflected components, Equation 2.3 describes a wave with an exponentially decaying and

rising component, and Equation 2.4 describes an outgoing plane wave. Given the conservation of the energy and the boundary condition, we get

$$k = k_1 = k_2 \quad = \quad \sqrt{\frac{2m_e E}{\hbar^2}} \tag{2.5}$$

and

$$\kappa \quad = \quad \sqrt{\frac{2m_e(V_0 - E)}{\hbar^2}}, \tag{2.6}$$

and the transmission coefficient

$$T = \frac{\left|C^2\right|}{\left|A_1^2\right|} \quad = \quad \frac{1}{1 + [(k^2 + \kappa^2)^2/4k^2\kappa^2]\sinh^2(\kappa s)}. \tag{2.7}$$

If the barrier is high or wide enough that $\kappa s \gg 1$, then the wave function would be strongly attenuated leading to

$$T \quad \approx \quad \frac{16k^2\kappa^2}{(k^2 + \kappa^2)^2} \cdot \exp(-2\kappa s). \tag{2.8}$$

The most significant finding here is the exponential dependence of the transmission coefficient on the barrier width. Typically, $\kappa \approx 0.1$ Å^{-1} leading to the drop of the tunneling current by one order of magnitude as the distance increases by only 1 Å. This guarantees the high spatial sensitivity of the STM.

2.3 Tersoff-Hamann model

In order to interpret what an STM measures, Tersoff and Hamann developed a simplest possible model which connects the measured tunneling current and differential conductance to fundamental properties of samples [31, 32].

This model is based on the work by Bardeen [33] who described the tunnel process from a different point of view as compared to the time-independent wave matching method. Within this approach a tunneling junction with two weakly coupled electrodes was studied. Then the tunneling of an electron can be viewed as an evolution of the electron from a state in the first electrode to another state in the second electrode. This problem can be solved with the *time-dependent* Schrödinger equation using time-dependent perturbation theory. Therein the probability of the transition can be calculated using Fermi's Golden Rule. As a consequence the

tunneling current between the sample and the tip separated by a vacuum barrier is given by

$$\begin{aligned} I &= \frac{2\pi e}{\hbar}\sum_{\mu,\nu}\left\{f(E_\mu^{\mathrm{T}})\left[1-f(E_\nu^{\mathrm{S}}+\mathrm{e}V)\right]-f(E_\nu^{\mathrm{S}}+\mathrm{e}V)\left[1-f(E_\mu^{\mathrm{T}})\right]\right\} \\ &\quad\cdot\left|M_{\mu\nu}\right|^2\cdot\delta(E_\mu^{\mathrm{T}}-E_\nu^{\mathrm{S}}), \end{aligned} \tag{2.9}$$

where V is the applied bias voltage with respect to the sample, $f(E)$ is the Fermi-Dirac distribution function, E_ν^{S} and E_μ^{T} are the Eigen energies respectively corresponding to the states ψ_ν^{S} in the sample and ψ_μ^{T} in the tip, and $M_{\mu\nu}$ is the tunneling matrix element describing the probability of the transition of the electron from the state ψ_ν^{S} in the sample to the state ψ_μ^{T} in the tip. The delta function describes the conservation of energy for the case of elastic tunneling. The tunneling matrix element can be calculated by

$$M_{\mu\nu} = \frac{-\hbar^2}{2m_{\mathrm{e}}}\cdot\int \mathrm{d}\vec{S}\cdot\left[(\psi_\mu^{\mathrm{T}})^*\vec{\nabla}\psi_\nu^{\mathrm{S}}-\psi_\nu^{\mathrm{S}}\vec{\nabla}(\psi_\mu^{\mathrm{T}})^*\right] \tag{2.10}$$

where the integral should be carried out over any surface lying entirely within the vacuum barrier. Obviously the calculation of the matrix element $M_{\mu\nu}$ requires the explicit expressions for the wave functions of the tip and sample, which is hampered by the difficulty in determining the atomic structure of the tip. Tersoff and Hamann [31, 32] used the simplest model for the tip as shown in Figure 2.3.

Within this model, the tip apex was assumed to be of a locally spherical symmetry and electronically only the s-type state with orbital quantum number $l = 0$ was taken into account. Often, most interesting physical phenomena are related to ground states or low-energy excited states in the vicinity of the Fermi level E_{F}. Therefore, Equation 2.9 can be reduced to

$$I = \frac{2\pi \mathrm{e}^2}{\hbar}V\cdot\sum_{\mu,\nu}\left|M_{\mu\nu}\right|^2\cdot\delta(E_\nu^{\mathrm{S}}-E_{\mathrm{F}})\cdot\delta(E_\mu^{\mathrm{T}}-E_{\mathrm{F}}) \tag{2.11}$$

for low temperatures and infinitesimally small bias voltages. Then within the s-wave approximation $M_{\mu\nu}$ can be derived and the tunneling current is given by

$$I \propto V\cdot\rho_{\mathrm{T}}(E_{\mathrm{F}})\cdot\rho_{\mathrm{S}}(E_{\mathrm{F}},\vec{r}_0)\cdot\exp(2\kappa R), \tag{2.12}$$

where $\rho_{\mathrm{T}}(E_{\mathrm{F}})$ is the tip's density of states at E_{F}, R is the tip radius, $\vec{r}_0$ is the center of the tip curvature, and $\kappa = \sqrt{2m_{\mathrm{e}}\phi}/\hbar$ is the decay rate with ϕ

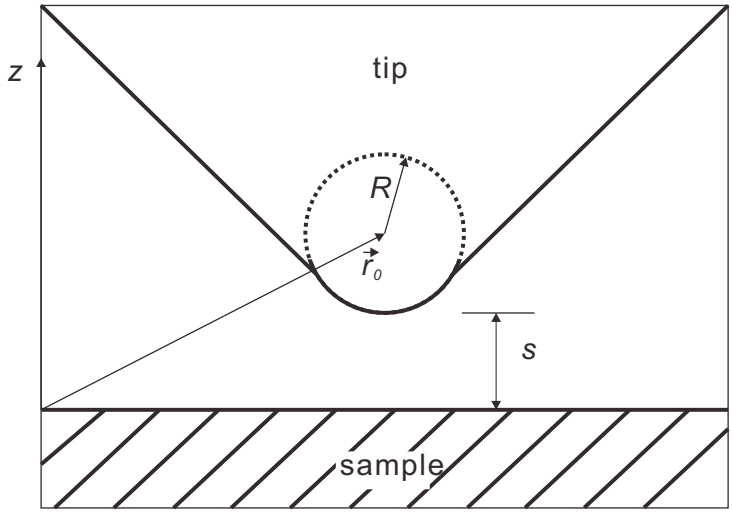

Figure 2.3: **Geometry of the tunneling junction in the Tersoff-Hamann model**. The tip apex has a spherical curvature of radius R with the center located at $\vec{r}_0$ and separated by the vacuum gap of thickness s from the sample surface.

the effective barrier height which is approximately equal to the average of the tip and sample surface work functions. $\rho_S(E_F, \vec{r}_0)$ is the local density of states (LDOS) of the sample surface at E_F evaluated at $\vec{r}_0$, given by

$$\rho_S(E_F, \vec{r}_0) \quad = \quad \sum_\nu \left|\psi_\nu^S(\vec{r}_0)\right|^2 \cdot \delta(E_\nu^S - E_F). \tag{2.13}$$

It is now clear that the STM topographs obtained at a low bias voltage in the constant current mode (see below) represent the surfaces of constant sample LDOS at E_F measured at the center of the tip curvature at low temperature. Since the wave functions decay exponentially into the vacuum, *i.e.*, $\psi_\nu^S(\vec{r}_0) \propto \exp(-\kappa(R+s))$, the exponential dependence of the tunneling current on the distance s becomes explicit as

$$I \quad \propto \quad \exp(-2\kappa s). \tag{2.14}$$

At finite bias voltages the tunneling current is a weighted convolution of the tip and sample density of states over a range of energies

$$I \quad \propto \quad \int_0^{eV} \rho_S(E_F + \epsilon, \vec{r}_0) \cdot \rho_T(E_F - eV + \epsilon) d\epsilon, \tag{2.15}$$

where $\rho_S(E_F + \epsilon, \vec{r}_0)$ is the energy dependent LDOS of the sample evaluated at $\vec{r}_0$, and $\rho_T(E_F - eV + \epsilon)$ is that of the tip atom. Within the Wentzel-Kramers-Brillouin (WKB) approximation the transmission coefficient of $\rho_S(E_F + \epsilon, \vec{r}_0)$

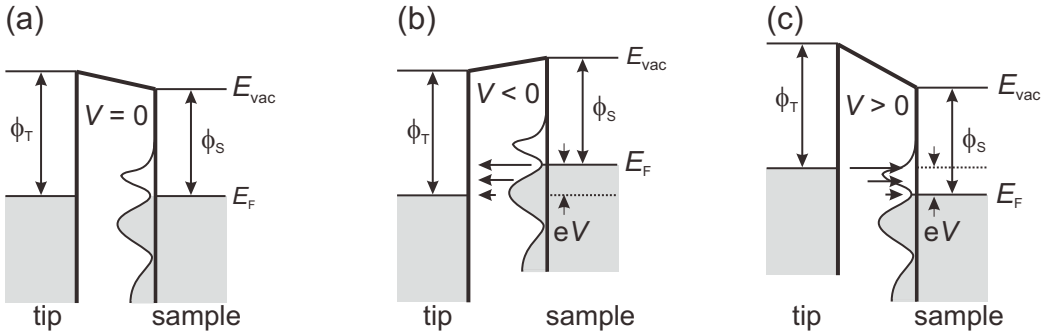

Figure 2.4: **Electronic states involved in the STM**. Filled states below E_F are indicated by shaded regions. The tip is assumed to have a flat density of states, while the sample exhibits features in the LDOS sketched by the curves. The tip and sample have different local work functions, resulting in a non-rectangular vacuum barrier. The application of a bias voltage shifts the tip and sample Fermi levels relatively. **(a)** Zero bias voltage. The tunneling junction is in equilibrium and no net tunneling current flows across the tunneling gap. **(b)** Negative bias voltage. Electrons from the filled states in the sample tunnel into empty states in the tip. **(c)** Positive bias voltage. Electrons from the filled states in the tip tunnel into the empty states in the sample. Figures are taken from [34].

is given by

$$T \quad (E_F + \epsilon, eV, s) = \exp\{-2(s+R) \cdot \sqrt{\frac{2m_e}{\hbar^2}\left[\frac{\phi_t + \phi_s + eV}{2} - (E_F + \epsilon - \frac{\hbar^2 k_\parallel^2}{2m_e})\right]}\}. \quad (2.16)$$

ϕ_T (ϕ_S) is the tip (sample) local work function. $k_\parallel$ is the component of the electron wave vector parallel to the surface. Obviously, $T(E_F + \epsilon, eV, s)$ favors states with vanishing $k_\parallel$. Therefore, the main contributions to the tunneling current originate from the states located in the vicinity of the center of the surface Brillouin zone $\bar{\Gamma}$, and the transmission coefficient is again exponentially dependent on the distance from the surface.

Figure 2.4 illustrates the electronic states involved in the tunneling with different bias voltages. The sample LDOS is assumed to exhibit features as indicated by the curves inside the barrier, while the tip has a flat density of states (DOS) which is a good approximation for a tungsten tip in the low tunneling bias range. The filled states below E_F are sketched by shaded regions. The arrows indicate the direction of the tunneling current and their length indicate the different contributions of states at

different energies due to the transmission coefficient. Without an applied bias voltage the Fermi levels of the tip and sample are aligned and no net tunneling current flows, as shown in Figure 2.4(a). The application of a negative bias voltage to the sample leads to the upward shift of the energy levels of the sample, resulting in the tunneling of electrons from the filled sample states in the energy window $[E_F, E_F + eV]$ into the empty states of the tip (Figure 2.4(b)). The current is reversed for a positive bias voltage and the electrons from the filled states of the tip tunnel into the empty states of the sample (Figure 2.4(c)).

2.4 Scanning tunneling spectroscopy and electronic properties

The STM is not only able to image the surface topography, but also to study the surface electronic structure. In order to gain knowledge about the electronic properties of the sample, the differential conductance can be analyzed by differentiating Equation 2.15 with respect to the bias voltage

$$\begin{aligned}\frac{dI}{dV}(V,\vec{r}_0) &\propto \rho_S(E_F + eV, \vec{r}_0)\cdot\rho_T(E_F) \\ &\quad + \int_0^{eV} \rho_S(E_F+\epsilon,\vec{r}_0)\cdot\frac{d\rho_T(E_F+\epsilon-eV)}{dV}d\epsilon. \end{aligned} \tag{2.17}$$

Note that here, the dependence of the dI/dV signal on the tip-sample separation s is taken implicitly into account in the sample density of states at $\vec{r}_0$ (tip location). With the approximation that the tip has a flat DOS ρ_T around E_F, it can be reduced to

$$\frac{dI}{dV}(V,\vec{r}_0) \propto \rho_S(E_F + eV, \vec{r}_0)\cdot\rho_T(E_F). \tag{2.18}$$

Therefore the energy-dependent LDOS of the sample at the location of the tip can be obtained by measuring the differential conductance in the spectroscopic mode of the STM.

In realistic experiments, the differential conductance is recorded at non-zero temperature by means of a lock-in technique with a modulation voltage V_{mod} added to V_{stab}. While the former gives rise to thermal broadening of the density of states, the latter determines the instrumental resolution limit. The energy resolution of the experiment can be analyzed by using the Fermi-Dirac distribution function and the deconvolution of the

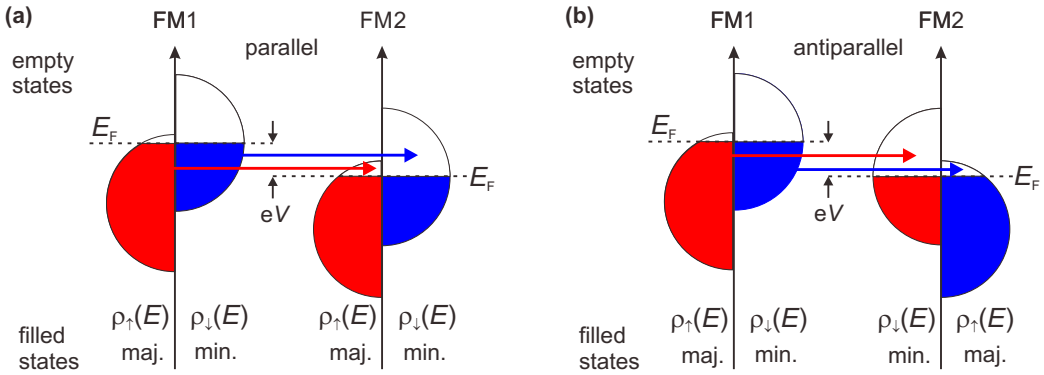

Figure 2.5: **Spin-dependent tunneling in a magnetic planar junction within the Stoner-Wohlfarth model for band magnetism** (only *d*-states are considered). **(a)** Parallel magnetic configuration. The majority and minority electrons of FM1 tunnel into the empty majority and minority states in FM2, respectively. **(b)** Antiparallel magnetic configuration. The majority and minority electrons of FM1 tunnel into the minority and majority states in FM1, respectively.

modulation and the LDOS, given by [35, 36]

$$\Delta E = \sqrt{\Delta E_{\text{therm}}^2 + \Delta E_{\text{mod}}^2} = \sqrt{(3k_{\text{B}}T)^2 + (2.5eV_{\text{mod}})^2}. \tag{2.19}$$

In order to detect features in the LDOS with a width less than ΔE, the temperature and V_{mod} have to be reduced as much as possible, which is exactly the reason why a low-temperature STM is used in this work (see Chapter 3).

2.5 Spin-polarized scanning tunneling microscopy / spectroscopy

In contrary to the previous discussion, where the spin degree of freedom of the tunneling electrons is not taken into account and all the expressions are spin-averaged, spin-dependent tunneling of the electrons has to be considered when the electrodes are both magnetic. In this case the STM is named as spin-polarized STM (SP-STM).

The SP-STM can be well demonstrated by considering the spin conserved tunneling between two ferromagnetic planar tunneling junctions which is essentially the spin valve effect, as shown in Figure 2.5. The band ferromagnetism of each electrode can be described with the Stoner

model for a $3d$, $4d$ or $5d$ magnetic metal. In this model the d-bands are decomposed into majority and minority subbands. The majority subband is shifted downwards relative to the minority subband by the amount of exchange interaction, which typically is in the eV-range. This spin imbalance in the filling number gives rise to a magnetization of the material, and thereby a spin polarization can be defined as

$$P(E) \equiv \frac{\rho^{\uparrow}(E) - \rho^{\downarrow}(E)}{\rho^{\uparrow}(E) + \rho^{\downarrow}(E)}, \tag{2.20}$$

where $\rho^{\uparrow}(E)$ and $\rho^{\downarrow}(E)$ are the density of states of the majority and minority electrons, respectively. Since usually most of the tunneling events are elastic, a negligible number of spin flips occur during tunneling, and hence spin-up and spin-down electrons in the first electrode FM1 can exclusively tunnel into the corresponding empty states in the second electrode FM2. For an arbitrary angle θ between the two electrodes, it was found theoretically and experimentally that the tunnel resistance R of free-like electrons at low bias voltage is given by

$$1/R = 1/R_0(1 + P_1 P_2 \cos\theta), \tag{2.21}$$

where P_1 and P_2 are the spin polarizations, and θ is the angle between the magnetization orientations of the electrodes [37, 38]. While the first term in the bracket is the spin-averaged contribution, the second one describes the spin-dependence. Figure 2.5 therefore illustrates the two limiting cases where the two electrodes' magnetizations are parallel ($\theta = 0$) and antiparallel ($\theta = \pi$). In the parallel case the majority (spin-up) and minority (spin-down) electrons of FM1 respectively tunnel into the empty majority (spin-up) and minority (spin-down) states in FM2 (Figure 2.5(a)). In the antiparallel case the majority (spin-up) and minority (spin-down) electrons of FM1 respectively tunnel into the empty minority (spin-up) and majority (spin-down) states (Figure 2.5(b)).

In order to interpret spin-polarized tunneling in STM, Wortmann *et al* [5, 39, 40] developed a theory starting from the Tersoff and Hamann model. Similarly, the main assumptions in this spin-polarized description are: i) the tip apex state is spherical; ii) both the majority and minority subbands of the tip are of s-wave symmetry with the same decay rate κ; iii) the tip's majority and minority density of states are both constant in energy but of different size. It is found that, in analogy to the case for magnetic planar tunneling junctions, the tunneling current at a low bias voltage consists of a spin-averaged and a spin-polarized contribution as

$$I(V, \vec{r}_0, \theta) \propto \rho_{\mathrm{T}} \tilde{\rho}_{\mathrm{S}}(V, \vec{r}_0) \left[1 + P_{\mathrm{T}} \tilde{P}_{\mathrm{S}}(V, \vec{r}_0) \cos\theta\right], \tag{2.22}$$

with

$$\tilde{\rho}_{\mathrm{S}}(V,\vec{r}_0) = \int_0^{\mathrm{e}V} \left[\rho_{\mathrm{S}}^{\uparrow}(E_{\mathrm{F}}+\epsilon,\vec{r}_0)+\rho_{\mathrm{S}}^{\downarrow}(E_{\mathrm{F}}+\epsilon,\vec{r}_0)\right]\mathrm{d}\epsilon \tag{2.23}$$

and

$$\tilde{P}_{\mathrm{S}}(V,\vec{r}_0) = \int_0^{\mathrm{e}V} \left[\rho_{\mathrm{S}}^{\uparrow}(E_{\mathrm{F}}+\epsilon,\vec{r}_0)-\rho_{\mathrm{S}}^{\downarrow}(E_{\mathrm{F}}+\epsilon),\vec{r}_0\right]\mathrm{d}\epsilon/\tilde{\rho}_{\mathrm{S}}(V,\vec{r}_0). \tag{2.24}$$

While $\tilde{\rho}_{\mathrm{S}}(V,\vec{r}_0)$ describes the energy-integrated spin-averaged density of states, $\tilde{P}_{\mathrm{S}}(V,\vec{r}_0)$ describes the energy-integrated local spin polarization of the sample. Therefore, the information on the sample spin structure relative to the tip magnetization can be revealed with constant current images, *i.e.*, within the SP-STM mode, which historically was the first mode introduced [41]. The SP-STM usually works in the vicinity of E_{F}, so that the difference in the filling numbers of the majority and minority subbands and thereby the magnetic contrast can be maximized leading to a strong contribution to the tunneling current. Atomic resolution for the spin structure was achieved within this mode [42].

It is also feasible to resolve the surface spin structure within the spectroscopy mode, *i.e.*, by SP-STS. Wortmann *et al* [5, 39, 40] derived an expression for the differential conductance $\mathrm{d}I/\mathrm{d}V$ at a low bias voltage, approximately given by

$$\begin{aligned}\frac{\mathrm{d}I}{\mathrm{d}V}(V,\vec{r}_0,\theta) \propto\ & \rho_{\mathrm{T}}(E_{\mathrm{F}})\cdot\rho_{\mathrm{S}}(E_{\mathrm{F}}+\mathrm{e}V,\vec{r}_0) \\ & \cdot\left[1+P_{\mathrm{T}}(E_{\mathrm{F}})P_{\mathrm{S}}(E_{\mathrm{F}}+\mathrm{e}V,\vec{r}_0)\cos\theta\right].\end{aligned} \tag{2.25}$$

Here $P_{\mathrm{S}}(V,\vec{r}_0)$ is the energy-dependent local spin polarization of the sample, and $P_{\mathrm{T}}(E_{\mathrm{F}})$ is the spin-polarization of the tip at E_{F}. Note that this description neglects the energy dependence of the tip's spin-polarization and thus strictly is only valid for small bias voltages around E_{F}. For larger bias voltages, the energy dependence of P_{T} has to be taken into account resulting in an additional term in Equation 2.25 similar to that in Equation 2.17. Different from the SP-STM mode, an appropriate bias voltage can be chosen to maximize the magnetic contrast. Usually, a spin-polarized surface state of the sample is very useful to map the surface spin structure. Since the difference in the spin structure can give rise to a variation in the height of the tip above the surface, care has to be taken that this height change is corrected when a quantitative evaluation of the spectroscopic signal is needed [43].

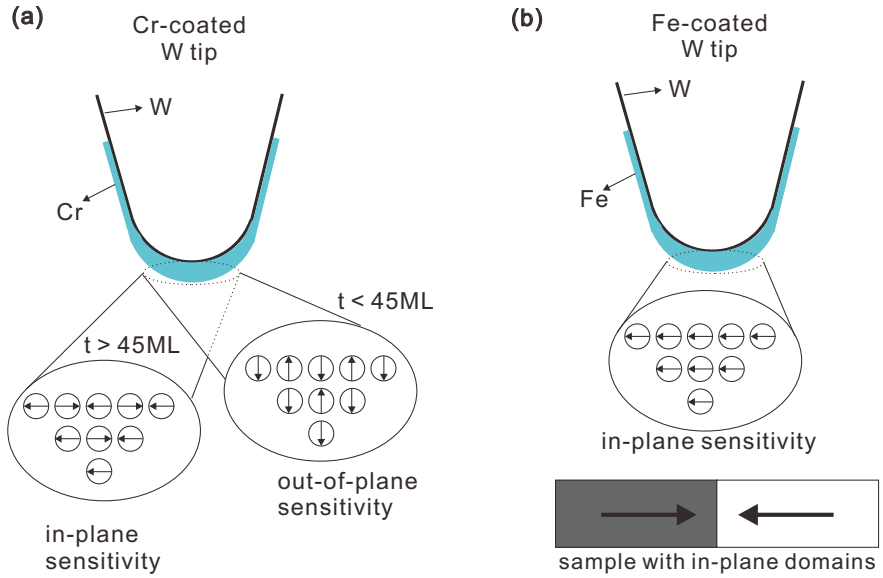

Figure 2.6: **Magnetic sensitivity of differently coated tips**. **(a)** Depending on the coverage of coated Cr, the tip can exhibit in-plane (coverage > 45 monolayers) or out-of-plane (coverage < 45 monolayers) magnetic sensitivity. **(b)** An Fe-coated W tip is usually sensitive to the in-plane magnetization. Figures are taken from [34].

Experimentally it is crucial for SP-STM measurements to have a magnetic tip with appropriate sensitivity to the in-plane or out-of-plane magnetization component of the sample and with a strong spin polarization around E_F. For this purpose, conventional W tips are flashed and then coated with thin ferromagnetic or antiferromagnetic films (see Chapter 4.2 for details). The flash makes the tip apex sufficiently blunt so that the coated magnetic film has a magnetic anisotropy either along or perpendicular to the tip axis. In experiments it is usually important to manipulate the tip and sample magnetizations separately. Therefore, a hard magnetic material is chosen as one electrode while a soft one is chosen as the second electrode. Fe is frequently used as a soft tip material, while an antiferromagnetic film, *e.g.*, Cr, is used in order to avoid magnetic stray field, which can heavily affect the magnetic states of the sample (see Chapter 6.6). As shown in Figure 2.6, for out-of-plane magnetization measurements a thin film of Cr with a coverage of less than 45 monolayers is deposited, while for in-plane magnetization measurements a thin film of Cr with a coverage of more than 45 monolayers, or a thin film of Fe with a coverage of around 10 monolayers is deposited.

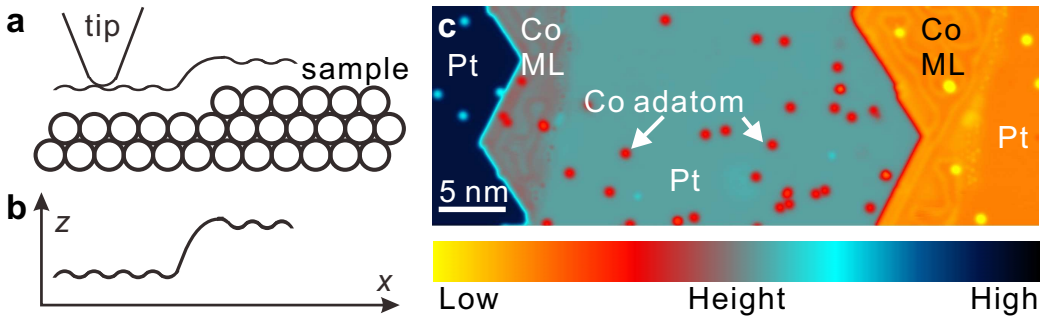

Figure 2.7: **Constant current mode of the STM**. In the constant current mode the tip follows approximately the surface topograph (**(a)**) and the height profile of the tip is recorded (**(b)**). **(c)** An image recorded in this mode showing the morphology of Co monolayers (ML) and Co adatoms on Pt(1 1 1). (Tunneling parameters: V_{stab} = +0.3 V, I_{stab} = 0.8 nA, and T = 0.3 K.)

2.6 Measurement modes

In this section different measurement modes in STM/STS experiments related to this thesis will be described. Basically, they can be divided into topographic and spectroscopic modes.

2.6.1 Constant current mode

All topographs in this thesis are recorded in the *constant current mode*. In this most common mode a bias voltage V_{stab} is applied to the sample and a current setpoint I_{stab} is chosen. Then the tip scans the sample surface line by line, and the current is kept constant with the feedback loop by using the exponential dependence of the tunneling current on the tip-sample distance (Equation 2.14). During scanning, the tip can be retracted from the sample surface when the tunneling current is higher than the setpoint and approached to the sample surface when it is below that. The height of the tip is recorded at every point of the scanning area (see Figure 2.7(a) and (b)). Therefore, if the sample surface is electronically, chemically and magnetically homogeneous, the tip follows the contour of the topography of the sample. Figure 2.7(c) presents exemplarily an image of Co monolayer (ML) stripes and Co adatoms on Pt(1 1 1) recorded in this mode, which shows the morphology of the sample surface.

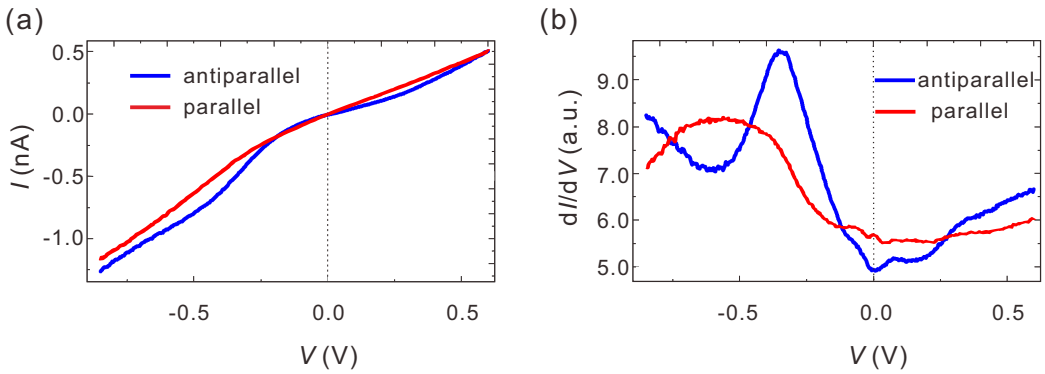

Figure 2.8: **Spin-resolved single point spectroscopy** taken on a Co ML stripe on Pt(1 1 1) using a magnetic tip. In the single point spectroscopy mode **(a)** an $I(V)$ and **(b)** a $\mathrm{d}I/\mathrm{d}V(V)$ curve over a point can be recorded in parallel. Since the tip is magnetic, the signal is spin-resolved resulting in different spectra for different relative orientation of the magnetizations of the two electrodes. (Tunneling parameters: V_{stab} = +0.6 V, I_{stab} = 1.0 nA, V_{mod} = 10 mV (rms), and T = 0.3 K.)

2.6.2 Single point spectroscopy

All $\mathrm{d}I/\mathrm{d}V$ curves in this thesis are recorded in the *single point spectroscopy* mode. Because the spin-resolved differential conductance is proportional to the spin-resolved LDOS of the sample at the corresponding energy at the tip apex according to Equation 2.25, it is a very basic mode to study the spin-resolved electronic structure of the sample. In this mode, the STM tip is stabilized over the point of interest on the sample surface with a bias voltage V_{stab} and a tunneling current setpoint I_{stab} which determine the tip-sample distance z during the measurement. Then the feedback loop is switched off with the tip kept at the stabilization position, and the current and $\mathrm{d}I/\mathrm{d}V$ are recorded while the bias voltage is ramped in a given range. While in principle the $\mathrm{d}I/\mathrm{d}V(V)$ curve can be obtained from the $I(V)$ curve by numerical differentiation, in this work it is measured by means of a lock-in technique in order to improve the signal-to-noise ratio. A small *ac* modulation voltage V_{mod} is added to the bias voltage and the tunneling current signal is fed to a lock-in amplifier. $V_{\mathrm{mod}} \approx 1$ mV to 50 mV with a frequency $f \approx 1$ kHz to 5 kHz is used. Figure 2.8 shows exemplarily $I(V)$ and a $\mathrm{d}I/\mathrm{d}V(V)$ curves recorded with a Cr-coated tip on a Co ML at opposite external magnetic fields. The magnetic field aligns the Co ML magnetization parallel and antiparallel to the tip magnetization. This difference in the relative orientation leads to a small change in the $I(V)$

curve which becomes significant in the dI/dV curve.

Since the measured dI/dV signal depends on the stabilization height above the sample surface as well as the contribution from the tip's electronic states, care has to be taken to evaluate dI/dV curves at the same tip-sample distance recorded with the same micro-tip. As a guideline, the stabilization voltage should be far away from E_{F} where the topographic contribution is sufficiently small. In this thesis, the apparent height variation is taken into account where necessary, and the spectra are normalized with the transmission coefficient using the one-dimensional WKB approximation for a trapezoidal barrier with the height as the mean value of ϕ_{S} and ϕ_{T} [43]. Moreover, several micro- and macro-tips are used to identify the sample's electronic states.

2.6.3 Spectroscopic fields

If full spectra on each spot of the whole scanning area are of interest, then the *spectroscopic field* mode is very useful. In this mode the scanning area is divided into a grid and a measurement of point spectroscopy is performed over each point of the grid. Simultaneously, an STM topograph of the area is recorded. This makes it possible to reveal the correlation of the electronic structure and the topographic properties on a local scale. The disadvantage of this mode is, that it is very time-consuming especially when spin-resolved spectroscopic properties are of interest and therefore requires a tunneling junction of high stability.

2.6.4 dI/dV maps

If only the spectroscopic contrast at a certain energy, instead of the full spectroscopic information, is of interest, then the dI/dV *map* mode can be of high efficiency. This is a less time-consuming method, as compared to the spectroscopic field mode, to get access to the spin-resolved electronic properties of the whole scanning area. In this mode the dI/dV signal at a certain bias voltage at every point of the scanning area is recorded using lock-in technique with a modulation voltage V_{mod}, *simultaneously* to regular constant-current images with *closed feedback*. Therefore, the spectroscopic and the topographic data can be recorded with high spatial resolution in a short time, which allows for a direct correlation of the spin-resolved electronic and the topographic properties on a local scale. This is particularly useful for imaging the magnetization with SP-STM (see below). However, different bias voltages usually stabilize the tip at

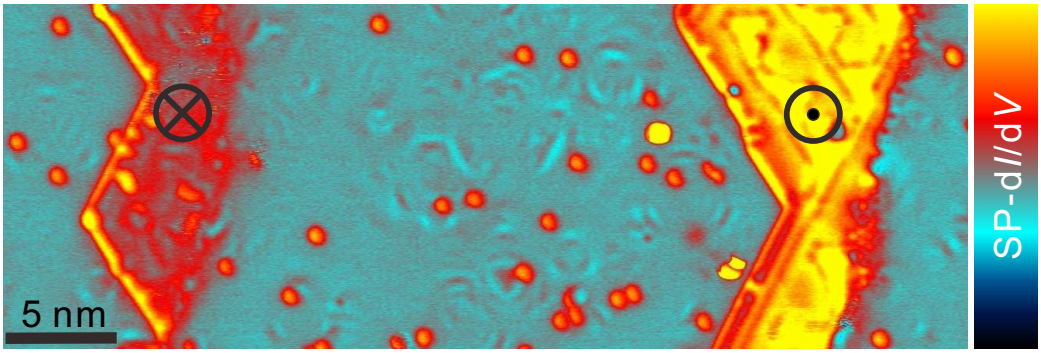

Figure 2.9: **dI/dV map taken on Co ML stripes using a magnetic tip**. dI/dV map recorded in parallel to the topograph presented in Figure 2.7(c) showing contrast from different magnetic domains within the Co MLs. (left: down pointing; right: up pointing). (Tunneling parameters: V_{stab} = +0.3 V, I_{stab} = 0.8 nA, V_{mod} = 20 mV (rms), and T = 0.3 K.)

distinctly different tip-sample distances making it complicated to compare dI/dV maps at different energies. Technically, since the feedback loop is closed when recording the dI/dV signal in this mode, care has to be taken that the modulation should be much faster as compared to the response of the feedback loop in order to avoid a crosstalk between topograph and dI/dV signal. Figure 2.9 shows a dI/dV map recorded with a Cr-coated tip on an area with two Co ML stripes and a couple of Co adatoms (see Figure 2.7(c) for topograph). A contrast is visible between the left and right stripes in the dI/dV map, which is due to the difference in the magnetization state (left: down pointing; right: up pointing). This demonstrates that magnetic domain structures can be mapped within the SP-STM mode.

Chapter 3

Experimental setup

This chapter describes the facility where the experiments presented in this thesis have been carried out, and is organized as follows. First the requirements raised by the aims of this work are discussed. Then the overall concept of the 300 mK UHV STM facility is shown, followed by the description of the cryostat and the low temperature STM. Finally, the performance of the facility is presented. Please refer to [34, 36, 44, 45] for a more detailed description.

3.1 Introduction

Because the principal aim of this thesis is the investigation of surface magnetism of magnetic nanostructures consisting of only a few atoms adsorbed on a nonmagnetic metallic substrate, atomically clean samples are required so that well-defined results can be achieved. Therefore all the experiments in this thesis had to be performed in an ultrahigh vacuum (UHV) system and much care has been taken with the preparation of the sample to significantly reduce contamination.

In order to study the correlation between structural, electronic and magnetic properties of nanostructures on the atomic scale, it is essential that the STM can work with sufficiently high spatial resolution. Moreover, the energy scale of many interaction effects related with single-atom magnetism like the Kondo effect [9, 10, 11, 12, 46], the spin excitations [19, 47, 48, 49, 50, 51, 52, 53] or the RKKY exchange interaction [54, 55, 56] can be in the sub-meV range. Hence a high energy resolution is required. While, as described in Chapter 2, the working principle, *i.e.*, the tunneling effect, can guarantee the high spatial resolution of a STM, the tip and sample have to be kept at low temperature to get a high energy

resolution. In order to get sub-meV-energy resolution, a cryostat with a base temperature of $T_b < \frac{0.1 \text{ meV}}{k_B} = 1$ K is necessary. This is achieved with a ^{3}He-based cryostat. Furthermore, a magnet is essential for spin-resolved measurements in order to manipulate the tip and adatom magnetizations separately. As a rule of thumb, the magnet needs to be strong enough to provide a Zeeman splitting of an order of magnitude larger than the base temperature, *i.e.*, $B > \frac{k_B T_b}{\mu_B} = 2$ T. Thus, a superconducting magnet is required.

The experimental facility used throughout this work is a multi-chamber UHV system which was designed and built by J. Wiebe and A. Wachowiak, and improved by F. Meier [34, 36, 44, 45]. It is equipped with a home-built low-temperature (LT) STM operated with the sample and tip held at a base temperature of 315 mK at an external magnetic field up to 12 T (14 T optional) perpendicular to the sample surface (along the STM tip axis). It can also work at a variable temperature between 315 mK and 100 K, and hence temperature dependent measurements are possible. Standard surface preparation and analysis equipment like an ion sputter gun, a sample and tip annealing stage, several molecular beam epitaxial (MBE) evaporators, a low energy electron diffraction (LEED) unit, and an Auger electron spectrometer (AES) are available, so that the preparation and analysis of the tip and sample can be performed *in situ*.

3.2 UHV setup

The overview of the facility is illustrated in Figure 3.1. It consists of three chambers, *i.e.*, a preparation chamber (9), an analysis chamber (8), and a transfer / STM chamber (7), which are separately pumped by 150 l/s ion getter pumps including a titanium sublimation unit. The base pressures are in the range of $p \leq 1 \times 10^{-10}$ mbar. An even lower pressure can be reached by operating cold traps inside the ion getter pumps using liquid nitrogen. A load lock (11) is attached for fast sample entry. The transfer of the sample between different chambers is done by the linear and rotary motion drives (10). The whole UHV system is mechanically decoupled from the building with the air damping system (4) and sand (2, 3, 5) to reduce external vibrations including acoustic coupling.

The preparation chamber (9) contains an x-y-z manipulator with an e-beam heater, two sputter guns, three MBE evaporators filled with Fe, Cr and Co, and a dosage valve for Ar and O_2. The cleaning including sputtering, annealing, and flashing of single crystal substrates, and the

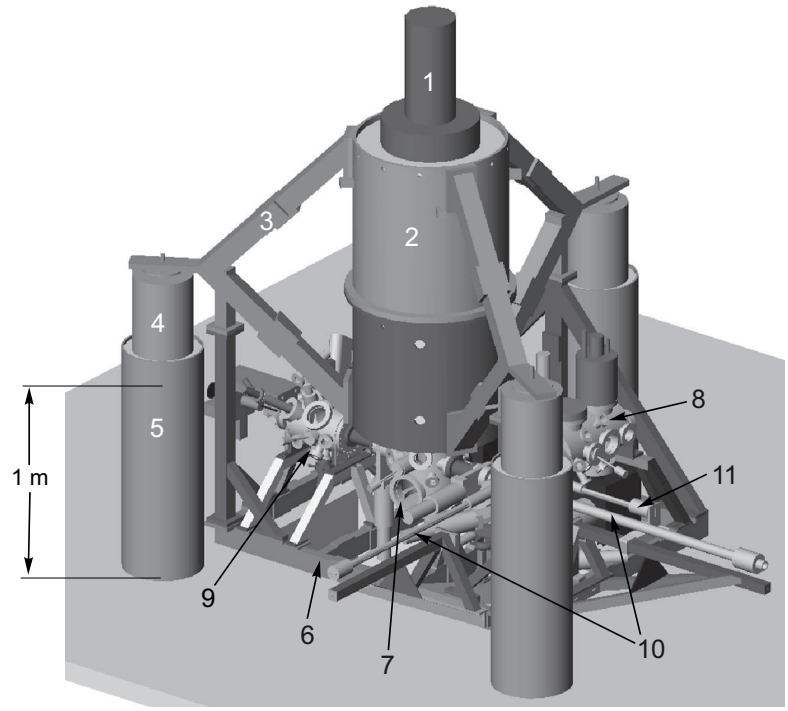

Figure 3.1: **Overview of the 300 mK UHV STM facility**. **(1)** Bottom loading cryostat. **(2)** Sand-filled outer aluminum barrel. **(3)** Sand-filled stainless-steel supports. **(4)** Air damping system. **(5)** Sand-filled supporting legs. **(6)** Sand-filled stainless-steel frame. **(7)** Central transfer chamber containing an MBE evaporator for low-temperature deposition of Co and Fe. **(8)** Analysis chamber containing a LEED/AES unit. **(9)** Preparation chamber containing an e-beam heater, and MBE evaporators for Fe, Cr and Co. **(10)** Magnetic linear and rotary motion drives. **(11)** Load lock. Figure is taken from [36].

fabrication including flashing and coating of the STM tip are carried out in this chamber. The analysis chamber (8) contains a room-temperature (RT) STM, and a LEED/AES unit. After the initial cleaning of the substrate in the preparation chamber, the surface quality can be checked quickly by the RT-STM in this chamber. The transfer chamber (7) contains the LT-STM and a triple MBE evaporator filled with Co, Fe and Cr. The sample and tip exchange into the LT-STM can be realized in this chamber. Low-temperature deposition of magnetic metals can be done with the sample in the LT-STM in exchange position at $T < 5$ K. The bottom loading cryostat (1) is connected to this chamber. A superconducting magnet (7 in Figure 3.2) is mounted at the bottom of the ^{4}He bath.

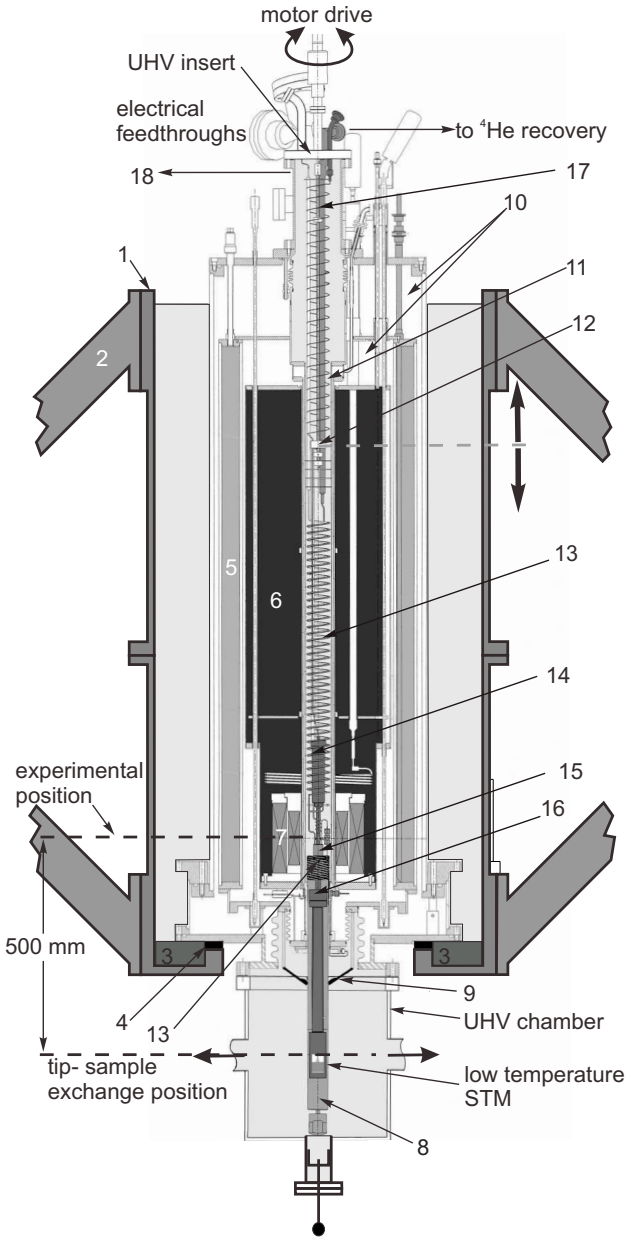

Figure 3.2: **Schematic view of the cryostat**. **(1)** Sand-filled aluminum barrel. **(2)** Sand-filled stainless-steel support. **(3)** Filled sand. **(4)** Rubber ring. **(5)** Liquid nitrogen dewar. **(6)** Liquid ^{4}He dewar. **(7)** Superconducting magnet. **(8)** Radiation shield. **(9)** Radiation flaps. **(10)** Isolation vacuum. **(11)** ^{3}He lines. **(12)** Traveling nut (aluminum-bronze). **(13)** ^{4}He line. **(14)** Charcoal sorption pump. **(15)** 1K pot. **(16)** ^{3}He pot. **(17)** Threaded leadscrew. **(18)** UHV tube. Figure is taken from [36].

3.3 Cryostat

Figure 3.2 shows the section view of the cryostat containing the single-shot ^{3}He refrigerator. The cryostat contains a super-insulated liquid nitrogen- (5) and liquid ^{4}He (6) dewar. The superconducting magnet (7) is located at the bottom of the liquid ^{4}He bath and can supply a magnetic field up to 12 T (14 T optional) perpendicular to the sample surface. The homogeneous region (0.3% over a 10 mm diameter spherical volume) of the magnetic field is large compared to the sample size of 3 mm×3 mm. The ^{3}He refrigerator (14, 15, 16) placed in a UHV tube comprises a charcoal sorption pump (14) connected to the ^{3}He pot (16) via a pumping line passing through the 1K pot (15). The STM is mounted to the ^{3}He pot via an OFHC-copper rod which is thermally coupled to the pot and to the STM by gold plated pressed contacts. The ^{3}He refrigerator and the STM are further shielded from the outside by a radiation shield (8) which is thermally connected to the 1K pot. In order to carry out measurements, the LT-STM is moved up and located at the core of the magnet, and the radiation flaps (9) are closed. The vertical movement of the insert is achieved over a 500 mm distance by a traveling nut (12) on a threaded leadscrew (17) driven by a motor outside the UHV via a rotary feedthrough at the top.

3.4 STM

For the spin-resolved measurements at temperatures below 1 K in the UHV system, several special criteria should be considered concerning the design of the STM. First, because the STM has to work at an external magnetic field up to 12 T, all the materials used for the set up should have a very weak susceptibility even at temperatures below 1 K so that the force from the superconducting magnet will not deflect the STM to the radiation shield. Second, these materials should have very low saturation vapor pressure so that they are UHV compatible. Third, the STM should be optimized to be as compact and rigid as possible in order to make it less susceptible against external vibrations.

Figure 3.3 shows a photo of the home-built STM head equipped in this facility which measures 26 mm in diameter and 85 mm in length. The compactness is achieved mainly by integrating the tube scanner (5) into the coarse-approach motor which is of the Walker design (”Pan-design”) [36, 57], as seen in Figure 3.3. The gold plated STM body is made of phosphorous bronze, which is a hard, nonmagnetic and UHV compatible copper alloy, and contains the coarse-approach motor and the

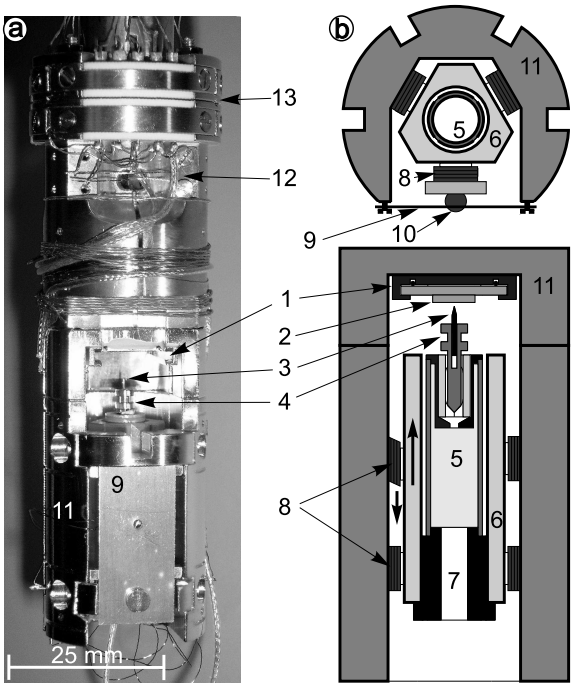

Figure 3.3: **Photograph and schematic view of the LT-STM**. **(a)** Photograph of the STM head. **(b)** Horizontal (top) and vertical (bottom) cross section views. (1) Sample stage, (2) sample, (3) tip, (4) tip holder (molybdenum), (5) tube scanner, (6) sapphire prism, (7) tube scanner holder, (8) shear-piezo stacks, (9) leaf spring (molybdenum), (10) titanium ball, (11) gold plated STM body (phosphorous bronze), (12) temperature sensor (Cernox), and (13) electrical plug (OFHC copper). Figure is taken from [36].

tube scanner.

The coarse-approach motor includes a sapphire prism (6) clamped between six Al_2O_3 plates glued on the top of shear-piezo stacks (8). The clamping is realized by a Mo leaf-spring (9) pressing the two shear-piezo stacks onto the sapphire prism. During operation, the motor is driven in a stick-slip mode by applying a saw-tooth high voltage to the shear-piezo stacks and walks a step of about 25 nm per 300 V at the base temperature. This way, a macroscopic separation of the tip and sample can be achieved, so that a safe exchange of them can be realized. During measurement, the vertical motion of the tip is accomplished by the tube scanner which in principle can move by several hundred nanometers.

3.5 Performance

The cooling procedure of the ^{3}He pot as well as of the thermally coupled STM is standardized as follows: After adsorbing all ^{3}He gas by the charcoal sorption pump by cooling it below 20 K, the sorption pump is heated up to 44 K so that the increasing pressure closes the thermal switch between the 1K pot and the ^{3}He pot. This results in cooling down of the ^{3}He pot to the 1K pot temperature. When it is below 2 K the ^{3}He gas starts to condense and fills the ^{3}He pot. After all the ^{3}He gas has condensed into liquid in the pot, the heater is switched off and the sorption pump is cooled to 7 K. Now the sorption pump starts to work and reduces the vapor pressure above the liquid ^{3}He surface, and hence opens the thermal switch. Thus, the temperature of the ^{3}He and the STM drops to the base temperature. Normally, this procedure takes about 1 hour. With an amount of 5 cm^3 of liquid ^{3}He the STM can stay at the base temperature of 315±5 mK for about 32 hours, until all the ^{3}He gas has been stored in the sorption pump. Then it starts to warm up to 4.2 K. Variable temperatures are accessible by regulating the sorption pump temperature (below 4.2 K) or using the resistive heater on the ^{3}He pot (above 4.2 K).

The vertical z-noise level of the tunneling junction at base temperature is determined as 2-5 pm with (or without) an external magnetic field up to 8 T, and with (or without) a closed feedback loop over a time period of 400 s, which is long enough for a typical high energy-resolution point spectroscopic measurement. This stability is good enough to perform atomically resolved measurements. A lateral scan range of 1 μm × 1 μm and a vertical range of 200 nm at the base temperature can be reached, which are sufficiently large for the measurements intended.

The energy resolution of the STM is limited by the thermal energy and the modulation voltage V_{mod} used for spectroscopic measurements, as given by Equation 2.19. It is found to be in the order of 100 μeV with $V_{\mathrm{mod}} = 20$ μV. This indicates that the electronic temperature of the sample and the tip is only slightly higher than that read from the temperature sensor on the STM head, and hence low-energy interaction effects can be investigated.

The spin sensitivity of the STM to the in-plane and out-of-plane magnetizations has been demonstrated on monolayers and double layers of Fe on the W(1 1 0) surface (see Chapter 4.2). Therefore, this machine is ideally suited to carry out SP-STM experiments to study the magnetism on the single-atom level.

Chapter 4

General properties of sample and tip

This chapter describes the preparation and basic properties of the sample, and the preparation and calibration of the spin-polarized tips used for this study. The preparation procedure, the morphology, and the electronic properties of the sample are presented. Finally, the fabrication of the spin-polarized tips is described followed by the calibration of the tip's spin polarization.

Part of the results presented in this chapter have been published in: F. Meier, L. Zhou, J. Wiebe and R. Wiesendanger, "Revealing magnetic interactions from single-atom magnetization curves", *Science* **320**, 82-86 (2008).

4.1 Sample

4.1.1 Sample fabrication

The study of single adatoms requires an atomically clean substrate, the preparation of which is quite elaborate. The single crystal Pt(1 1 1) is cleaned by repeated cycles of (i) Ar^+ ion sputtering at room temperature (15 ML) and annealing at 1400 K for 30 min, (ii) sputtering at room temperature (12 ML) and annealing at 1100 K for 18 min, and a final flash to 1300 K. (i) is performed to get a depletion layer where typical impurities, as *e.g.*, carbon are completely etched, while (ii) is performed to get rid of the contamination on the surface produced during the first step. Occasionally, annealing at 1000 K in an oxygen atmosphere of 2×10^{-6} mbar for 60 min is needed to remove carbon from the bulk. The Pt(1 1 1) crystal prepared

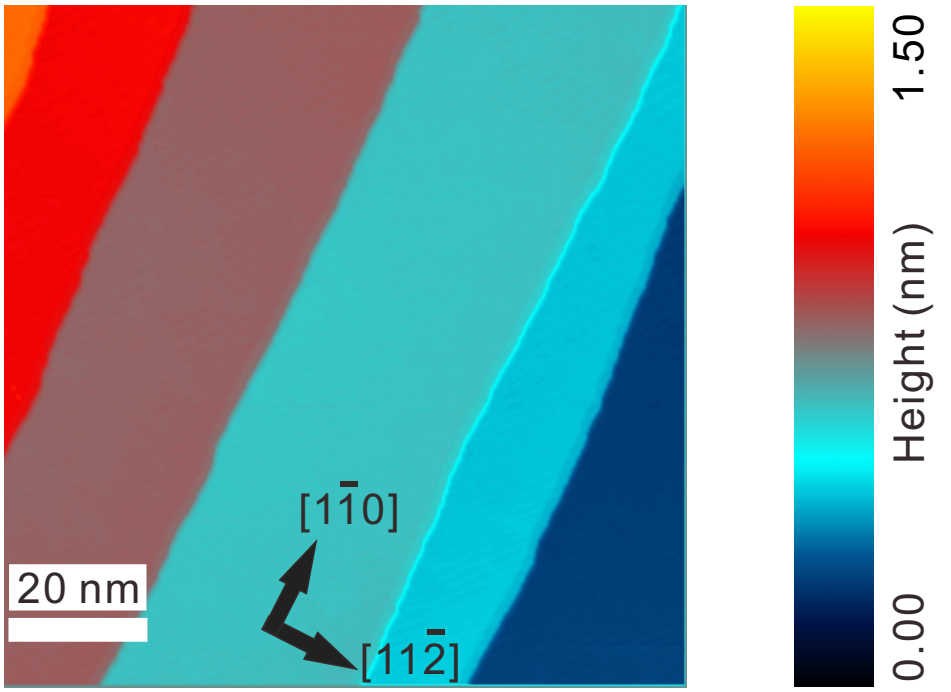

Figure 4.1: **Atomically clean Pt**(1 1 1) **surface**. STM topograph of an atomically clean Pt(1 1 1) surface after several cycles of sputtering and annealing as described in the text. It contains several large straight terraces. (Tunneling parameters: V_{stab} = +1.0 V, I_{stab} = 0.5 nA, and T = 40 K.)

in this way is terminated with an atomically clean surface with sufficiently large straight terraces, as seen in Figure 4.1. A density of defects on the order of one per 100 nm^2 is counted. Note that in order to reduce the contamination taking place during sputtering a sputter-gun with a Wien mass-filter and a differential pumping stage is used to obtain Ar^+ ions of high purity.

Sub-monolayers of Co are first deposited onto the Pt(1 1 1) surface at room temperature with an e-beam evaporator at a rate of 0.05 ML/min. The temperature is high enough for the Co to grow in the step-flow mode, which leads to the formation of one atomic layer high Co stripes (sometimes also called "nanowire" in this thesis) with several-nanometer width decorating the Pt step edges [17]. The sample is then cooled down to below 30 K in the cryogenic STM, and individual Co atoms are deposited with a rate of about 0.05 ML/min for a couple of seconds. The temperature is low enough that the diffusion of Co atoms is avoided. As a result, single Co adatoms, pairs and triplets on the bare Pt terraces and on the Co ML stripes can be found as shown in Figure 4.2. The sample prepared in

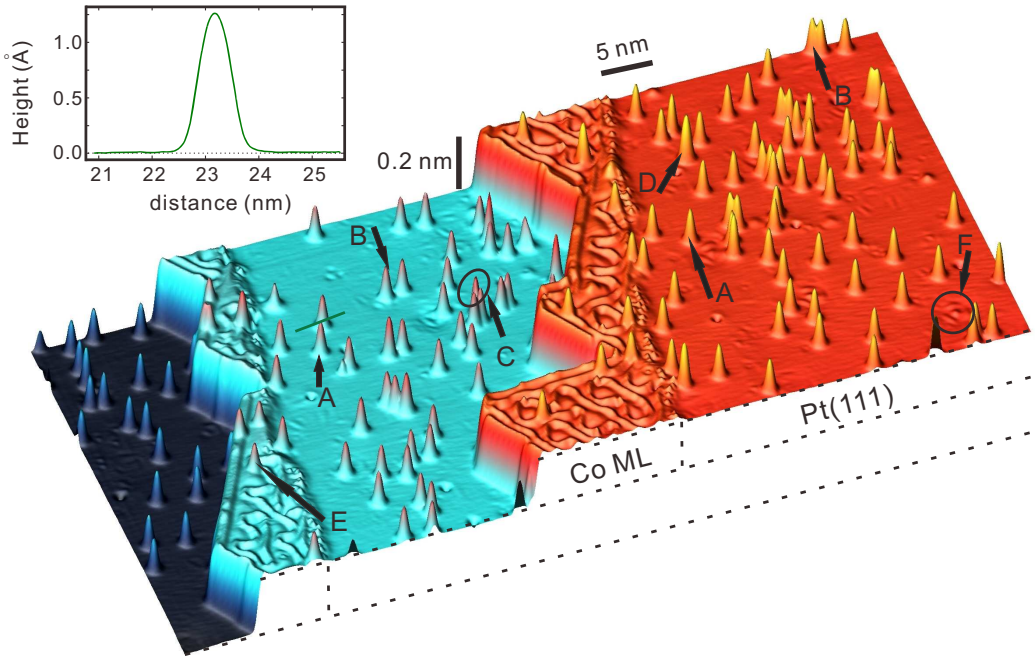

Figure 4.2: **Sample overview**. 3D view of an STM topograph of the sample with single Co adatoms (A), Co pairs (B), Co triples (C) and presumable Co-H complexes (D) on Pt(1 1 1), and single Co adatoms (E) on Co ML stripes decorating the Pt step edges. Electronic scattering patterns (F) originating from subsurface defects are also visible. The line profile (top left) shows the section across a single Co adatom (green straight line). (Tunneling parameters: V_{stab} = +0.3 V, I_{stab} = 0.8 nA, and T = 0.3 K.)

this way makes it possible to investigate various Co nanostructures in one experiment and subsequently do a well-defined comparison.

4.1.2 Sample morphology and electronic properties

Figure 4.2 shows an overview of the sample, which is a 3D view of an STM topograph. Various Co adatom nanostructures can be found. Co ML stripes attach to the Pt(1 1 1) step edges with a dislocation network due to the coexistence of *fcc* and *hcp* stacked Co areas [17]. While on the Pt(1 1 1) terraces most adsorbates are single Co adatoms (A) with a height of 1.3 Å (see line profile in Figure 4.2), Co pairs (B) and Co triplets (C) with different separations are also seen. A few atomic defects (D) can be found which are presumable Co-H complexes (see below). Some Co adatoms (E) are sitting on Co ML stripes. Electronic scattering states (F) are visible as

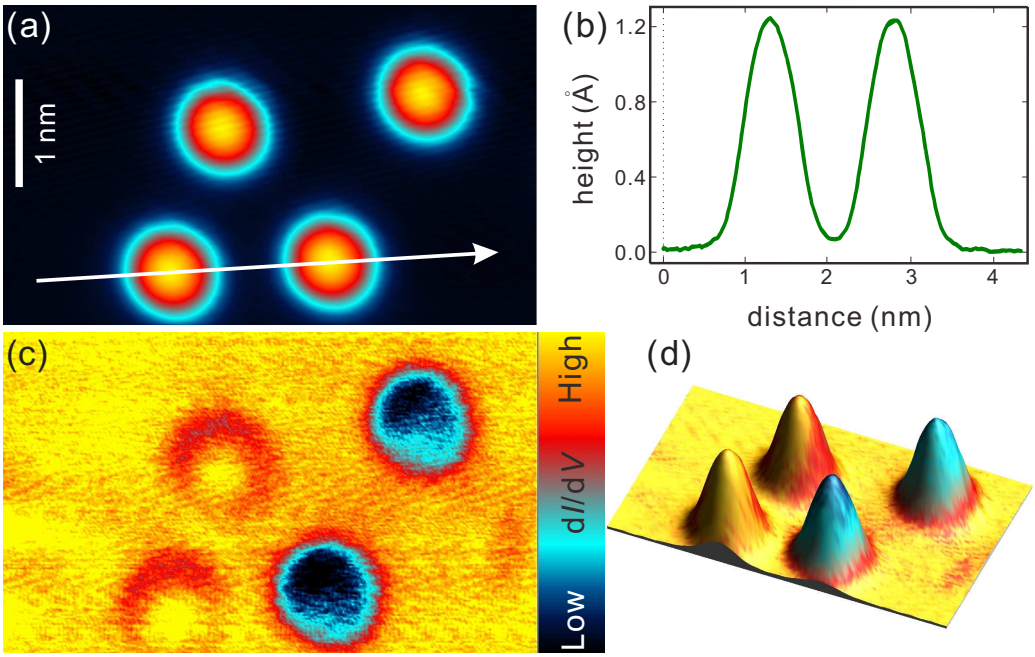

Figure 4.3: **Bimodal spectroscopic signature of Co adatoms**. **(a)** STM topograph of an area with four Co adatoms with the line profile shown in **(b)**. **(c)** dI/dV map recorded without magnetic field shows electronic contrast between adatoms. **(d)** 3D view of the STM topograph (a) colored with the dI/dV signal (b). (Tunneling parameters: V_{stab} = -0.1 V, I_{stab} = 0.3 nA, V_{mod} = 20 mV (rms), and T=0.3 K.)

corrugation of three-fold symmetry on the Pt(1 1 1) terraces (see below).

Spectroscopic signature of *fcc* and *hcp* Co adatoms

First I focus on the spectroscopic signature of Co adatoms. Figure 4.3(a) shows the STM topograph of an area containing four Co adatoms. The line profile demonstrates that all the adatoms have an identical height of 1.3 Å as seen in Figure 4.3(b). However, the simultaneously recorded dI/dV map at -0.1 V exhibits a spectroscopic contrast between adatoms as visible in Figure 4.3(c). Obviously, there are two types of Co adatoms on Pt(1 1 1) with identical height but distinct electronic signature at the energy of -0.1 eV in the vicinity of E_{F}. Using atomic manipulation by the STM tip, it was proven that the adsorption of Co adatoms on the two different binding sites, *i.e.*, *fcc* or *hcp*, gives rise to this bimodal electronic signature [34, 58]. However, it was not yet shown which spectroscopic signature belongs

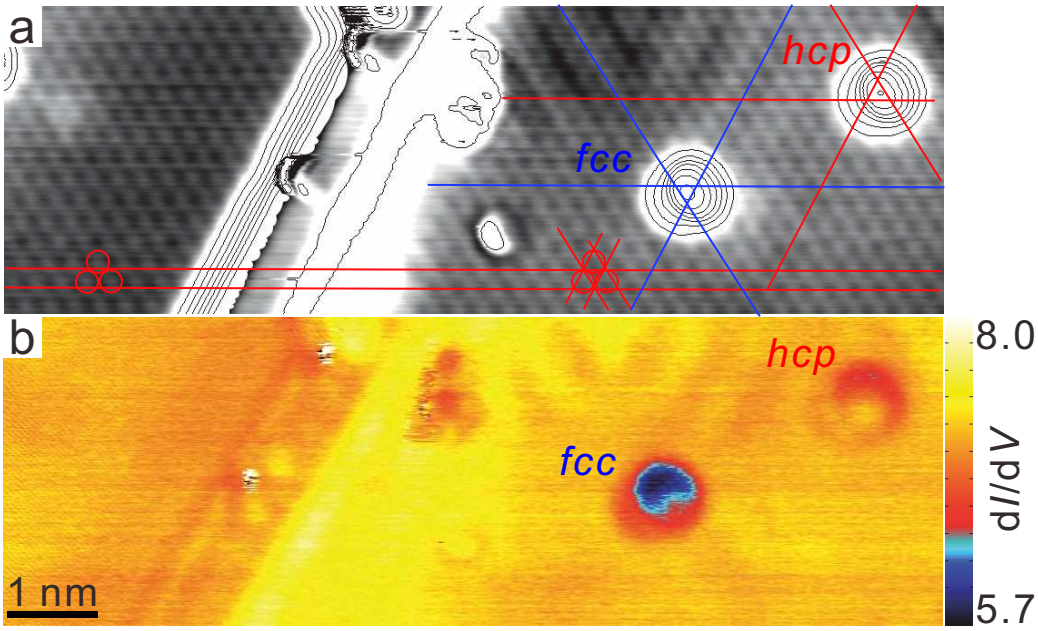

Figure 4.4: **Identification of adsorption sites using steps**. **(a)** Atomically resolved STM topograph of two adjacent Pt(1 1 1) terraces with two Co adatoms on the upper (right) terrace. The contrast is maximized for the two terraces independently. The measured atomic corrugation of the Pt(1 1 1) terrace is 2 pm. Contour lines are used to indicate the height at the monoatomic step, on the Co ML stripe and on the adatoms. (Tunneling parameters: V_{stab} = -0.05 V, I_{stab} = 0.6 nA, and T = 0.3 K). **(b)** dI/dV map of the same sample area showing the electronic contrast between the adatom on the *hcp* lattice site and on the *fcc* lattice site. (Tunneling parameters: V_{stab} = -0.1 V, I_{stab} = 0.3 nA, V_{mod} = 20 mV (rms), and T = 0.3 K.)

to which binding site. The stacking can be distinguished without any ambiguity by investigating the differential conductance at a low negative bias voltage and atom-resolved STM topographs simultaneously, as will be shown in the following.

Figure 4.4(a) shows the STM topograph with atomic resolution taken on an area with two adjacent Pt(1 1 1) terraces separated by a monoatomic step to which a very narrow Co ML stripe is attached. The two possible adsorption sites for Co adatoms are the three-fold hollows which are centered in the upwards or in the downwards pointing triangles formed by the Pt lattice [58]. The hexagonal Pt atom lattice visible on the lower (left) terrace can be used to assign the two adsorption sites on the upper (right) terrace to *hcp* and *fcc* (see red lines and circles). Consequently, the upwards

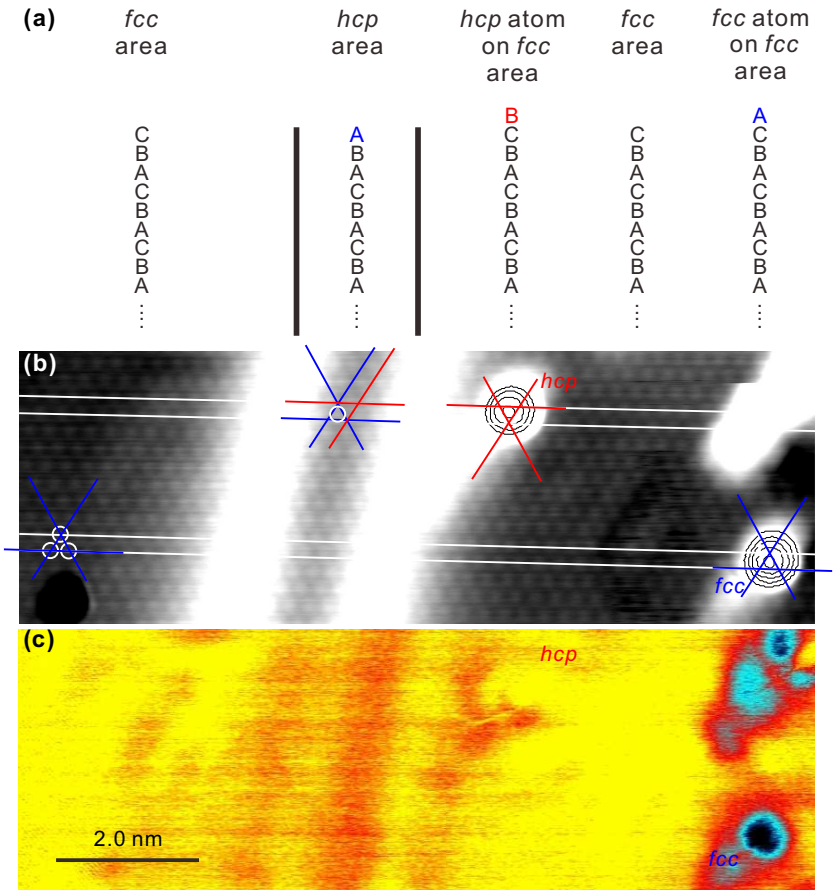

Figure 4.5: **Identification of adsorption sites of Co adatoms using double-row reconstruction**. **(a)** Stacking sequences in different areas. **(b)** Atomically resolved STM topograph of a Pt(1 1 1) terrace with an *hcp* area separated by a double-line reconstruction from *fcc* areas. Two Co adatoms are sitting on the *fcc* area. Contour lines are used to indicate the center of adatoms. The white line is drawn on top of the atoms in the separated *fcc* surface areas. The atoms in the *hcp* area are slightly shifted to a position above these lines. Consequently, the upwards pointing (blue) triangles correspond to *fcc* adatoms (A) while the downwards pointing (red) triangles correspond to *hcp* adatoms (B). (Tunneling parameters: V_{stab} = -0.01 V, I_{stab} = 1.5 nA, and T = 0.3 K.) **(c)** dI/dV map of the same area exhibiting the electronic contrast between the adatom on the *hcp* lattice site and on the *fcc* lattice site. (Tunneling parameters: V_{stab} = -0.1 V, I_{stab} = 0.3 nA, V_{mod} = 20 mV (rms), and T = 0.3 K.)

pointing triangles correspond to the *hcp* sites (red lines and circles), while the downwards pointing triangles correspond to the *fcc* sites (blue lines). The two adatoms on the upper terrace are thus positioned on an *fcc* site (left atom) and on an *hcp* site (right atom). As visible in Figure 4.4(b) the *hcp* adatom has a higher dI/dV intensity at -0.1 V (yellow) while the *fcc* adatom has a lower intensity (blue).

This conclusion is further confirmed by atomically resolved STM topographs taken on a Pt terrace with a Co induced double row reconstruction line. When Co is deposited on the Pt(1 1 1) surface at room temperature, a number of Co atoms can replace the surface Pt atoms and are embedded into the surface layer, which causes double row reconstruction lines running along the [1 1 $\bar{2}$] direction perpendicular to the close-packed rows, as visible in Figure 4.5(b) [59, 60, 61, 62]. The double row reconstruction line separates an *hcp* area from the surrounding *fcc* area [59, 60, 61, 62]. In this *hcp* area the surface Pt atoms laterally displace to the fault position with respect to the underlying *fcc* substrate. The surface-terminating atoms at the *fcc* area are sitting on position C and those at the *hcp* area sitting on position A, as illustrated in Figure 4.5(a). Consequently, it is immediately clear that the adatom sitting on position A has the stacking sequence of *fcc* and the adatom sitting on position B has the stacking sequence of *hcp*. By comparing the stacking sites of the adatoms with the terminating atoms at the *hcp* area, the upwards pointing triangles on the *fcc* area are assigned to the *fcc* sites (blue lines), while the downwards pointing triangles are assigned to the *hcp* sites (red lines), as indicated in Figure 4.5(b). This leads to the same conclusion on the assignment of the electronic contrast (Figure 4.5(c)).

With the exact knowledge of the binding sites, the bimodal electronic signatures can be studied in more detail. dI/dV curves are recorded on *fcc* and *hcp* adatoms and shown in Figure 4.6. A peak is observed at about -0.05 V below E_F. This peak is *not* due to the Kondo resonance as often observed on magnetic adatoms on noble metal surfaces [9, 10, 11, 12], because of the following reasons: (i) the peak is too strongly shifted away from E_F and too broad; (ii) as will be shown in Chapter 5 and Chapter 6, this peak is not split in an external magnetic field; and (iii) the typical Kondo temperature (T_K) for Co diluted in Pt bulk is about 1 K [8, 63], and usually T_K for adatoms on the surface is reduced by an order of magnitude due to the reduced coordination making it unobservable at 0.3 K. Furthermore, it has been checked in spectra with increased energy resolution that there are no indications for a Kondo effect on Co adatoms on Pt(1 1 1) [34]. Instead the peak is believed to be due to a characteristic

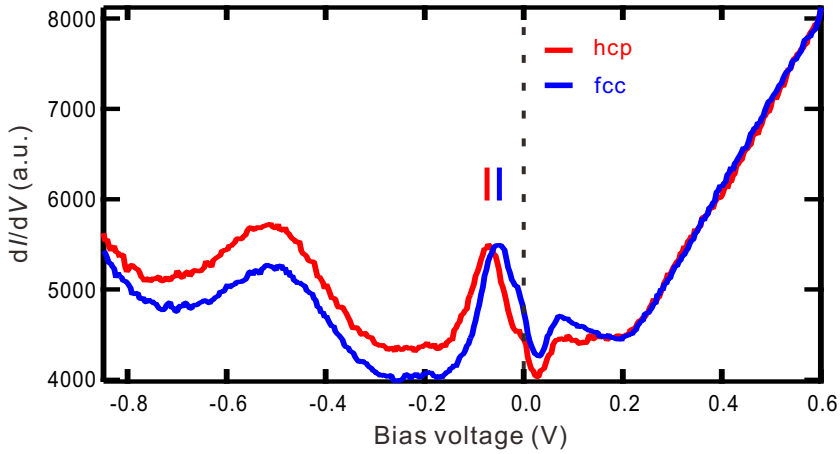

Figure 4.6: **Spectroscopy of Co adatoms on different binding sites**. dI/dV curves recorded on an *fcc* (blue) and an *hcp* (red) Co adatom. A relative shift of the characteristic peaks right below E_F is observed, which leads to the spectroscopic contrast in the dI/dV map recorded at -0.1 V (see Figure 4.4(b)). (Tunneling parameters: V_{stab} = +0.6 V, I_{stab} = 1.0 nA, V_{mod} = 10 mV, and T = 0.3 K.)

state of the Co adatoms on Pt(1 1 1) which is sharpened on the energy scale by electron-electron correlation effects [64]. At about 0.1 V above E_F there is another peak. Starting from 0.2 V the signal increases steeply, which can be attributed to the contribution of the unoccupied surface state of the underlying Pt(1 1 1) substrate [65]. Comparing the curves for the *fcc* and the *hcp* adatoms, a slight shift of the pronounced peak at -0.05 eV is visible. The bimodal electronic contrast in dI/dV maps (Figure 4.3, 4.4 and 4.5) can be traced back to this relative shift of the characteristic state in the LDOS in the vacuum. A similar stacking-induced spectroscopic signature was also observed by STM measurements on Co surfaces grown on different substrates [17, 66, 67, 68, 69]. However, therein the characteristic states are located at -0.3 V below E_F.

The electronic signature at -0.05 eV is used to identify the lattice binding sites of the adatoms throughout this work. Together with an exact calibration of the STM scanner piezo and the knowledge of the orientation of the close packed rows of the Pt(1 1 1) surface from the orientation of the Co step edges, the exact relative position in Co-pairs can also be determined (see Chapter 7.3).

It was shown by calculations that the *fcc* Co adatom's binding energy is 25 meV lower than that of the *hcp* adatoms separated by a diffusion barrier of $\sim$ 200 meV [70, 71]. This barrier is two orders of magnitude larger than

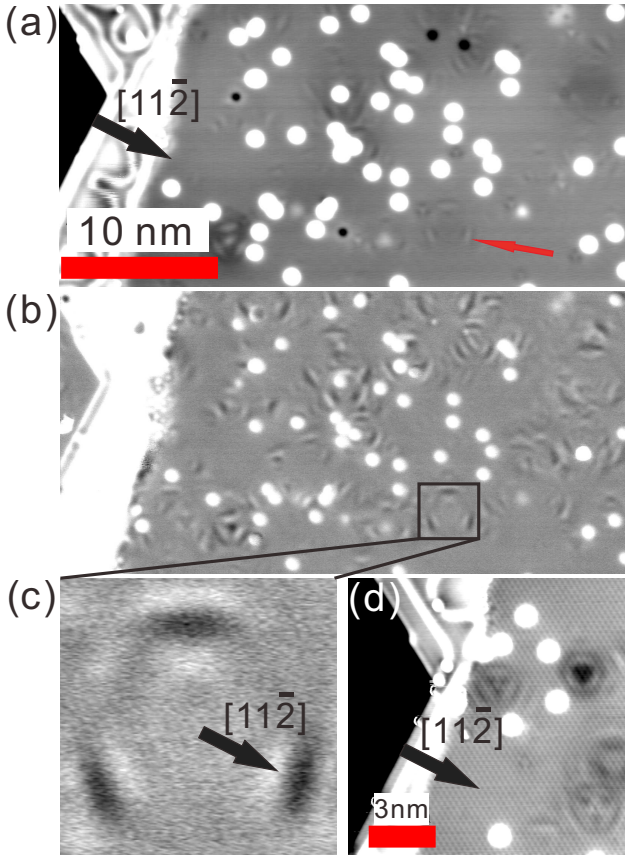

Figure 4.7: **Electron scattering states**. **(a)** STM topograph of an area with several Co adatoms. An electronic state scattered at a subsurface defect is marked by a red arrow. (Tunneling parameters: V_{stab} = +0.3 V, I_{stab} = 0.8 nA, and T = 0.3 K.) **(b), (c)** dI/dV maps recorded simultaneously with (a) showing that the maximum modulation of the amplitude of the scattering occurs in [1 1 $\bar{2}$] directions. (Tunneling parameters: V_{stab} = +0.3 V, I_{stab} = 0.8 nA, V_{mod} = 20 mV, and T = 0.3 K.). **(d)** Atomically resolved STM topograph confirming the orientation of scattering patterns. (Tunneling parameters: V_{stab} = -0.05 V, I_{stab} = 0.6 nA, and T = 0.3 K.)

the temperature at which the Co atoms are deposited ($T < 30\,\mathrm{K} \sim 2.6\,\mathrm{meV}$). Therefore, an equal distribution of *fcc* and *hcp* adatoms is expected. In fact in all the experiments 423 adatoms were counted and 200 were found sitting on *hcp* and 223 sitting on *fcc* sites. This result indicates that the low temperature efficiently blocks the diffusion of Co adatoms, in contradiction to one assumption of [19].

Scattering states

I now turn to the description of the electron-scattering states which are visible on STM topographs of Pt(1 1 1) terraces (F in Figure 4.2). Figure 4.7 shows an STM topograph of an area with several scattering patterns. These patterns are getting more obvious in the corresponding dI/dV map (Figure 4.7(b)). Such scattering states are due to the interference of the forward electron wave with the backward wave when scattered at sub-surface defects in the substrate [65, 72]. As shown in Figure 4.7(c) the scattering states appear with a strong three-fold symmetry. The maximum modulation of the scattering amplitude is found along the [1 1 $\bar{2}$] directions as confirmed by atomically resolved topographs shown in Figure 4.7(d). The scattering states have different diameters, because they originate from defects in a different depth below the surface.

In order to check whether the scattering states are temperature- or energy-dependent, Figure 4.8 shows the scattering states recorded at different bias voltages at the temperature of 0.3 K (left) and 4.2 K (right) for comparison. The STM topograph (Figure 4.8(a) and (b)) demonstrates that the adatom distribution configuration remains unchanged. The dI/dV maps recorded at +0.3 V (Figure 4.8(c) and (d)) and at -0.1 V (Figure 4.8(e) and (f)) show a considerable change with the bias voltage indicating a weak dispersion of the corresponding state. No change in the amplitude and the wavelength of the scattering state with the temperature is visible. The scattering states are most probably due to scattering of a bulk *d*-state with a 10% localization in the surface, which starts at -0.4 eV, and is upwards dispersing, crossing E_F at 1.6 nm with an effective mass of 1.5 $\mathrm{m_e}$ [65]. This state is most probably responsible for an RKKY interaction between Co adatom nanostructures described in Chapter 7. The strong three-fold symmetry is most probably induced by the electron focusing effect, which directly reflects the symmetry of the Fermi surface [72]. The depth of the subsurface defect in Figure 4.7(c) is estimated as 0.59 nm, *i.e.*, 2~3 layers below the surface.

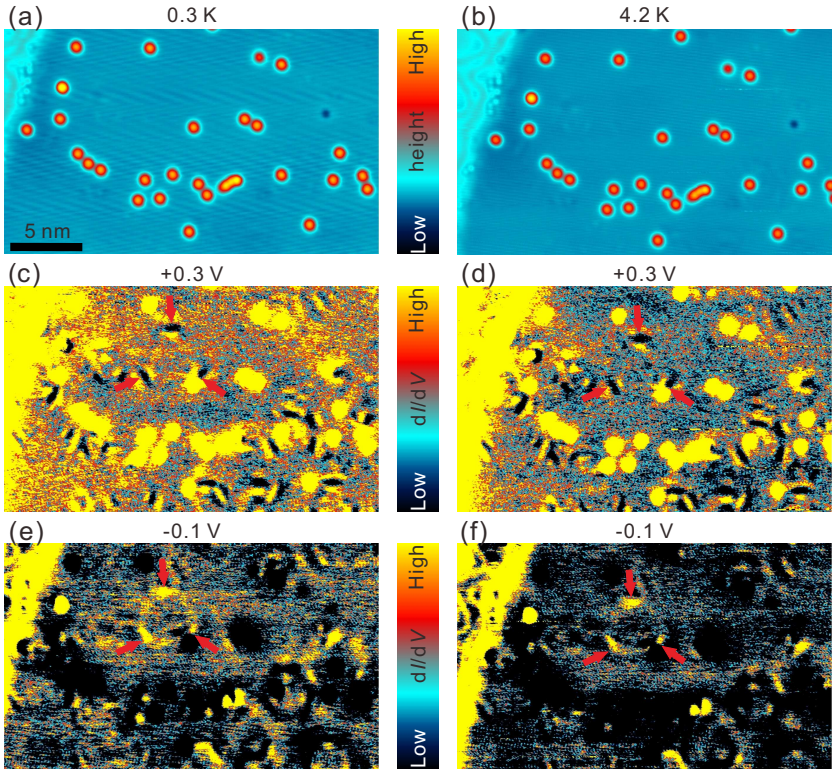

Figure 4.8: **Electron scattering states** at 0.3 K (left) and at 4.2 K (right). **(a), (b)** STM topograph of an area with several Co adatoms. (Tunneling parameters: V_{stab} = +0.3 V, and I_{stab} = 0.8 nA.) **(c), (d)** dI/dV maps recorded at +0.3 V of the same area simultaneously with (a) and (b), respectively. (Tunneling parameters: V_{stab} = +0.3 V, I_{stab} = 0.8 nA, and V_{mod} = 20 mV.) **(e), (f)** dI/dV maps recorded at -0.1 V of the same area simultaneously with (a) and (b), respectively. (Tunneling parameters: V_{stab} = -0.1 V, I_{stab} = 0.3 nA, and V_{mod} = 20 mV.) An electronic scattering state is marked by red arrows in (c)-(f). Image size: 23 nm×13.8 nm (left), 25 nm×15 nm (right); note that the image size has been adjusted in order to correct for the different calibration of the scanner piezo at 0.3 K and 4.2 K.

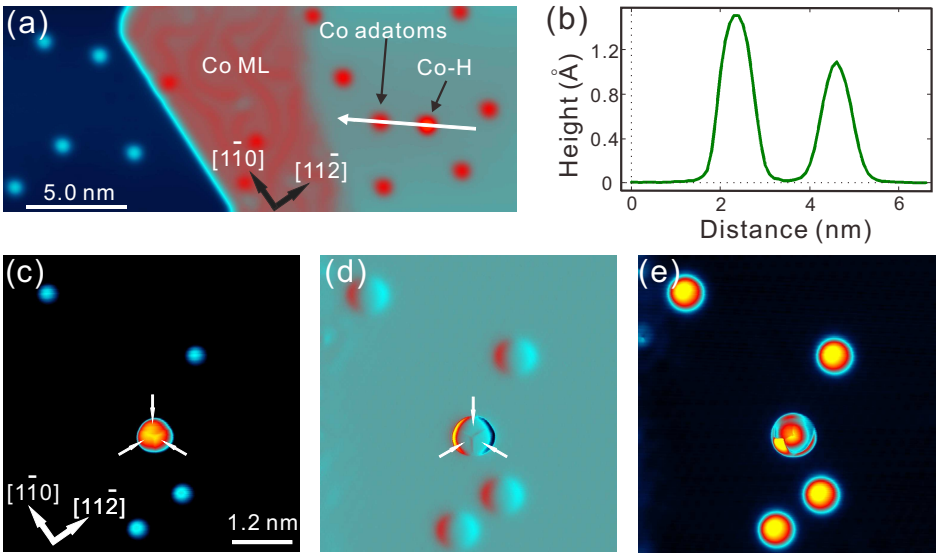

Figure 4.9: **STM topographs of a presumable Co-H complex**. **(a)** STM topograph of an area containing a presumable Co-H complex. (Tunneling parameters: V_{stab} = -1.0 V, I_{stab} = 1 nA, and T = 0.3 K.) **(b)** Line profile along the white arrow in (a) demonstrates that the complex appears higher than single Co adatoms. **(c)** STM topograph showing a three-fold symmetry on the complex. (Tunneling parameters: V_{stab} = -0.6 V, I_{stab} = 1 nA, T = 0.3 K, and B = 0 T.) **(d)** Differentiated image of (c). **(e)** STM topograph recorded at a smaller tip-sample distance indicates that the complex is unstable. (Tunneling parameters: V_{stab} = -0.1 V, I_{stab} = 1.0 nA, and T = 0.3 K.)

Presumable Co-H complexes

In rare cases, Co-H complexes are observed on the surface, as will be described in the following. Figure 4.9(a) shows an STM topograph of an area with an atomic scale defect that appears higher than single Co adatoms with a height of 1.5 Å at -1.0 V (Figure 4.9(b)). It appears with a three-fold symmetry in the STM topograph at -0.6 V (Figure 4.9(c)) which is getting more obvious when the image is laterally differentiated (Figure 4.9(d)). When the tip is quite close to the defect, the tunneling electrons seem to manipulate the shape of the defect (Figure 4.9(e)) indicating that the defect is unstable. Figure 4.10 shows three STM topographs of an area with two Co adatoms and one of the unknown defects imaged in series. In Figure 4.10(a) it is observed that while the tip is scanning from bottom to top over the bottom right most unknown defect, its height is changed to the normal Co adatom height. A few scanlines further, suddenly the middle Co adatom switches its height and becomes the unknown defect.

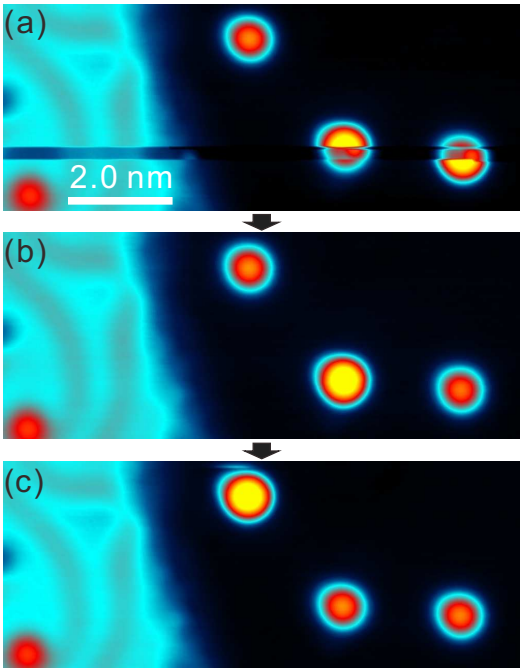

Figure 4.10: **Hopping of presumable H atom**. **(a)** The jumping of a presumable H atom from the bottom Co adatom to the middle one during scanning. This image has been taken with the fast scan direction being horizontal, and the slow scan direction from bottom to top. (Tunneling parameters: V_{stab} = -1.0 V, I_{stab} = 1.0 nA, and T = 0.3 K.) **(b)** A presumable Co-H complex is formed after the jumping. **(c)** The presumable H atom has jumped from the middle Co adatom to the top one, and consequently a Co-H is formed there. (Tunneling parameters: V_{stab} = -0.6 V, I_{stab} = 1.0 nA, and T = 0.3 K.)

This height switching can again be observed between the middle Co and the left Co in Figure 4.10(c). Consequently, the unknown defect is due to an atom or molecule, which is only weakly bound to a Co adatom, *i.e.*, a Co-complex.

In the spectroscopy of the complex (Figure 4.11) the characteristic state for Co adatoms on Pt(1 1 1) right below E_F also appears although its intensity is strongly reduced as compared to Co adatoms. The peak right above E_F becomes stronger as compared to single Co adatoms (Figure 4.11).

It is believed that the unknown defect is a Co-H complex due to the following reasons: (i) hydrogen is a common adsorbate species especially in cryogenic STM experiments on single adatoms [73]; (ii) it is known to weakly bound to the tip and can be scanned across the surface [74, 75]; and

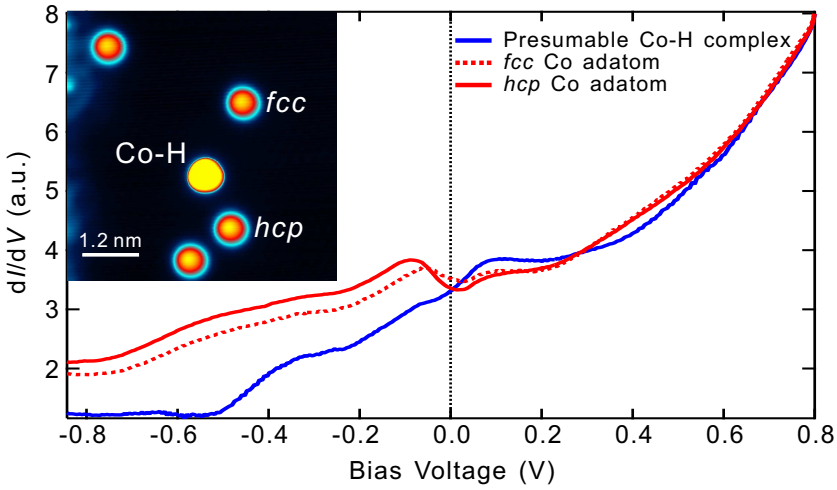

Figure 4.11: **Spectroscopy of a presumable Co-H complex**. The comparison of the spectra on the complex with those on single Co adatoms reveals a strong correlation between them. Similar features right below and above E_F are observed as on single Co adatoms. **Inset** shows the area where the spectra are recorded. (Tunneling parameters: V_{stab} = +0.8 V, I_{stab} = 1.0 nA, V_{mod} = 40 mV (rms), and T = 0.3 K.)

(iii) the defects are quite frequently observed, if the Co evaporator is not thoroughly out-gassed. However, the final proof for the Co-H complex by intentional adsorption of H is so far lacking. It might be interesting to study the magnetism of the Co-H complex in the future.

4.2 Tip

4.2.1 Tip preparation

In order to investigate the surface magnetism of nanostructures with atomic resolution, great care has to be taken in the fabrication of the spin-polarized tips. All the tips used for the STM results presented in this thesis are made from Cr coated polycrystalline W wire. They are very suitable for STM measurements, because stable sharp tips can be achieved by following

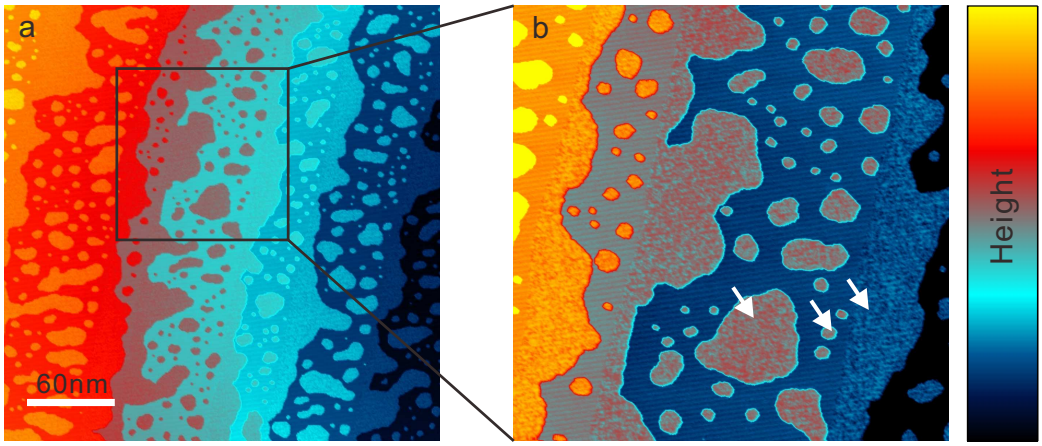

Figure 4.12: **Calibration of the Cr evaporation rate for the tip coating**. **(a)** STM topograph of the W(1 1 0) surface partially covered with Cr. **(b)** Zoom shows one atomic layer high Cr islands indicated with arrows. (Tunneling parameters: $V_{\text{stab}} = +1.0$ V, $I_{\text{stab}} = 0.1$ nA, and $T = 40$ K.)

a standardized preparation procedure as described in the following.

First the tips are electrochemically etched from W wire in a 8% NaOH solution by using the so-called reverse electrochemical etching [76, 77] and cleaned with distilled water. The etched tips are then clamped into a tip holder made of molybdenum and transferred into the UHV chamber with a tip shuttle, and flashed to about 1900 K by electron beam bombardment for a couple of seconds. The flash is useful to remove the contamination and oxide film from the tip surface and to make the apex blunt which is of advantage both for stable spectroscopic measurements and for a well-defined magnetization after the deposition of magnetic films onto the tip [78].

The nonmagnetic tips prepared in this way allow only for spin-averaged measurements. In order to characterize magnetic properties of surfaces, a chromium (Cr) film with a thickness of 45±20 atomic layers is deposited onto the tip end with a growth rate of ~1.4 ML/min followed by a soft annealing at 500 K for a couple of minutes [17, 36, 79, 78]. This usually yields a magnetization of the tip perpendicular to the sample surface after removing some of the Cr material by a tip-treatment like voltage pulsing. Since the tip material Cr is antiferromagnetic, it has a negligible stray field acting on the sample making it very suitable to study soft magnetic materials. Note that here a coverage of one atomic layer is defined as a complete cover of a W(1 1 0) surface with Cr atoms. In order to calibrate the growth rate of Cr, a W(1 1 0) crystal is cleaned by repeated cycles of annealing in oxygen atmosphere (2×10^{-7} mbar) for one hour and flashing

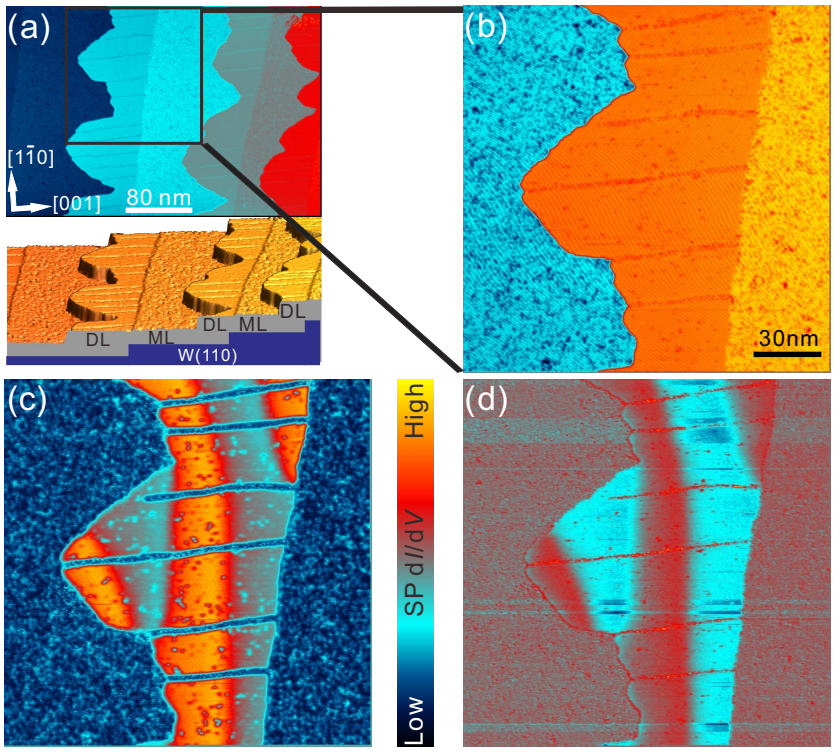

Figure 4.13: **Initial characterization of a Cr-coated W tip on Fe/W**(1 1 0). **(a) (Top)** STM topograph of 1.5 ML Fe/W(1 1 0) recorded with a Cr coated W tip. **(Bottom)** 3D view of the STM topograph with the ML and DL stripes as indicated. (Tunneling parameters: V_{stab} = +1.0 V, I_{stab} = 0.3 nA, and T = 0.3 K.) **(b)** STM topograph zoom recorded with the same Cr coated W tip at a different bias voltage. (Tunneling parameters: V_{stab} = +0.7 V, I_{stab} = 0.3 nA, and T = 0.3 K.) **(c)** Spin-resolved dI/dV map recorded simultaneously with (b) showing the out-of-plane magnetic domain contrast on the double layer with domain walls perpendicular to the dislocation lines. (Tunneling parameters: V_{stab} = +0.7 V, I_{stab} = 0.3 nA, V_{mod} = 20 mV (rms), and T = 0.3 K.) **(d)** Spin-resolved dI/dV map recorded with the same tip but at a different bias voltage. The DL also exhibits out-of-plane magnetic domain contrast at this energy. (Tunneling parameters: V_{stab} = -0.3 V, I_{stab} = 0.3 nA, V_{mod} = 20 mV (rms), and T = 0.3 K.)

twice to 2200 K for a couple of seconds [80]. Then after waiting for 10 minutes Cr is deposited for 20 seconds and a soft annealing is performed for 15 minutes. The STM topograph of the resulting W(1 1 0) surface partially covered by Cr is shown in Figure 4.12. It is seen that the growth is quite smooth. While a part of Cr decorates the step edges of W(1 1 0), atomic layer high islands are also visible on the terraces. From the image, a coverage of 0.45 ML is deduced, being the basis of the calibration of the growth rate for the tip coating.

The out-of-plane spin sensitivity of the Cr coated W tip is demonstrated on the double-layer Fe films on W(1 1 0) at low temperature, the magnetic properties of which have been well studied by SP-STM [43, 79, 81, 82, 83]. It was shown that Fe ML stripes on the W(1 1 0) have in-plane domains while double layer (DL) stripes have out-of-plane domains separated by Néel-type domain walls [84]. The W(1 1 0) substrate is cleaned as described before. After the final flash and a time delay of 90 sec, 1.5 ML Fe are deposited onto the hot surface resulting in a smooth film. Figure 4.13(a) and (b) show the STM topograph of Fe/W(1 1 0) recorded at two different bias voltages. The ML stripe is quite rough as compared to the DL which is probably caused by the difference in the adsorption of residual gas and other contaminants. On the DL stripes faint lines are visible which are the dislocation lines along the [0 0 1] crystallographic direction. Figure 4.13(c) is the dI/dV map recorded at +0.7 V. Contrast is observed on the DL stripes while there is no contrast on the ML. This is the magnetic contrast due to the out-of-plane magnetic domains in the DL stripes [79, 81, 83]. A similar magnetic contrast is also observed at a different bias voltage (4.13(d)). There is only a small difference in the contrast between the left rim of the domains, which appears a little brighter, and the right rim, which appears a little dimmer. This indicates only a slight canting of the tip magnetization relative to the surface normal. Therefore, this Cr-coated W tip is mostly sensitive to the out-of-plane magnetization of the sample.

4.2.2 Tip calibration

While it is quite routine to prepare a magnetic tip with out-of-plane spin sensitivity for magnetic surfaces such as Fe DL on the W(1 1 0) surface (Figure 4.13) by coating Cr films with a certain thickness, usually additional effort has to be spent in retaining sufficiently strong magnetic contrast on single adatoms. The reason for a possible loss of the spin sensitivity of the tip in this case is the following: after changing the sample from Fe-DL/W(1 1 0) to Co adatoms on Pt(1 1 1), the micro-tip used for imaging

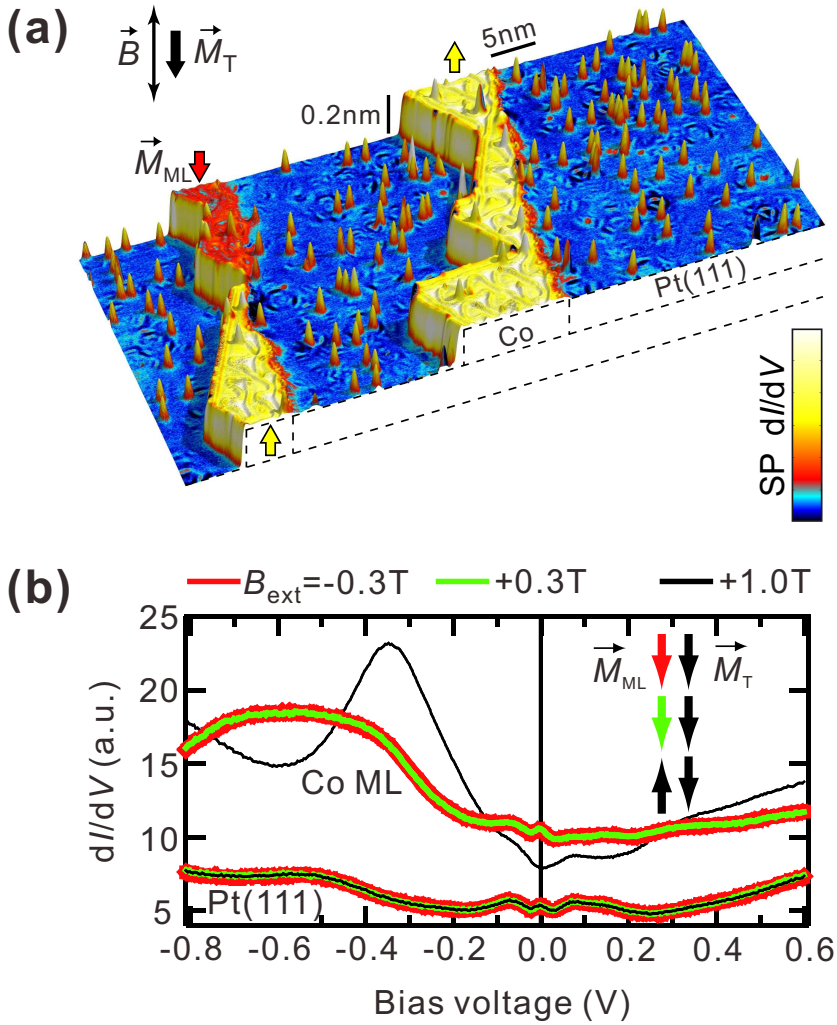

Figure 4.14: **Further calibration of a Cr-coated W tip on Co-ML/Pt**(1 1 1). **(a)** 3D STM topograph of the sample of Figure 4.2 colored with the simultaneously recorded spin-polarized dI/dV map. (Tunneling parameters: V_{stab} = +0.3 V, I_{stab} = 0.8 nA, V_{mod} = 20 mV (rms), and T = 0.3 K.) **(b)** dI/dV curves from the Co ML stripe (top curves) and from the Pt terrace (bottom curves) at different external magnetic fields $\vec{B}_{ext}$ as indicated at the top and consequently different relative orientations of the Co ML magnetization $\vec{M}_{ML}$ and the tip magnetization $\vec{M}_T$ as indicated on the right. (ML curves are offset for clarity. Tunneling parameters: V_{stab} = +0.6 V, I_{stab} = 1 nA, V_{mod} = 10 mV, and T = 0.3 K.)

the surface can be different due to a slightly different angle of the sample surfaces and due to the bluntness of the tip. In order to recover a spin polarization of the tunneling part of the tip, Cr-coated W tips are eventually dipped into a magnetic layer, after which the contrast and magnetization direction are examined by checking the magnetic contrast on the domains of the magnetic layer. Moreover, because the magnetic contrast depends both on the energy-dependent spin polarizations of the tip and the sample (see Chapter 2.5), it is valuable to calibrate the tip on a well studied magnetic film which can be taken as a calibration reference. Therefore, we need a ferromagnetic layer with out-of-plane magnetic anisotropy on the same sample as where the atoms are deposited. In the experiments of this work, the Co ML stripes on Pt(1 1 1) are taken as the reference magnetic system. It is believed that some Co nanoclusters are attached to the Cr-coated tip upon the dipping. The exchange coupling of the nanoclusters with the antiferromagnetic Cr film gives rise to a relative large coercivity which enables to align the tip and sample magnetizations parallel or antiparallel by an external field perpendicular to the sample surface. The calibration of the tip's spin polarization on the Co ML stripes is explained in detail in the following.

Figure 4.14(a) shows the overview of the sample on the same area as in Figure 4.2, which is now the STM topograph colorized with the spin-resolved dI/dV signal simultaneously recorded at +0.3 V. Because the tip is spin-polarized with a sensitivity to the out-of-plane magnetization component, the up-pointing (yellow) and down-pointing (red) domain contrast is visible in the Co ML stripes [17] (also see Chapter 2.5).

The calibration is achieved by regularly recording dI/dV curves on the Co ML stripes and on the Pt terraces for each tip. Figure 4.14 shows corresponding dI/dV curves taken at different magnetic field $\vec{B}$. The dI/dV curves are identical for ±0.3 T because the ML magnetization as well as the magnetization of the tip remain unchanged at small $\vec{B}$ (in this case the tip magnetization points in the direction of negative field). At +1 T the Co ML stripe is aligned with $\vec{B}$, while the tip magnetization is still opposite to $\vec{B}$, leading to a characteristic change in the dI/dV curve recorded on the ML stripes [17]. However, the curve recorded on the Pt is still unchanged. Such curves prove that the magnetization and the electronic structure of this tip are stable at least up to ±1 T and that the tip has a strong polarization in the entire energy range from -0.8 V to +0.6 V. Additionally, during recording magnetic field dependent dI/dV maps (see Chapter 6.3), a part of a Co ML stripe is always within the image area. Thereby, it is always checked, that the dI/dV signal on the Co ML stripe is not changed

during the measurement of magnetization curves, indicating that the tip magnetization is not canting. Furthermore, tip switches from upward to downward or vice versa are thereby identified and the corresponding magnetization curves can be corrected(see Chapter 6.3). Note that the critical switching field may vary from tip to tip because differently sized clusters of magnetic materials are attached on top of the Cr layers due to the eventual dipping of the tip into the magnetic layers (Co ML stripes). For the dI/dV curve of Pt terraces, care has to be taken that the curves are recorded far from Co nanostructures to avoid the proximity effect (see Chapter 8.2).

Chapter 5

Spin-resolved spectroscopy of Co adatoms

In this chapter the spin-resolved spectroscopic measurements on Co adatoms are reported. The spin-resolved differential conductance through a magnetic tunnel junction consisting of a Cr coated W tip, a vacuum barrier and a single Co adatom on a Co monolayer is measured. It is proved, that the spin polarization at the Fermi level (E_F) above this atomic protrusion is reversed with respect to the atomically flat Co layer, and thus dominated by majority electrons. Experiments with the same Cr tip electrode and Co adatoms or dimers on Pt(1 1 1) as the second electrode suggest that the inversion might be unique for single atomic protrusions due to the reduced coordination.

This chapter is organized as follows: after an introduction on the research background, the results of the spin-resolved spectroscopic measurement on Co adatoms are presented, followed by a discussion on the leading mechanism giving rise to the inversion of the spin polarization in the vacuum above adatoms at E_F. Finally, a brief summary is given with the main conclusion drawn from the measurements.

The results of this chapter have been published in: L. Zhou, F. Meier, J. Wiebe and R. Wiesendanger, "Inversion of spin polarization above individual magnetic adatoms", *Phys. Rev. B.* **82**, 012409 (2010).

5.1 Introduction

Magnetic atoms adsorbed on surfaces (adatoms) are of great interest due to their importance to the science of nanomagnetism and to the technology of spin-based solid quantum devices, *i.e.*, spintronics [1]. The ultimate

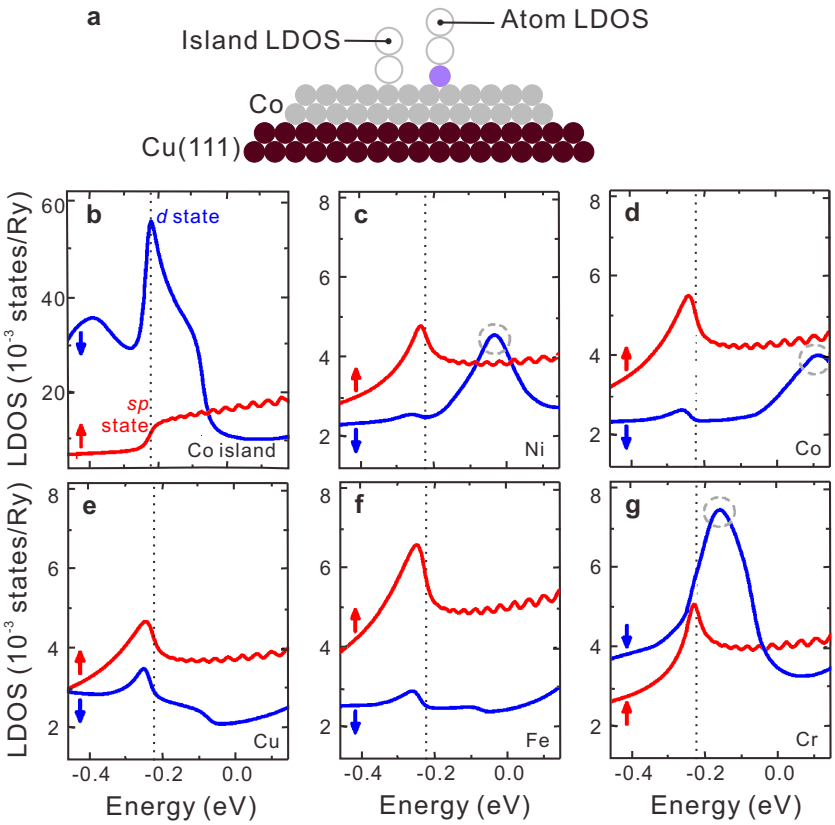

Figure 5.1: **Calculated vacuum LDOS above magnetic adatoms on Co bilayer on Cu**(1 1 1). Both spin-majority (red) and spin-minority (blue) channels are presented. **(a)** Sketch of the calculation setup. **(b)** Vacuum LDOS of Co *hcp* bilayer islands on the Cu(1 1 1) surface. **(c)-(g)** Vacuum LDOS above Ni, Co, Cu, Fe, and Cr adatoms on the Co island. Figure is taken from [85].

miniaturization of magnetic devices towards single atoms requires exact knowledge about the spin-resolved electronic density of states at the corresponding size level. In particular, the spin polarization at E_F of magnetic nanostructures is of crucial importance because it determines the magnetic properties of materials, as *e.g.*, the tunnel magnetoresistance of a magnetic tunnel junction (MTJ) [86]. Therefore, MTJs can, in turn, be exploited to study the spin polarization of electrode materials. A well defined realization of a MTJ is the magnetic sample and a magnetically coated tip of a SP-STM, separated by a vacuum barrier [5, 41, 42, 55, 78, 87, 88]. Such a prototypical system has several appealing advantages: first, the atomic geometry of the sample electrodes can be determined by constant-current

images accurately and thereby the interfaces of MTJs are highly controllable; second, the spin-resolved LDOS *above* samples can be probed directly at the tip apex; and finally the comparison to first-principles calculations is feasible.

There are many experimental and theoretical studies on the spin resolved LDOS above *atomically flat surfaces* near E_F using STM [17, 66, 67, 68, 69, 87, 90, 91, 92, 93], among which, in particular, the dominance of minority electrons for cobalt surfaces was revealed [17, 66, 67, 68, 69, 93]. There are also many theoretical results on the spin-resolved electronic structure of single adatoms [23, 27, 28, 29, 30] which unfortunately only predict the dominance of the minority LDOS *at* the adatoms. However, the important quantity for tunneling devices is the spin-resolved LDOS *above* adatoms, which was calculated in [85, 89]. It was predicted in [85] to exhibit a reversal of the spin polarization with respect to the magnetic substrate in a certain energy window associated with a substrate spin-polarized free-electron like surface state of majority character (see Figure 5.1), while in [89] a reversal in the vicinity of E_F was found to be correlated with dominating atomic *sp*-states of majority character (see Figure 5.2). Figure 5.1 shows the calculation results for the LDOS in the vacuum above various magnetic adatoms on a Co island on the Cu(1 1 1) surface [85]. In Figure 5.1(b) the LDOS of the Co bilayer islands is presented, where the resonance of minority character at -0.22 eV is of *d* symmetry while the step-like onset of majority character at the same energy is of *sp* symmetry. This dispersive *sp* state is buried below the *d* resonance, and hence the minority states are dominant above the Co island. However, when a magnetic atom is adsorbed on the island, the electrons of the adatom are scattered more strongly by the *sp* electrons in the substrate because they are more free as compared to the *d* electrons. This spin-dependent scattering leads to the inversion of the spin polarization above the adatom, *i.e.*, the dominance of the majority state in the corresponding energy range (Figure 5.1(c)-(f); Figure 5.1(g): Cr is special, see [85] for details). Figure 5.2 shows the calculation results for the LDOS of Co adatoms on Mn/W(1 1 0). The LDOS in the Co muffin tin shows that minority states are dominating at the Co adatom at E_F, to which the d_{xz} state contributes most. However, in the vacuum this state is suppressed due to the mismatch of the symmetry while only the *s* and *p* states contribute a larger amount, resulting in the dominance of the majority states at E_F. Experimentally, four results on the direct measurement of the spin-resolved LDOS *above* atomic protrusions [55, 56, 94, 89] were reported; however, the spin character was discussed only in [89]. The key issue in such experiments is a separate characterization of the tip and sample spin-polarizations in order to find out the spin characters without

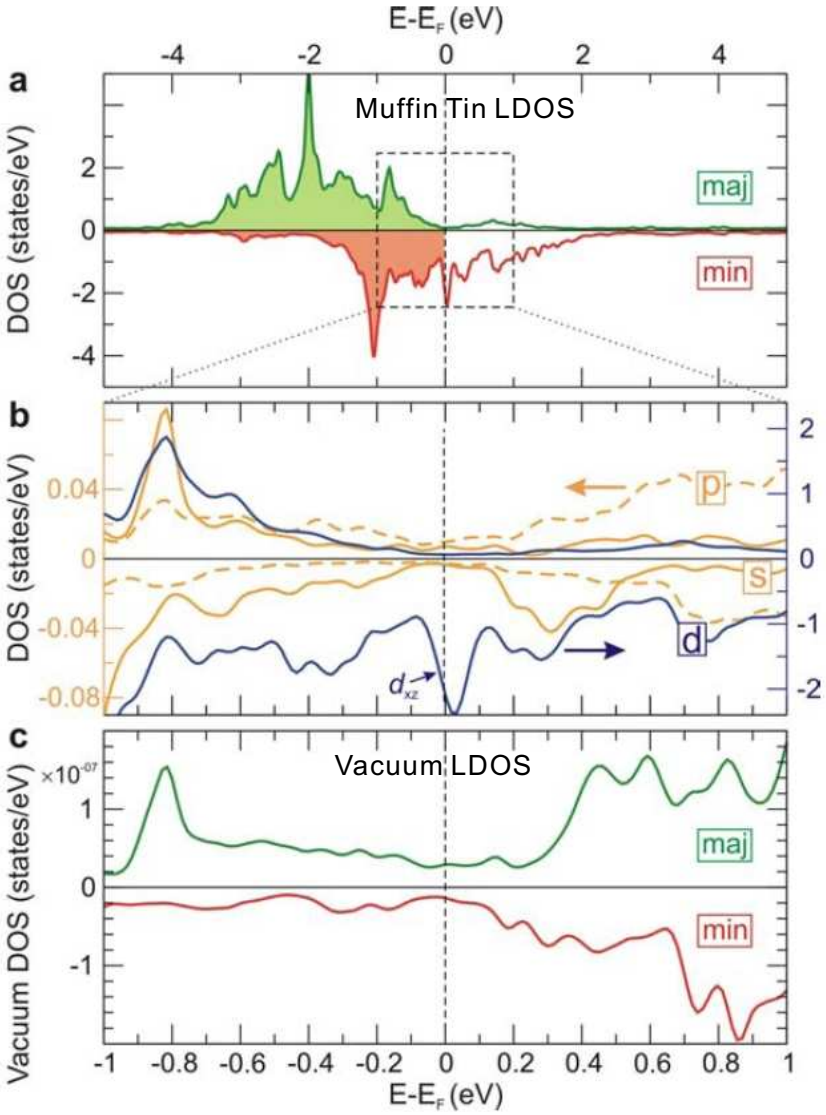

Figure 5.2: **Calculated LDOS above Co adatoms on Mn/W**(1 1 0). Both spin-majority (positive) and spin-minority (negative) channels are presented. **(a)** LDOS in the Co muffin tin shows the dominance of minority states. **(b)** Decomposition demonstrates that the d_{xz} state contributes most to the spin-minority LDOS. **(c)** Vacuum LDOS above the Co adatom shows that the d_{xz} state is strongly suppressed in the vacuum. Figure is taken from [89].

comparison to theory.

Here I present a direct measurement of the spin-resolved LDOS *above* adatoms on different substrates using low temperature SP-STS. The ability of using exactly the same tip electrode for the four different sample electrodes, namely Co monolayer, Co adatom on Co monolayer, Co adatom on Pt(1 1 1) and Co dimer on Pt(1 1 1) in one experiment enables to determine the spin characters of both the tip and sample electrodes separately.

In the experiments exactly the same sample as described in Chapter 4.1 and in [55, 56] is used as the first electrode. As the second electrode a Cr-coated W tip with the magnetization $\vec{M}_\mathrm{T}$ perpendicular to the sample electrode surface [55, 56] is used, the fabrication of which has been described in Chapter 4.2.

5.2 Spin-resolved spectroscopy of Co adatoms: Inversion of spin polarization

In order to gain information about the LDOS $\rho_\mathrm{S}(E, \vec{r}_\mathrm{T})$ *above* the sample and that of the tip $\rho_\mathrm{T}(E_\mathrm{F})$, as well as their spin polarizations P_S and P_T, the spin-resolved differential tunneling conductance $\mathrm{d}I/\mathrm{d}V$ is measured in the spectroscopic mode. For a small voltage range around the Fermi energy, it is approximately given by Equation 2.25

$$\begin{aligned}\frac{\mathrm{d}I}{\mathrm{d}V}(V, \vec{r}_0, \theta) \quad &\propto \quad \rho_\mathrm{T}(E_\mathrm{F}) \cdot \rho_\mathrm{S}(E_\mathrm{F} + \mathrm{e}V, \vec{r}_0) \\ &\quad \cdot \left[1 + P_\mathrm{T}(E_\mathrm{F}) P_\mathrm{S}(E_\mathrm{F} + \mathrm{e}V, \vec{r}_0) \cos\theta\right], \end{aligned} \tag{5.1}$$

where $\vec{r}_0$ is the position of the foremost tip atom and θ is the angle between its magnetization $\vec{M}_\mathrm{T}$ and the time-averaged magnetization of sample $< \vec{M}_\mathrm{S} >$. The time window for averaging is determined by the lock-in time constant. Since the tip electrode material is Cr, an external magnetic field perpendicular to the sample surface can be used to align the magnetization of the sample either parallel ($\uparrow\uparrow$) or antiparallel ($\uparrow\downarrow$) with respect to the tip [55], resulting in the spin-resolved differential tunneling conductance $\mathrm{d}I^{\uparrow\uparrow}/\mathrm{d}V(\mathrm{V})$ and $\mathrm{d}I^{\uparrow\downarrow}/\mathrm{d}V(\mathrm{V})$. Assuming a constant distance between the tip and sample for the two cases ($\uparrow\uparrow$, $\uparrow\downarrow$), the product of the two electrodes' spin-polarizations can be deduced from the magnetic asymmetry

$$\begin{aligned} A_\mathrm{mag}(V) \quad &\equiv \quad (\mathrm{d}I^{\uparrow\uparrow}/\mathrm{d}V - \mathrm{d}I^{\uparrow\downarrow}/\mathrm{d}V)/(\mathrm{d}I^{\uparrow\uparrow}/\mathrm{d}V + \mathrm{d}I^{\uparrow\downarrow}/\mathrm{d}V) \\ &= \quad P_\mathrm{T}(E_\mathrm{F}) \cdot P_\mathrm{S}(E_\mathrm{F} + \mathrm{e}V, \vec{R}_\mathrm{T}). \end{aligned} \tag{5.2}$$

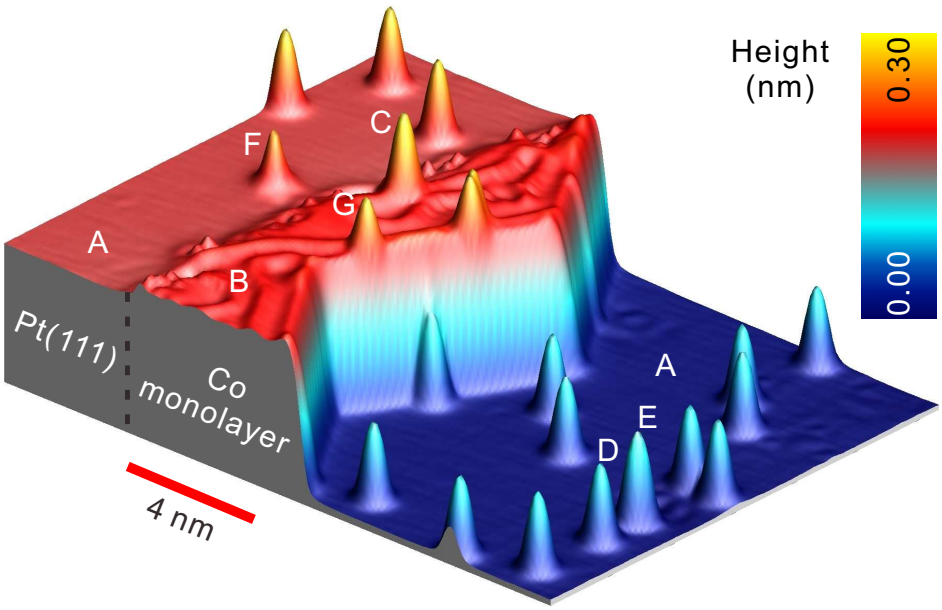

Figure 5.3: **Overview of the sample-electrode** with Pt(1 1 1) terraces (A), Co monolayer (B), Co adatoms on Co monolayer (C), Co adatoms on Pt(1 1 1) (D), and Co dimer on Pt(1 1 1) (E). A Co dimer (E) is higher than single Co adatoms (D) on the platinum terrace. Co adatoms on the Co monolayer (C) appear higher than those at the Co-monolayer edge (G) at this bias voltage. A defect (F) is also visible on the platinum terrace. (Tunneling parameters: $V_{\mathrm{stab}} = +0.3$ V, $I_{\mathrm{stab}} = 0.8$ nA, and $T = 0.3$K.)

Thus the sample spin-polarization can be extracted only with the knowledge of the tip spin-polarization. This can be achieved by measuring the voltage dependent A_{mag} on Co monolayers with well-known $P_{\mathrm{S}}(E_{\mathrm{F}}+\mathrm{e}V, \vec{R}_{\mathrm{T}})$ to calibrate P_{T} and then using exactly the same tip to characterize the Co adatoms with unknown $P_{\mathrm{S}}(E_{\mathrm{F}} + \mathrm{e}V, \vec{R}_{\mathrm{T}})$. Care has to be taken to evaluate $\mathrm{d}I/\mathrm{d}V$ curves at the same tip-sample distance. While there is no distance change for Co adatoms and dimers on Pt(1 1 1), we take into account the measured apparent height variation on Co adatoms on Co monolayers of less than 14 pm due to the magnetization switching and normalized the spectra with the transmission coefficient using the one-dimensional Wentzel-Kramers-Brillouin (WKB) approximation for a trapezoidal barrier with the height Φ calculated from the Cr and Co workfunctions Φ_{Cr}, Φ_{Co}: $\Phi = (\Phi_{\mathrm{Cr}} + \Phi_{\mathrm{Co}})/2 = (4.5\ \mathrm{eV} + 5.0\ \mathrm{eV})/2$ [43].

A representative overview of the sample is displayed in Figure 5.3 where Co adatoms on different substrates can be found. This makes it

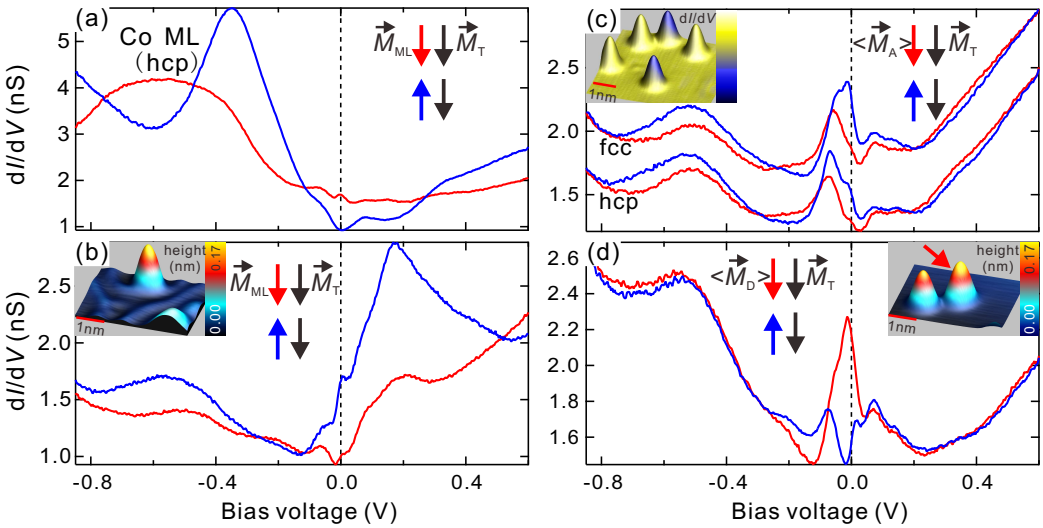

Figure 5.4: **Spin-resolved spectroscopy of Co adatoms and dimers on different surfaces**. **(a)** Spin-resolved dI/dV curves acquired over an *hcp* area of a monolayer as illustrated in the inset of (b). **(b)** Spin-resolved dI/dV curves acquired over a single adatom on an *fcc* region of a monolayer. **Inset**: STM topograph of the area with the single adatom sitting on the monolayer. The dislocation network on the monolayer surface is visible [17]. **(c)** Spin-resolved dI/dV curves acquired over single adatoms sitting on *fcc* and *hcp* lattice sites on a platinum terrace. (Curves from *fcc* adatoms are vertically offset by 0.5 nS for clarity.) **Inset**: STM topograph colored with the simultaneously recorded dI/dV map at I_{stab} = 0.3 nA and V_{stab} = -0.1 V of an area with several *fcc* (purple) and *hcp* (gold) adatoms (vertical scale from 0 to 0.17 nm). **(d)** Spin-resolved dI/dV curves acquired over the center of a dimer with both adatoms sitting on nearest neighbouring *fcc* sites on a platinum terrace. **Inset**: STM topograph of the area with a single adatom and the compact dimer (arrow). Curves in (a)-(d) change with the relative orientation of sample and tip magnetizations as indicated. (Tunneling parameters: V_{stab} = +0.6 V, I_{stab} = 1.0 nA, V_{mod} = 10 mV (rms), and T = 0.3 K.)

possible to compare the results of adatoms in distinct surroundings in a well-defined way. A Co monolayer patch (B) decorates the step edge of the Pt(1 1 1) and exhibits a dislocation network induced by the coexistence of face-centered cubic (*fcc*) and hexagonal closed-packed (*hcp*) stacked areas [17]. On the platinum terraces (A), single Co adatoms (D) and Co dimers (E) are visible. There are also single adatoms (C) residing on the monolayer. Figure 5.4(a)-(d) show the dI/dV curves of the MTJ using the same tip electrode but with a Co monolayer (a), a Co adatom on a Co monolayer (b), a Co adatom on Pt(1 1 1) (c), and a Co dimer on Pt(1 1 1) (d) as the second electrode in (↑↑) and (↑↓) configurations. Figures 5.5(a)-(d) show A_{mag} calculated from Figure 5.4(a)-(d), respectively. These curves will also serve to choose a proper bias voltage to image the magnetization of Co adatoms (see Chapter 6).

In order to calibrate P_{T} the Co monolayer is first characterized with different relative orientation of sample's and tip's magnetizations (Figure 5.4(a)). These spectra are recorded over the *hcp* area of the monolayer depicted in the inset of Figure 5.4(b). As seen from Figure 5.5(a), the tunneling junction has a large positive A_{mag} at E_{F}, *i.e.*, $P_{\mathrm{T}}(E_{\mathrm{F}}) \cdot P_{\mathrm{S}}^{\mathrm{ML}}(E_{\mathrm{F}}, \vec{R}_{\mathrm{T}}) > 0$. The spin-resolved LDOS *above* Co monolayers on Pt(1 1 1) was recently studied using SP-STS and first-principles calculations [17]. Figure 5.6 shows the calculation results of the spin-resolved LDOS in the vacuum 6.7 Å above Co monolayers using the Tersoff-Hamann model. The results for the majority and minority channels as well as the sum of both for both *fcc* and *hcp* stacked areas are presented. The resonance at -0.35 V was assigned to a *d*-like minority surface resonance [17], which is commonly accepted as the fingerprint of Co surfaces on various substrates [17, 66, 67, 68, 69, 93]. The calculations showed that the minority character is extended to E_{F}, i.e. $P_{\mathrm{S}}^{\mathrm{ML}}(E_{\mathrm{F}}, \vec{R}_{\mathrm{T}}) < 0$ [17]. Therefore, it is immediately clear that the tip also has a negative spin polarization at E_{F}, i.e. $P_{\mathrm{T}}(E_{\mathrm{F}}) < 0$. This conclusion is consistent with the fact that Cr is negatively polarized around E_{F} [95]. Note that A_{mag} changes the sign between E_{F} and -0.35 V, which indicates a reversal of the Cr-tip spin-polarization around -0.1 V as also found by Pietzsch *et al.* [68].

Let us now use a single Co adatom sitting on an *fcc* area of the Co monolayer surface as the second electrode (Figure 5.4(b)). The adatom is stabilized by the underlying monolayer through direct ferromagnetic exchange interaction [17, 85]. The measured dI/dV spectra show that the strong *d*-like surface resonance at -0.35 V is quenched and an additional state appears at +0.2 V (Figure 5.4(b)). More importantly, by comparing A_{mag} of the Co adatom (Figure 5.5(b)) to that of the monolayer (Figure 5.5(a))

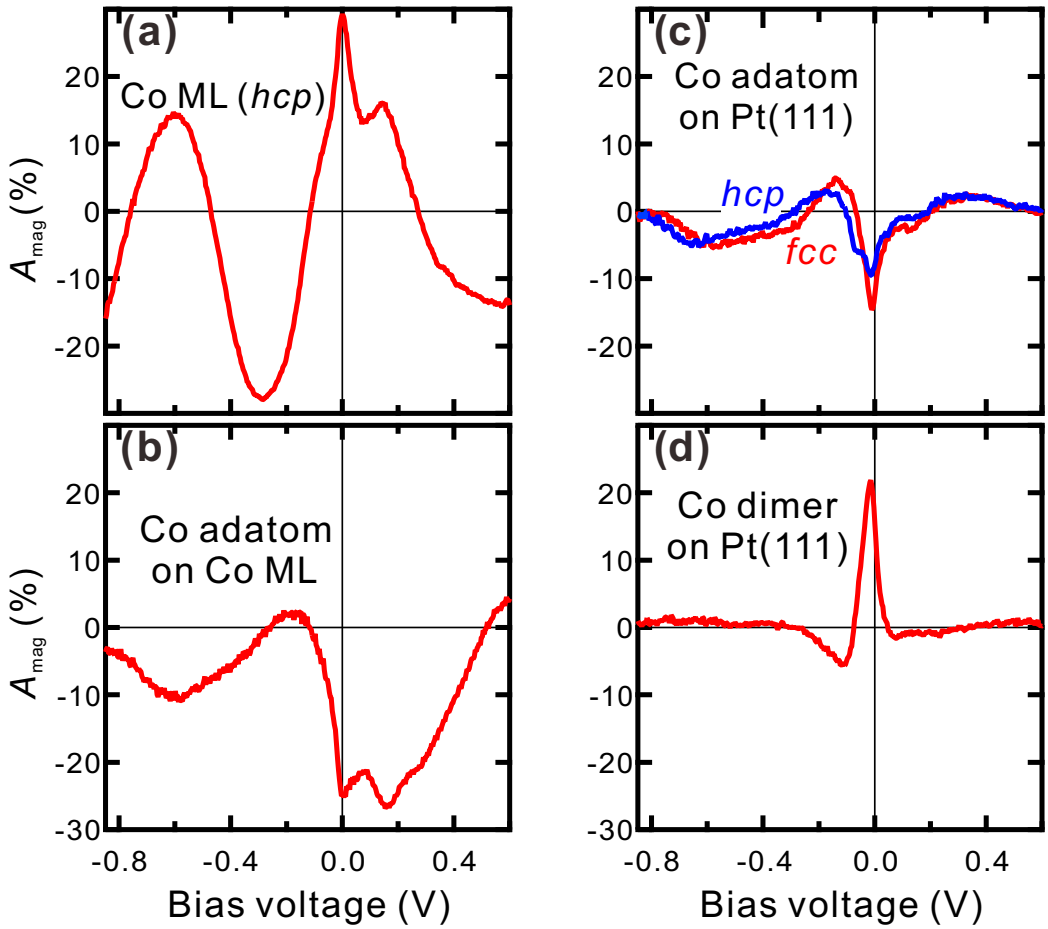

Figure 5.5: **(a)-(d). Magnetic asymmetry** A_{mag} calculated from the spin-resolved dI/dV curves in Figures 5.4(a)-(d), respectively. Note that the tip's spin-polarization is negative around E_{F} and has a sign reversal at about -0.1 V.

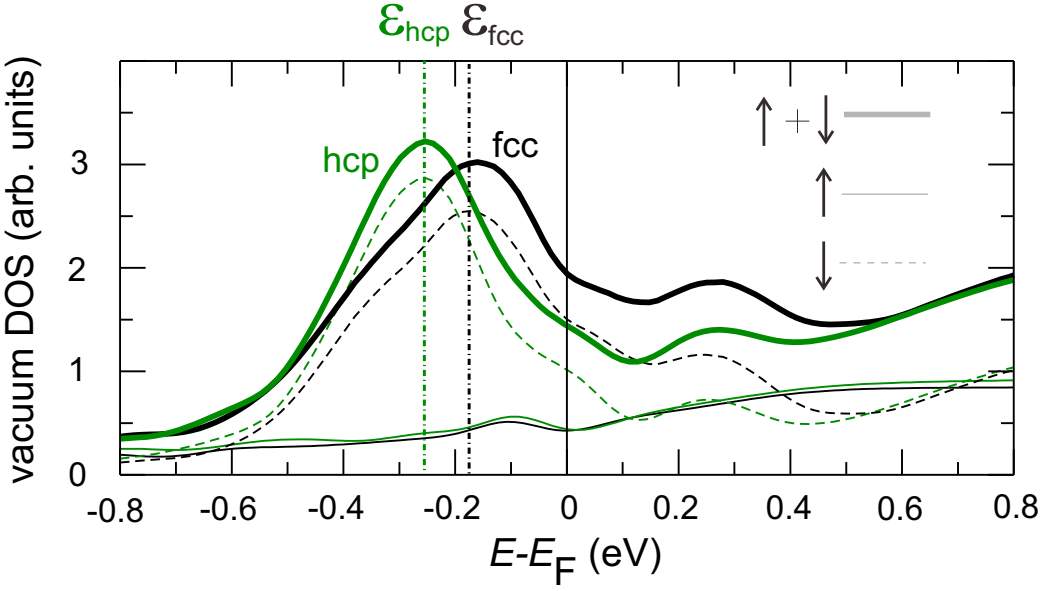

Figure 5.6: **Vacuum LDOS for Co monolayer stripes**. The spin-majority (thin solid line), spin-minority (thin dashed line) channels and the sum of both (thick solid line) for *fcc* and *hcp* stacked areas are presented. Figure is taken from [17].

it is seen that now the sign of the spin polarization around E_F is reversed and a dominance of majority electrons is found instead. Thus, one main finding is that even one atomic protrusion at the interface of a MTJ can reverse the sign of the spin polarization. Such a significant effect of single atomic defects on the vacuum tunneling is also proposed from calculations on magnetic adatoms on magnetic substrates [85]. However, this result is in contrast to the measurements on single Fe and Cr adatoms on Co islands [94], above which minority spin states in the energy region near E_F are still dominating. Contrary to the prediction of the calculations in [85] there is no indication that the sign change of the spin polarization at E_F is due to the resonant scattering of electrons from the spin-polarized surface state of the underlying Co substrate, which is of minority character and located at about -0.35 eV below E_F.

In order to find out the reason for the inversion of the spin polarization of the LDOS in the vacuum, the spin polarization above Co adatoms on Pt(1 1 1) is investigated. Different from cobalt surfaces, Pt(1 1 1) is known to have no occupied spin-polarized surface state [65] and consequently a spin imbalance due to the spin-polarized resonant scattering effect can be excluded [85]. As shown in the STM topograph colored with the dI/dV

map simultaneously recorded at -0.1 V (Figure 5.4(c) inset), two types of adatoms are found with identical height but distinct spectroscopic signature. This spectroscopic signature is induced by the two possible binding sites and can be traced back to a slight shift of a pronounced peak at -0.05 V in their LDOS in the vacuum (Figure 5.4(c)) [55, 58], which has been studied in detail in Chapter 4.1.2. When the magnetization orientation relative to the tip magnetization switches from parallel to antiparallel, its intensity increases for both types of adatoms. As visible from A_{mag} in Figure 5.5(c), the corresponding state at -0.05 V for both *fcc* and *hcp* adatoms has a majority character leading to an opposite spin polarization with respect to that of the monolayer. This finding is quite significant, because all theoretical calculations so far predicted a dominance of the minority density of states *at* the adatom [23, 27, 28, 29, 30]. It is anticipated that the inversion of the spin-polarization in the vacuum region might be a particular property of single adatoms on atomically flat substrates.

To further test this conclusion, A_{mag} is examined when just one additional Co atom is added and a closed packed dimer is formed. The Co dimer is well suited for direct comparison, since apart from the broadening of the *d* band no drastic changes in the LDOS *at* the dimer with respect to that of the single adatom are expected from calculations [23, 27]. In particular, minority states are still expected to dominate at E_{F}. Consequently, the main difference of the Co dimer with respect to the Co adatom is an increase of symmetry breaking which can affect the electronic state in the vacuum. Figure 5.4(d) illustrates the dI/dV curves obtained over the center of the dimer. An area containing a single adatom and a dimer (arrow) is shown in the inset. This dimer is composed of two nearest neighbouring *fcc* adatoms, i.e. a compact dimer, and appears elliptical and higher than single adatoms. The two adatoms are coupled through direct ferromagnetic exchange interaction as shown by calculations [23, 27, 56]. By comparing the spectra with Figure 5.4(c), it is found that the dimer spectrum resembles that of single adatoms in the energy range from -0.8 V to -0.2 V and above +0.2 V. However, near E_{F} the spin polarization of the state at -0.05 V is clearly reversed. This is also visible in Figure 5.5(d) where the dominating minority state leads to a negative spin polarization of the LDOS at E_{F} *above* the dimer as found for the complete monolayer.

5.3 Discussion: Mechanism of the inversion

The comparison of the Co adatom on two different surfaces indicates that the substrates play a minor role in the inversion, and the mechanism of

the spin-dependent resonant scattering can be readily excluded. While from the comparison of the Co adatoms and dimers it is immediately clear that the coordination plays a key role in determining the spin character of LDOS especially at E_F, another possible mechanism has to be excluded first. It is believed that the exchange interaction between the tip and adatoms through the vacuum barrier may reverse the spin polarization in the vacuum [96]. If the exchange interaction is ferromagnetic, then it acts as an effective magnetic field and hence aligns the spin of adatoms in the direction of the tip magnetization resulting in the dominance of majority states. However, this mechanism can also be excluded in the current experiment. First, the direct exchange interaction between the Co adatom and the Co monolayer is much stronger than the exchange interaction between the adatom and the tip if there is any, but the inversion of the spin polarization is still observed. Second, for the tip-adatom distance geometry defined by V_{stab} = +0.3 V and I_{stab} = 0.8 nA the effective magnetic field from the tip is in the order of 0.1 T (see Chapter 6.6), and therefore the field that has been applied during recording the spectra in Figure 5.4 and 5.5, *i.e.*, ±1 T, is strong enough to saturate the adatom magnetization.

In the following the coordination effect is discussed. The comparison of the Co adatom and dimer highlights the importance of the coordination on the spin character of the LDOS especially at E_F and implies, that the observed inversion of the sign of the spin polarization is unique for single magnetic atoms adsorbed on atomically flat metallic surfaces. Electronically, coordination can change the hybridization and symmetry of the adatoms' electronic states. Therefore, one possible mechanism responsible for the inversion is that *sp* electrons, of which the spin state might be opposite to that of the *d* electrons due to the hybridization, contribute most strongly to the spin polarization at E_F in the vacuum. Single adatoms have the highest rotational symmetry normal to the surface and therefore possess a LDOS at E_F with large contribution from high-symmetry electrons e.g. *s*, p_z and d_{z^2} electrons. Upon vacuum tunneling the *d* electrons decay faster than *sp* electrons leading to the dominance of *sp* over *d* electrons at E_F in the vacuum above them. However, the formation of a dimer or a monolayer increases the lateral coordination number and, as a result, reduces the rotational symmetry of the atomic state. This disfavors those electrons of high symmetry electrons and could explain the disappearance of the effect for the dimer. In fact, such a mechanism is found to be dominant in the vacuum tunneling on 3*d* adatoms and pyramids on (0 0 1) and (1 1 0) magnetic surfaces (Figure 5.2) [89, 97], and might be present even for (1 1 1) surfaces. Because this discussion is based on the symmetry consideration, it implies that the observed inversion of the spin polarization

might be unique for single magnetic atoms adsorbed on atomically flat metallic surfaces.

5.4 Summary

In summary, spin-resolved spectroscopic measurements have been carried out on Co adatoms, and the spin-resolved LDOS in the vacuum above Co adatoms on different substrates has been investigated. A spin polarization in a wide energy range from -0.8 V to +0.6 V on Co adatoms on Pt(1 1 1) is observed, that can be used to measure magnetization curves of single atoms as shown in the next chapter. The measurements reveal that a single Co atomic protrusion can lead to the reversal of the sign of the local vacuum spin polarization at E_F with respect to the atomically flat Co surface. The comparison with other Co adatom nanostructures implies that the dominance of majority electrons might be unique for single magnetic adatoms. In order to identify the responsible mechanism, state-of-the-art first-principles calculations are demanding.

Chapter 6

Single-atom magnetization curves

This chapter explains the newly developed methodology for the measurement of magnetization curves of individual adatoms. Single Co adatoms on Pt(1 1 1) possess a vacuum spin-polarization in a wide energy range around E_F as revealed by the spin-resolved spectroscopic measurements (see Chapter 5.2). This is exploited to image the magnetization of single adatoms. By taking dI/dV maps at successive magnetic field, the magnetization curves of single Co adatoms can be obtained. Such curves are well described within a quasi-classical Langevin model for paramagnetic adatoms, from which the magnetic moment and the magnetic stability are deduced. It is found that the magnetization of Co adatoms is switching in the time domain with a period much shorter than the time resolution of the experiment.

This chapter is organized as follows: First, an introduction on the research background is presented; then the ability of imaging the magnetization of single adatoms is demonstrated, after which the methodology to measure magnetization curves is presented, and the modeling of the curves is described; finally the possible mechanisms responsible for the switching of the adatom magnetization in the time domain will be discussed followed by a brief conclusion.

Part of the results presented in this chapter have been published in: F. Meier, L. Zhou, J. Wiebe and R. Wiesendanger, "Revealing magnetic interactions from single-atom magnetization curves", *Science* **320**, 82-86 (2008).

6.1 Introduction

The measurement of the magnetization during sweeping an external magnetic field is called the *magnetization curve* of a magnetic material. It has played a key role in the development of modern research on magnetism, because such curves can directly supply information on the basic properties of magnetic materials, as *e.g.*, the hysteretic properties, magnetic moment, magnetic anisotropy, and magnetic interaction [98].

There are a couple of techniques which are able to image the magnetization and record the magnetization curve of materials, as *e.g.*, surface magneto-optic Kerr effect measurements [99], vibrating sample magnetometry [100, 101], XMCD [4], and superconducting quantum interference device (SQUID) magnetometry [102, 103]. The miniaturization of samples from bulk over thin films to single adatoms requires an ever increasing sensitivity of this method. Lately, XMCD has been demonstrated to be able to measure magnetization curves of adatoms on a non-magnetic substrate, but the technique is limited to large ensembles [4]. SQUID is conventionally an extremely sensitive magnetic-field detector and therefore is an approach of natural choice. However, to date the smallest single nanoparticle which has been studied by a micro-bridge-dc-SQUID, is a 1000-atom Co nanocluster with a magnetic moment of $\sim 2550\ \mu_B$ [2]. Recently, in order to further increase the sensitivity the same group used a carbon nanotube as the insulating barrier in the Josephson junctions resulting in a so-called nanoSQUID [3]. Such a device is believed to be able to measure changes in the magnetic moment of a single magnetic molecule, as *e.g.*, Mn_{12}, but no experimental results have been reported mainly due to the difficulty in attaching molecules onto the device with the required precision. While it is still possible to address the molecules via a certain chemical reaction [104], the attachment of individual magnetic atoms seems almost impossible without the help from STM or atomic force microscopy. Moreover, although the diameter of the key part of the nanoSQUID, *i.e.*, the nanotube, (~1 nm) is comparable to the dimension of a magnetic molecule leading to a sufficiently strong coupling of the molecule flux into the SQUID loop, it seems too large as compared to the size of an atom. As a result, very little of the magnetic field generated by the atom would penetrate the loop making it undetectable.

Different scanning probe approaches are potentially able to detect individual spins with nanometer spatial resolution ranging from magnetic resonance force microscopy (MRFM) [105] over magnetic exchange force microscopy [106, 107] to STM/STS [49, 54, 108, 109, 110, 111]. The resolution of the MRFM is limited to 25 nm; moreover, its efficiency is extremely

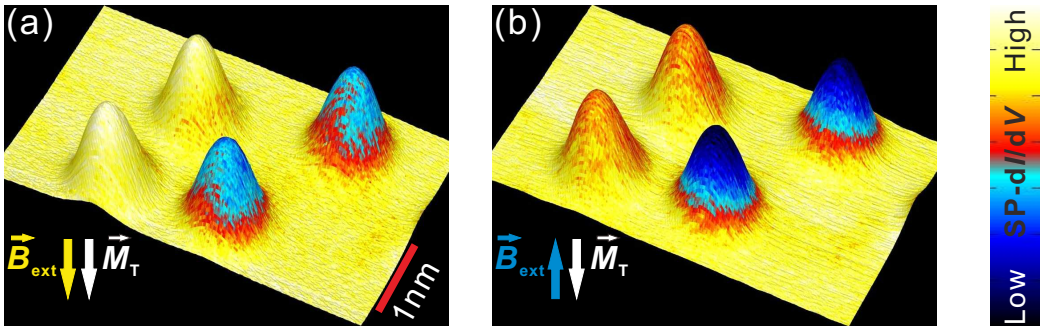

Figure 6.1: **(a)-(b)**. STM topograph colored with simultaneously recorded dI/dV map of two *fcc* and two *hcp* Co adatoms in opposite magnetic fields with the tip and adatoms' magnetization directions orientated parallel **(a)** and antiparallel **(b)**. (Tunneling parameters: V_{stab} = -0.1 V, I_{stab} = 0.3 nA, V_{mod} = 20 mV (rms), and T = 0.3 K.)

low due to a weak signal-to-noise ratio [105]. Spin-averaged STS was used to indirectly deduce the properties of single and coupled spins via the Kondo effect [54], the detection of noise [108, 109] or the observation of exchange splittings [110, 111]. Inelastic electron tunneling spectroscopy (IETS) was exploited to detect the spin flip and measure the magnetic moments and anisotropy as well as the magnetic dynamics of individual atoms [19, 20, 47, 48, 49, 53]. However, this method is limited to the study of the excited states and therefore cannot map static spin configurations. As a complementary method SP-STM can detect the ground state of individual spins in a nonmagnetic surrounding as will be shown in the following [55].

6.2 Magnetic imaging of adatoms

As has been described in Chapter 2.5, the differential conductance detected by SP-STM depends on the relative orientation of the tip and sample magnetizations, and therefore it can be used to map the surface spin structure of the sample.

In order to image the magnetization of single adatoms by SP-STM, care has to be taken to choose an appropriate bias voltage at which the adatom exhibits spin contrast.

As shown in A_{mag} in Figure 5.5(c) of Chapter 5, for single Co adatoms on Pt(1 1 1) the strongest spin contrast occurs at the energy of the prominent peak below E_{F}. Figure 6.1 shows the spin-polarized dI/dV maps at the corresponding bias voltage recorded at the external magnetic field B_{ext}

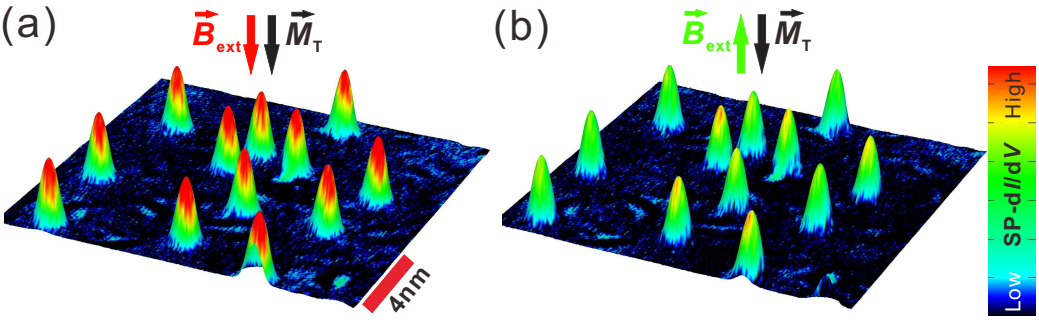

Figure 6.2: **(a)-(b)**. STM topographs colored with the simultaneously recorded dI/dV maps of Co adatoms in opposite magnetic fields with the tip and adatoms' magnetization directions parallel **(a)** and antiparallel **(b)**. (Tunneling parameters: V_{stab} = +0.3 V, I_{stab} = 0.8 nA, V_{mod} = 20 mV (rms), and T = 0.3 K.)

of −0.5 T and +0.5 T on an area with two *fcc* and two *hcp* Co adatoms. The magnetic field aligns the adatoms' magnetization in the parallel and antiparallel orientations with respect to the tip's at these two fields, as will be shown in the next section. It is obvious that the adatoms exhibit magnetic contrast between the two configurations. Unfortunately, the contrast between different adatoms at the same magnetic field is also strong, which is due to different binding sites and has been studied in detail in Chapter 4.1.2. In this case the magnetic imaging is not intuitive, and a strong effort is needed to separate the magnetic and electronic contributions.

Therefore, a bias voltage farther from E_{F} is used in order to avoid electronic contrast due to stacking. It is found in the A_{mag} curve in Figure 5.5(c) that the spin-polarized dI/dV signal of Co adatoms at +0.3 V has a sufficient asymmetry and the binding site has negligible influence. Therefore, it is mainly used to image the magnetization and measure magnetization curves throughout this work. The resulting spin contrast in dI/dV maps recorded at this bias voltage is shown in Figure 6.2 for parallel and antiparallel orientations of tip and adatom magnetizations. As in the dI/dV curves (Figure 5.4(c)), the dI/dV signal on the adatoms is reduced for antiparallel configuration of $\langle\vec{M}_{\text{A}}\rangle$ and $\vec{M}_{\text{T}}$. The electronic contrast is negligible at this bias voltage. One important result is, that the magnetic contrast is localized on a region of ~ 1 nm diameter around the center of each adatom. The polarization of the substrate induced by a single adatom is obviously too small to be detected. It will be shown in Chapter 8, that a larger number of Co-atoms is needed to induce a sufficiently large polarization within the Pt that can be detected.

6.3 Single-atom magnetization curves

With the ability of imaging the magnetization of single magnetic adatoms, it becomes possible to measure their magnetization curve. In the following, it is assumed, that the differential conductance is measured on the same atom at the same tip-atom distance, and only the atom magnetization is changed by the application of an external magnetic field. In this case, the corresponding tip and sample spin polarizations in Equation 2.25 are proportional to the magnetizations of the tip $\vec{M}_{\mathrm{T}}$ and sample $\vec{M}_{\mathrm{A}}$. When the magnetization is time dependent, as *e.g.*, for Co adatoms on Pt(1 1 1), this Equation 2.25 reads:

$$\frac{\mathrm{d}I}{\mathrm{d}V}(V,\vec{r}_0) \propto \frac{\mathrm{d}I}{\mathrm{d}V_0}(V,\vec{r}_0) + [\frac{\mathrm{d}I}{\mathrm{d}V_0}(V,\vec{r}_0)]_{\mathrm{SP}}\vec{M}_{\mathrm{T}} \cdot \left\langle \vec{M}_{\mathrm{A}} \right\rangle, \tag{6.1}$$

where $\vec{M}_{\mathrm{T}}$ is assumed to be constant, and $\left\langle \vec{M}_{\mathrm{A}} \right\rangle$ denotes the time-averaged magnetization of the adatom. The time window is determined by the sampling duration, 10 ms here. In this section isolated adatoms will be investigated which have a mean nearest neighbour distance of 2.4 ± 1 nm to each other and a distance more than 8 nm from the Co nanowires.

Spin-polarized dI/dV maps are recorded at +0.3 V at successive external magnetic fields B_{ext} being varied in sufficiently small steps from -7.5 T to +7.5 T and back to -7.5 T. To record dI/dV maps with a pixel resolution of 20-25 points/nm, a scan speed of 25 nm/s and a lock-in time constant of 1 ms are typically used. With these settings, the time duration to record dI/dV maps in forward and backward channels simultaneously with topographs of an area of 25 nm × 15 nm is in the order of 15 min, and hence the time period to record a full magnetization curve is in the order of 12 hours. The holding time is long enough for the measurements. As will be shown below, the adatoms are already saturated at a field lower than 1.0 T at 0.3 K; therefore only the dI/dV maps recorded in the range of ±1.5 T are presented in Figure 6.3(III)-(X X X VIII), which are taken for an area as shown in Figure 6.3(I). As visible in the figure, a patch of a Co nanowire is always included in the scanned area so that the magnetization state of the tip can be always monitored simultaneously; the initial $\vec{M}_{\mathrm{T}}$ and sample's magnetizations are aligned by the positive field (up). In order to reveal the possible relation of the magnetic properties with the binding site, the dI/dV map at -0.1 V is always recorded in the backward channel as well, as shown in Figure 6.3(II) (see Chapter 4.1.2). As visible, four of the eight adatoms are sitting on the *fcc* sites and appear blue, while the remaining four ones are on the *hcp* sites and appear with almost the same color as the Pt(1 1 1) substrate.

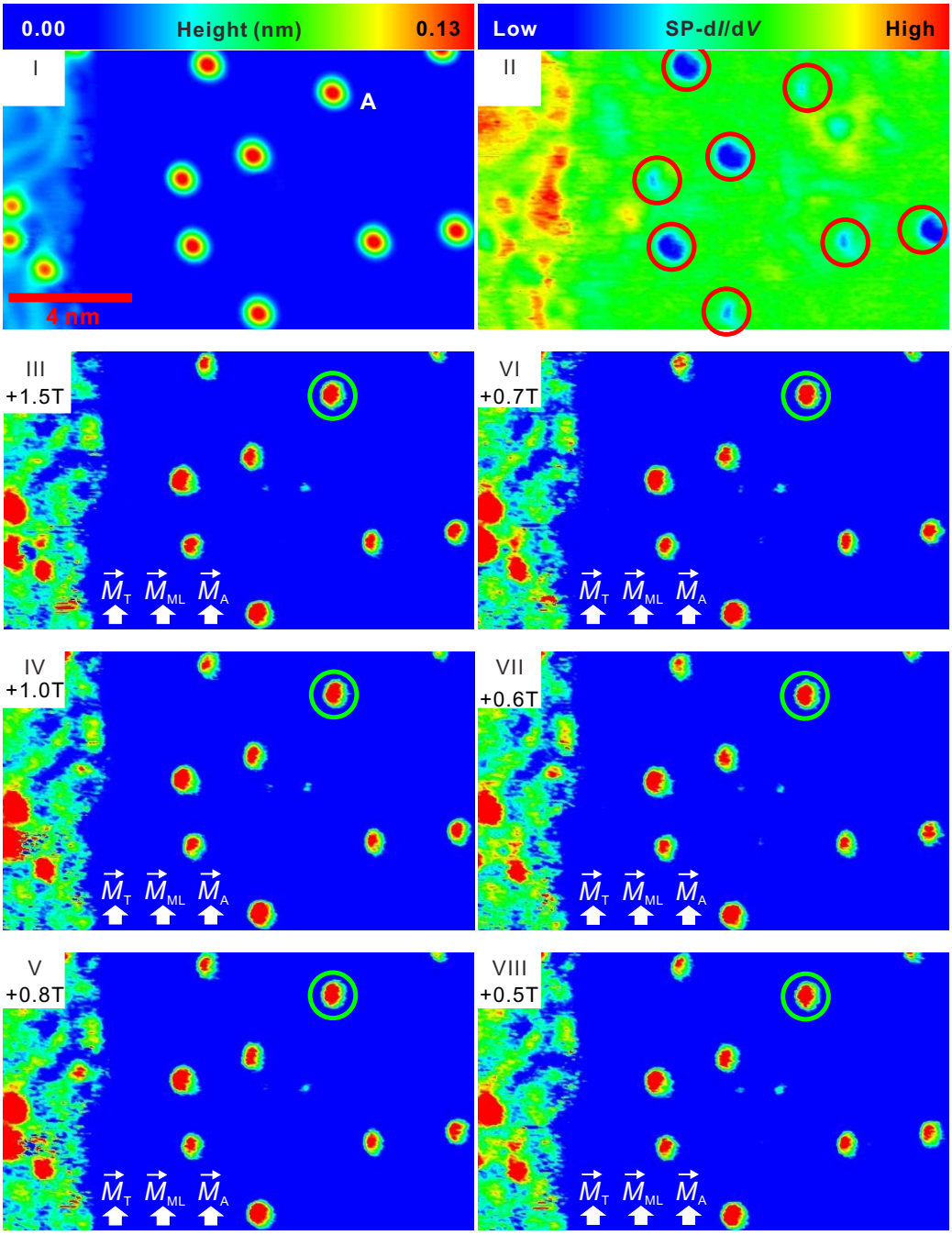
0.00
Height (nm)
0.13
Low
SP-dI/dV
High
I
A
4 nm
II
III
+1.5T
VI
+0.7T
IV
+1.0T
VII
+0.6T
V
+0.8T
VIII
+0.5T
$\vec{M}_T$ $\vec{M}_{ML}$ $\vec{M}_A$

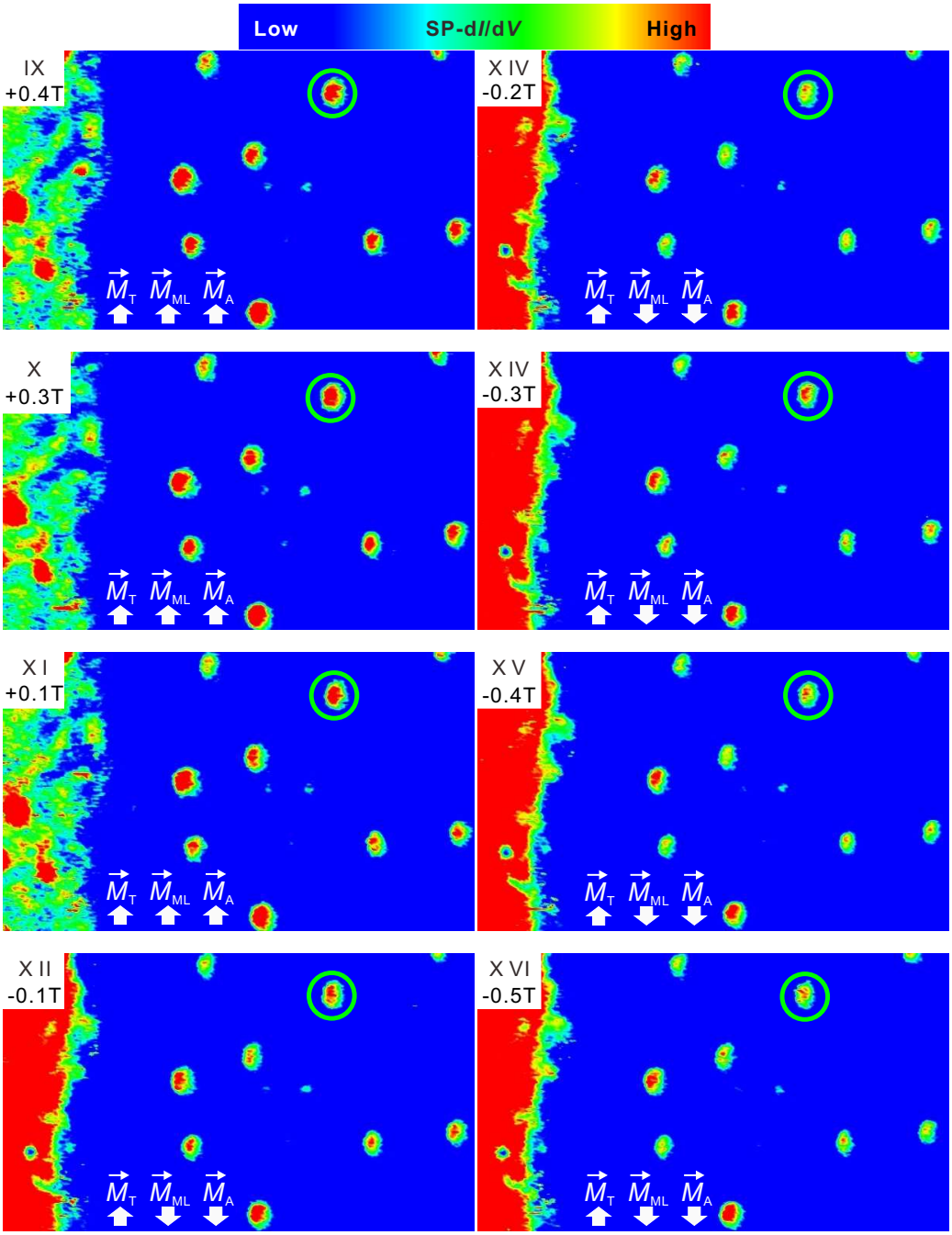
Low
SP-dI/dV
High
IX
+0.4T
X IV
-0.2T
X
+0.3T
X IV
-0.3T
X I
+0.1T
X V
-0.4T
X II
-0.1T
X VI
-0.5T
$\vec{M}_T$ $\vec{M}_{ML}$ $\vec{M}_A$

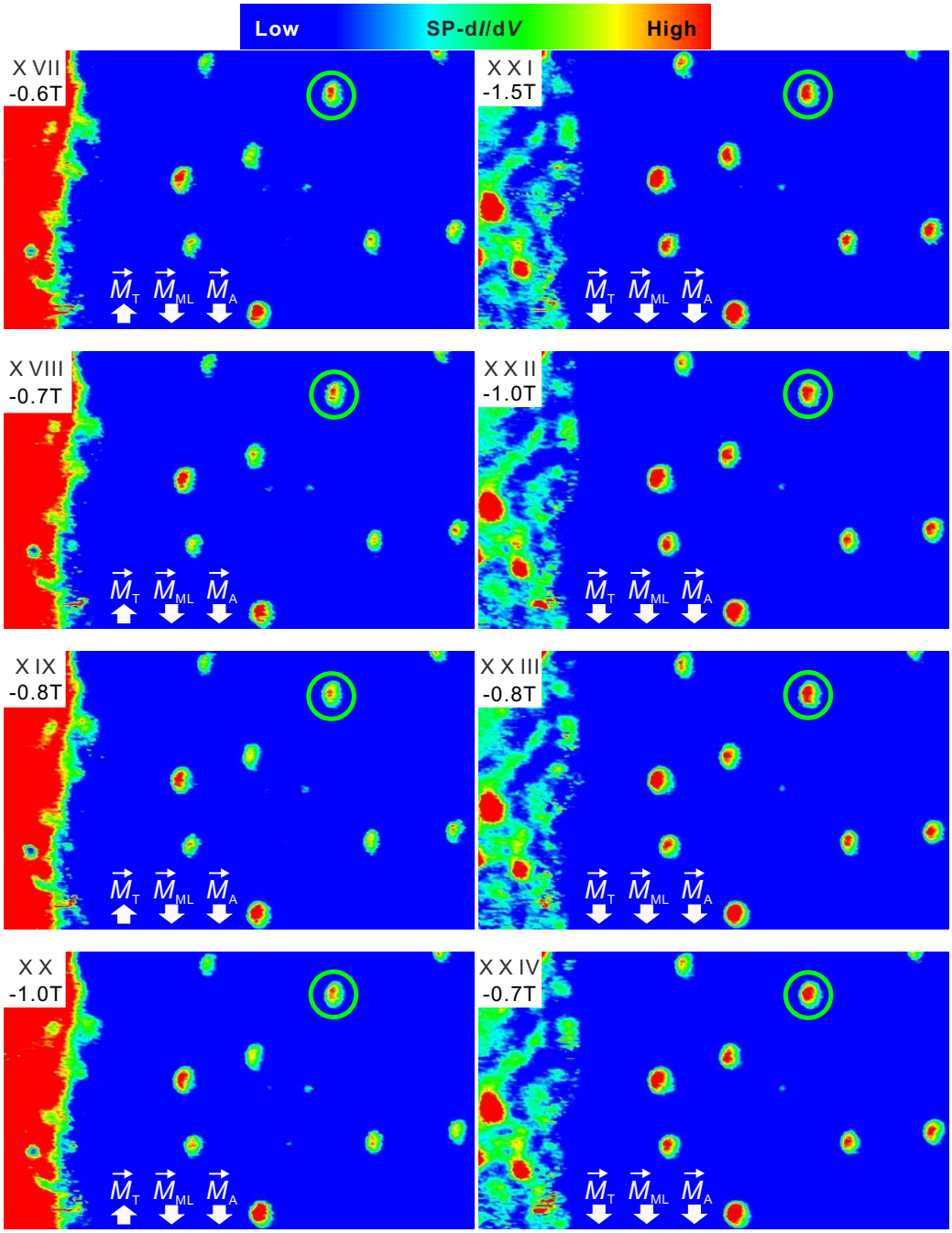
Low
SP-dI/dV
High
X VII
-0.6T
X X I
-1.5T
X VIII
-0.7T
X X II
-1.0T
X IX
-0.8T
X X III
-0.8T
X X
-1.0T
X X IV
-0.7T
$\vec{M}_T$ $\vec{M}_{ML}$ $\vec{M}_A$

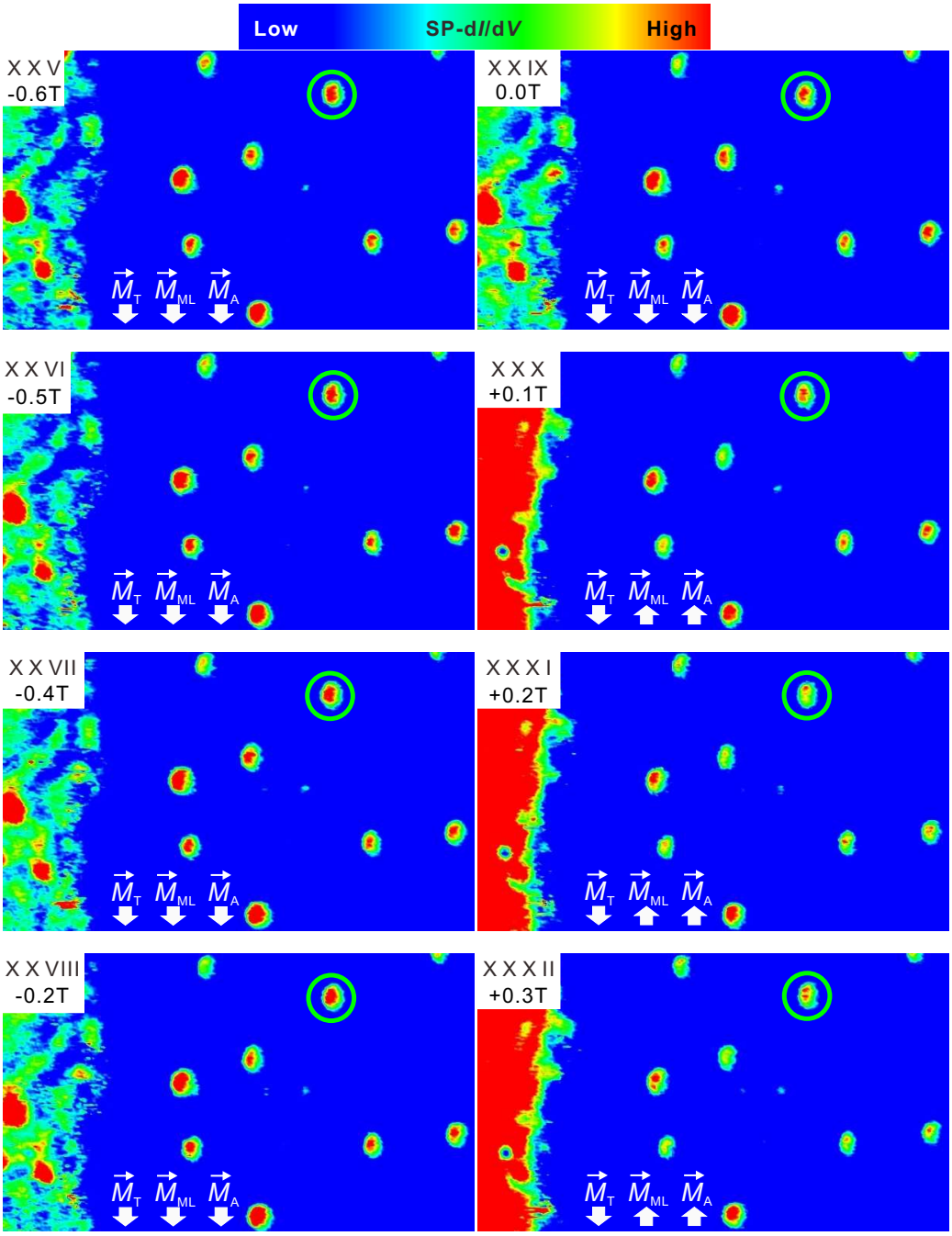
Low
SP-dI/dV
High
X X V
-0.6T
X X IX
0.0T
X X VI
-0.5T
X X X
+0.1T
X X VII
-0.4T
X X X I
+0.2T
X X VIII
-0.2T
X X X II
+0.3T
$\vec{M}_T$ $\vec{M}_{ML}$ $\vec{M}_A$

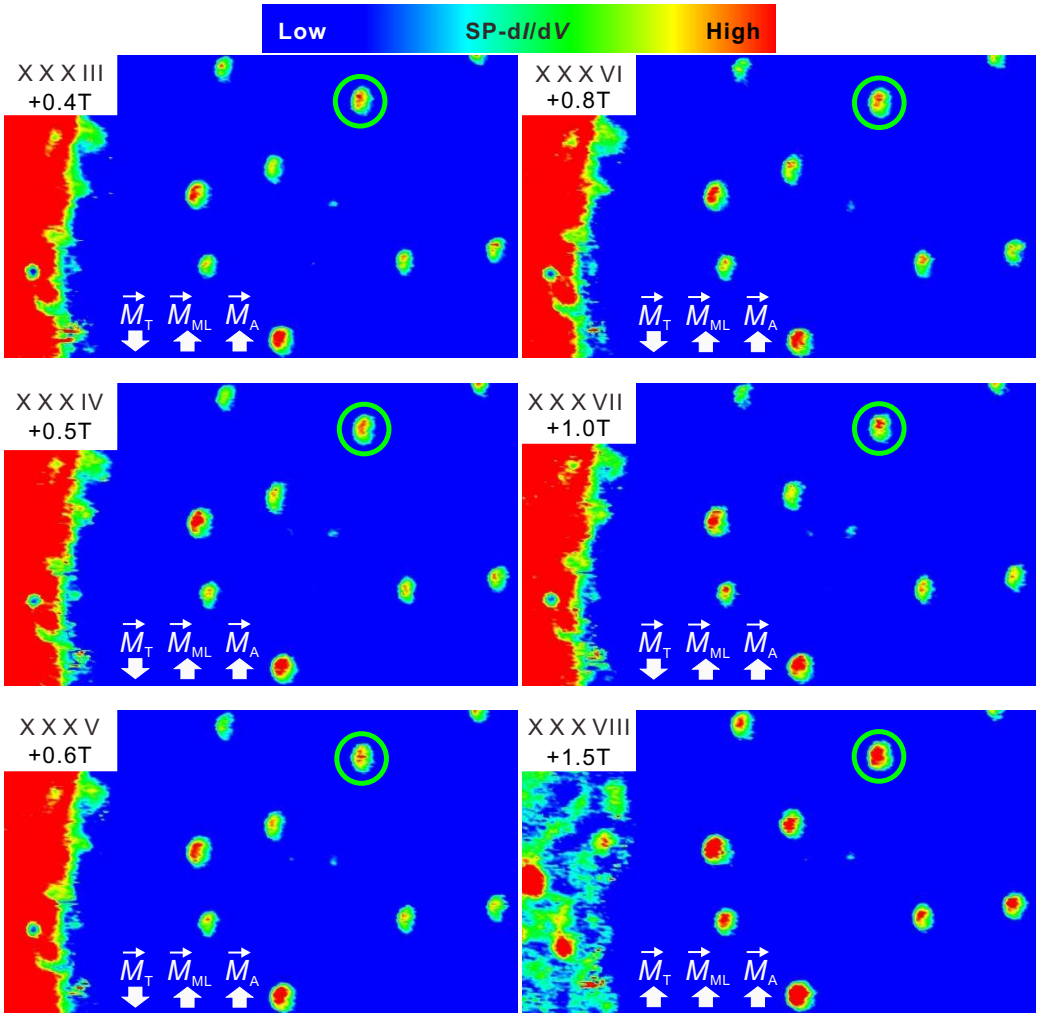

Figure 6.3: **dI/dV maps at successive $\vec{B}_{\mathrm{ext}}$ which form the data set for extracting single-atom magnetization curves**. **(I)** STM topograph of an area containing a patch of Co ML (left) and several single Co adatoms on Pt(1 1 1) (blue). (Tunneling parameters: $V_{\mathrm{stab}} = +0.3$ V, $I_{\mathrm{stab}} = 0.8$ nA, and $T = 0.3$ K.) **(II)** dI/dV map recorded on the same area as **(I)** showing stacking contrast on top of Co adatoms (red circles). (Tunneling parameters: $V_{\mathrm{stab}} = -0.1$ V, $I_{\mathrm{stab}} = 0.3$ nA, $V_{\mathrm{mod}} = 20$ mV (rms), and $T = 0.3$ K.) **(III)-(X X X VIII)** dI/dV maps recorded on the same area as **(I)** at successive $\vec{B}_{\mathrm{ext}}$ for a full magnetization curve. Magnetization orientation of $\vec{M}_{\mathrm{T}}$, $\vec{M}_{\mathrm{ML}}$ and $\langle \vec{M}_{\mathrm{A}} \rangle$ are depicted in the lower left corner of each image. Adatom A indicated with a green circle exemplarily exhibits different intensity depending on the field (as do all other adatoms). $\vec{M}_{\mathrm{ML}}$ is switched by $\vec{B}_{\mathrm{ext}}$ in **(X II)** and in **(X X X)**. $\vec{M}_{\mathrm{T}}$ is switched by $\vec{B}_{\mathrm{ext}}$ in **(X X I)** and in **(X X X VIII)**. (Tunneling parameters: $V_{\mathrm{stab}} = +0.3$ V, $I_{\mathrm{stab}} = 0.8$ nA, $V_{\mathrm{mod}} = 20$ mV (rms), and $T = 0.3$ K.)

Now I focus on the signal change of the particular *hcp*-adatom A with the magnetic field during the down sweep from +1.5 T to -1.5 T (Figure 6.3(III)-(X X I)). When B_{ext} is swept from +1.5 T to +0.3 T (Figure 6.3(III)-(VII)), both the signal of the nanowire and of adatom A have no visible change, meaning that the tip magnetization $\vec{M}_T$ is stable and the adatom A magnetization $\vec{M}_A$ is saturated above +0.3 T. Only when B_{ext} is lower than +0.3 T, the signal of adatom A starts to decrease; from +0.3 T to -0.5 T (Figure 6.3(X)-(X VI)) the signal decreases very rapidly and then gets saturated again (-0.6 T to -1 T; Figures 6.3(X VII) to (X X)). In parallel, the color on the Co nanowire is changed in between +0.1 T and -0.1 T (Figure 6.3(X II), which is due to the switching of the nanowire magnetization $\vec{M}_{ML}$ by B_{ext}, from positive field direction (up) to negative field direction (down). From -1.0 T to -1.5 T (Figure 6.3(X X)-(X X I)) both the signal on the nanowire and the signal on all the adatoms suddenly change. This is because $\vec{M}_T$ is aligned by the strong B_{ext}. Note that due to the inversion of the spin polarization of the stripe with respect to that of adatoms at +0.3 V, a parallel orientation of $\vec{M}_{ML}$ relative to $\vec{M}_T$ leads to lower dI/dV signal, while for the adatom it leads to higher dI/dV signal (see Figure 5.5 in Chapter 5). Similar behavior is observed in the up-sweep from -1.5 T to +1.5 T (Figure 6.3(X X I)-(X X X VIII)); however, $\vec{M}_{ML}$ and $\vec{M}_T$ are now switched at positive field, *i.e.*, +0.1 T and +1 T respectively, proving the ferromagnetic hysteresis of $\vec{M}_{ML}$ and $\vec{M}_T$.

The dI/dV signal is averaged above all individual adatoms with an area of about 0.25 nm^2, and plotted as a function of the external magnetic field. Note that the dI/dV signal above adatoms is not always symmetric due to a weak asymmetry in the tip. Therefore, the area in the dI/dV map which has been used to measure the magnetization curve has been chosen in the following way: (i) the center of each adatom is determined in the corresponding STM topograph which is recorded simultaneously with the dI/dV map; (ii) a square is defined with the adatom as the center; and (iii) the dI/dV signal inside the square is averaged for each adatom. Figure 6.4(a) (top and middle curves) shows the typical raw data of the magnetization curves extracted for an *fcc* and *hcp* adatom from a set of dI/dV maps (different from that in Figure 6.3) recorded by a tip that is reversing its magnetization $\vec{M}_T$ at about |0.75| T. For the up-sweep the dI/dV signal suddenly increases between +0.6 T and +1.0 T due to the reversal of $\vec{M}_T$ from down to up. The same behavior is observed for the down-sweep with a tip reversal from up to down between -0.6 T and -1.0 T. The interplay of adatom magnetization reversal at ≈ 0 T and tip magnetization reversal at

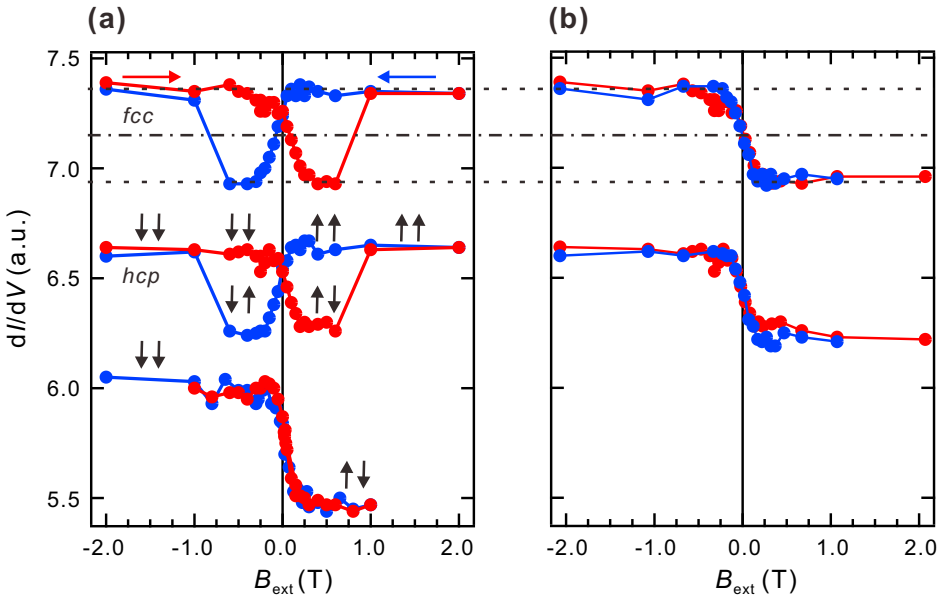

Figure 6.4: **Raw data of single-atom magnetization curves and correction for the tip reversal effect**. **(a)** Magnetization curves of three different adatoms recorded with two different tips (curves offset for clarity). The red curves (blue curves) are recorded during the up (down) sweep of B_{ext} from -2 T to +2 T (+2 T to -2 T). The top and middle curves are respectively taken on an *fcc* and *hcp* adatom, with a tip that is reversing its magnetization $\vec{M}_{\text{T}}$ at about $|\vec{B}| = 0.75$ T. The bottom curve is recorded with a different tip that is not reversing its magnetization. The arrow pairs in the middle and bottom curves indicate the relative orientation of adatom $\langle \vec{M}_{\text{A}} \rangle$ (left arrow) and tip magnetization $\vec{M}_{\text{T}}$ (right arrow). The dash-dotted (dashed) subsidiary lines in the top curve indicate the dI/dV signal corresponding to $\langle \vec{M}_{\text{A}} \rangle = 0$ (saturated $\langle \vec{M}_{\text{A}} \rangle$). (Tunneling parameters: $V_{\text{stab}} = +0.3$ V, $I_{\text{stab}} = 0.8$ nA, $V_{\text{mod}} = 20$ mV (rms), and $T = 0.3$ K). **(b)** Magnetization curves derived from (a) by correcting for the tip reversal and stray field.

± 0.75 T results in a butterfly-shaped curve with the relative orientations of $\langle\vec{M}_A\rangle$ and $\vec{M}_T$ as indicated by the arrow pairs in the curve. Close inspection reveals that the S-shaped part of the magnetization curve near B_{ext} = 0 T, which indicates the adatom-magnetization reversal, is not symmetric with respect to zero magnetic field: The red curve ($\vec{M}_T$ downwards) is shifted by +0.1 T while the blue curve ($\vec{M}_T$ upwards) is shifted by -0.1 T. Note, that these shifts also result in a vertical shift of the intersection points of the red and blue curves at B_{ext} = 0 T, which is above the line indicating $\langle\vec{M}_A\rangle = 0$ (see dash-dotted line). For some of the tips, significantly different shifts are observed for upwards and downwards pointing $\vec{M}_T$. The butterfly-shaped hysteretic behavior is only observed when $\vec{M}_T$ is reversed during recording the magnetization curve. The bottom curve in Figure 6.4(a) shows for comparison an example recorded with a stable tip from B_{ext} = -2 T to +1 T and backwards. There is no indication for a difference in the up- and down-sweep curves. This proves that the adatoms behave paramagnetic at 0.3 K, and their properties revealed from such magnetization curves will be discussed in Chapter 6.4 and 6.5. Nevertheless, both curves are slightly shifted to the right indicating a downwards pointing tip magnetization which is consistent with the overall symmetry of the curve (large dI/dV at negative B, small dI/dV at positive B_{ext}). The possible reasons for the horizontal shift in the magnetization curves induced by the tip magnetization will be discussed in Chapter 6.6.

To correct for the reversal of the tip magnetization a method similar to that used in [112] is applied. Therefore, the part of the magnetization curve recorded with the upwards pointing $\vec{M}_T$ is mirrored at the average of the dI/dV signals (see dash-dotted subsidiary line in Figure 6.4) as well as shifted by +0.1 T. The part of the magnetization curve recorded with the downwards pointing tip magnetization is shifted by −0.1 T. This results in the symmetric curves, which are shown in Figure 6.4(b) and have been used to fit the magnetic moments (see the following section). Similar magnetization curves have been recorded on tens of different adatoms as shown in Figure 6.5(b).

The magnetization curves at a temperature of 4.2 K have also been recorded. For comparison Figure 6.5(a) shows exemplarily the magnetization curves for the same adatom at T = 4.2 K and T = 0.3 K. S-shaped curves are observed for both temperatures, but with strongly different saturation fields $B_{sat} \approx 5$ T (T = 4.2 K) and $B_{sat} \approx 0.3$ T (T = 0.3 K). It is worth pointing out that the saturation field at 4.2 K is in good agreement with that obtained by XMCD at 5.5 K [4]. The curves recorded at 0.3 K

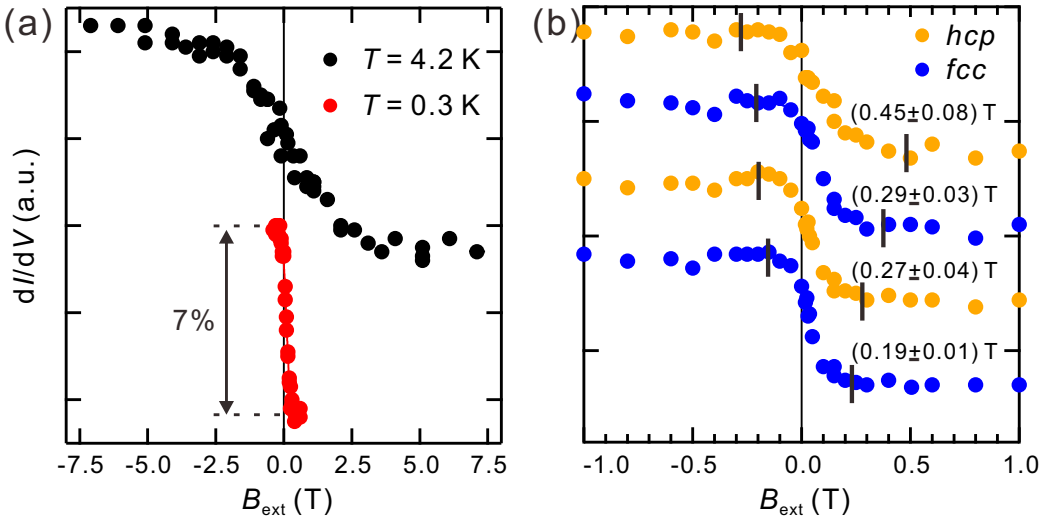

Figure 6.5: **Single-atom magnetization curves**. **(a)** Magnetization curves of a Co adatom at 4.2 K (top) and 0.3 K (bottom) have distinct saturation fields. The curve at 4.2 K is vertically shifted for clarity. **(b)** Magnetization curves recorded at 0.3 K on different adatoms show variant slope around $B_{\mathrm{ext}} = 0$ and different saturation fields as indicated by the black solid bars and corresponding numbers. Reversal of $\vec{M}_{\mathrm{T}}$ is corrected. (Tunneling parameters: $V_{\mathrm{stab}} = +0.3$ V, $I_{\mathrm{stab}} = 0.8$ nA, and $V_{\mathrm{mod}} = 20$ mV (rms).)

for different adatoms exhibit variant slopes around B_{ext} due to a different saturation field, as indicated in Figure 6.5(b). Figure 6.6 shows the magnetization curves for the same adatom recorded at +0.3 V and -0.1 V to check for effects of different bias voltages, but no distinct difference in these two curves is observed.

Since there are no signs of hysteresis in the magnetization curves at 0.3 K and 4.2 K, the magnetization behaves paramagnetic and statistically switches between up and down with a rate much faster than the current time resolution of the experiment (> 100 Hz). It has been reported that Co adatoms on Pt(1 1 1) have a large out-of-plane magnetocrystalline anisotropy of $K = -9.3$ meV (at 5.5 K) corresponding to an energy barrier between up- and downwards pointing $\vec{M}_{\mathrm{A}}$ of about 100 K [4]. Since the lowest temperature is 350 times smaller, thermally induced switching of $\vec{M}_{\mathrm{A}}$ across such a barrier can be excluded [113]. Thus, if the description in [4] is correct, these results imply the dominance of a temperature independent switching process. This will be discussed in detail in Chapter 6.5.

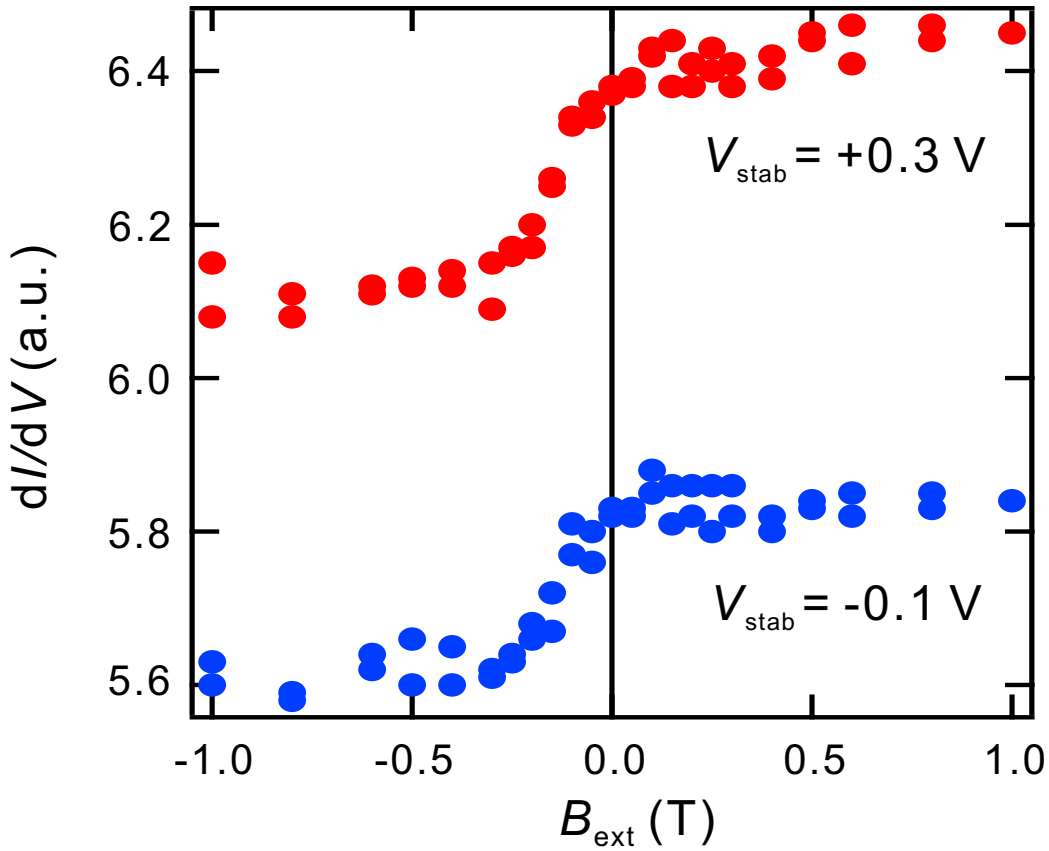

Figure 6.6: **Single-atom magnetization curves recorded at different bias voltages**. The magnetization curves of the same Co adatom at +0.3 V (top) and -0.1 V (bottom) exhibit no distinct difference. (Tunneling parameters: top: V_{stab} = +0.3 V, I_{stab} = 0.8 nA, V_{mod} = 20 mV (rms), and T = 0.3 K; Bottom: V_{stab} = -0.1 V, I_{stab} = 0.3 nA, V_{mod} = 20 mV (rms), and T = 0.3 K.)

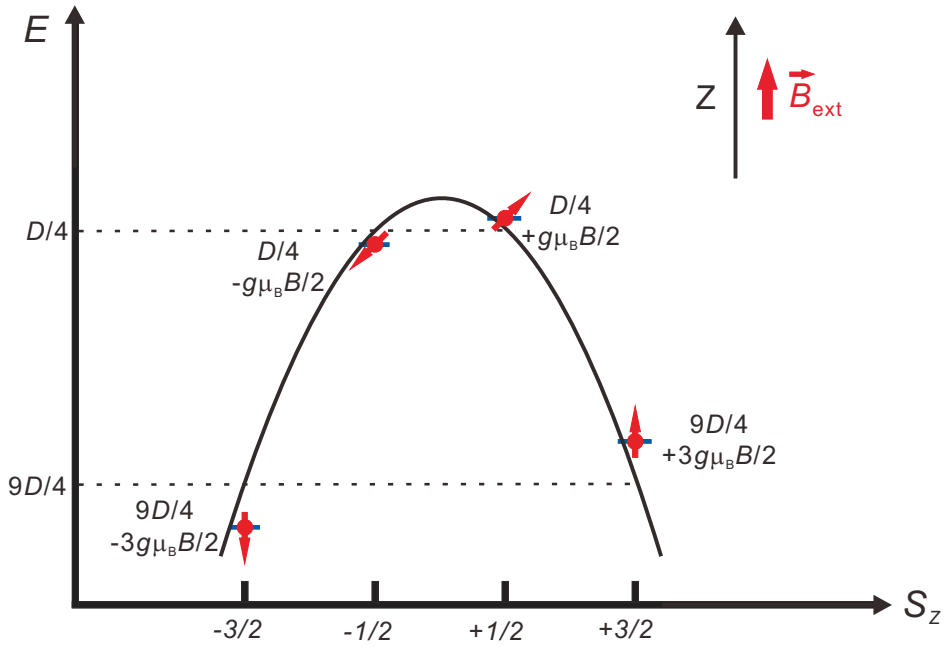

Figure 6.7: **Schematic sketch of the energy levels of a quantum spin with $S = 3/2$.** The energy levels of the total angular momentum S of the adatom depend on its z-component S_z. Nonzero D and B lift the degeneracy resulting in the energy levels as indicated by the blue lines.

6.4 Theoretical modeling

In order to gain information on the basic properties of single magnetic adatoms from single-atom magnetization curves, it is important to model these curves. Here, only the isolated adatoms are considered. In this work, adatoms with a separation larger than 2.4 nm from other adatoms and larger than 8 nm from Co monolayer stripes are modeled as isolated adatoms. It will be shown in Chapter 7.4 that these adatoms still feel a mean field of indirect exchange interactions from other adatoms even with a mean nearest neighbor distance of 2.4±1 nm, which can be considered by a variation in the effective magnetic moment.

The total angular momentum of the adatom S is the superposition of spin and orbital momentum of the adatom and of the neighbouring polarized Pt atoms [4]. If the adatom would be sufficiently decoupled from the substrate conduction electrons as on insulating layers [47, 48, 49], the spin is quantized and hence one could use a single-ion spin Hamiltonian

for an isolated atom within a quantum mechanical model as

$$\hat{H} = D\hat{S}_z^2 + E(\hat{S}_+^6 + \hat{S}_-^6) + g\mu_B\vec{B}\cdot\hat{\vec{S}}, \tag{6.2}$$

where $\hat{S}_+$ and $\hat{S}_-$ are the ladder operators of S, $\hat{S}_z$ is the operator of the out-of-plane (z) component of S, g is the Landé factor, $\vec{B}$ is the magnetic field, and D and E take into account the spin-orbit coupling with the substrate and describe the out-of-plane and (sixfold) in-plane magnetic anisotropy in harmonic approximation. Here $E = 0$ and $D < 0$ due to the out-of-plane easy axis anisotropy [4]. Let us assume as an example $S = 3/2$. The energy levels of such a quantum spin at a magnetic field B are shown in Figure 6.7. Without the perpendicular magnetic anisotropy energy ($D\hat{S}_z^2$) and the magnetic field B, all the states are degenerate. Nonzero D removes the degeneracy of $S_z = \pm 1/2$ with $S_z = \pm 3/2$ states which results in the energy levels indicated by the parabolic curve. Upon applying B along the z direction the degeneracy of $S_z = +1/2$ with $S_z = -1/2$ and $S_z = +3/2$ and $S_z = -3/2$ is further lifted, and the energy levels are symmetrically separated from the parabolic curve by the Zeeman splitting $g\mu_B S_z B$ (blue lines).

However, the isolated spin Hamiltonian is a very crude approximation due to the strong hybridization of the Co states with the Pt bands [4]. This hybridization produces broad resonances, as also indicated by the large linewidth in the IETS spectra indicating a rather short lifetime of the excited states [19, 20]. Consequently, the total angular momentum is no longer half-integer. This is further supported by the mean magnetic moment of the Co adatoms of $m \approx 3.5\mu_B$ (see below) resulting in a non-half integer number for $S = \frac{m}{g\mu_B} = 1.75$. Therefore, a quasi-classical description (continuum description) via the correspondence principle $S_z = S \cdot \cos\theta$ is more appropriate. The energy function within this model is

$$E(\theta, B_z) = DS^2\cos^2\theta + g\mu_B S B_z\cos\theta = K\cos^2\theta - mB_z\cos\theta, \tag{6.3}$$

where $K = DS^2$ is the perpendicular magnetic anisotropy energy (MAE), $m = -g\mu_B S$ is the effective magnetic moment, and B_z is the out-of-plane component of the magnetic field.

Since paramagnetic behavior is observed on the nanoclusters comprised of a single Co adatom and the surrounding Pt atoms, naturally the superparamagnetism model will be considered. However, this model was so far only used to describe the spatial- and time-averaged statistical behavior of a large ensemble of magnetic nanoclusters. It is interesting to evaluate whether this description is appropriate to model the switching behavior without ensemble averaging. While the experimental magnetization curve is taken on a single adatom and there is no ensemble

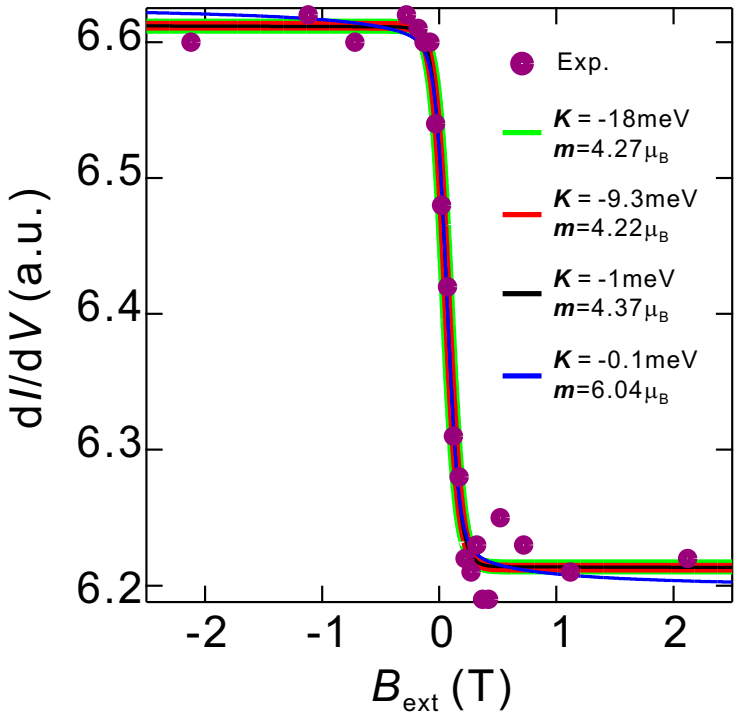

Figure 6.8: **Single-atom magnetization curve fitted with different** K. The experimental data can be fitted quite well with $K = -9.3$ meV, -1.0 meV and -18.0 meV, while a large deviation is visible for the fitting with $K \approx k_B T$ ($K = -0.1$ meV). (Tunneling parameters: $V_{stab} = +0.3$ V, $I_{stab} = 0.8$ nA, $V_{mod} = 20$ mV (rms), and $T = 0.3$ K.)

averaging in the experiments, the detected dI/dV signal is time averaged over a window of 10 ms which is about 10-12 orders of magnitude longer than the life time of excited states of magnetic adatoms on metallic surfaces [19, 20, 114]. Therefore, it is assumed that this time is sufficiently long to allow the adatom to travel around the whole phase space resulting in a thermal equilibrium, and map its statistical behavior to superparamagnetism, given by

$$\langle M_A \rangle = M_{sat} \frac{\int_0^{2\pi} d\phi \int_0^{\pi} d\theta \sin\theta \cos\theta e^{-E(\theta,B_z)/k_B T}}{\int_0^{2\pi} d\phi \int_0^{\pi} d\theta \sin\theta e^{-E(\theta,B_z)/k_B T}}. \tag{6.4}$$

where M_{sat} is the saturation magnetization. The magnetic energy function of the adatom $E(\theta, B_z) = -m(B_{ext} + B_T)\cos\theta + K\cos^2\theta$ takes into account the external magnetic field $\vec{B}_{ext}$ and tip stray field $\vec{B}_T$ in easy axis direction (see Chapter 6.6).

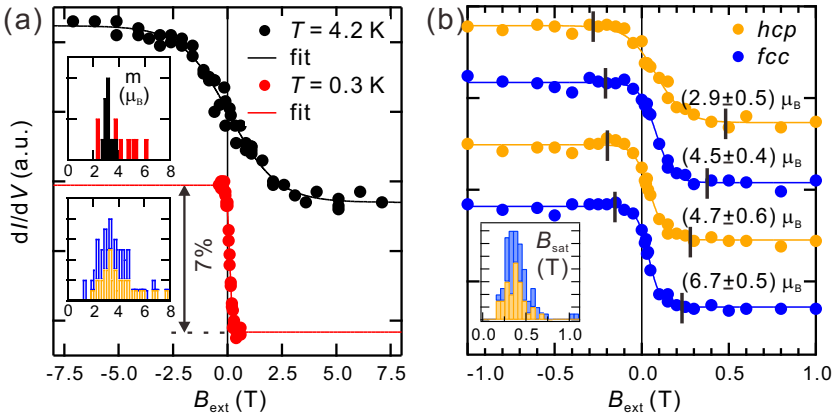

Figure 6.9: **Fitting the single-atom magnetization curves**. **(a)** The Langevin model is used to fit to the experimental magnetization curves of a Co adatom at 4.2 K (top) and at 0.3 K (bottom). The insets show the histograms of the fitted m (in μ_B) for the same 11 adatoms at 4.2 K (black) and at 0.3 K (red) (top histogram) and for 46 *fcc* (blue) and 38 *hcp* (orange) adatoms (bottom histogram, *fcc* bars stacked on *hcp*). **(b)** Magnetization curves of 4 adatoms at 0.3 K with fit curves and fitted m. The black bars indicate the magnetic field B_{sat} needed to saturate the magnetization. The inset shows the histogram of B_{sat} (in T) for the same adatoms used in the bottom histogram in (a). Curves in (a) and (b) are vertically offset for clarity. (Tunneling parameters: V_{stab} = +0.3 V, I_{stab} = 0.8 nA, and V_{mod} = 20 mV (rms).)

This Langevin model is used to numerically fit the measured magnetization curves, with m, M_{sat} and $\vec{B}_T$ taken as the variable parameters. Using an external magnetic field along the easy axis, it is impossible to get the well-defined knowledge of the magnetic anisotropy energy. Figure 6.8 shows a single-atom magnetization curve fitted to the Langevin model with different K. No apparent difference is observed for the fitting with K = −9.3 meV, -1.0 meV and -18.0 meV. Only when a K in the order of the measurement temperature (k_BT = 25 μeV) is assumed, a large deviation is observed at $|B_{ext}| \geq 0.5$ T. This deviation cannot be corrected by choice of a different m. For the curves at T = 4.2 K the fits start to deviate already for $|K| \leq 1$ meV. Consequently, it is found that a variation of K in a reasonable range 1 meV < $|K|$ < 20 meV will not change the fitted moment value at T = 0.3 K and 4.2 K because such temperatures are too low to turn the magnetization considerably into the hard axis direction. Therefore, a fixed value K = −9.3 meV is used [4]. The corresponding fit curves are shown exemplarily in Figure 6.9 which excellently reproduce the experimental

single-atom magnetization curves. Note that the fitted m is an effective value including both the adatom magnetic moment and the induced Pt magnetic moment.

Similar magnetization curves as in Figure 6.9 have been recorded using several tips for about 80 different adatoms showing qualitatively the same paramagnetic shape. The insets show the histograms of the fitted m. The arithmetic means at 0.3 K for *hcp* and *fcc* adatoms are $m_{hcp} = (3.9 \pm 0.2)\ \mu_B$ and $m_{fcc} = (3.5 \pm 0.2)\ \mu_B$, respectively, which are larger than the 4.2 K values ($m_{hcp} = (3.0 \pm 0.3)\ \mu_B$ and $m_{fcc} = (3.1 \pm 0.1)\ \mu_B$). Surprisingly, the magnetic moment exhibits a very broad distribution at 0.3 K, from about 2 μ_B to 6 μ_B. The variance in m for the same adatoms decreases significantly at $T = 4.2$ K. The mechanism for this behavior can be related to a spatially inhomogeneous mean field of indirect exchange interaction, which will be studied in detail in Chapter 7.4.

6.5 Discussion: Possible reasons for magnetization switching

In the following the mechanism being responsible for the magnetization switching is discussed. The first possibility is that the magnetization is switched by the tunneling current through inelastic processes. In an STM experiment inelastic tunneling is about one order of magnitude less probable than the dominant elastic tunneling. However, as illustrated in Figure 6.10, when the bias voltage is higher than a certain threshold, the tunneling electron can transfer its energy and momentum to the adatom. As a result, the electron finds an additional tunneling channel by losing some of its energy and changes its spin quantum number by one, while the adatom is left in the excited state for some time. The excited state has a lifetime τ. If τ is sufficiently long, so that enough electrons can drive the adatom out of equilibrium step by step until its energy becomes higher than the magnetic anisotropy barrier, the adatom can relax to the global ground state. This way, the magnetization of the adatom is switched. Such an effect might exist in the experiment since the bias voltage used to record magnetization curves is higher than the threshold energy. However, it was revealed that τ is in the order of 20-200 fsec for magnetic adatoms in contact to metallic surfaces [19, 20, 114]. In the experiment, the tunneling current of 0.8 nA is used, from which the time between consecutive electrons can be extracted as 0.2 nsec. This value is $10^3 - 10^4$ larger than the typical lifetime. Therefore, the tunneling electrons always interact with adatoms

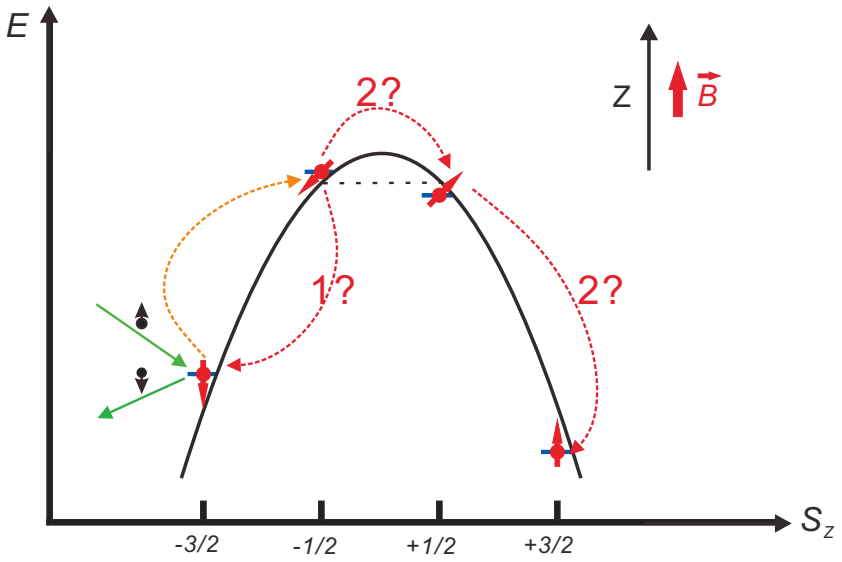

Figure 6.10: **Illustration of the excitation of the adatom (red dots) by energy and momentum transfer from an inelastically scattering tunneling- or conduction-electron (black dots)** within the isolated spin model assuming $S = 3/2$. The tunneling electron loses its energy and switches its spin orientation, while the adatom is excited to a higher state (orange dotted line). Depending on the magnetic anisotropy barrier and the lifetime of the excited state, the adatom can relax to the local (path 1) or global (path 2) ground state.

in equilibrium with the environment, and only excitations by single electrons occur. Consequently, the tunneling electrons alone cannot not flip the adatom's spin to the global ground state.

The situation is changed when the conduction electrons in the substrate are also involved in the spin-flip scattering. Such an effect due to the coherent spin-flip scattering of the conduction electrons with Co adatoms could explain the observation of the fast switching of the spins. Actually, Balashov *et al.* [19], Schuh *et al.* [20] and Khajetoorians *et al.* [114] claimed that such a process was observed in their experiments with inelastic tunneling spectroscopy.

Another possible mechanism is the quantum tunneling of magnetization. It was found in experiments that the magnetization of molecular magnets can quantum mechanically tunnel through a barrier and change the orientation if there is finite transverse magnetic anisotropy or external magnetic field. Recently Loth *et al.* also found indications that the Fe-Cu dimer on a Cu_2N overlayer on Cu(0 0 1) relaxes out of the excited spin

state due to quantum tunneling with a relaxation time between 50 to 250 nsec [115]. In the system of Co adatoms on Pt(1 1 1), due to the three-fold rotational symmetry of Pt(1 1 1), an in-plane magnetic anisotropy of at least sixth order is expected (see Equation 6.2) which, however, vanishes because of $S < 3$. Moreover, because the hybridization in this system is very strong, such a quantum effect is very unlikely.

6.6 Tip-adatom interaction

There are three possible reasons for a shift in the magnetization curves of the adatoms induced by the switching of the magnetization of the tip observed in Figure 6.4: (i) the imbalance of majority and minority electrons tunneling from the tip to the adatom could result in a spin torque which drives the magnetization of the adatom into one direction [52, 116]. (ii) Magnetic exchange interaction between the foremost tip atom and the adatom leads to an exchange bias field [96]. (iii) The stray field $\vec{B}_{\mathrm{T}}$ of the tip composed of the Cr layer and an unknown Co coverage adds to the external magnetic field $\vec{B}_{\mathrm{ext}}$. (i) and (ii) would always lead to a symmetric shift of the magnetization curves for up and down tip magnetization because these effects are fully determined by the spin polarization of the foremost tip atom, which reverses its sign. On the other hand, the reversal of the foremost tip-atom magnetization may happen without switching the overall tip magnetization. This would result in a different absolute value of $\vec{B}_{\mathrm{T}}$ for the two tip orientations. Therefore, the observation of an asymmetric shift for some of the tips favours the stray field effect (iii). The absolute values of the observed shifts are in reasonable agreement with the stray fields measured for GdFe tips of $200 - 300$ mT [79] taking into account the smaller magnetic moment of Co as compared to GdFe. Here it is assumed that the Cr-coated tip has picked up a Co nanocluster upon dipping it into the Co nanowire in order to enhance the spin contrast (see Chapter 4.2.2).

Magnetization curves are also recorded by varying the stabilization current over about one order of magnitude, corresponding to a tip-adatom distance change of about 1 Å, and changing the bias voltage and its polarity. There is no significant change in the magnetization curve shift as a function of current and voltage. This again disfavours the explanation by spin torque (i) which would depend most sensitively on a current and bias polarity change [52, 116]. It is therefore thought that the stray field effect (iii) dominates and an effective magnetic field ($\vec{B}_{\mathrm{ext}} + \vec{B}_{\mathrm{T}}$) is used to fit the magnetization curves.

6.7 Summary

In summary, the magnetization of single Co adatoms on Pt(1 1 1) has been imaged. With this ability, the magnetization curves of single Co adatoms can be recorded. The modeling of such curves has been discussed in detail, from which the magnetic stability and magnetic moment can be studied. The switching of the magnetization in the time domain at 0.3 K is probably due to the quantum tunneling of the magnetization, or the spin-flip scattering of the adatom with the conduction electrons in the substrate and with the spin-polarized tunneling electrons.

It is expected that an increase in the time resolution will additionally allow for the investigation of the dynamics in single and coupled spin systems and reveal the mechanism of the switching of the magnetization [115, 116].

Chapter 7

Mapping magnetic interactions on the atomic scale

This chapter describes how surface magnetic interactions can be mapped on the atomic scale through investigating single-atom magnetization curves by SP-STM. While the isolated Co adatoms on Pt(1 1 1) are paramagnetic, those close to the Co ML stripes (nanowires) are found to be stabilized by the indirect exchange interaction from the nearby nanowires. This coupling is oscillating between ferromagnetic and antiferromagnetic with distance, and is of the type of the one-dimensional RKKY exchange. The same indirect exchange interaction is also observed in Co pairs, and exhibits strong anisotropy with respect to the substrate crystallographic direction. In the ensemble of randomly distributed Co adatoms, a spatially inhomogeneous mean field is observed which leads to a strong change in the effective magnetic moment value from adatom to adatom.

This chapter is organized as follows: first an introduction is given on the background, after which the measurement and analysis of the RKKY exchange interactions between different Co nanostructures on Pt(1 1 1) are presented, and finally a short conclusion is given.

Part of this chapter has been published in: F. Meier, L. Zhou, J. Wiebe and R. Wiesendanger, "Revealing magnetic interactions from single-atom magnetization curves", *Science* **320**, 82-86 (2008); L. Zhou, J. Wiebe, S. Lounis, E. Vedmedenko, F. Meier, S. Blügel, P. H. Dederichs, and R. Wiesendanger, "Strength and directionality of surface Ruderman-Kittel-Kasuya-Yosida interaction mapped on the atomic scale", *Nature Physics* **6**, 187-191 (2010).

7.1 Introduction

RKKY interaction [117, 118, 119] is an indirect magnetic coupling between localized spins in a nonmagnetic host mediated by conduction electrons, where the localized magnetic moment is screened by the spatially oscillating long-range spin polarization of the host conduction electrons [120]. When magnetic moments are diluted in a conducting nonmagnetic host, RKKY interaction becomes dominant whenever there is a sufficiently strong exchange coupling between the localized moments and the conduction electrons. Then, the spins of the conduction electrons, which are on average unpolarized, get polarized into a preferred direction in the vicinity of each moment. This preferential direction oscillates with increasing distance from the moment. A second localized moment will interact with this spin-density oscillation and either perceive a ferromagnetic (FM) or an antiferromagnetic (AF) coupling to the first, depending on their relative distance. Therefore, it is also called indirect magnetic exchange.

RKKY interaction is dominating in dilute magnetic systems and determines the system's magnetic state. It played a key role in the development of layered giant magneto-resistance devices [121, 122], drives the ferromagnetism in heavy rare earth elements [123] as well as diluted magnetic semiconductors [124], and gives rise to complex magnetic ground states such as spin glasses [8, 125]. The first indications of indirect magnetic exchange via conduction electrons came with the research on dilute magnetic bulk alloys, where the dependence of the interaction strength on the distance between the moments with the oscillation period of half the Fermi wavelength was proposed with an isotropic and continuous model [117, 118, 119]. For many bulk systems, the treatment of the conduction electrons in this way is sufficient to correctly describe the RKKY interaction. However, such a model can be misleading if the typical length scale of the interaction becomes comparable with inter-atomic distances, as *e.g.*, in magnetic nanostructures consisting of separate magnetic atoms adsorbed on the surface of a nonmagnetic material, which is yet to be examined.

Experimentally, direct evidence for RKKY-like coupling of magnetic layers through transition metal layers was obtained only by spatially averaging techniques as neutron-diffraction [126], light scattering from spin waves [127], or transport and magnetization measurements [128, 129]. Such experiments detect only ensemble averages of a distribution of magnetic moments, which is not known exactly, thus hampering a direct comparison to theory. However, since magnetic devices are getting smaller and approach the limit of nanostructures built by separate atoms, knowledge

of the carrier mediated indirect exchange on the atomic scale is essential. By using STS it became possible to investigate magnetic interactions in atom pairs [110, 111, 48], but their RKKY coupling was yet detected only *indirectly* via the Kondo effect [54].

7.2 Co adatoms stabilized by Co nanowires

7.2.1 Experimental results

It has been reported in Chapter 6.3 that at 0.3 K the isolated Co adatoms are paramagnetic and their spins are switching in the time domain with a characteristic time scale much shorter than the time resolution of the experiment. However, the situation changes completely when they are located close to Co nanowires.

Figure 7.1(d) shows exemplarily an STM topograph of an area with a Co ML stripe and three Co adatoms with a lateral distance d less than 3 nm to the stripe. These adatoms are separated more than 2.5 nm from other adatoms, and therefore a dominant interaction from other adatoms can be excluded (see Chapter 7.3). Figure 7.1(a) contains the magnetization curve of this monolayer stripe and of the adatom with a distance of $d \approx 1.5$ nm (atom A in Figure 7.1(d)). The ML shows a regular square-like hysteresis curve corresponding to typical ferromagnetic behavior. In the down sweep (blue curve) its magnetization switches from up (low signal) to down (high signal) at the external magnetic field $B_{\mathrm{ext}} = -0.5$ T and in the up sweep (red curve) it switches from down to up at +0.5 T. The adatom behaves completely different than the previously described isolated ones (see Chapter 6) and shows hysteresis, indicating that it is now stabilized by some kind of interaction. In the down sweep its magnetization switches from up to down already at large positive $B_{\mathrm{ext}} = +0.7$ T (see black arrow), and points downward at zero field while the stripe magnetization points upward. It then switches back to up simultaneously with the reversal of the stripe at -0.5 T. Only at -0.7 T the adatom's magnetization is again forced into the down state (see arrow). Note that due to the inversion of the spin polarization of the stripe with respect to that of adatoms at +0.3 V, a parallel orientation of $\vec{M}_{\mathrm{ML}}$ relative to $\vec{M}_{\mathrm{T}}$ leads to lower dI/dV signal, while for the adatom it leads to higher dI/dV signal (see Figure 5.5 in Chapter 5 and Figure 6.3 in Chapter 6). The same behavior is observed for the up sweep but now with the stripe magnetization pointing downward and the adatom magnetization pointing upward at zero field. Obviously, the adatom feels an AF coupling to the stripe which is broken by an exchange

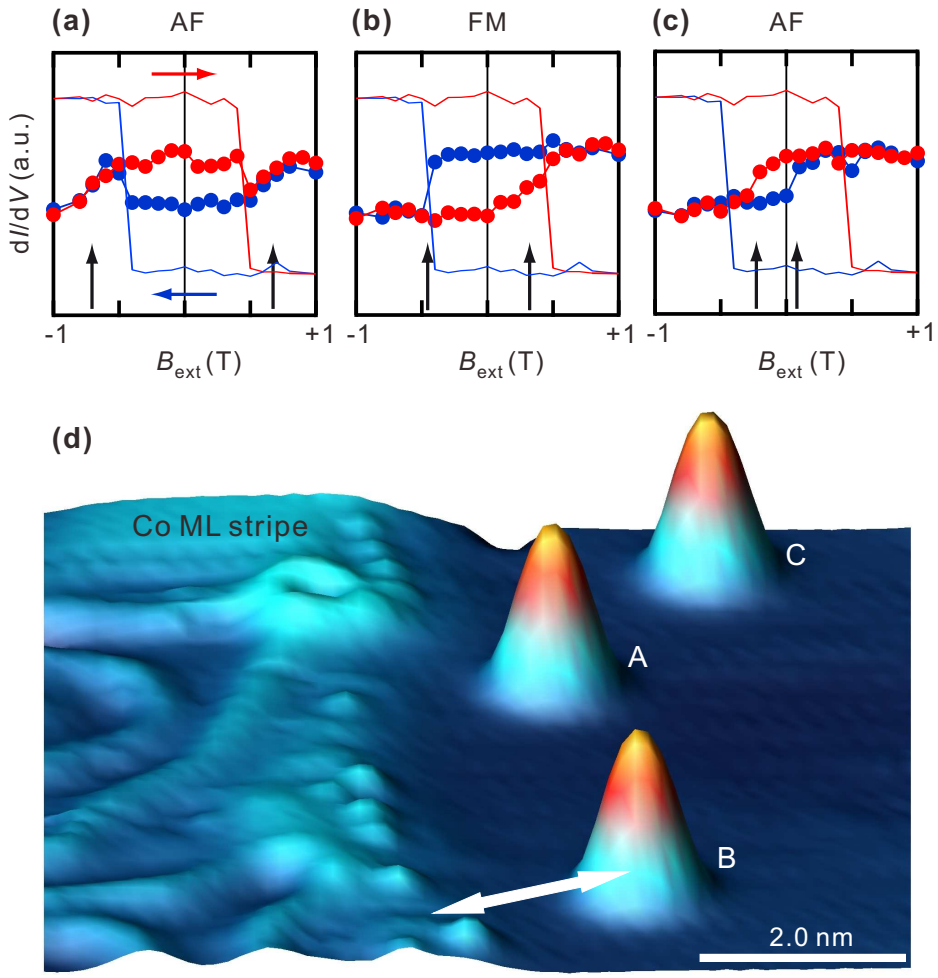

Figure 7.1: **Magnetization curves of stabilized Co adatoms**. **(a)-(c)** Magnetization curves measured on the Co ML stripe (solid lines) and on the three Co adatoms (dots) A, B, and C marked in (d). The blue color indicates the down sweep from B_{ext} = +1 T to -1 T (and red, the up sweep from -1 T to +1 T). The vertical arrows indicate the exchange bias field, B_{ex}, which is converted into the exchange energy (using m = 3.7 μ_{B}) for the corresponding magenta points in the plot of Figure 7.2. **(d)** STM topograph of an area with a Co ML and three Co adatoms nearby. Arrow indicates the measured distance with an angle of 50° to $[1\,1\,\bar{2}]$. (Tunneling parameters: V_{stab} = +0.3 V, I_{stab} = 0.8 nA, V_{mod} = 20 mV (rms), and T = 0.3 K.)

bias of $B_{ex} = \pm 0.7$ T. The interaction can be thus deduced as $J = -m \cdot B_{ex} \approx -150$ μeV (an average value of $m = 3.7$ μ_B is taken, see Chapter 6.4). The magnetization curve in Figure 7.1(b) of adatom B which is slightly farther from the ML shows a FM coupling, *i.e.*, the adatom magnetization is forced parallel to the stripe at zero field ($J > 0$). An even more distant adatom C again is antiferromagnetically coupled but with a lower B_{ex}, smaller than the stripe coercivity (Figure 7.1(c)).

Similar magnetization curves are measured on many adatoms with different distance to nanowires, and the determined interaction energies J as a function of the distance are plotted in Figure 7.2. Due to the orientation of the steps of Pt(1 1 1), this distance is oriented with an angle of 50° to the $[1\,1\,\bar{2}]$ direction, the error bar ±0.2 nm of which is due to the roughness of the Co-ML-edge as visible in the STM topograph (see Figure 7.1). A damped oscillatory behavior which is reminiscent of RKKY-like exchange is observed [117, 118, 119]. Note that the coupling behavior is still observable even at a distance of 4.5 nm.

7.2.2 Theoretical modeling

The direct exchange interaction can be immediately excluded to be responsible for the finding because of the long range of the coupling behavior. In order to evaluate the role of dipole-dipole interaction, the interaction energy between a Co adatom and a Co ML stripe is calculated according to the equation

$$J_{\mathrm{dip-dip}}(d) = \sum_{j} \frac{1}{r_j^3}[\vec{m} \cdot \vec{m}_j - 3(\vec{m} \cdot \hat{r}_j)(\vec{m}_j \cdot \hat{r}_j)], \tag{7.1}$$

where the summation is over all the atoms of the stripe, $\vec{m}$ and $\vec{m}_j$ are the magnetic moments of the adatom and of the atoms of the stripe, and $\vec{r}_j$ ($\hat{r}_j$) is the relative distance (unit vector). Considering the perpendicular magnetic anisotropy, it can be reduced to

$$J_{\mathrm{dip-dip}}(d) = \vec{m} \cdot \sum_{j} \frac{1}{r_j^3}\vec{m}_j. \tag{7.2}$$

It is assumed that the Co stripe has a width of 10 nm and a homogeneous saturation magnetization of 1.3×10^6 A/m so that m_j can be deduced. The calculated result is shown with the black line in Figure 7.2. It is found that $J_{\mathrm{dip-dip}}$ always favors AF and is negligible even at very short distance. Therefore, it is concluded that the interaction is dominated by indirect exchange via the Pt conduction electrons.

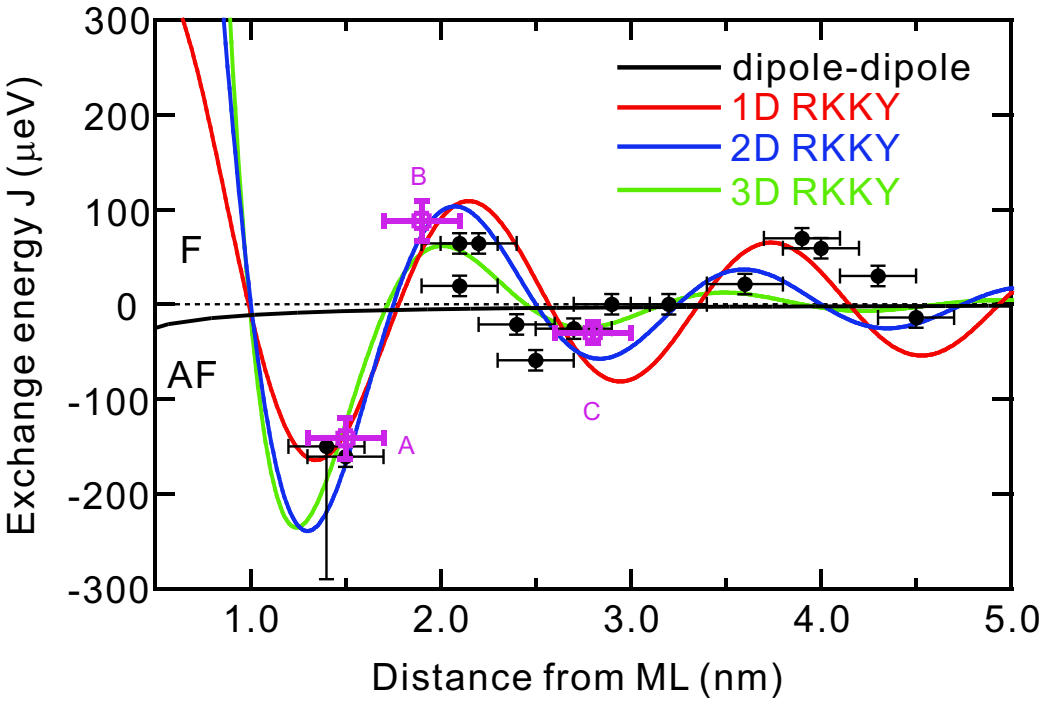

Figure 7.2: **RKKY coupling of adatoms to nanowires**. Dots show the measured interaction energy as a function of distance from ML stripes as indicated by the arrow in Figure 7.1(d). The black line is the dipolar interaction calculated as described in the text. The red, blue, and green lines are fits to 1D, 2D, and 3D range functions for RKKY interaction. Magenta points correspond to atom A, B, and C in Figure 7.1. Horizontal error bars are due to the roughness of the Co-ML-stripe edge, whereas the vertical ones are due to the uncertainty in B_{ex}. (Tunneling parameters: V_{stab} = +0.3 V, I_{stab} = 0.8 nA, V_{mod} = 20 mV (rms), and T = 0.3 K.)

If only isotropic exchange is considered (neglect Dzyaloshinskii-Moriya interaction, see Chapter 7.3.2), the interaction can be described by the following Hamiltonian:

$$\hat{H} = J(\vec{d}_{ij})\hat{\vec{S}}_i \cdot \hat{\vec{S}}_j. \tag{7.3}$$

Here, $\hat{\vec{S}}_i$ and $\hat{\vec{S}}_j$ are the spin operators of the atoms at position $\vec{r}_i$ and $\vec{r}_j$, and $J(\vec{d}_{ij})$ is the exchange constant that depends on their distance $\vec{d}_{ij} = \vec{r}_i - \vec{r}_j$. $J(\vec{d}_{ij})$ usually depends on the distance $|\vec{d}_{ij}|$ as well as on the direction of $\vec{d}_{ij}$. However, in an isotropic itinerant electron system, one can assume $J(\vec{d}_{ij}) = J(d_{ij})$. If the exchange is dominated by three-dimensional (3D) electrons, $J(d)$ is given by the following so called range function [117, 118, 119],

$$J(d) = 6\pi Z J^2 N(E_F)[\frac{\sin(2k_F d)}{(2k_F d)^4} - \frac{\cos(2k_F d)}{(2k_F d)^3}], \tag{7.4}$$

where Z is the number of conduction electrons per atom, J is the *s-d* exchange constant, $N(E_F)$ is the density of states at E_F, and $k_F = 2\pi/\lambda_F$ is the Fermi wave-vector. So it contains short- and long-range terms, and reduces to

$$J(d) = \frac{J_0 \cos(2k_F d + \delta)}{(2k_F d)^3} \tag{7.5}$$

at large distance, where a phase factor δ is included to account for the scattering phase due to the charge difference between impurity and host and due to the former's angular momentum [8]. J_0 depends on the density of the conduction electrons, the *s-d* exchange constant and the density of states at E_F. The $\cos(2k_F d)$ term determines the oscillating period as half the Fermi wavelength, while $(2k_F d)^3$ determines the decay rate, *i.e.*, the larger k_F the faster it decays. In order to evaluate the difference of the approximation Equation 7.5 from Equation 7.4, Figure 7.3(a) shows the curves calculated from these two equations assuming $k_F = 2\pi/(1.6\text{ nm})$ which is a typical value for the Pt(1 1 1) surface-related electrons. It can be concluded from the curves that the short-range term $\sin(2k_F d)/(2k_F d)^4$ is already negligible in this case when $d > 1$ nm while the long-range term $\cos(2k_F d)/(2k_F d)^3$ decays relatively slowly oscillating between FM and AF with distance.

Because RKKY interaction is mediated by conduction electrons, it depends on their dimensionality. In the case of isotropic D-dimensional electron systems which mediate the interaction, the long-range behavior

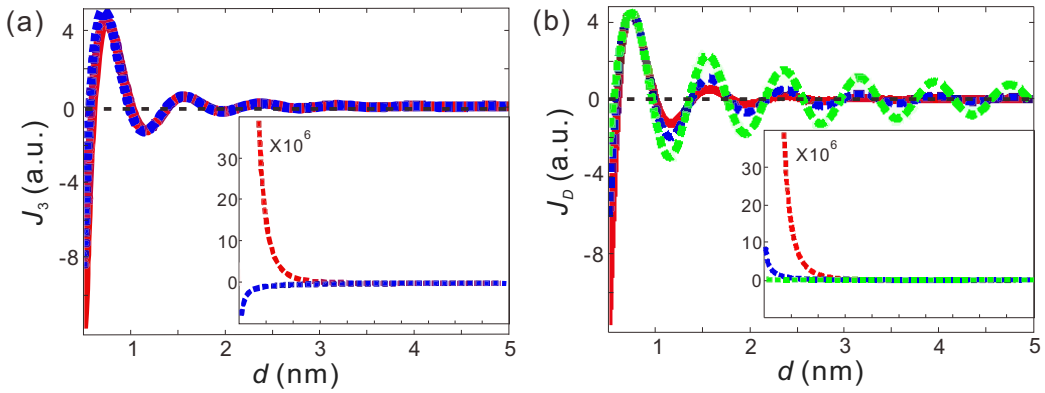

Figure 7.3: **RKKY model within free electron approximation**. **(a)** Comparison of the range functions of Equation 7.4 (blue) and Equation 7.5 (red) for 3D RKKY interaction at large distance. **Inset** shows the short-distance behavior, from 0 to 0.5 nm. **(b)** Dimensionality dependent range functions. Red: 3D; Blue: 2D; Green: 1D. **Inset** shows the short-distance behavior, from 0 to 0.5 nm.

correspondingly can be generalized to [130, 131, 132]

$$J(d) = \frac{J_0 \cdot \cos(2k_F d + \delta)}{(2k_F d)^D}. \tag{7.6}$$

Figure 7.3(b) shows curves calculated for different dimensionalities with the same k_F as in Figure 7.3(a). Obviously, the 1D curve decays most slowly and is still visible at $d = 5$ nm where the 2D and 3D curves are already very weak. Therefore, RKKY interaction becomes important for a low-dimensional system especially of the size comparable with the Fermi wavelength. This conclusion is understandable, because a low-dimensional electron gas is more unstable and therefore can be more easily perturbated by impurities.

In order to test whether an RKKY description is appropriate, the data points of Figure 7.2 are fitted using Equation 7.6 with different assumed dimensionalities, D. J_0, k_F and δ are taken as variable parameters. Figure 7.2 shows the corresponding result. A good agreement is found for $D = 1$ and a wavelength of $\lambda_F = 2\pi/k_F \approx 3 \pm 1$ nm, corresponding to an oscillation period of the exchange energy of 1 to 2 nm.

For the RKKY interaction at the surface between adatoms and ML stripes a dimensionality below 2 is indeed expected. The interaction is dominated by surface related (2D) states due to their smaller k_F as compared to those of the bulk. The superposition of the contributions from all Co atoms along the stripe edge attenuates the decay further resulting in a

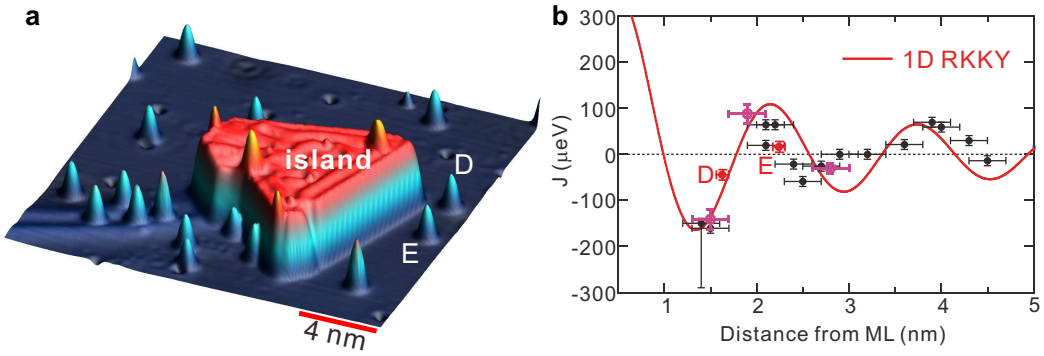

Figure 7.4: **RKKY coupling of Co adatoms to a Co ML island**. **(a)** STM topograph of an area with a Co ML island and Co adatoms nearby. Note that the island is located on the same terrace as the adatoms. **(b)** Same as Figure 7.2 but including the exchange energy of adatom D and E with the island (red points) whose topography is shown in (a). Due to the sharpness of the island-Pt edge, the horizontal error bars for points D and E are smaller. (Tunneling parameters: V_{stab} = +0.3 V, I_{stab} = 0.8 nA, V_{mod} = 20 mV (rms), and T = 0.3 K.)

dimensionality close to $D = 1$. This conclusion is analogous to the case of the exchange interaction between ferromagnetic layers separated by non-magnetic spacer layers where the dominating states are bulk (3D) states, while the summation over the atoms in the layer can result in a 2D asymptotic behavior [133]. It can be concluded that the experimentally observed indirect exchange is due to a state with a strong localization in the surface. The measured period of the RKKY interaction is consistent with the period extracted from the pairwise exchange (see Chapter 7.3) and from the KKR calculations of the spin polarization in the Pt(1 1 1) (see Chapter 8.3). It will be shown later by investigating the exchange interaction between adatom pairs, that the responsible state for the RKKY interaction is most probably the same surface resonance with an effective mass of 1.5 m_{e} which is also responsible for the electron scattering at subsurface defects described in Chapter 4.1.2.

The RKKY interaction curve shown in Figure 7.2 is measured on adatoms residing on the Pt terrace which is adjacent to and thus one atomic layer higher than the one the nanowire is grown on. There are also adatoms found in the vicinity to the Co ML which are on the same Pt terrace than the ML. Because the hybridization of the nanowire to the Pt layer in these two cases is different leading to a different $s - d$ exchange, one could expect a different strength of the RKKY interaction. Figure 7.4(a)

illustrates an atomic layer high Co island on the Pt(1 1 1) terrace. Several adatoms can be found nearby, of which single-atom magnetization curves are recorded. Similar to the previous case, AF and FM couplings are found. For instance, the adatom D is coupled AF and the adatom E is coupled FM to the Co island. The coupling strength values are plotted with red dots in Figure 7.4(b). Obviously, the coupling strength is consistent with the previous case.

In conclusion, it has been demonstrated in this section that the RKKY interaction can be directly detected with atomic resolution at an energy scale of tens of μeV by recording single-atom magnetization curves. The interaction with nearby Co nanowires can stabilize the magnetization of Co adatoms.

7.3 Directionality and strength of pairwise RKKY interactions

So far an RKKY model in an isotropic continuum conduction electron sea has been assumed [117, 118, 119]. This model works quite well to describe the magnetic behavior of diluted magnetic bulk systems. However, it may be misleading or even collapse when the system size becomes comparable with or even smaller than the Fermi wavelength, where the discontinuity and the anisotropy due to the crystalline lattice become non-negligibly important. There have been theoretical [133, 134, 135] and experimental [136] hints, that accurate RKKY models have to take into account the topology of the Fermi surface and the discrete distribution of magnetic moments on the atomic lattice. However, a direct proof was hampered by the fragmentary information on this distribution based on spatially averaging experimental techniques. This issue will be addressed in this section.

As demonstrated in the previous section, a direct detection of magnetic interactions is feasible with the technique of measuring magnetization curves of individual atoms using spin-polarized STS [55]. This section presents a study of the RKKY interaction in well-defined pairs of Co adatoms with different orientations and distances both experimentally by measuring single-atom magnetization curves and by first-principles calculations using the fully-relativistic Korringa-Kohn-Rostoker Green function (KKR) method [137, 138].

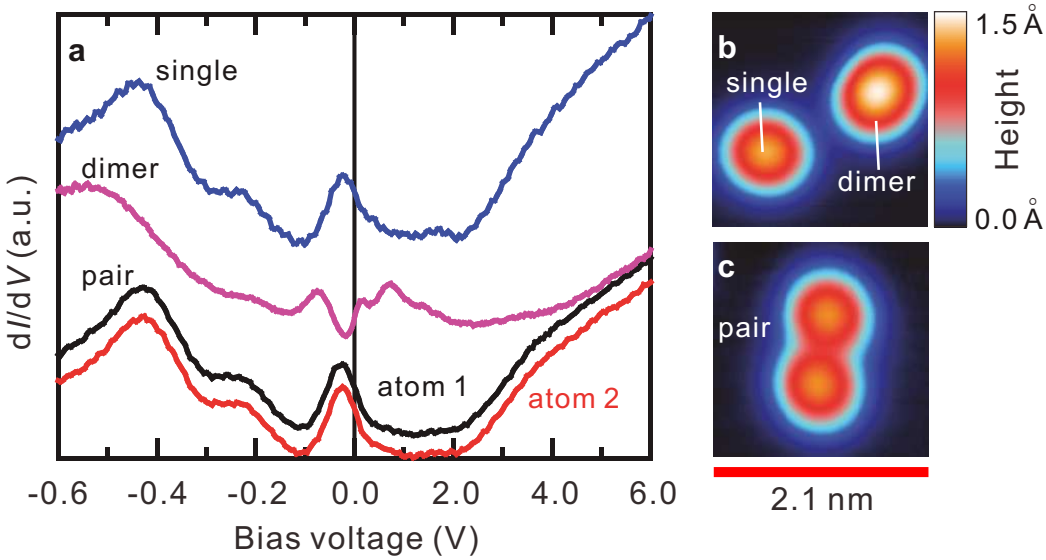

Figure 7.5: **Spectroscopy on single adatoms, pairs and dimers**. **(a)** dI/dV curves measured on a single *fcc* adatom, on a dimer (two atoms on next neighbor *fcc* binding sites), and on the two adatoms in an *fcc* pair with a distance of 0.74 nm (curves are offset for clarity, tunneling parameters: I_{stab} = 1 nA, V_{stab} = +0.6 V and +0.8 V, V_{mod} = 10 mV and 20 mV (rms), and T = 0.3 K). The single adatom and the dimer are visible in the STM topograph in **(b)**, the adatom pair is shown in **(c)**.

7.3.1 Experimental results

Direct exchange interaction requires a strong overlap of the electronic orbitals of atoms, which results in a distinct change of the electronic density of states of the involved atoms compared to that of isolated atoms, and hence occurs only at a short distance. This interaction can be excluded in Co adatom pairs with a separation larger than one lattice constant. Since the dI/dV curve is closely related to the LDOS of the sample (see Chapter 2.4), direct exchange would result in a drastic change in the local dI/dV curve measured on the adatoms of a pair compared to the curve measured on an individual adatom. Figure 7.5 presents dI/dV curves measured on single atoms, adatom pairs and dimers. Dimers from two adatoms on next nearest neighboring *fcc* binding sites appear slightly elliptical and higher (1.5 Å) than the single *fcc* adatom (1.3 Å) (Figure 7.5(b)) and than the adatoms in the pairs (Figure 7.5(c)). While the dI/dV curve taken on the dimer shows a distinct change near E_{F}, the dI/dV curves measured on the two adatoms of the pair are identical to that measured on the single adatom

(Figure 7.5(a)). Therefore, it is concluded, that the adatoms in pairs with separations of more than one lattice spacing behave electronically identical to individual adatoms, and are thus dominated by the *indirect* exchange via the substrate, *i.e.*, RKKY interaction. Interactions in such adatom pairs will be studied in the following.

Examples of isolated adatom pairs with decreasing separations between five to two lattice constants are shown in Figure 7.6(a) to (e). Their lattice sites given in Figure 7.6(k) to (o) can be extracted without ambiguity (see Chapter 4.1.2) and only *fcc* adatoms are studied. Their corresponding magnetization curves are shown in Fig. 7.6(f) to (j), which exhibit distinct shapes.

The two adatoms in the pair with the largest separation of 1.21 nm (Figure 7.6(a)) have typical S-shaped magnetization curves shown in Figure 7.6(f) similar to the ones measured on isolated adatoms (see Chapter 6.3). These two adatoms are thus both paramagnetic and their magnetizations are aligned in parallel to the magnetic field direction. When the separation in the pair is decreased by about one lattice constant (Figure 7.6(b)) the corresponding magnetization curves are drastically changed (Figure 7.6(g)) and a plateau appears around zero field $B_{\mathrm{ext}} = 0$ T. Obviously, the two magnetic moments of the pair couple to zero. Only when B exceeds a critical value $|B_{\mathrm{crit}}| \approx 0.25$ T does the antiparallel coupling break and the magnetizations of both adatoms saturate parallel to $\vec{B}_{\mathrm{ext}}$. For another pair with identical distance but with a different neighbourhood of surrounding adatoms and defects (Figure 7.6(c)), the right adatom shows the usual paramagnetic behavior but with a low slope, whereas the left adatom behaves diamagnetically at low magnetic field (Figure 7.6(h)), *i.e.*, its magnetization turns opposite to the magnetic field direction and is forced to be aligned antiparallel to that of the right adatom. The coupling again breaks for $|B_{\mathrm{crit}}| \approx 0.48$ T, and the magnetizations are again aligned in parallel to $\vec{B}_{\mathrm{ext}}$. The same behavior is found for the pair with a slightly lower separation (Figure 7.6(d) and (i)), but now with even lower slopes in the magnetization curves and a significantly larger $|B_{\mathrm{crit}}| \approx 1.25$ T. When the inter-atomic distance is still smaller (Figure 7.6(e,j)) the magnetization curves look again similar to those of isolated adatoms, indicating parallel alignment of the two spins.

The shape of the curves will be interpreted in terms of the magnetic interactions between the Co adatoms in the following. Obviously, the adatoms 1 and 2 in the pair are subject to an oscillatory coupling energy J_{12} which forces their magnetizations to be aligned parallel (FM coupling, $J_{12} > 0$) for pair (a) and (e) and antiparallel (AF coupling, $J_{12} < 0$) for pair

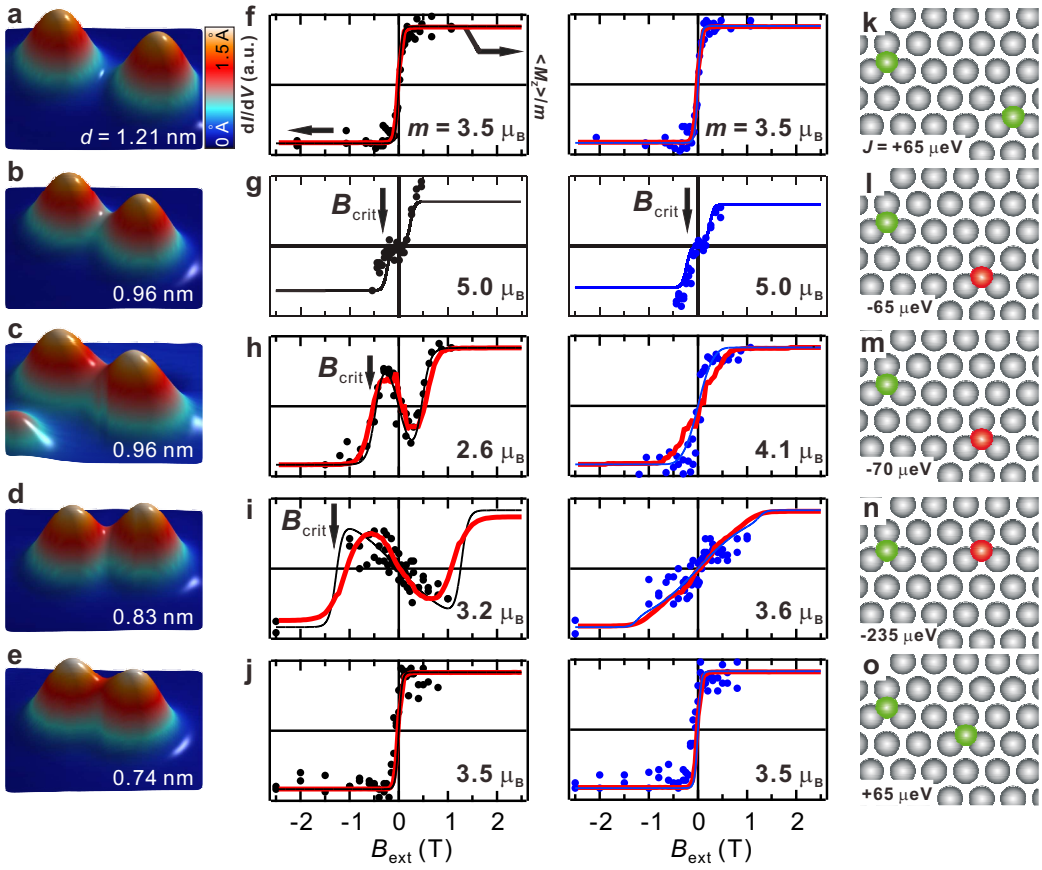

Figure 7.6: **Magnetization curves of Co pairs**. **(a)-(e)** STM topographs (2.1 nm × 2.1 nm) of Co pairs with decreasing distance as indicated. **(f)-(j)** Single-atom magnetization curves measured on the left adatom (black dots) and on the right adatom (blue dots) of each pair. The curves are vertically normalized to the saturation magnetization and horizontally offset to compensate for the effective tip field B_T (see Chapter 6). The black and blue straight lines are calculated from the Ising model assuming magnetic moments m given in each panel, while the red straight lines are calculated from the Monte Carlo simulations within the quasi-classical Heisenberg limit with the same parameters within the error bars of ±60%. **(k)-(o)** Ball models of the atomic configuration in the pairs and exchange coupling constants J resulting from the Ising model fit. The same color indicates ferromagnetic coupling, different colors indicate antiferromagnetic coupling. (Tunneling parameters: V_{stab} = +0.3 V, I_{stab} = 0.8 nA, V_{mod} = 20 mV (rms), and T = 0.3 K).

(b), (c) and (d).

7.3.2 Theoretical modeling

In order to theoretically describe the observations, the experimental magnetization curves are modeled with the following Hamiltonian

$$\begin{aligned} \hat{H} &= -\frac{1}{2}\sum_{\mathrm{i,j(i\neq j)}} J_{\mathrm{ij}}\left(\vec{r}_{\mathrm{ij}}\right)\hat{\vec{S}}_{\mathrm{i}}\cdot\hat{\vec{S}}_{\mathrm{j}} + \sum_{\mathrm{i,j(i\neq j)}}\vec{D}_{\mathrm{ij}}\cdot(\hat{\vec{S}}_{\mathrm{i}}\times\hat{\vec{S}}_{\mathrm{j}}) \\ &+ K\sum_{\mathrm{i}}\left(\hat{S}_{\mathrm{i}}^{z}\right)^{2} - \sum_{\mathrm{i}} m_{\mathrm{i}}\hat{\vec{S}}_{\mathrm{i}}\cdot\vec{B}_{\mathrm{ext}} \end{aligned} \tag{7.7}$$

where i(j) numbers the adatoms, $\hat{\vec{S}}_{\mathrm{i}} = \hat{\vec{M}}_{\mathrm{i}}/m_{\mathrm{i}}$ are the operators of the normalized magnetic moments, and m_{i} are their absolute values (in μ_{B}). The first sum describes the collinear distance-dependent exchange interactions. The second sum describes the anisotropic exchange coupling due to Dzyaloshinskii-Moriya interaction. It is well known, that strong spin-orbit coupling which is present on Pt(1 1 1) might lead to a significant Dzyaloshinskii-Moriya type of exchange resulting in a canting of the two spins in the pair [88], but it is ignored in the present analysis due to the following reason. The KKR calculations show that the components of $\vec{D}_{\mathrm{ij}}$ are at most of the same strength as J_{ij}. However, even then, because of the large K, the resulting canting angle is small (6°) and will not affect the measured magnetization curves considerably. The third sum describes a uniaxial anisotropy favoring an out-of-plane (z) orientation of magnetization for the negative K = - 9.3 meV/atom [4], and the fourth sum is the Zeeman energy. Because the dipolar interaction is found to be at least three times smaller than the measurement temperature, it was omitted immediately. Two different models are applied: (i) an Ising limit ($\hat{\vec{S}}_{\mathrm{i}} = \pm 1\cdot\hat{e}_z$) and (ii) a quasi-classical Heisenberg limit $\hat{\vec{S}}_{\mathrm{i}} = \vec{S}_{\mathrm{i}}$ where $\vec{S}_{\mathrm{i}}$ is a classical vector. The expectation values of the atom magnetizations $\langle M_{\mathrm{i}}^{z}\rangle$ have been calculated exactly. Moreover, it has been demonstrated that the thermodynamic behavior of single Co adatoms and clusters on Pt(1 1 1) with a giant magnetic anisotropy, may be successfully described in the framework of the Langevin model (see Chapter 6.4 and [4]). As the Langevin distribution can be very well reproduced by means of Monte-Carlo simulations, the expectation values $\langle M_{\mathrm{i}}^{z}\rangle$ have also been calculated within the model (ii) in

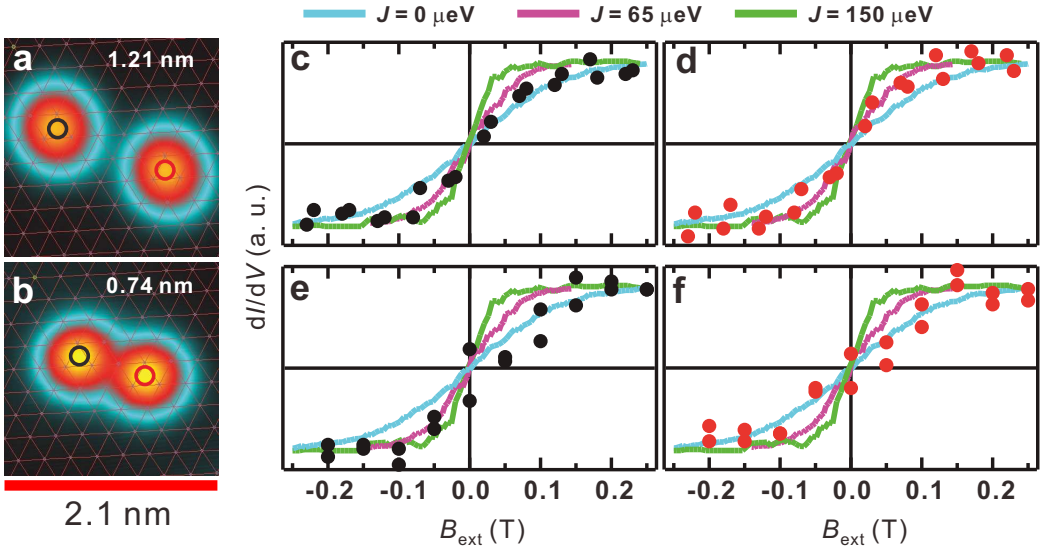

Figure 7.7: **Uncertainty in determining J for Co pairs with ferromagnetic coupling**. **(a)**, **(b)** STM topographs of two Co pairs with ferromagnetic coupling. The positions on the Pt(1 1 1) lattice (red mesh) as well as the distances are indicated. **(c)**, **(d)**, **(e)**, **(f)** Single-atom magnetization curves measured on the left (black dots) and the right (red dots) adatoms of the two pairs of **(a)** and **(b)**, respectively. The straight lines show Monte Carlo simulated curves assuming different exchange energies J as indicated at the top and a magnetic moment of $m = 3.5\ \mu_B$ for each adatom. (Tunneling parameters for magnetization curves: $V_{stab} = 0.3$ V, $I_{stab} = 0.8$ nA, $V_{mod} = 20$ mV (rms), and $T = 0.3$ K.)

the framework of this technique. For the Monte-Carlo simulation, a temperature of $T = 0.3$ K and the Metropolis single flip algorithm have been used. Up to 10^7 Monte-Carlo steps have been performed for each value of B_{ext} after the system has reached thermal equilibrium. An additional averaging over several identical systems has been performed.

m_1, m_2 and J_{12} are varied to fit the measured magnetization curves. It is found that the two different models (i) and (ii) are undistinguishable within the experimental error because of the large magnetic anisotropy which forces the magnetization to point out-of-plane. The results from the Ising model and from Monte-Carlo simulations with same parameters within the error bars of ±60% are shown in Figure 7.6(f) to (j) together with the corresponding m values and J values. This demonstrates an excellent reproduction of the measured data.

The error bar in the determination of J is given by the uncertainty in

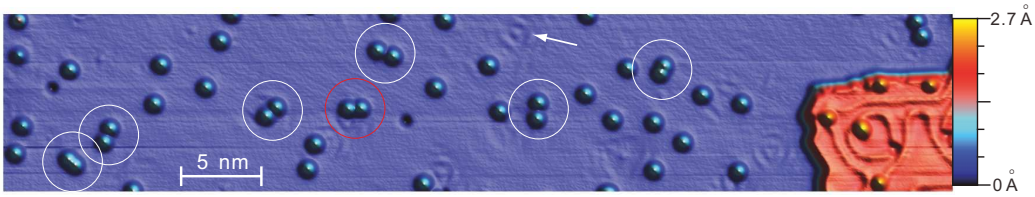

Figure 7.8: **Co pairs in different surroundings**. Overview STM topograph of an area with several adatom pairs marked by circles. The adatom pair marked by the red circle is the one evaluated in Figure 7.6(d) and (i). The arrow points to a subsurface scattering pattern. A part of the Co monolayer stripe is visible on the right corner of the image. (Tunneling parameters: V_{stab} = +0.3 V, I_{stab} = 0.8 nA, and T = 0.3 K.)

the effective magnetic moments that can vary by ±2 μ_{B} around the average value of 3.5 μ_{B} (see Chapter 7.4). The resulting error in J is ±60% in the AFM case, while the situation is different in the FM case. Figure 7.7 shows a magnification around B_{ext} = 0 T of the magnetization curves of the two ferromagnetic pairs in Figure 7.6(a) and (e). The straight lines are Monte-Carlo simulated magnetization curves of the quasi-classical Heisenberg model assuming three different exchange energies $J \ll \mathrm{k_B}T$ = 25 μeV, $J \approx 2\mathrm{k_B}T$ and $J \gg \mathrm{k_B}T$. Such a strong variation of J causes a relative small change in the zero field slope of the curves, which is within the noise of the experimental data. Therefore, the exact value of the exchange energies cannot be determined in the ferromagnetic case and consequently large error bars have to be assumed in Figure 7.10.

For many adatom pairs, the two magnetization curves taken on each adatom are different (see, *e.g.*, Figure 7.6(h) and (i)). Accordingly, there is an additional effect that breaks the symmetry in the pair, resulting in the asymmetric shape of the two magnetization curves. The symmetry breaking can be explained by a difference in the magnetic moments m_1 and m_2 of the two adatoms. The origin of the symmetry breaking is discussed in the following.

Figure 7.8 shows an overview topograph of some of the adatom pairs, which are used to extract the indirect exchange-interaction energy from single-atom magnetization curves. In particular, the adatom pair evaluated in Figure 7.6(d) and (i) is marked by a red circle. There are basically two possible effects: (i) the substrate is electronically inhomogeneous due to subsurface-defect induced conduction-electron scattering. Scattering states are visible in Figure 7.8 as an oscillation with three-fold symmetry (see arrow). Therefore, adatoms can have a different electronic background

which could cause a different effective magnetic moment for each adatom. (ii) The adatom pairs are surrounded by other adatoms, which induce a mean field by their long-range RKKY interaction as will be discussed in Chapter 7.4. There it is shown that this effect results in effective magnetic moments that can vary by $\pm 2\ \mu_B$ around the average value of $3.5\mu_B$.

The impact of these two effects on the deduced J values can be further illustrated by measuring single-atom magnetization curves on pairs with the same distance but located in different surroundings on the substrate (Figure 7.9). Pair 1 is far from any defect and far from other adatoms, so it can represents a clean pair. Consequently, the magnetization curves measured on the two adatoms in that pair are rather symmetric and show a plateau for $|B_{ext}| \leq |B_{crit}|$. This behavior is consistent with the assumption of equal magnetic moments for the two adatoms as shown by the fitted Ising-model curves in Figure 7.9(a). Instead, in pair 2 the left atom is located close to a defect and closer to other adatoms (Figure 7.9(b)) which breaks its symmetry. The corresponding magnetization curve shows a diamagnetic slope for $|B| \leq |B_{crit}|$ indicating a reduced magnetic moment. The resulting Ising-model fit confirms, that the two magnetic moments are now slightly different ($m_1 = 2.6\ \mu_B$, $m_2 = 4.1\ \mu_B$). However, more importantly, the resulting coupling strength $J = -70\ \mu$eV is still the same as for the "clean" pair 1 within the error bars of ±60%. Another example is pair 3, which is part of a triplet (Figure7.9(c)) (magnetization curve of the leftmost adatom in the triplet is shown in Chapter 7.3.4). Here, the leftmost adatom of the triplet breaks the symmetry because it couples ferromagnetically to the left adatom in the pair by RKKY interaction. Now, the left adatom in the pair has a paramagnetic curve but the right adatom shows a diamagnetic slope for $|B_{ext}| \leq |B_{crit}|$. Fitting Ising-model curves to the three triplet magnetization curves results in equal magnetic moments for all three adatoms ($m_1 = m_2 = m_3 = 3.5\ \mu_B$) and an exchange coupling constant of $J = -40\ \mu$eV for the pair. If the leftmost adatom in the triplet is ignored in the Ising model, a twice as large magnetic moment has to be assumed for the left atom in the pair ($m_1 = 7.6\ \mu_B$) in order to account for the ferromagnetic coupling to the third adatom. But also in this case, the fitted J is still the same within the error bars.

These examples prove, that (i) defects and (ii) the RKKY coupling to other statistically distributed adatoms can break the symmetry in the pair. However, the symmetry breaking only affects the effective magnetic moments of the adatoms, but *not* the deduced exchange coupling constants J, which are the same as for the "clean" pair. Note that pairs inside triplets are not included for the evaluation of the pairwise exchange constants.

Using Equation 7.7 one can show that, for antiferromagnetic interaction

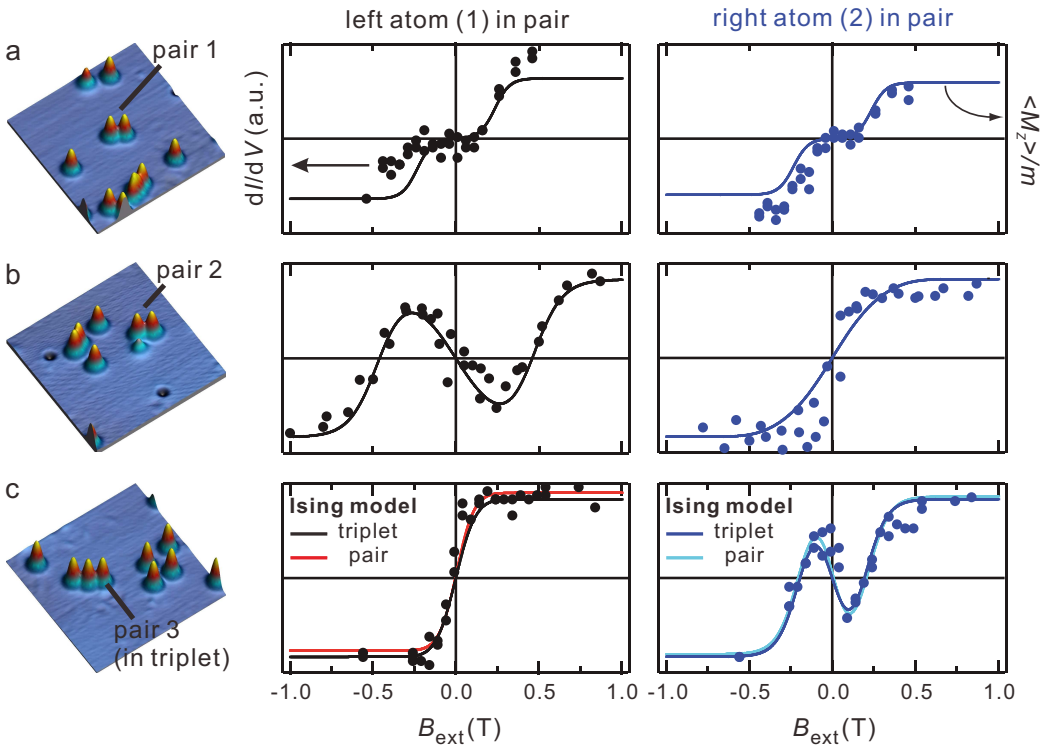

Figure 7.9: **Symmetry breaking in Co pairs with the same distance (0.96 nm) but in different surroundings**. **Left panels**: STM topographs (10 nm × 10 nm) of the three pairs and their environments. **Middle and right panels**: Single-atom magnetization curves measured on the left adatom (black dots) and on the right adatoms (blue dots) in each pair. The straight lines are fits to the Ising model resulting in the following magnetic moments m and exchange coupling constants J; **(a)** Pair 1: J = -60 μeV, $m_1 = m_2 = 5\ \mu_B$. **(b)** Pair 2: J = -70 μeV, m_1 = 2.6 μ_B, m_2 = 4.1 μ_B. **(c)** Pair 3 (part of a triple): Ising fit including third adatom (black and blue straight lines): J = -40 μeV, $m_1 = m_2 = m_3$ = 3.5 μ_B. Ising fit ignoring third adatom (red and cyan-colored straight lines) J = -40 μeV, m_1 = 7.6 μ_B, m_2 = 3.5 μ_B. (Tunneling parameters: V_{stab} = +0.3 V, I_{stab} = 0.8 nA, V_{mod} = 20 mV (rms), and T = 0.3 K.)

between two atoms with magnetic moments m_1 and m_2 ($m_1 \leq m_2$, w.l.o.g.), the coupling can be broken if the external magnetic field gets larger than $|B_{\mathrm{crit}}| = -J_{12}/m_1$. Assuming $m_1 = 3.5\ \mu_B$ this simple formula results in an antiferromagnetic interaction of $J \approx -100\ \mu$eV for pair (b,c) and $J \approx -250\ \mu$eV for pair (d) which is already close to the results from the fits in Figure 7.6.

Fits are performed for about 10 pairs with different distances d placed at different locations on the bare Pt(1 1 1) substrate. The resulting interaction energies $J(d)$ are shown in Figure 7.10(a) together with the relative position of the two adatoms on the lattice in Figure 7.10(c). The J values from adatom triplets are also included (see Chapter 7.3.4).

Note that the orientation of the pairs relative to the underlying Pt(1 1 1) lattice is changing, when the distance in the pairs is increased. The measurements show, that the RKKY interaction is ferromagnetic for small distances, gets maximally antiferromagnetic for a distance of three lattice spacings in the $[1\,\bar{1}\,0]$ direction ($J \approx -250\ \mu$eV), and then shows a damped oscillation between ferromagnetic and antiferromagnetic coupling. However, there is no well defined wavelength. The data of the pairs along the closed packed direction $[1\,\bar{1}\,0]$ may be fitted to a 2D isotropic continuous RKKY model with Equation 7.6 using a Fermi wavelength $\lambda_F = 2\pi/k_F = 2 \pm 0.5$ nm (Figure 7.10(a)). However, for slightly different orientations, the isotropic model fails, and a strongly different wavelength has to be assumed (cyan-colored, yellow and red data points). This proves a strong directionality of the RKKY interaction on the atomic scale.

In order to explore the directionality further, the interaction energy J of adatom pairs is calculated using density functional theory within the local spin density approximation, in connection with the KKR method [56].

The calculations show that, since the sizes of cobalt and platinum atoms are extremely different, the deposited adatoms sink towards the substrate by about 20% of the surface interlayer distance. The total magnetic moment of a single cobalt adatom with its four neighbouring platinum shells reaches a value of $m = 3.53\mu_B$ in which the spin(orbital) contribution is about 3.05 μ_B(0.48 μ_B). The pairwise magnetic exchange interactions have been extracted by mapping the *ab-initio* calculations to the Heisenberg model (Equation 7.7) and considering two magnetic configurations: a ferromagnetic solution with energy $E_{\uparrow\uparrow}$ where both magnetic moments are parallel (perpendicular to the surface) and an antiferromagnetic solution with $E_{\uparrow\downarrow}$ where the magnetic moments are antiparallel to each other. J_{ij} is then given by: $(E_{\uparrow\downarrow} - E_{\uparrow\uparrow})/2$.

The calculated $J(d)$ shown in Figure 7.10(b) reveals the same direction

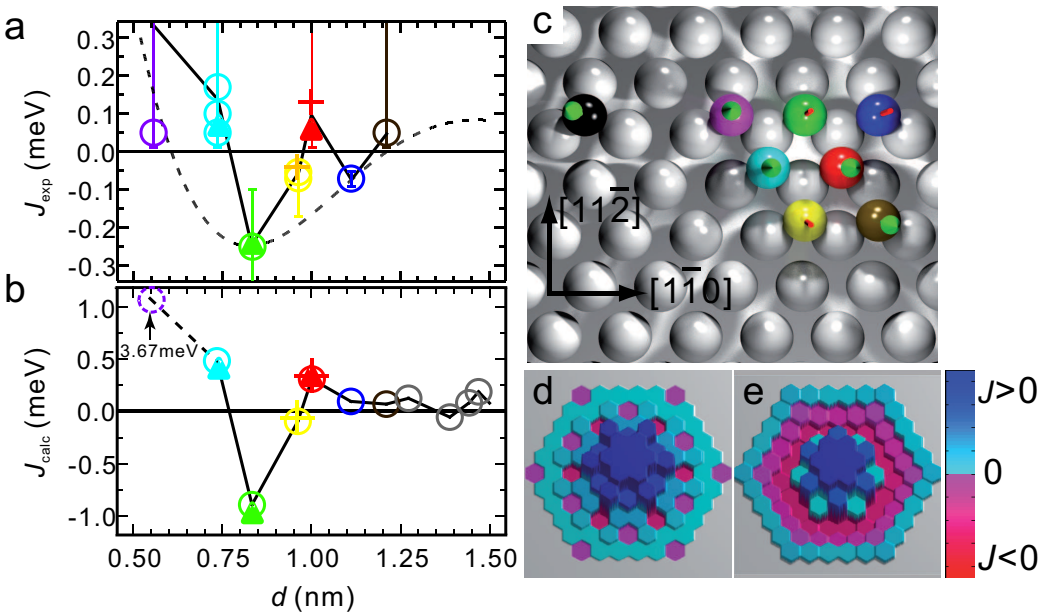

Figure 7.10: **Distance dependence and directionality of RKKY interaction**. **(a),(b)** Measured J_{exp} and calculated J_{calc} in Co pairs (circles) and triplets (triangles, triangular triplet; crosses, straight triplet (see Chapter 7.3.4)) as a function of distance d. The data points are colored corresponding to the lattice positions of the adatoms in the pairs shown in **(c)** (first adatom: black ball with spin up; second adatom: colored ball with spin direction as indicated by the arrow). Values in **(a)** are extracted from the magnetization curves by fitting to the Ising model. The dotted line is a fit to the data of the pairs oriented along [1 $\bar{1}$ 0] using a 2D isotropic continuous RKKY model (see Chapter 7.2.2). **(d)** Plot of the calculated J values of **(b)** as a function of position in the (1 1 1) plane. Each hexagon corresponds to the lattice site of the second adatom in a specific pair with the first adatom fixed in the center. The height and color of each hexagon corresponds to the size of J. **(e)** Same as **(d)**, but with J values from the 2D isotropic continuous RKKY model but evaluated on the discrete lattice.

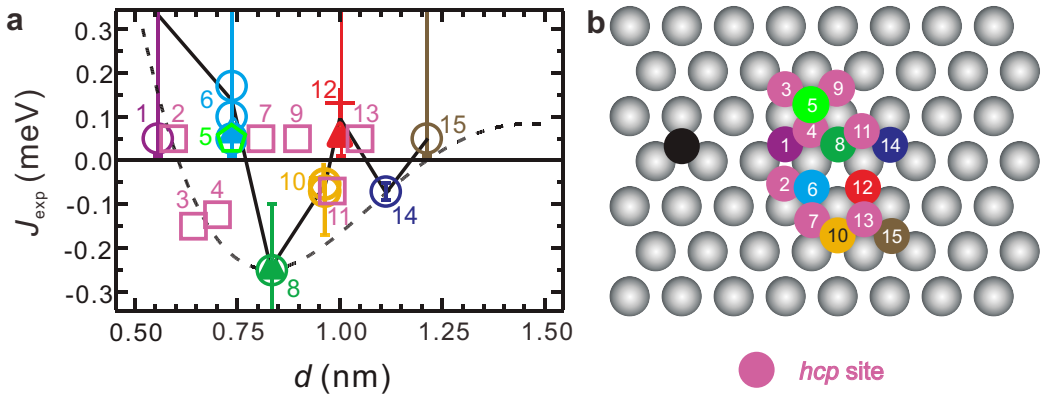

Figure 7.11: **RKKY interaction for adatom pairs on different binding sites**. **(a)** Same as Figure 7.10(a) but additionally including data points experimentally evaluated on *fcc-hcp* pairs (pink rectangles) and a *hcp-hcp* pair (green pentagon). Colors and numbers indicate the binding sites as illustrated with the ball-model in **(b)** corresponding to those in the interaction curve in (a) (First adatom: black ball; second adatom: colored ball). Pair 5 is of *hcp-hcp* configuration.

dependency as the measured data with a maximum in the antiferromagnetic coupling for a distance of three lattice spacings in $[1\,\bar{1}\,0]$ direction. The values are a factor of about three times larger than the experimental ones. Given the small absolute values of J of only several tens of μeV, the correspondence is remarkably good. Figure 7.10(d) shows a different view of the calculated J values in a 3D plot, which highlights the strong anisotropy of the RKKY interaction at the surface when being compared to a similar plot of the 2D isotropic RKKY model in Figure 7.10(e). The strongest variation of J with increasing interatomic distance is observed along $[1\,\bar{1}\,0]$, while it is weaker along $[1\,1\,\bar{2}]$.

7.3.3 Discussion of directionality

Both the experimental and theoretical results demonstrate that the RKKY interaction in adatom nanostructures is strongly directional and has a strong tensorial character. It is proposed that the upward dispersing surface resonance crossing E_F at $\lambda_F \approx 1.6$ nm with an effective mass of about 1.5 m_e could be mediating the observed RKKY interaction (see Chapter 4.1.2, Chapter 7.2 and Chapter 8.3) [65]. Since this surface resonance resides at the Fermi surface of the material, anisotropies of the Fermi surface could naturally explain the observed directionality in RKKY exchange.

Indeed, even the shape of the rather simple Fermi surface of copper modifies strongly the electron motion as demonstrated recently [72]. In platinum, moreover, on top of the Fermi-surface hot spots there exists a Stoner enhancement for the investigated adatom-pair distances, which further modifies the interaction (see Chapter 8). This result will be important for the design of novel nanostructures exploiting the indirect exchange in other materials, which usually have even more complex Fermi surfaces.

The data presented so far were all measured on *fcc-fcc* adatom pairs. It would be interesting to see whether the directionality of RKKY interaction can also be observed for adatom pairs on different binding sites. Figure 7.11 shows the same curves as in Figure 7.10 but now including additional data points experimentally evaluated on *fcc-hcp* and *hcp-hcp* pairs. The *hcp-hcp* pair (5) shows FM interaction consistent with the *fcc-fcc* pair having the same distance (6). Obviously, the RKKY interaction does not depend crucially on the overall stacking of the pair. However, the additional pairs with mixed *fcc-hcp* stacking further prove the strong directionality of the RKKY interaction. It gets most obvious by comparing pair 4 and 6 whose separations are very close while the exchange changes the sign because the two pairs are oriented along different crystallographic directions (Figure 7.11(b)). A similar result is also observed for pair 7 and 8.

7.3.4 Prediction: A step towards tailoring nanomagnetism

Here it will be demonstrated that the pairwise indirect exchange $J(d)$ from Figure 7.10 allows for the prediction of the behavior of nanostructures built from a larger number of adatoms. Triplets shown in Figure 7.12 are investigated. Figure 7.12(a) represents a triplet with an almost equidistant triangular shape with atom positions shown in panel c. From the map of the pairwise interaction in Figure 7.10(a) and (b), it is expected that there is a weak ferromagnetic coupling between the black and the red, and between the green and the red adatoms, and a strong antiferromagnetic coupling between the black and the green adatoms. The measured magnetization curves are shown in Figure 7.12(e) to (g) together with the calculated magnetization curves from the Ising model and from the Monte Carlo simulations (Equation 7.7). The fitted J values are also included in Figure 7.10(a). Indeed, the J values deduced from the triplet are consistent with the values from the according pairs. Note that the experimental curves are very noisy around zero magnetic field, indicating that the moments are magnetically frustrated and switch between different almost degenerate

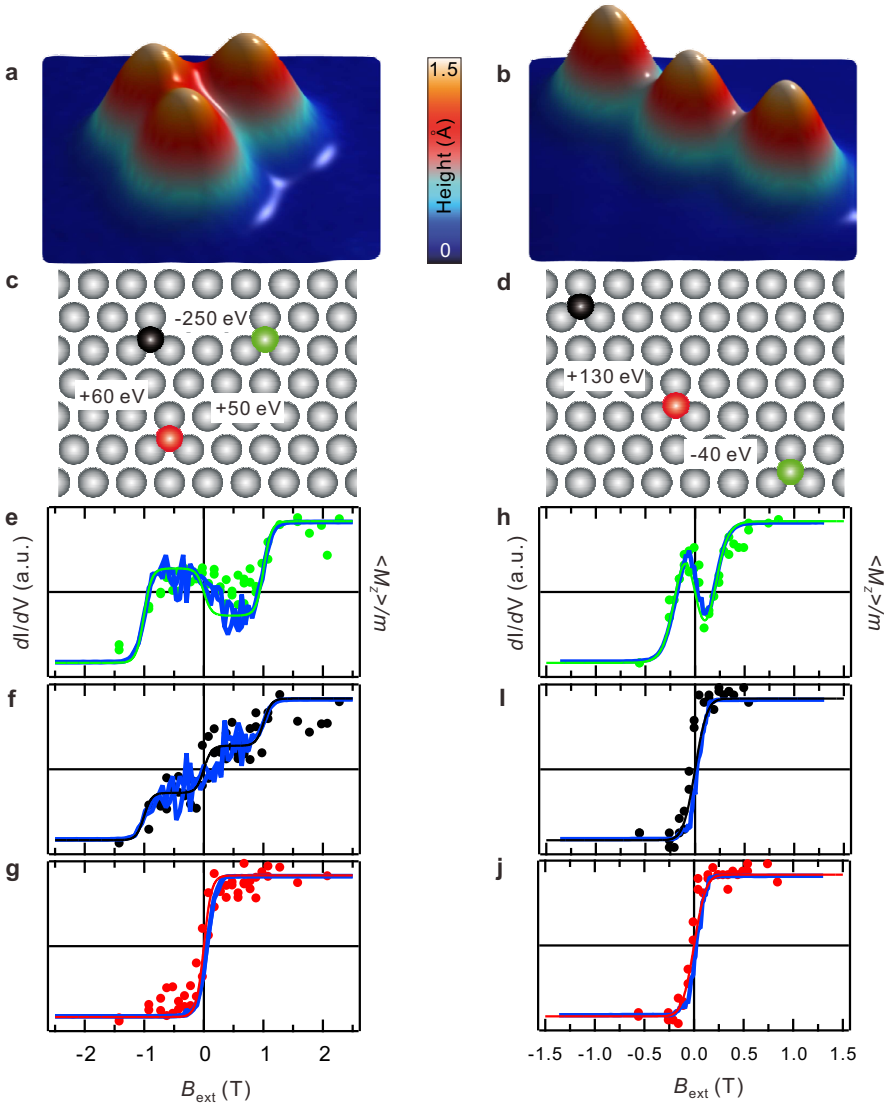

Figure 7.12: **Magnetization curves of Co triplets**. **(a)**, **(b)** STM topographs (2.8 nm × 2.8 nm) of Co triplets with triangular (**a**) and straight (**b**) shape. **(c)**, **(d)** Ball models and relative distance of the atom configuration in the triplets. **(e)-(j)** Single-atom magnetization curves (dots with color corresponding to **c**, **d**) measured on the three adatoms in the triangular triplet (**e-g**) and straight triplet (**h-j**). The green, black and red straight lines are calculated from the Ising model assuming $m_i = 3.5\ \mu_B$ and J_{ij} as indicated in **c**, **d**, while the blue straight lines are calculated from Monte Carlo simulations within the quasi-classical Heisenberg limit with the same parameters within the error bars of ±60%. (Tunneling parameters: V_{stab} = +0.3 V, I_{stab} = 0.8 nA, V_{mod} = 20 mV (rms), and T = 0.3 K.)

ground states. The fitted J values in panel (c) in fact show that the energy difference between the two configurations $\left(S^z_{\text{black}}, S^z_{\text{green}}, S^z_{\text{red}}\right) = (\uparrow\downarrow\uparrow)$ and $(\downarrow\uparrow\uparrow)$ is only 20 μeV, which is lower than the thermal energy. As visible in Figure 7.12 the Monte-Carlo simulated curves for the black and the green adatoms around zero magnetic field are frequently fluctuating between up and down states confirming the conclusion.

The same comparison can be done for a triplet with an almost straight shape shown in Figure 7.12(b). The calculated J values from the KKR method for these two triplet geometries are included in Figure 7.10(b), also showing that the deviation from the pair interactions is negligible, i.e. $J_{\text{ij}}^{\text{triplet}} \simeq J_{\text{ij}}^{\text{pair}}$. Figure 7.10 thus allows to precisely predict the magnetic state for larger adatom nanostructures coupled by indirect exchange simply by superposition of pairwise interactions.

7.4 RKKY mean field: Interaction between distant Co adatoms

It has been demonstrated in Chapter 6.4, that the effective magnetic moment of isolated Co adatoms (mean nearest neighbor distance of 2.4 ± 1 nm) exhibits a very broad scattering. The origin of this scattering was not yet discussed. In this section this issue will be addressed.

As already shown in Chapter 6.4, the magnetic moments m have a broad distribution at 0.3 K from 2 μ_{B} to 6 μ_{B} independent of the binding sites (see Figure 7.13(a)). The distribution of m for the same adatoms becomes very narrow at 4.2 K, as shown in Figure 7.13(b). This variance in m is visible as the change of the slope of the corresponding single-atom magnetization curves (see Figure 6.5(b) in Chapter 6.3), which can be approximately characterized by the difference of the saturation dI/dV signal divided by the magnetic field which is necessary to saturate the adatom up and down (B_{sat}). Since the saturation dI/dV signal stays almost the same for all adatoms, a distribution of the saturation fields B_{sat} can also reflect the variance in m, which is shown in Figure 7.13(c).

Because the peculiar spreading in the fitted m is observed similarly for both *fcc* and *hcp*, an adsorption-site-induced variance in m can be excluded immediately. Another possible origin of this broad distribution is the electronic inhomogeneity in the substrate surface due to the scattering of electrons at sub-surface defects (see Chapter 4.1.2). However, the dominance of this mechanism is very unlikely. As shown in Figure 4.8 in Chapter 4.1.2 the scattering patterns remain unchanged at 4.2 K from

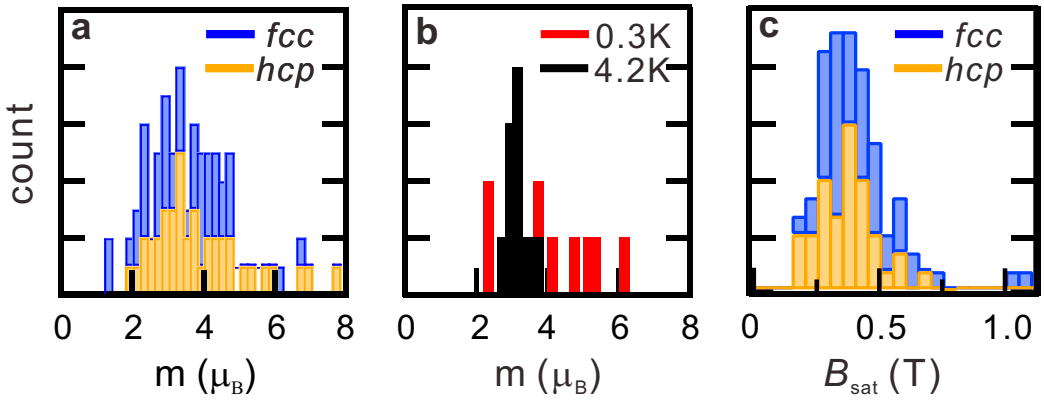

Figure 7.13: **Effect of RKKY mean field on magnetic moment and saturation field**. **(a)** The magnetic moment of Co adatoms exhibits a wide spreading independent of the binding sites at 0.3 K. **(b)** This spreading becomes very narrow at 4.2 K as compared to that at 0.3 K. **(c)** The spreading of the magnetic moment manifests as a wide distribution of the saturation field B_{sat} in the corresponding single-atom magnetization curves.

those at 0.3 K. This result cannot explain the observation that the distribution of the magnetic moment is much broader at 0.3 K than at 4.2 K. Moreover, there is no obvious correlation between m and the distribution of the scattering state. Therefore, the scattering can only be explained by a magnetic interaction J changing B_{sat}, as described in the following. In the investigated systems every Co adatom is interacting with the others through the RKKY exchange. If a particular adatom i is considered, the sum of all RKKY-interactions can be modeled by a mean field $\vec{B}_{\mathrm{RKKY}}(\vec{r}_{\mathrm{i}})$, which depends on the position of the adatom $\vec{r}_{\mathrm{i}}$. Due to the random distribution of the Co adatoms on Pt(1 1 1), $\vec{B}_{\mathrm{RKKY}}(\vec{r}_{\mathrm{i}})$ is spatially inhomogeneous which frustrates the magnetization of each adatom. However, since the adatoms have a very strong perpendicular magnetic anisotropy [4] and behave paramagnetically, $\vec{B}_{\mathrm{RKKY}}(\vec{r}_{\mathrm{i}})$ is also out of plane of the sample surface and scales from zero to a saturation value $B^{\mathrm{sat}}_{\mathrm{RKKY}}(\vec{r}_{\mathrm{i}})$ with increasing external magnetic field. As a result, a Co adatom at the position $\vec{r}_{\mathrm{i}}$ at external magnetic field $\vec{B}_{\mathrm{ext}}$ feels an effective magnetic field $\vec{B}_{\mathrm{eff}}$ which is the superposition of $\vec{B}_{\mathrm{ext}}$ and $\vec{B}_{\mathrm{RKKY}}(\vec{r}_{\mathrm{i}}, \vec{B}_{\mathrm{ext}})$ at $\vec{r}_{\mathrm{i}}$, as

$$\vec{B}_{\mathrm{eff}} = \vec{B}_{\mathrm{ext}} + \vec{B}_{\mathrm{RKKY}}(\vec{r}_{\mathrm{i}}, \vec{B}_{\mathrm{ext}}). \tag{7.8}$$

Consequently, the saturation magnetic field B_{sat} of each adatom will be slightly different, due to the variance in $B^{\mathrm{sat}}_{\mathrm{RKKY}}(\vec{r}_{\mathrm{i}})$.

The energy scale of the interaction can be estimated from the maximum (0.7 T) and minimum (0.2 T) in the distribution of B_{sat} (see Figure 7.13(c)) as $J = m \cdot (0.7\ \mathrm{T} - 0.2\ \mathrm{T})/2 \approx 50\ \mu\mathrm{eV}$. This is consistent with the value estimated from the temperature dependence of m, as $k_{\mathrm{B}} \cdot 0.3\ \mathrm{K} = 25\ \mu\mathrm{eV}$. It has been seen in the previous Sections that the energy scale of the RKKY interaction is indeed tens of μeV.

In conclusion, a spatially inhomogeneous RKKY mean field with an energy scale of several tens of μeV has been observed which leads to a strongly changing effective magnetic moment for each adatom. This also leads to the symmetry breaking in the magnetization curves recorded on the pairs shown in Chapter 7.3.1. The ensemble of randomly distributed Co adatoms behave like a spin-liquid at 0.3 K and could serve as a model system for the study of spin glasses, if the density of Co adatoms is further increased.

7.5 Summary

In summary, the RKKY interactions between various Co nanostructures at a very low-energy scale are directly investigated with single-atom magnetization curves. The results show, that an exact knowledge of the RKKY interaction on the atomic scale can be essential even for systems exhibiting a rather simple Fermi surface. Furthermore, it is demonstrated that the determined map of RKKY interaction can serve to tailor the magnetism of more complex adatom arrangements.

Using this knowledge together with the technique of tip induced adatom manipulation it will be possible to design and build artificial adatom assemblies with interesting functionalities. E.g., chains of coupled adatoms, which communicate the spin state via RKKY interaction, can serve to build elements for spin-logic circuits performing conventional binary computation using only the spin degree of freedom [139]. Finally, it is anticipated that the demonstrated methods for extracting the interactions between individual magnetic atoms can be applied to other systems where a detailed knowledge of the indirect exchange is still lacking.

Chapter 8

Polarization of Pt(1 1 1) surface

This chapter presents an investigation of the spin polarization above the Pt(1 1 1) surface in the vicinity of Co ML stripes. An exponential decay of the spin polarization laterally away from the Pt/Co interface is observed. This effect is detectable for distances from the stripe larger than three Pt lattice spacings where the RKKY interaction provides already an AFM coupling as shown in Chapter 7.2. The interplay of induced magnetic moments within the surface and the spin-resolved electronic density of states above the surface is addressed, by performing first-principles calculations of the electronic structure. The calculated induced magnetic moments in the Pt surface close to embedded Co atoms show a distance dependent oscillation between FM and AFM alignment, while the vacuum spin-polarization at particular energies shows an exponential decay in the lateral direction.

The work of this chapter has been published in: F. Meier, S. Lounis, J. Wiebe, L. Zhou, S. Heers, P. Mavropoulos, P. H. Dederichs, S. Blügel, and R. Wiesendanger, "Spin-polarization of platinum (1 1 1) induced by the proximity to cobalt nanostripes", *Phys. Rev. B* **83**, 075407 (2011).

8.1 Introduction

Since in diluted magnetic systems the localized magnetic moment of an impurity atom is screened by a spatially oscillating long-range spin-polarization of the host conduction electrons [120] which mediate the RKKY interaction between localized magnetic moments (see Chapter 7), it is instructive to investigate the magnetic behavior of host metals. Moreover, it is of additional importance when the host metal serves as a substrate. The remarkable properties of magnetic nanostructures grown on non-magnetic metal surfaces rely significantly on the electronic coupling between the

atoms within the nanostructure and substrate atoms underneath [140]. This electronic coupling determines, *e.g.*, the strength and direction of the magnetic anisotropy as well as the total magnetic moment [4]. Additionally the substrate electrons govern the collective behavior of ensembles of magnetic nanostructures, *e.g.*, by providing ferromagnetic order due to RKKY interaction between separated nanostructures [141, 142]. However in diluted magnetic systems where the host metal nearly fulfills the Stoner criterion and therefore are nearly ferromagnetic, such as Pt and Pd, another important effect takes place. In these so called giant moment dilute alloys the 3*d* impurities induce relatively strong magnetic moments in the neighboring host atoms which form a spin-polarized cluster [143]. Since this effect can cause an additional exchange interaction between magnetic atoms in nanostructures it is important to obtain knowledge about the size of the polarization cloud and the decay of the induced magnetization with increasing distance from the magnetic atom [144, 145].

Both mechanisms are considered to be important for multilayer systems [128], like Co-Pt, which consist of sequences of ferromagnetic Co layers separated by non-magnetic Pt spacer layers [133, 146]. The magnetic interlayer coupling between the ferromagnetic layers often shows deviations from a pure RKKY behavior, indicating that other mechanisms contribute to the total magnetic interaction. One contribution originates from magnetoelastic interactions due to interface roughness between the magnetic and non-magnetic layers [147, 148] while with decreasing temperatures the induced magnetic moments of Pt becomes relevant for the magnetic coupling [149]. In order to qualify specific contributions to the overall interaction a profound knowledge on the local configuration of the interface is required. While the interface in multilayer systems is inaccessible directly, the sample system of Co nanostructures grown on Pt(1 1 1) is very suited for such a study.

8.2 Experimental results

Figure 8.1 (a) shows a Co ML stripe attached to a Pt step edge between two Pt terraces and individual Co adatoms. Obviously the stripe appears higher than the Pt as visible in the line profile in Figure 8.1 (b). The stripe is ferromagnetic with an out-of-plane anisotropy [17] (also see Chapter 4.2.2).

Figures 8.1 (c)-(e) show the resulting $\mathrm{d}I/\mathrm{d}V(\vec{r}, V)$ spectra taken on locations indicated in the inset on the Co ML stripe, and on the Pt(1 1 1) close and far from the ML stripe. Here, $\vec{M}_{\mathrm{T}}$ is switched up or down by B_{ext} fields of +0.2 T and −0.2 T while $\vec{M}_{\mathrm{ML}}$ is constant. This allows to measure the

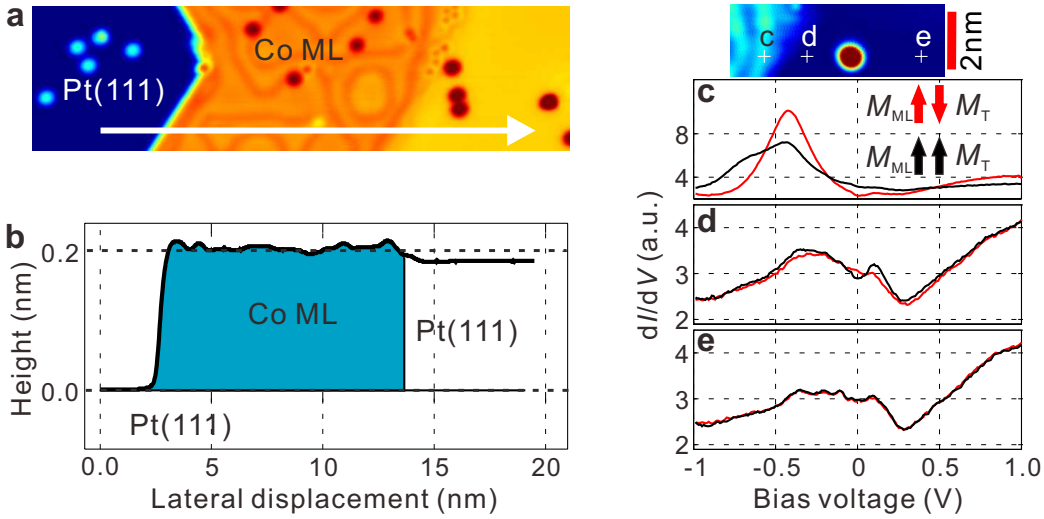

Figure 8.1: **(a)** STM topograph of two Pt(1 1 1) terraces with individual Co adatoms and Co ML stripe attached to a Pt step edge. **(b)** Line profile along the line marked in (a). **(c-e)** dI/dV spectra taken at positions indicated in the STM topograph above, which displays the interface between the Co ML stripe (left) and the Pt(1 1 1) terrace. The relative orientation of the tip and stripe magnetization, $\vec{M}_{\mathrm{T}}$ and $\vec{M}_{\mathrm{ML}}$, is indicated by arrows. (Tunneling parameters: V_{stab} = +1.0 V, I_{stab} = 1.0 nA, V_{mod} = 10 mV (rms), T = 0.3 K.)

dI/dV signal for parallel and antiparallel alignment of $\vec{M}_{\mathrm{T}}$ and $\vec{M}_{\mathrm{ML}}$. On the Co ML stripe the spin resolved dI/dV spectra show a dominant peak located at -0.4 eV below E_{F} which originates from the d-like Co surface resonance of minority-spin character (see Chapter 5.2). The intensity of this state is changing considerably for parallel and antiparallel alignment of $\vec{M}_{\mathrm{T}}$ and $\vec{M}_{\mathrm{ML}}$ (see Chapter 5.2). In contrast to that, the spectra on the bare Pt far from the stripe in Figure 8.1 (e) do not show the electronic signature of the d-like surface resonance but the onset of the unoccupied surface state at eV = 0.3 eV is visible [65]. Furthermore, no dependency on $\vec{M}_{\mathrm{T}}$ is found as expected for a non-magnetic material. Figure 8.1 (d) shows spectra which have been taken on Pt but only at a distance of around 1 nm with respect to the stripe. The spectra show the typical signature of a bare Pt(1 1 1) surface far from the stripe (see Figure 8.1(e)). However, a clear dependency on the relative orientation of $\vec{M}_{\mathrm{T}}$ and $\vec{M}_{\mathrm{ML}}$ is now observed in an energy range from -0.5 eV to +0.5 eV around E_{F}. Neither from the topographic nor spectroscopic data any indications are observed for Co incorporation into the Pt surface or sub-surface layers within the probed area [62, 150]. This experimental result already proves a spin-polarization

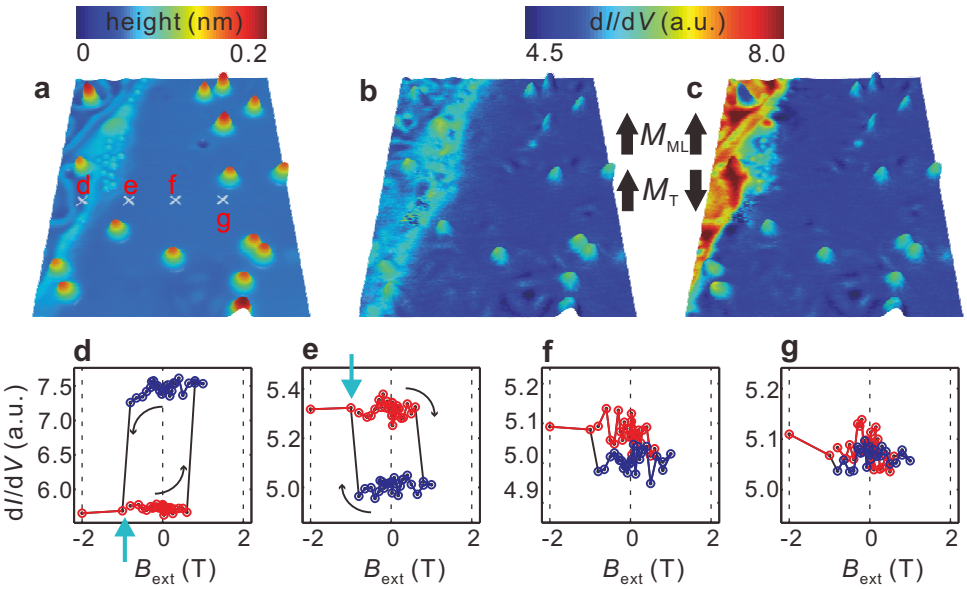

Figure 8.2: **Magnetization curves of Pt surface**. **(a)** STM topograph in 3D view (size 11.6×15.6 nm^2). **(b),(c)** STM topograph in 3D view colored with the simultaneously recorded spin-resolved dI/dV map obtained at $B_{\mathrm{ext}} = +0.6$ T and + 1.0 T, respectively. Relative orientation of $\vec{M}_{\mathrm{T}}$ and $\vec{M}_{\mathrm{ML}}$ is indicated by arrows. **(d)-(g)** Magnetization curves taken at positions marked by crosses in (a). Positions are separated by 2.3 nm. Arrows in (d) and (e) mark the start and direction of rotation of the B_{ext} field loop. Blue and red color indicate dI/dV values representing parallel and antiparallel orientation of $\vec{M}_{\mathrm{T}}$ and $\vec{M}_{\mathrm{ML}}$ for each hysteresis. (Tunneling parameters: $V_{\mathrm{stab}} = +0.3$ V, $I_{\mathrm{stab}} = 0.8$ nA, $V_{\mathrm{mod}} = 20$ mV (rms), and $T = 0.3$ K.)
.

of the clean Pt(1 1 1) at a distance of larger than three lattice spacings to the Co ML stripe.

In order to obtain information about this induced spin polarization, dI/dV maps are recorded on a boundary area shown in Figure 8.2 (a). For this area dI/dV maps have been recorded at $V = +0.3$ V in a complete B_{ext}-field loop starting from -0.8 T to +1.0 T and back to -2.0 T. Figures 8.2 (b) and (c) show exemplary 3D STM topographies colored with simultaneously measured dI/dV maps obtained at $B_{\mathrm{ext}} = +0.6$ T and + 1.0 T, where the relative orientation of $\vec{M}_{\mathrm{T}}$ and $\vec{M}_{\mathrm{ML}}$ has changed due to B_{ext}. The dI/dV signal above the Pt terrace appears the same in both figures. However, a difference in dI/dV intensity above Pt close the stripe is observed.

From the sequence of magnetic field B_{ext} depending dI/dV maps *local*

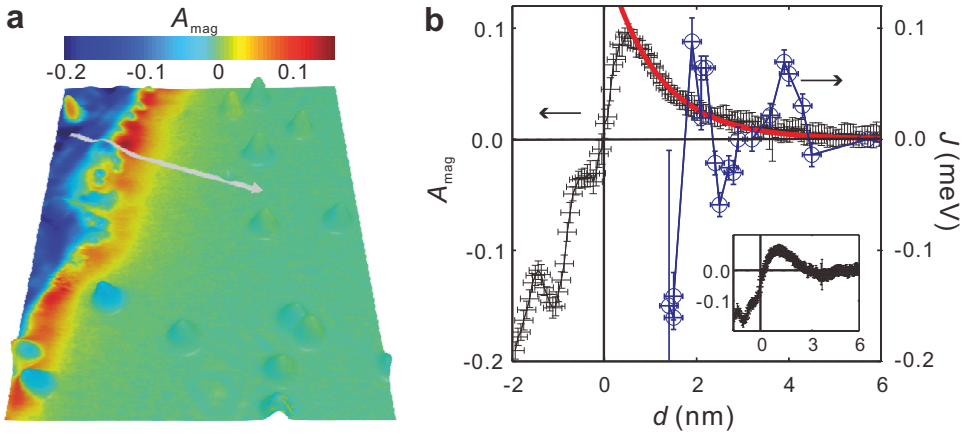

Figure 8.3: **Magnetic asymmetry of Pt surface**. **(a)** STM topograph in 3D view colored with the calculated A_{mag} map obtained from local magnetization curves (V_{stab} = +0.3 V). **(b)** Crosses: A_{mag} values below line section indicated in (a). Open circles: magnetic exchange energy J for the coupling between Co ML stripe and individual Co atoms taken from Chapter 7.2. '0' indicates the border between the ML stripe and Pt layer. The red line shows an exponential fit according to Equation 8.2. **Inset**: A_{mag} values as in (a) for $V_{stab} = -0.1$ V.

magnetization curves are obtained by plotting the dI/dV signal at one image point as a function of B_{ext} (see Chapter 6.3). Figure 8.2 (d)-(g) show local magnetization curves taken at positions as marked in Figure 8.2 (a). The magnetization curve of the stripe in Fig. 8.2 (d) shows two magnetic states and a square-like hysteresis indicating its ferromagnetic state and a coercivity of $B_C = 0.70 \pm 0.05$ T. Strikingly, the magnetization curves measured on the Pt in the vicinity of the Co ML stripe show that there is an explicit link between the magnetic state of the Co stripe and the spin polarization measured on the Pt. Similar magnetization curves have been recorded for each point of the area of Figure 8.2(a). From these magnetization curves the so-called magnetic asymmetry A_{mag} is calculated by

$$A_{mag} = \frac{dI^{\uparrow\uparrow}/dV - dI^{\uparrow\downarrow}/dV}{dI^{\uparrow\uparrow}/dV + dI^{\uparrow\downarrow}/dV}. \tag{8.1}$$

which characterizes the square-like magnetization curves and is a measure for the spin-polarization at eV in the vacuum [5, 78] (also see Chapter 2.5 and Chapter 5.2). d$I^{\uparrow\uparrow}$/dV and d$I^{\uparrow\downarrow}$/dV denote averaged dI/dV values from all red and blue data points in the magnetization curves (Figure 8.2(d)-(g)),

i.e., for parallel and antiparallel alignment of $\vec{M}_{\mathrm{T}}$ and $\vec{M}_{\mathrm{ML}}$ in each curve. An asymmetry value is obtained for each image point. This results in an asymmetry map shown in Figure 8.3 (a). The Co stripe shows a strong negative A_{mag} while on the Pt terrace far from the stripe A_{mag} is zero. Above the Pt close to the Co stripe an area with positive A_{mag} is visible which fades out for an increasing distance from the stripe. The decay is further analyzed in Figure 8.3 (a) as a function of the distance d from the stripe. In order to quantify the decay behavior the graph in Figure 8.3 (b) has been fitted to a simple exponential function

$$f = Ce^{-d/\lambda} \tag{8.2}$$

where C and λ denote the amplitude and the decay length, respectively. Even though the exact value of λ depends on the specific line section, values in the range from 0.9 nm to 1.2 nm are obtained corresponding to more than three next nearest neighbor distances within the Pt lattice. the same quantitative behavior is observed in A_{mag} calculated from $\mathrm{d}I/\mathrm{d}V(\vec{r})$ maps recorded at $V = -0.1$ V (see inset of Figure 8.3). Together with the dependency on the spin-resolved $\mathrm{d}I/\mathrm{d}V$-curves measured close to the Co stripe (Figure 8.1 (d)) it is concluded that the observed spin-polarization is present in a large energy window around E_{F}. This result suggests that the measured spin-polarization is due to an exponentially decaying magnetic moment m_{Pt} induced by the proximity to the Co ML stripe.

Figure 8.3 (b) also includes the experimentally obtained RKKY interaction energies, J, between Co ML stripe and single Co adatoms as already presented in Chapter 7.2. A positive J corresponds to a ferromagnetic coupling while a negative value corresponds to an antiferromagnetic coupling. A damped oscillatory exchange interaction is present in the same range where the exponentially decaying Pt vacuum spin-polarization is measured. These observations raise the question, how exactly the measured Pt spin-polarization is linked to the induced magnetization within the Pt surface.

8.3 Theoretical modeling

In order to obtain deeper insight into the relation between the measured spin polarization in the vacuum and the induced magnetic moments, calculations on three different arrangements of Co *on* or *in* a Pt(1 1 1) surface layer have been performed, the setup of which is shown in Figure 8.4 (a). First, the case that a single Co atom is deposited on (adatom) or embedded in (inatom) the first surface layer of Pt(1 1 1) is considered. These two

arrangements differ mainly in the coordination which is tripled for the inatom with respect to the adatom case. Therefore a comparison of these two cases provides an important information concerning the hybridization of the Co electronic states with those of the Pt surface leading to the magnetization of the surrounding Pt atoms.

In order to model the experimental setup as close as possible, a chain of five Co atoms embedded in the surface of Pt(1 1 1) is considered. This model arrangement reflects the experimental fact that Pt surface atoms which show a vacuum spin-polarization are located at the same layer than the Co atoms which form the stripe. The chain is oriented along a direction perpendicular to the direction probed experimentally concerning the spin polarization (Figure 8.3(b)). The exact experimental setup is of course difficult to achieve since a non-regular step edge of platinum interfacing a cobalt stripe is impossible to reproduce with methods based on Density Functional Theory at the actual stage. The method of investigation is the KKR Green function method within the framework of density functional theory [137].

KKR is based on multiple scattering theory with Green function G of the system of interest calculated after solving the Dyson equation:

$$G = G_0 + G_0 \Delta V G \tag{8.3}$$

where all quantities are matrices that are site, energy, orbital, and spin dependent. As can be seen from this equation, two quantities are required to obtain G: the Green function G_0 for a perfect Pt(1 1 1) surface and the potential difference ΔV induced by the presence of impurities.

The real-space solution of the Dyson equation requires a cluster of perturbed atomic potentials that include the potential of Co impurities and the first shell of neighboring cells. It is important to note that the vacuum region is filled with cellular (Voronoi) potentials. Since the aim is to explain the STM measured spectra, the Tersoff-Hamann theory is used to calculate the LDOS in the vacuum at 4.1 Å () above the substrate [31, 32]. After obtaining a self-consistent Co potential with its neighboring shell, one additional calculation is performed including Pt atoms as well as their neighboring vacuum cells at 4.1 Å above the substrate along a given direction.

For an individual Co adatom and Co inatom, the induced magnetic moments m_{Pt} in the Pt substrate along two directions, as indicated in Figure 8.4 (a), are calculated. Figures 8.4 (a)-(d) show m_{Pt} as a function of the distance d from the impurity for the $[1\,\bar{1}\,0]$ and $[1\,1\,\bar{2}]$ direction. Concerning the $[1\,\bar{1}\,0]$ direction we find for both arrangements a long-range oscillation

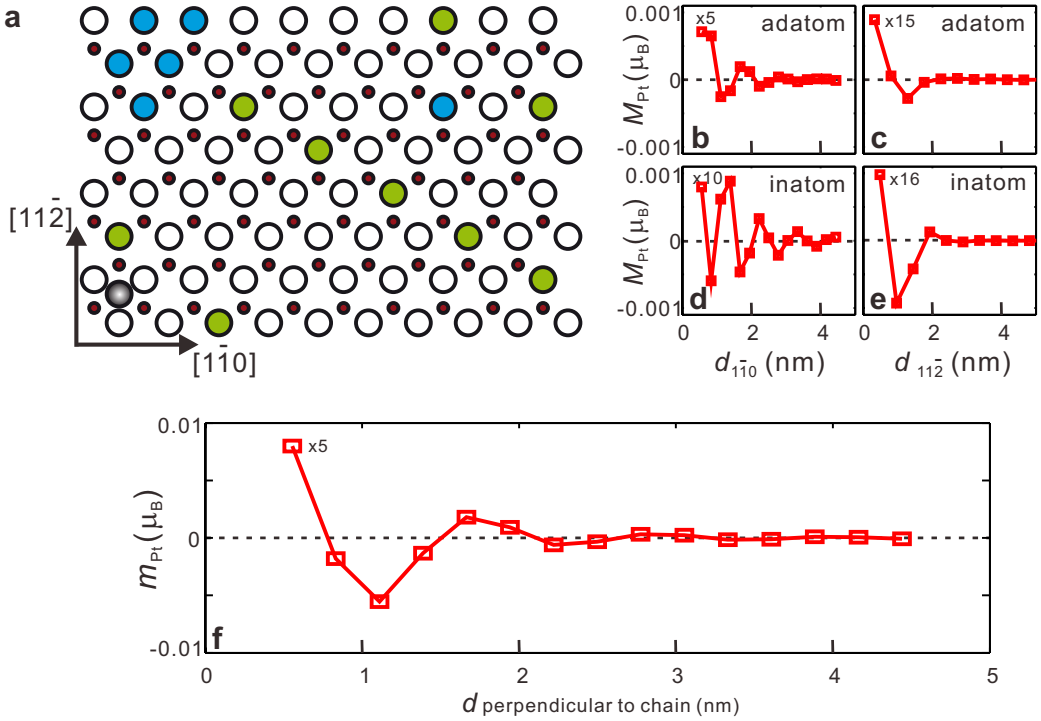

Figure 8.4: **Calculated induced magnetic moment in Pt surface**. **(a)** Sketch of the three considered sample setups for calculations. Large and small open circles represent Pt(1 1 1) surface and subsurface atoms, respectively. Filled blue circles indicate the locations of the embedded Co atom chain and the Co inatom. Gray circle marks the position of Co adatom. Filled green circles indicate the closest considered atoms for the calculation of the induced magnetic moments in each specific direction. Filled green circle close to a Co atom mark first considered Pt atoms for specific direction. **(b)-(e)** Induced magnetic moments in Pt atoms m_{Pt} for two indicated directions as a function of distance d from a Co adatom and Co inatom. **(f)** Induced magnetic moments in Pt atoms as a function of distance d from an embedded Co chain for experimentally relevant direction. Some values in (b)-(f) have been scaled down by the indicated factors in order to fit into the figure.

in m_{Pt} with a wavelength of about 1 nm for the adatom (Figure 8.4 (b)) and a slightly smaller one for the inatom (Figure 8.4 (d)). The oscillation indicates that m_{Pt} is either ferromagnetically or antiferromagnetically aligned with the Co impurity depending on the distance. However, the total integrated magnetic moment of the Pt atoms is positive. Along the $[1\,1\,\bar{2}]$ direction the oscillatory behavior is much weaker than the one obtained along the $[1\,\bar{1}\,0]$ direction for both arrangements (Figure 8.4 (c),(e)). Here more Pt atoms are coupled ferromagnetically to the Co impurity. This directional dependence proves that the induced magnetization is anisotropic which originates from the non-spherical Fermi surface characterizing this system as found in the directional dependent RKKY interactions between Co adatoms on a Pt(1 1 1) surface (see Chapter 7.3) or in the anisotropic induced charge oscillations caused by Co impurities buried below Cu surfaces [72]. A comparison of m_{Pt} for the same direction shows that for the same distances the intensity is always higher for the embedded atom than for the adatom. This emphasizes the importance of the number of neighboring atoms and indicates a dependence of coupling between the Co and Pt electronic states depending on the coordination and environment. To favor the coupling to the impurity states, the electronic states controlling the studied long-range magnetization must be localized at the surface. Constant-energy contours at E_{F} are plotted in Figure 8.5(a) for the simulated Pt(1 1 1) surface with their relative localization on the surface layer. There is a finite number of contours due to the fact that the surface is simulated with a finite number of Pt layers. The shape of the contours is non-trivial indicating the complexity of the problem. This type of calculations indicate the presence of several states which are resonant-like. To measure the degree of coupling between these states and those of the Co impurity, the Fermi surface is decomposed in 10 parts represented within the red-yellow triangle in Figure 8.5. Each part includes more or less localized states. Afterwards, the induced magnetization at E_{F} induced by every part is calculated. For the inatom case, it seems that parts 7, 8 and 10 are contributing most to m_{Pt} (Figure 8.5(b)). By summing up all parts, the total energy integrated magnetization is approximately recovered (see Figure 8.4(d)). They are not expected to be equal since with the decomposition scheme some scattering events cancel each other and other "back-scattering" events are not taken into account properly. This theoretical experience demonstrates the non-trivial link between the induced long-range magnetization, their degree of localization on the surface layers and coupling strength with the impurities.

Figure 8.4 (f) shows m_{Pt} for Pt atoms perpendicular to the embedded Co

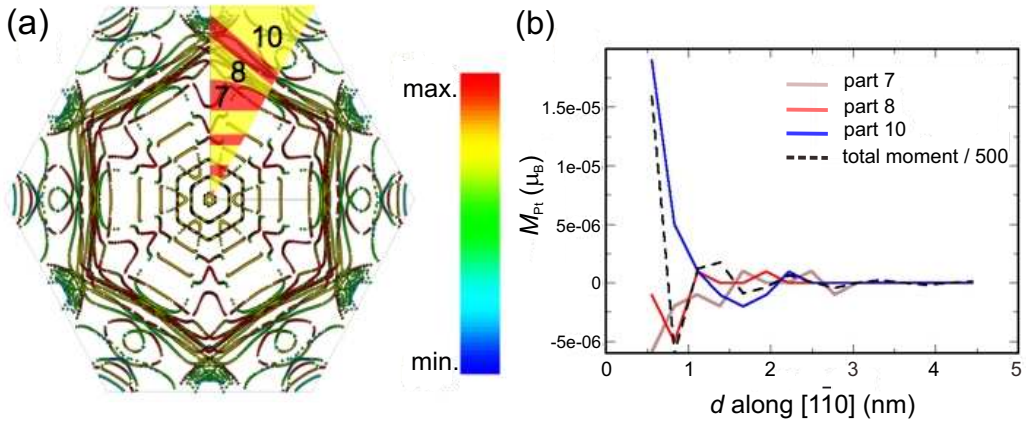

Figure 8.5: **(a)** Constant energy contours calculated at E_F where colors represent the degree of localization of the different electronic states on the surface layer of Pt(1 1 1): red for maximum localization, blue for minimum. In addition, a triangle divided in ten regions is superimposed on the energy contours. Depending on the region considered, m_{Pt} in the surrounding Pt surface atoms changes. As an example, **(b)** shows m_{Pt} along the [1 $\bar{1}$ 0] direction for the inatom case induced by the most contributing constant energy contours: 7, 8 and 10.

chain (Figure 8.4(a)), as a function of distance d from the chain, which is the setup similar to the experimental one. In contrast to the experimentally observed decreasing of the vacuum spin-polarization, an oscillating behavior decaying m_{Pt} is observed. Similar to curves in Figures 8.4 (b)-(e) the curve clearly exhibits the same damped oscillating behavior but shows overall higher and distance dependent intensities which reflects the contributions from all the Co atoms within the chain. The oscillation period of about 1.3 nm is very close to that found for the RKKY interaction between Co nanostructures in the relevant direction (see Chapter 7), suggesting that the surface RKKY interactions between different Co nanostructures on Pt(1 1 1) are mediated by the upward-dispersing surface resonance crossing E_F at 1.6 nm with a strong localization at the surface of Pt(1 1 1) [65] (also see Chapter 4.1.2).

In order to investigate the relation between the induced magnetic moments m_{Pt} and the energy-dependent spin polarization, the vacuum LDOS is calculated for majority and minority spin states above the Pt atoms along the direction perpendicular to the chain at a vertical distance of 4.1 Å. This corresponds to two interlayer distances from the surface and is the range of the experimental z-height of the tip. Figures 8.6 (a)-(d) show the spin

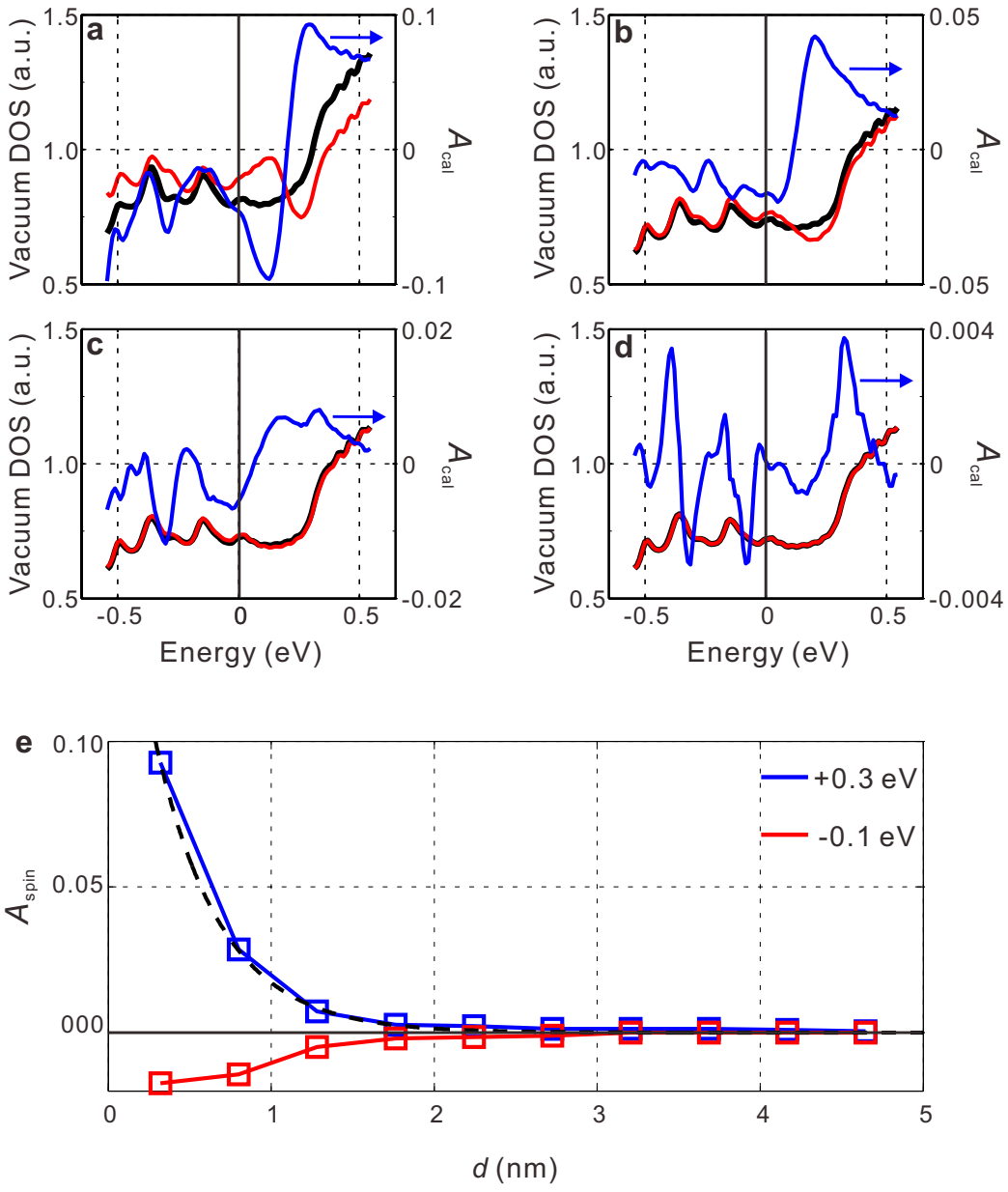

Figure 8.6: **Calculated LDOS in the vacuum above Pt surface**. **(a)-(d)** Calculated vacuum DOS above the first, second, third as well as fifth Pt atom close to the embedded Co chain for the majority spin state (black) and the minority spin state (red) as well as the corresponding energy dependent asymmetry (blue). The vacuum DOS has been calculated at a height of 4.1 Å above the Pt atoms. **(e)** Vacuum magnetic asymmetry calculated from vacuum DOS above Pt atoms at +0.3 eV (blue) and -0.1 eV (red). The dashed line shows an exponential fit for the calculated spin-polarization at 0.3 eV

resolved vacuum LDOS for the first, second, third and fifth Pt atom located in the experimental relevant direction. They reveal an intensity increase starting at about +0.3 eV which is due to the Pt surface state [65]. Concerning differences for both spin types it is quite obvious that the Pt atom closest to the chain experiences the strongest imbalance of majority and minority electrons. This is visualized by a corresponding calculated magnetic asymmetry $A_{\mathrm{cal}}(E)$ given by

$$A_{\mathrm{cal}}(E) = \frac{\mathrm{LDOS}_{\mathrm{maj}}(E) - \mathrm{LDOS}_{\mathrm{min}}(E)}{\mathrm{LDOS}_{\mathrm{maj}}(E) + \mathrm{LDOS}_{\mathrm{min}}(E)} \tag{8.4}$$

where $\mathrm{LDOS}_{\mathrm{maj}}(E)$ and $\mathrm{LDOS}_{\mathrm{min}}(E)$ denote the energy E dependent vacuum LDOS for majority and minority electrons. $A_{\mathrm{cal}}(E)$ is plotted in Figures 8.6 (a)-(d) for the Pt atoms as well. These curves reveal that neither the absolute value nor the sign of the magnetic asymmetry $A_{\mathrm{cal}}(E)$ is conserved when scanning at different bias voltages around E_{F}. Additionally the absolute value of $A_{\mathrm{cal}}(E)$ at given energies changes with increasing distance from the Co chain. At some energies even a sign change is observed. Figure 8.6 (e) shows the calculated $A_{\mathrm{cal}}(E)$ for +0.3 eV and -0.1 eV, which are experimentally relevant, for different distances from the chain. A comparison of these curves with the the experimental data obtained at +0.3 V as shown in Figure 8.3 (b) reveals that $A_{\mathrm{cal}}(+0.3)$ eV follows the shape of the experimental curves, *i.e.*, it is always positive and shows an exponentially decaying behavior. A fit as in Equation 8.2 gives a value for the decay length λ of about 4 Å which is less than half of the experimental value. The calculated $A_{\mathrm{cal}}(-0.1)$ eV shows a similar behavior but with reversed sign. This change of sign in comparison to experiment is most likely due to a change of the tip's spin-polarization which is known for these kind of tips for a bias voltage range below E_{F} (see Chapter 5.2).

8.4 Discussion

Recently several theoretical studies concentrated on probing and describing magnetic properties of Co nanostructures on Pt(1 1 1) quantitatively and qualitatively. They treated Co in different configurations and environments, like Co overlayers on Pt(1 1 1) [27], Co nanowires attached to Pt(1 1 1) step edges [151, 152] and isolated Co adatoms on bare Pt(1 1 1) surfaces [28, 30]. Even though these configurations lead to different coordination numbers, which results in different numbers of underlying Pt atoms per Co atom, they show consistently an induced spin moment m_{S} of the nearest neighboring Pt atoms in the range from 0.1-0.3 μ_{B} which is

about one magnitude larger than the orbital moments m_O. Therefore the total induced magnetic moment m_{Pt} of Pt atoms is mainly determined by the spin moment m_S.

Additionally it has been found in these calculations that the induced Pt magnetization decreases very rapidly with the distance from the Co structures by about one order of magnitude for the second and third nearest neighbors as shown for the Co ML wires in [151]. Here m_S has been probed experimentally and theoretically for longer distances far from the Co impurities. It is found that induced magnetic moments in the surrounding Pt surface atoms are not constantly parallel or antiparallel aligned with the the magnetic moment of the Co impurity. The sign as well as the strength of the induced magnetic moments is additionally highly influenced by the strong anisotropy of the Fermi surface of Pt. Both underline that for the probed arrangements of Co on and in the Pt(1 1 1) surface one cannot expect a constantly aligned polarization cloud as found for Co-Pt and Fe-Ir multilayers [149, 153].

The apparent contradiction of the measured monotonously decaying A_{mag} in the vacuum and the calculated oscillating m_{Pt} for the embedded Co chain arrangement can be explained by local changes of the electronic structure of the Pt atoms close to the embedded chain (see Figures 8.6 (a)-(d)). It is evident also that the hybridization between the Pt and the Co states changes with increasing the distance from the chain. Therefore also the spin-averaged LDOS changes laterally which can be obtained by calculating the arithmetic mean of the LDOS for both spin types in Figures 8.6 (a)-(d). According to [39] the measured spin resolved dI/dV signal and the deduced magnetic-asymmetry is a measure of the energy-dependent spin polarization of the sample. *This quantity is only a measure for the magnetization, which is an integrated quantity of majority and minority states up to E_F, if the spin-averaged LDOS is constant*. Therefore the induced magnetization of the Pt cannot be deduced from the experimentally detected spin-polarization in the Pt only.

8.5 Summary

In summary, this chapter has presented a measurement of the spin polarization in the vacuum above the Pt(1 1 1) surface due to the proximity to Co ML stripes. The measured vacuum spin-polarization decays exponentially as a function of the distance from the Co stripe with a decay length of about 1 nm. Self-consistent electronic-structure calculations of a Co chain embedded in the Pt(1 1 1) surface, of the neighboring Pt atoms

and of the vacuum LDOS above the Pt allow to prove that the measured spin-polarization is induced by an oscillating and highly anisotropic magnetization within the Pt surface in the proximity to Co. By investigating the Fermi surface contours of Pt(1 1 1) and their degree of localization on the surface layer, several states with anisotropic shapes have been found that could couple to the electronic states of Co impurities and thus contribute to the long-range induced magnetization.

Chapter 9

Fe adatoms on Cu(1 1 1)

In order to demonstrate that the technique of measuring single-atom magnetization curves also works on a different sample system, experiments are carried out on Fe adatoms on the Cu(1 1 1) surface which is substantially different from the Pt(1 1 1) surface. The intention is two-fold. First, since the manipulation of atoms adsorbed on the Cu(1 1 1) surface is easier than in the case of Pt(1 1 1) [71], it is possible to make artificial adatom nanostructures and then characterize them by single-atom magnetization curves. This would be a step towards tailoring the magnetism in artificial nanostructures. Second, according to Anderson impurity model [154], the magnetic properties depends on the competition of the Coulomb interaction of electrons with opposite spins, the hybridization between the localized orbital of the impurity and the conduction band states of the host, and the electron density of the host. Because the Cu(1 1 1) surface has a partly occupied surface state leading to a high *s* electron density at the surface [155, 156, 157, 158, 159], the hybridization between the adatom *d* states and the substrate *s* states is different from the case of Co adatoms on Pt(1 1 1). Additionally, the hybridization of the *d* states of adatoms with the *d* states of the substrate is also different. This could result in distinct magnetic behavior of the adatoms. The surface state resides deeply inside the projected bulk *sp*-band gap and has an effective mass of 0.58 m_e. As revealed by angle-resolved photoemission spectroscopy (Figure 9.1), it starts at -0.39 eV below E_F and at the $\bar{\Gamma}$ point [155]. Because it is located quite close to the center of the Brillouin zone, it can contribute strongly to the tunneling current. This leads to a sharp onset at -0.4 eV in the dI/dV curves and Friedel oscillations / scattering states are visible in the STM topograph recorded at a bias voltage higher than the onset energy [46, 156, 160]. There are a couple of calculation results concerning the magnetic properties of 3*d* adatoms and clusters on the Cu(1 1 1) surface, as *e.g.*, spin-polarized

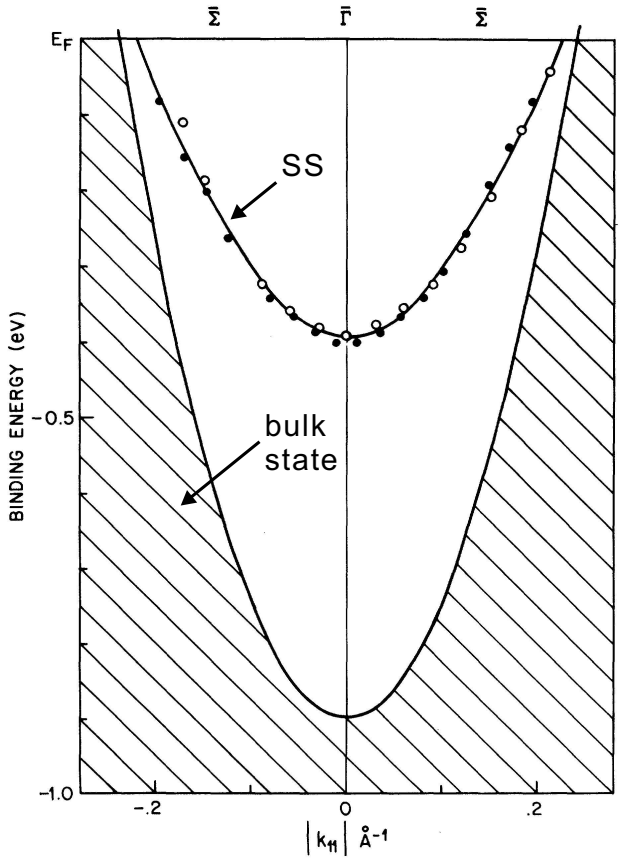

Figure 9.1: **Surface state of Cu**(1 1 1). Angle-resolved photoemission spectroscopy measurements revealed a surface state (SS) residing in the projected bulk *sp*-band gap, which starts at -0.39 eV below E_F and at the center of the Brillouin zone. Figure is taken from [155].

surface states [161, 162], magnetic structures [163, 164, 165] and magnetic interactions [166, 167, 168, 169, 170, 171]. However, STS experiments have focused on the Co adatom on Cu(1 1 1) where the Kondo effect was observed [11, 46]. On the Fe adatoms on Cu(1 1 1), photoemission spectroscopy measurements indicated a strong reduction of hybridization of the Fe 3*d* state with the conduction-band states and an enhanced effective Coulomb interaction for the Fe 3*d* electrons in Fe adatoms [172]. The first nontrivial question concerning the Fe adatom on Cu(1 1 1) is whether it preserves a magnetic moment upon adsorption onto the surface and hence can be studied by single-atom magnetization curves.

This chapter will present the initial results of SP-STM measurements on Fe adatoms on Cu(1 1 1). The work of this chapter has been published in:

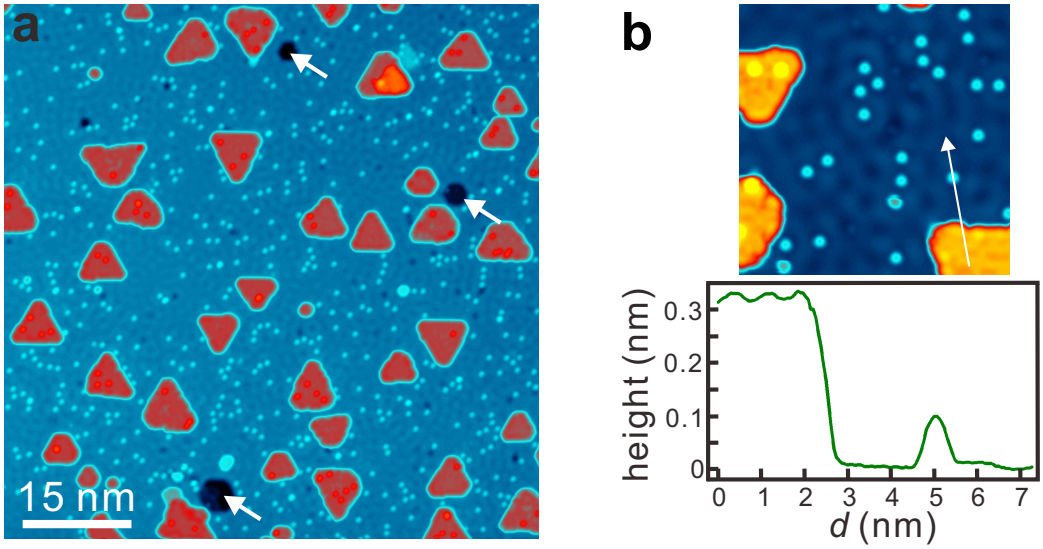

Figure 9.2: **Sample overview**. **(a)** STM topograph of the sample shows a random distribution of Co islands and of Fe adatoms on the Cu(1 1 1) surface. Intermixing- and etching-induced defects are indicated with arrows. **(b)** Line profile along the white arrow across a Co island and an Fe adatom. (Tunneling parameters: V_{stab} = -10 mV, I_{stab} = 1.0 nA, and T = 0.3 K.)

A. A. Khajetoorians, S. Lounis, B. Chilian, A. T. Costa, L. Zhou, D. L. Mills, J. Wiebe, and R. Wiesendanger, "Itinerant nature of atom-magnetization excitation by tunneling electrons", *Phys. Rev. Lett.* **106**, 037205 (2011).

9.1 Sample preparation

Cu is a noble metal and the preparation of an atomically clean surface is quite routine as compared to that of Pt(1 1 1). A conventional sputter-gun without the Wien mass-filter is used in this work. The single crystal Cu(1 1 1) is cleaned by repeated cycles of Ar^+ ion sputtering and annealing at 900 K. The Cu(1 1 1) crystal prepared in this way is terminated with sufficiently large terraces separated by straight step edges.

First, Co with a coverage of 0.5 monolayer is deposited onto Cu(1 1 1) at room temperature using an e-beam evaporator, forming triangular double-layer high islands with a height of 0.32 nm (see Figure 9.2(b)). These Co islands were well-studied by SP-STM and found to have an out-of-plane magnetization [68, 173]. Therefore, they are used to calibrate the magnetic tip in this work. The sample is then cooled down to below 6 K in the cryogenic STM, and individual Fe atoms are deposited with a coverage

of 0.005 monolayer. These Fe adatoms have a height of 1.0 Å and are distributed randomly, as shown in Figure 9.2. Although the sample is transfered into the cryogenic STM as soon as possible after the deposition of Co, a small number of defects due to the intermixing and etching still occur, as indicated with arrows in Figure 9.2(a).

A Cr-coated tip is prepared as described in Chapter 4.2.1. Its magnetic sensitivity to the out-of-plane magnetization component is confirmed by switching the magnetization of a Co island, as shown in Figure 9.3(c) and (d).

9.2 Initial experimental results

Due to the low diffusion barrier for adatoms on Cu(1 1 1), Fe adatoms are easily manipulated with the STM tip using moderate bias voltages and tunneling currents. However, this means that for stable imaging of adatoms the bias voltage needs to be low enough. It is found in the measurements that the Fe adatoms are stable if the bias voltage is below ±30 mV.

Figure 9.3(c)-(d) shows the dI/dV maps recorded at a magnetic field of -0.06 T and +0.10 T, respectively. The corresponding STM topograph is shown in Figure 9.3(a) with its 3D view shown in (b). Scattering of the surface state electrons is visible both in the STM topograph and in the dI/dV maps as a wavy pattern. A Co island is contained in the image and used as a magnetic reference for the spin-polarized tip. The magnetization of the island switches when the magnetic field is increased to +0.1 T, as indicated by the color change from dark to bright. For the isolated adatoms B and C, a switching in the contrast from dark to bright is observed in the dI/dV maps which is due to the magnetization reversal of the adatoms. In contrast, the adatom A switches its spin-polarized dI/dV signal from bright to dark. This is the indication of the indirect exchange coupling of the adatom to the island.

However, there are two issues. First, as visible in Figure 9.3, the island surface appears fuzzy attributed to the adsorption of hydrogen which can be removed by applying a voltage pulse with the tip located above the island [174]. The hydrogen reduces the spin polarization of the island severely and also reduces the magnetic anisotropy as obvious from the small coercivity field. Later in the experiments, the cryogenic STM was degassed by warming up to 50 K, which significantly improves the sample quality. Second, the scattering pattern of the surface state appears very strong in dI/dV maps, making the evaluation of the signal quite elaborate.

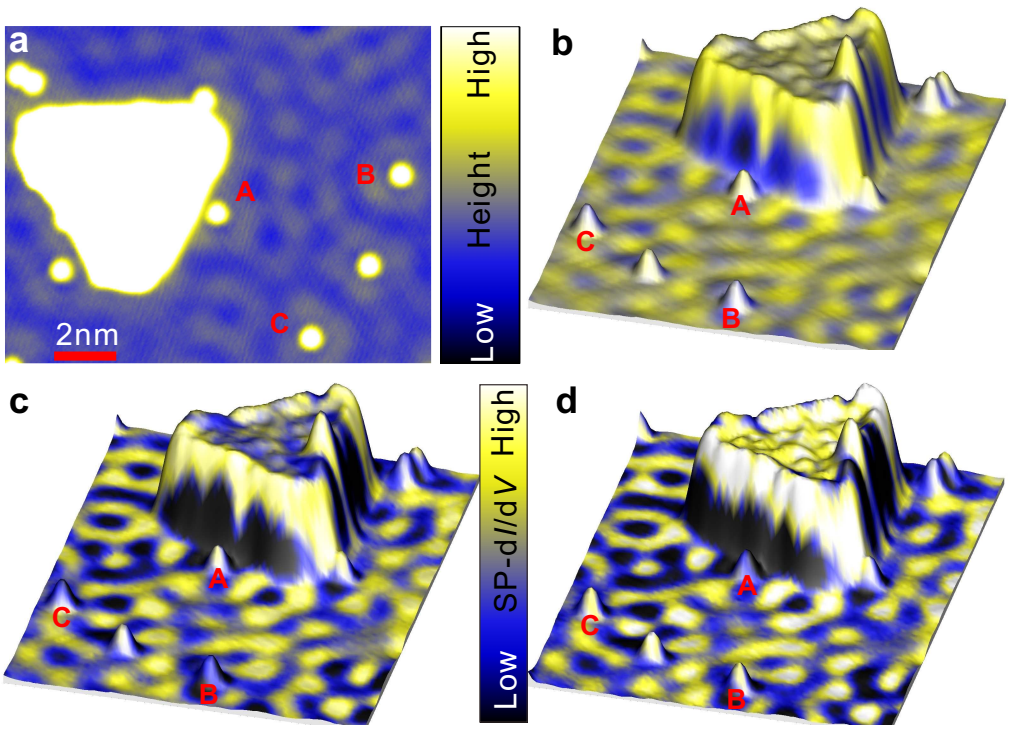

Figure 9.3: **Magnetic imaging of Fe adatoms**. **(a)** STM topograph of an area with a Co island and a couple of Fe adatoms. **(b)** 3D STM topograph of the same area. **(c)**, **(d)** 3D STM topograph colored with simultaneously recorded dI/dV signal taken with a Cr-coated tip at the magnetic field of -0.06 T and +0.1 T, respectively. The Co island switches its magnetization from (c) to (d); simultaneously, the adatom A switches its magnetization, indicating an indirect exchange coupling between the island and the adatom. A spin contrast is visible for the adatoms B and C between (c) and (d). (Tunneling parameters: V_{stab} = -25 mV, I_{stab} = 0.65 nA, V_{mod} = 6 mV (rms), and T = 0.3 K.)

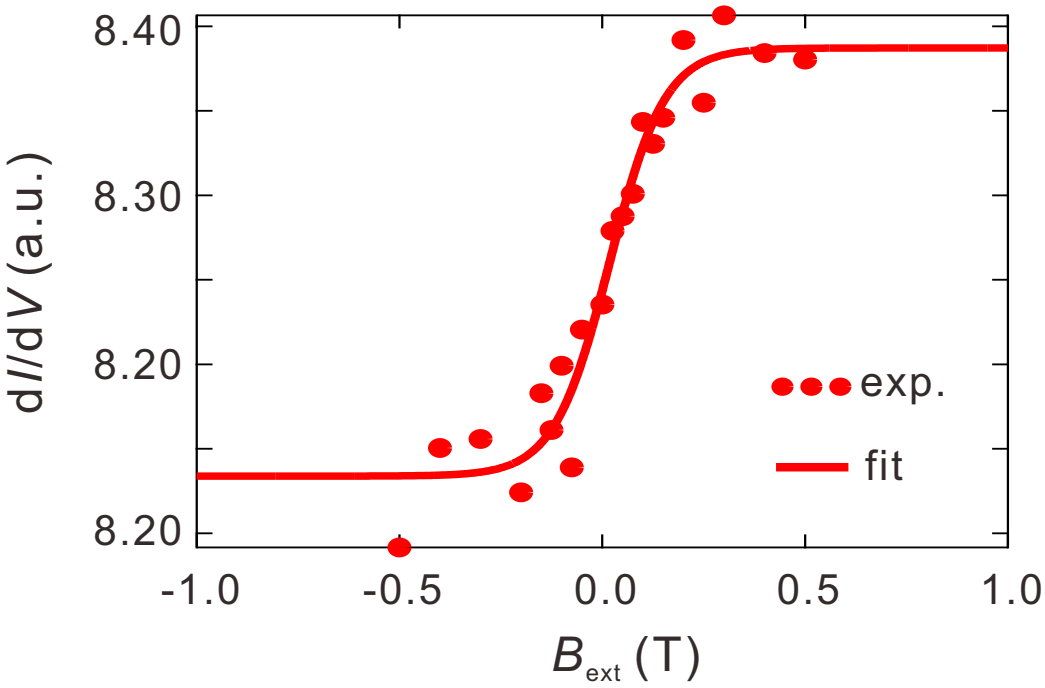

Figure 9.4: **Magnetization curve of an Fe adatom on Cu**(1 1 1). Dots show the magnetization curve recorded on an isolated Fe adatom on Cu(1 1 1). The experimental data is fitted to a quasiclassic paramagnetic model (Equation 6.4 in Chapter 6.4) resulting in an effective magnetic moment of 2.03 μ_B for this particular adatom. (Tunneling parameters: V_{stab} = -25 mV, I_{stab} = 0.65 nA, V_{mod} = 6 mV (rms), and T = 0.3 K.)

Figure 9.4 presents the magnetization curve recorded as described in Chapter 6.3 on an isolated Fe adatom. Similar to Co adatoms on Pt(1 1 1), Fe adatoms behave paramagnetically, and therefore the magnetization curve can be fitted to the Langevin model (see Equation 6.4 in Chapter 6.4) assuming again an out-of-plane anisotropy [175]. This fit results in a mean value of the magnetic moment of 3.5 μ_B (analyzed for about 70 adatoms), in good agreement with the first-principles calculation results [162, 175]. Interestingly, a strong spreading of the magnetic moment is also observed as in the case for Co adatoms on Pt(1 1 1) (see Chapter 6.4).

This result already demonstrates that the method of single-atom magnetization curves is also applicable to this sample system and that a strong RKKY coupling between the adatoms is also present on Cu(1 1 1). However, a detailed study of this system is beyond the scope of this thesis.

Chapter 10

Conclusion and perspectives

This thesis presents the first investigation of magnetization curves of individual magnetic moments of the order of a Bohr magneton, accomplished with a low-temperature SP-STM. This method reads out the expectation value of the ground state spin of a single atom on a surface at a magnetic field, and therefore is complementary to spin-flip spectroscopy which detects the excitations; a further developed method would combine both of them: using IETS to excite, and single-atom magnetization curves to read out the spin state. Using such single-atom magnetization curves I have studied some of the basic properties of atomic size magnetic nanostructures, in particular the low-energy indirect exchange interactions with a scale of tens of μeV.

The spin-resolved electronic structure of Co adatoms has been studied. The spin polarization at E_F in the vacuum above single adatoms is found to be reversed with respect to those above Co surfaces and Co dimers, and dominated by spin-majority electrons. This inversion might be due to the decreased lateral coordination which leads to an enhancement of the rotation symmetry, and is predicted to be general for atomic protrusions of magnetic layers.

The magnetization of isolated Co adatoms is not stabilized by the strong perpendicular magnetic anisotropy barrier. Instead, it is switching with a period much shorter than the time resolution of the facility (msec), probably in the order of several tens to several hundreds of fsec. This results in a paramagnetic behavior as observed in their magnetization curves. The possible mechanisms are: the spin-flip scattering of the Co adatom (i) with the conduction electrons in the substrate, and (ii) with the spin-polarized tunneling electrons. In order to answer the question which mechanism dominates requires an improvement of the time resolution of the facility, low-bias measurements as well as first-principles calculations. Recently it

was reported that a study of nsec dynamics of the adatom spin is ready for electrical pump-probe STM measurements [115]. Furthermore, it was shown that the fsec dynamics of transient carriers in a semiconductor can be imaged by an optical pump-probe STM experiments [176]. These pump-probe techniques might be exploited to address this issue.

While the isolated Co adatoms are unstable, those residing close to the Co nanowires are stabilized by the RKKY exchange to the nanowires with an energy scale of several tens of μeV. This RKKY exchange is most probably mediated by a bulk state with strong localization in the surface of Pt(1 1 1) [65]. The corresponding RKKY exchange between neighbouring Co adatoms does not stabilize the involved adatoms, and the magnetization is still switching fast. This pairwise RKKY exchange exhibits strong tensor characteristics due to a non-spherical Fermi surface of platinum. A map of the pairwise RKKY exchange is obtained both experimentally and theoretically, the correspondence between which is remarkable. This map is demonstrated to be reliable to predict magnetic properties of nanostructures of a larger number of atoms. When Co adatoms are separated randomly, a spatially inhomogeneous RKKY exchange mean field is formed. This mean field changes the saturation field from adatom to adatom, resulting in the spreading of the effective magnetic moment with a mean value of 3.5 μ_B. This makes the investigated sample a model system for the study of spin glass behavior and can serve to transmit spin-information from one to another adatom. The Pt(1 1 1) surface in the proximity to Co nanowires is found to be spin-polarized, the polarization of which decays exponentially with a decay length of larger than 1 nm. The correlation of this spin polarization with the RKKY exchange is nontrivial, as confirmed by the results from first-principles calculations.

As a first step to demonstrate the strength of the method for other interesting sample systems, it has been applied in Fe adatoms on Cu(1 1 1). A spin polarization of the Fe adatoms has been observed in the vicinity of E_F, and their single-atom magnetization curves also show hints for RKKY interaction.

As the next step, on the sample of Fe adatoms on Cu(1 1 1), the SP-STM's ability of atomic manipulation without the loss of the tip's spin polarization [89] will be combined with the method of single-atom magnetization curves to tailor magnetic properties from the measured pairwise RKKY interactions. One idea is to construct RKKY controlled logic gates to conduct and process information only via spin states.

The method of single-atom magnetization curves is not limited to a metallic substrate. This opens up another unique oppotunity to study the magnetism of systems which are at the heart of nanospintronics, *i.e.*,

magnetic molecules [177, 178], magnetic dopants in semiconductors [53, 111, 179] or in semiconductor quantum dots [180, 181, 182] or on topological materials [183, 184, 185], nitrogen-vacancy centers in diamond [186, 187, 188, 189, 190], or phosphorus spins in silicon [191, 192].

Bibliography

[1] H. Brune. Nanomagnetism: Probing Magnetism at the Nanoscale. *Nature Nanotechnology*, **2**(11):674 (2007).

[2] M. Jamet, W. Wernsdorfer, C. Thirion, D. Mailly, V. Dupuis, P. Mélinon, and A. Pérez. Magnetic Anisotropy of a Single Cobalt Nanocluster. *Phys. Rev. Lett.*, **86**(20):4676-4679 (2001).

[3] J.-P. Cleuziou, W. Wernsdorfer, V. Bouchiat, T. Ondarcuhu, and M. Monthioux. Carbon Nanotube Superconducting Quantum Interference Device. *Nature Nanotechnology*, **1**(1):53-56 (2006).

[4] P. Gambardella, R. Rusponi, M. Veronese, S. S. Dhesi, C. Grazioli, A. Dallmeyer, I. Cabria, R. Zeller, P. H. Dederichs, K. Kern, C. Carbone, and H. Brune. Giant Magnetic Anisotropy of Single Cobalt Atoms and Nanoparticles. *Science*, **300**(5622):1130-1133 (2003).

[5] R. Wiesendanger. Spin Mapping at the Nanoscale and Atomic Scale. *Rev. Mod. Phys.*, **81**(4):1495-1550 (2009).

[6] R. Wiesendanger. *Scanning Probe Microscopy and Spectroscopy*. Cambridge University Press, Cambridge (1994).

[7] H. Brune and P. Gambardella. Magnetism of Individual Atoms Adsorbed on Surfaces. *Surf. Sci.*, **603**(10-12):1812-1830 (2009).

[8] J. A. Mydosh. *Spin Glasses: An Experimental Introduction*. Taylor & Francis, London & Washington, DC (1993).

[9] J. Li, W. Schneider, R. Berndt, and B. Delley. Kondo Scattering Observed at a Single Magnetic Impurity. *Phys. Rev. Lett.*, **80**(13):2893-2896 (1998).

[10] V. Madhavan, W. Chen, T. Jamneala, M. F. Crommie, and N. S. Wingreen. Tunneling into a Single Magnetic Atom: Spectroscopic Evidence of the Kondo Resonance. *Science*, **280**(5363):567-569 (1998).

[11] N. Knorr, M. A. Schneider, L. Diekhöner, P. Wahl, and K. Kern. Kondo Effect of Single Co Adatoms on Cu Surfaces. *Phys. Rev. Lett.*, **88**(9):096804 (2002).

[12] P. Wahl, L. Diekhöner, M. A. Schneider, L. Vitali, G. Wittich, and K. Kern. Kondo Temperature of Magnetic Impurities at Surfaces. *Phys. Rev. Lett.*, **93**(17):176603 (2004).

[13] P. Gambardella, M. Blanc, H. Brune, K. Kuhnke, and K. Kern. One-Dimensional Metal Chains on Pt Vicinal Surfaces. *Phys. Rev. B*, **61**(3):2254-2262 (2000).

[14] P. Gambardella, A. Dallmeyer, K. Maiti, M.C. Malagoli, W. Eberhardt, K. Kern, and C. Carbone. Ferromagnetism in One-Dimensional Monatomic Metal Chains. *Nature*, **416**(6878):301-304 (2002).

[15] P. Gambardella, A. Dallmeyer, K. Maiti, M. C. Malagoli, S. Rusponi, P. Ohresser, W. Eberhardt, C. Carbone, and K. Kern. Oscillatory Magnetic Anisotropy in One-Dimensional Atomic Wires. *Phys. Rev. Lett.*, **93**(7):077203 (2004).

[16] P. Gambardella, S. Rusponi, T. Cren, N. Weiss, and H. Brune. Magnetic Anisotropy from Single Atoms to Large Monodomain Islands of Co/Pt(111). *Comptes Rendus Physique*, **6**:75-87 (2005).

[17] F. Meier, K. von Bergmann, P. Ferriani, J. Wiebe, M. Bode, K. Hashimoto, S. Heinze, and R. Wiesendanger. Spin-Dependent Electronic and Magnetic Properties of Co Nanostructures on Pt(111) Studied by Spin-Resolved Scanning Tunneling Spectroscopy. *Phys. Rev. B*, **74**(11):195411 (2006).

[18] F Meier, K von Bergmann, J Wiebe, M Bode, and R Wiesendanger. Co Double-Layer Nanostructures on Pt(111) Studied by Spin-Polarized Scanning Tunnelling Microscopy. *Journal of Physics D: Applied Physics*, **40**(5):1306-1311 (2007).

[19] T. Balashov, T. Schuh, A. F. Takács, A. Ernst, S. Ostanin, J. Henk, I. Mertig, P. Bruno, T. Miyamachi, S. Suga, and W. Wulfhekel. Magnetic Anisotropy and Magnetization Dynamics of Individual Atoms and Clusters of Fe and Co on Pt(111). *Phys. Rev. Lett.*, **102**(25):257203 (2009).

[20] T. Schuh, T. Balashov, T. Miyamachi, A. F. Takacs, S. Suga, and W. Wulfhekel. Lifetimes of Magnetic Excitations in Fe and Co Atoms and Clusters on Pt(111). *J. Appl. Phys.*, **107**(9):09E156 (2010).

[21] A. Lehnert, S. Dennler, P. Błoński, S. Rusponi, M. Etzkorn, G. Moulas, P. Bencok, P. Gambardella, H. Brune, and J. Hafner. Magnetic Anisotropy of Fe and Co Ultrathin Films Deposited on Rh(111) and Pt(111) Substrates: An Experimental and First-Principles Investigation. *Phys. Rev. B*, **82**(9):094409 (2010).

[22] U. Pustogowa, J. Zabloudil, C. Uiberacker, C. Blaas, P. Weinberger, L. Szunyogh, and C. Sommers. Magnetic Properties of Thin Films of Co and of (CoPt) Superstructures on Pt(100) and Pt(111). *Phys. Rev. B*, **60**(1):414-421 (1999).

[23] B. Lazarovits, L. Szunyogh, and P. Weinberger. Magnetic Properties of Finite Co Chains on Pt(111). *Phys. Rev. B*, **67**(6):024415 (2003).

[24] B. Újfalussy, B. Lazarovits, L. Szunyogh, G. M. Stocks, and P. Weinberger. Ab Initio Spin Dynamics Applied to Nanoparticles: Canted Magnetism of a Finite Co Chain along a Pt(111) Surface Step Edge. *Phys. Rev. B*, **70**(10):100404 (2004).

[25] A. B. Shick, F. Máca, and P. M. Oppeneer. Anomalous Ferromagnetism of a Monatomic Co Wire at the Pt(111) Surface Step Edge. *Phys. Rev. B*, **69**(21):212410 (2004).

[26] Y. Xie and J. A. Blackman. Theory of Enhanced Magnetic Anisotropy Induced by Pt Adatoms on Two-Dimensional Co Clusters Supported on a Pt(111) Substrate. *Phys. Rev. B*, **74**(5):054401, (2006).

[27] O. Šipr, S. Bornemann, J. Minár, S. Polesya, V. Popescu, A. Šimunek, and H. Ebert. Magnetic Moments, Exchange Coupling, and Crossover Temperatures of Co Clusters on Pt(111) and Au(111). *J. Phys.: Condens. Matter*, **19**(9):096203 (2007).

[28] C. Etz, J. Zabloudil, P. Weinberger, and E. Y. Vedmedenko. Magnetic Properties of Single Atoms of Fe and Co on Ir(111) and Pt(111). *Phys. Rev. B*, **77**(18):184425 (2008).

[29] A. B. Shick and A. I. Lichtenstein. Orbital Moment of a Single Co Atom on a Pt(111) Surface - a View from Correlated Band Theory. *J. Phys.: Condens. Matter*, **20**(1):015002 (2008).

[30] P. Blonski and J. Hafner. Density-Functional Theory of the Magnetic Anisotropy of Nanostructures: An Assessment of Different Approximations. *J. Phys.: Condens. Matter*, **21**(42):426001 (2009).

[31] J. Tersoff and D. R. Hamann. Theory and Application for the Scanning Tunneling Microscope. *Phys. Rev. Lett.*, **50**(25):1998-2001 (1983).

[32] J. Tersoff and D. R. Hamann. Theory of the Scanning Tunneling Microscope. *Phys. Rev. B*, **31**(2):805-813 (1985).

[33] J. Bardeen. Tunnelling from a Many-Particle Point of View. *Phys. Rev. Lett.*, **6**(2):57-59 (1961).

[34] F. Meier. *Co on Pt(111) Studied by Spin-Polarized Scanning Tunneling Microscopy and Spectroscopy*. PhD thesis, Institute of Applied Physics, University of Hamburg (2006).

[35] D. Haude. *Rastertunnelspektroskopie auf der InAs(110)-Oberfläche: Untersuchungen an drei-, zwei-, und nulldimensionalen Elektronensystemen im Magnetfeld*. PhD thesis, Institute of Applied Physics, University of Hamburg (2001).

[36] J. Wiebe, A. Wachowiak, F. Meier, D. Haude, T. Foster, M. Morgenstern, and R. Wiesendanger. A 300mk Ultra-High Vacuum Scanning Tunneling Microscope for Spin-Resolved Spectroscopy at High Energy Resolution. *Rev. Sci. Instrum.*, **75**(11):4871-4879, (2004).

[37] J. C. Slonczewski. Conductance and Exchange Coupling of Two Ferromagnets Separated by a Tunneling Barrier. *Phys. Rev. B*, **39**(10):6995-7002 (1989).

[38] T. Miyazaki and N. Tezuka. Giant Magnetic Tunneling Effect in Fe/Al_2O_3/Fe Junction. *J. Magn. Magn. Mater.*, **139**(3):L231-L234 (1995).

[39] D. Wortmann, S. Heinze, Ph. Kurz, G. Bihlmayer, and S. Blügel. Resolving Complex Atomic-Scale Spin Structures by Spin-Polarized Scanning Tunneling Microscopy. *Phys. Rev. Lett.*, **86**(18):4132-4135 (2001).

[40] S. Heinze. *First Principle Theory of Scanning Tunneling Microscopy Applied to Transition-Metal Surfaces*. PhD thesis, Institute of Applied Physics, University of Hamburg (2000).

[41] R. Wiesendanger, H. J. Güntherodt, G. Güntherodt, R. J. Gambino, and R. Ruf. Observation of Vacuum Tunneling of Spin-Polarized Electrons with the STM. *Phys. Rev. Lett.*, **65**(2):247-250 (1990).

[42] S. Heinze, M. Bode, A. Kubetzka, O. Pietzsch, X. Nie, S. Blügel, and R. Wiesendanger. Real-Space Imaging of Two-Dimensional Antiferromagnetism on the Atomic Scale. *Science*, **288**(5472):1805-1808 (2000).

[43] A. Kubetzka, O. Pietzsch, M. Bode, and R. Wiesendanger. Determining the Spin Polarization of Surfaces by Spin-Polarized Scanning Tunneling Spectroscopy. *Appl. Phys. A*, **76**(6):873-877 (2003).

[44] J. Wiebe. *Aufbau einer 300mK-Ultrahochvakuum-Rastertunnelmikroskopie-Anlage mit 14T-Magnet und Untersuchung eines stark ungeordneten zweidimensionalen Elektronensystems*. PhD thesis, Institute of Applied Physics, University of Hamburg (2003).

[45] A. Wachowiak. *Aufbau einer 300mK-Ultrahochvakuum-Rastertunnelmikroskopie-Anlage mit 14 Tesla Magnet und spinpolarisierte Rastertunnelspektroskopie an ferromagnetischen Fe-Inseln*. PhD thesis, Institute of Applied Physics, University of Hamburg (2003).

[46] H. C. Manoharan, C. P. Lutz, and D. M. Eigler. Quantum Mirages Formed by Coherent Projection of Electronic Structure. *Nature*, **403**(6769):512-515 (2000).

[47] A. J. Heinrich, J. A. Gupta, C. P. Lutz, and D. M. Eigler. Single-Atom Spin-Flip Spectroscopy. *Science*, **306**(5695):466-469 (2004).

[48] C. F. Hirjibehedin, C. P. Lutz, and A. J. Heinrich. Spin Coupling in Engineered Atomic Structure. *Science*, **312**(5776):1021-1024 (2006).

[49] C. F. Hirjibehedin, C. Lin, A. F. Otte, M. Ternes, C. P. Lutz, B. A. Jones, and A. J. Heinrich. Large Magnetic Anisotropy of a Single Atomic Spin Embedded in a Surface Molecular Network. *Science*, **317**(5842):1199-1203 (2007).

[50] A. F. Otte, M. Ternes, K. von Bergmann, S. Loth, H. Brune, , C. P. Lutz, C. F. Hirjibehedin, and A. J. Heinrich. The Role of Magnetic Anisotropy in the Kondo Effect. *Nature Physics*, **4**(11):847-850 (2008).

[51] A. F. Otte, M. Ternes, S. Loth, C. P. Lutz, C. F. Hirjibehedin, and A. J. Heinrich. Spin Excitations of a Kondo-Screened Atom Coupled to a Second Magnetic Atom. *Phys. Rev. Lett.*, **103**(10):107203 (2009).

[52] S. Loth, K. von Bergmann, M. Ternes, A. F. Otte, C. P. Lutz, and A. J. Heinrich. Controlling the State of Quantum Spins with Electric Currents. *Nature Physics*, **6**(5):340-344 (2010).

[53] A. A. Khajetoorians, B. Chilian, J. Wiebe, S. Schuwalow, F. Lechermann, and Roland Wiesendanger. Detecting Excitation and Magnetization of Individual Dopants in a Semiconductor. *Nature*, **467**(7319):1084-1087 (2010).

[54] P. Wahl, P. Simon, L. Diekhöner, V. S. Stepanyuk, P. Bruno, M. A. Schneider, and K. Kern. Exchange Interaction between Single Magnetic Adatoms. *Phys. Rev. Lett.*, **98**(5):56601 (2007).

[55] F. Meier, L. Zhou, J. Wiebe, and R. Wiesendanger. Revealing Magnetic Interactions from Single-Atom Magnetization Curves. *Science*, **320**(5872):82-86 (2008).

[56] L. Zhou, J. Wiebe, S. Lounis, E. Vedmedenko, F. Meier, S. Blügel, P. H. Dederichs, and R. Wiesendanger. Strength and Directionality of Surface Ruderman-Kittel-Kasuya-Yosida Interaction Mapped on the Atomic Scale. *Nature Physics*, **6**(3):187-191 (2010).

[57] S. H. Pan. International Patent Publication No. WO 93/19494 (International Bureau, World Intellectual Property Organization). September 30, 2003.

[58] Y. Yayon, X. Lu, and M. F. Crommie. Bimodal Electronic Structure of Isolated Co Atoms on Pt(111). *Phys. Rev. B*, **73**(15):155401 (2006).

[59] P. Grütter and U. T. Dürig. Growth of Vapor-Deposited Cobalt Films on Pt(111) Studied by Scanning Tunneling Microscopy. *Phys. Rev. B*, **49**(3):2021-2029 (1994).

[60] P. Grütter and U. T. Dürig. Scanning Tunneling Microscopy of Co on Pt(111). *J. Vac. Sci. Technol. B*, **12**(3):1768-1771 (1994).

[61] P. Grütter and U. T. Dürig. Quasidendritic Growth of Co Induced by Localized Reconstruction of Pt(111). *Surf. Sci.*, **337**(1-2):147-152 (1994).

[62] E. Lundgren, B. Stanka, W. Koprolin, M. Schmid, and P. Varga. An Atomic-Scale Study of the Co Induced Dendrite Formation on Pt(111). *Surf. Sci.*, **423**(2-3):357 (1999).

[63] L. Shen, D. S. Schreiber, and A. J. Arko. Low-Temperature Resistivity in a "Giant" Moment Alloy. *Phys. Rev.*, **179**(2):512-514 (1969).

[64] V. V. Mazurenko, S. N. Iskakov, A. N. Rudenko, V. I. Anisimov, and A. I. Lichtenstein. Renormalized Spectral Function for Co Adatom on the Pt(111) Surface. *arXiv*, 1009.1452v1 (2010).

[65] J. Wiebe, F. Meier, K. Hashimoto, G. Bihlmayer, S. Blügel, P. Ferriani, S. Heinze, and R. Wiesendanger. Unoccupied Surface State on Pt(111) Revealed by Scanning Tunneling Spectroscopy. *Phys. Rev. B*, **72**(19):193406 (2005).

[66] S. N. Okuno, T. Kishi, and K. Tanaka. Spin-Polarized Tunneling Spectroscopy of Co(0001) Surface States. *Phys. Rev. Lett.*, **88**(4):066803 (2002).

[67] L. Diekhöner, M. A. Schneider, A. N. Baranov, V. S. Stepanyuk, P. Bruno, and K. Kern. Surface States of Cobalt Nanoislands on Cu(111). *Phys. Rev. Lett.*, **90**(23):236801 (2003).

[68] O. Pietzsch, A. Kubetzka, M. Bode, and R. Wiesendanger. Spin-Polarized Scanning Tunneling Spectroscopy of Nanoscale Cobalt Islands on Cu(111). *Phys. Rev. Lett.*, **92**(5):057202 (2004).

[69] J. Wiebe, L. Sacharow, A. Wachowiak, G. Bihlmayer, S. Heinze, S. Blügel, M. Morgenstern, and R. Wiesendanger. Scanning Tunneling Spectroscopy on Co(0001): Spectroscopic Signature of Stacking Faults and Dislocation Lines. *Phys. Rev. B*, **70**(3):35404 (2004).

[70] R. F. Sabiryanov, K. Cho, M. I. Larsson, W. D. Nix, and B. M. Clemens. Growth and Properties of Small Co Islands on a Strained Pt Surface. *J. Magn. Magn. Mater.*, **258-259**:365-368 (2002).

[71] M. Ternes, C. P. Lutz, C. F. Hirjibehedin, F. J. Giessibl, and A. J. Heinrich. The Force Needed to Move an Atom on a Surface. *Science*, **319**(5866):1066-1069 (2008).

[72] A. Weismann, M. Wenderoth, S. Lounis, P. Zahn, N. Quaas, R. G. Ulbrich, P. H. Dederichs, and S. Blügel. Seeing the Fermi Surface in Real Space by Nanoscale Electron Focusing. *Science*, **323**(5918):1190-1193 (2009).

[73] M. Ternes. *Scanning Tunneling Spectroscopy at the Single Atom Scale*. PhD thesis, Institut de Physique des Nanostructures, Ecole Polytechnique Federale de Lausanne, Switzerland (2006).

[74] R Temirov, S Soubatch, O Neucheva, A C Lassise, and F S Tautz. A Novel Method Achieving Ultra-High Geometrical Resolution in Scanning Tunnelling Microscopy. *New Journal of Physics*, **10**:053012 (2008).

[75] C. Weiss, C. Wagner, C. Kleimann, M. Rohlfing, F. S. Tautz, and R. Temirov. Imaging Pauli Repulsion in Scanning Tunneling Microscopy. *Phys. Rev. Lett.*, **105**(8):086103 (2010).

[76] P. J. Bryant, H. S. Kim, Y. C. Zheng, and R. Yang. Technique for Shaping Scanning Tunneling Microscope Tips. *Rev. Sci. Instrum.*, **58**(6):1115-1115 (1987).

[77] M. Fotino. Tip Sharpening by Normal and Reverse Electrochemical Etching. *Rev. Sci. Instrum.*, **64**(1):159-167 (1993).

[78] M. Bode. Spin-Polarized Scanning Tunneling Microscopy. *Rep. Prog. Phys.*, **66**(4):523-582 (2003).

[79] A. Kubetzka, M. Bode, O. Pietzsch, and R. Wiesendanger. Spin-Polarized Scanning Tunneling Microscopy with Antiferromagnetic Probe Tips. *Phys. Rev. Lett.*, **88**(5):057201 (2002).

[80] M. Bode, S. Krause, L. Berbil-Bautista, S. Heinze, and R. Wiesendanger. On the Preparation and Electronic Properties of Clean W(110) Surfaces. *Surf. Sci.*, **601**(16):3308-3314 (2007).

[81] O. Pietzsch, A. Kubetzka, M. Bode, and R. Wiesendanger. Real-Space Observation of Dipolar Antiferromagnetism in Magnetic Nanowires by Spin-Polarized Scanning Tunneling Spectroscopy. *Phys. Rev. Lett.*, **84**(22):5212-5215 (2000).

[82] M. Bode, A. Kubetzka, S. Heinze, O. Pietzsch, R. Wiesendanger, M. Heide, X. Nie, G. Bihlmayer, and S. Blügel. Spin-Orbit Induced Local Band Structure Variations Revealed by Scanning Tunneling Spectroscopy. *J. Phys.: Condens. Matter*, **15**(5):S679-S692 (2003).

[83] E. Y. Vedmedenko, A. Kubetzka, K. von Bergmann, O. Pietzsch, M. Bode, J. Kirschner, H. P. Oepen, and R. Wiesendanger. Domain Wall Orientation in Magnetic Nanowires. *Phys. Rev. Lett.*, **92**(7):077207 (2004).

[84] S. Meckler, N. Mikuszeit, A. Preßler, E. Y. Vedmedenko, O. Pietzsch, and R. Wiesendanger. Real-Space Observation of a Right-Rotating

Inhomogeneous Cycloidal Spin Spiral by Spin-Polarized Scanning Tunneling Microscopy in a Triple Axes Vector Magnet. *Phys. Rev. Lett.*, **103**(15):157201 (2009).

[85] B. W. Heinrich, C. Iacovita, M. V. Rastei, L. Limot, J. P. Bucher, P. A. Ignatiev, V. S. Stepanyuk, and P. Bruno. Spin Structure of an Atomic Protrusion: Probing Single Atoms on Cobalt Nanoislands. *Phys. Rev. B*, **79**(11):113401 (2009).

[86] M. Julliere. Tunneling between Ferromagnetic Films. *Phys. Lett. A*, **54**(3):225–226 (1975).

[87] M. Bode, M. Getzlaff, and R. Wiesendanger. Spin-Polarized Vacuum Tunneling into the Exchange-Split Surface State of gd(0001). *Phys. Rev. Lett.*, **81**(19):4256-4259 (1998).

[88] M. Bode, M. Heide, K. von Bergmann, P. Ferriani, S. Heinze, G. Bihlmayer, A. Kubetzka, O. Pietzsch, S. Blügel, and R. Wiesendanger. Chiral Magnetic Order at Surfaces Driven by Inversion Asymmetry. *Nature*, **447**(7141):190-193 (2007).

[89] D. Serrate, P. Ferriani, Y. Yoshida, S. Hla, M. Menzel, K. von Bergmann, S. Heinze, A. Kubetzka, and R. Wiesendanger. Imaging and Manipulating the Spin Direction of Individual Atoms. *Nature Nanotechnology*, **5**(5):350-353 (2010).

[90] J. A. Stroscio, D. T. Pierce, A. Davies, R. J. Celotta, and M. Weinert. Tunneling Spectroscopy of bcc (001) Surface States. *Phys. Rev. Lett.*, **75**(16):2960-2963 (1995).

[91] M. Bode, M. Getzlaff, A. Kubetzka, R. Pascal, O. Pietzsch, and R. Wiesendanger. Temperature-Dependent Exchange Splitting of a Surface State on a Local-Moment Magnet: Tb(0001). *Phys. Rev. Lett.*, **83**(15):3017-3020 (1999).

[92] T. K. Yamada, M. M. J. Bischoff, G. M. M. Heijnen, T. Mizoguchi, and H. van Kempen. Observation of Spin-Polarized Surface States on Ultrathin bct Mn(001) Films by Spin-Polarized Scanning Tunneling Spectroscopy. *Phys. Rev. Lett.*, **90**(5):056803 (2003).

[93] M. A. Barral, M. Weissmann, and A. Llois. Characterization of the Surface States of Co(0001), Co(111), and Ultrathin Films of Co on Cu(111). *Phys. Rev. B*, **72**(12):125433 (2005).

[94] Y. Yayon, V. W. Brar, L. Senapati, S. C. Erwin, and M. F. Crommie. Observing Spin Polarization of Individual Magnetic Adatoms. *Phys. Rev. Lett.*, **99**(6):067202, (2007).

[95] C. Rau and S. Eichner. Electron-Spin Polarization at Single-Crystalline Cr and Ni Surfaces Determined with Electron-Capture Spectroscopy. *Phys. Rev. Lett.*, **47**(13):939-942 (1981).

[96] K. Tao, V. S. Stepanyuk, W. Hergert, I. Rungger, S. Sanvito, and P. Bruno. Switching a Single Spin on Metal Surfaces by a STM Tip: Ab Initio Studies. *Phys. Rev. Lett.*, **103**(5):057202 (2009).

[97] P. Ferriani, C. Lazo, and S. Heinze. Origin of the Spin Polarization of Magnetic Scanning Tunneling Microscopy Tips. *Phys. Rev. B*, **82**(5):054411 (2010).

[98] S. Chikazumi, editor. *Physics of Magnetism*. Wiley, New York (1964).

[99] Z. Q. Qiu and S. D. Bader. Surface Magneto-Optic Kerr Effect (SMOKE). *J. Magn. Magn. Mater.*, **200**(1-3):664-678 (1999).

[100] S. Foner. Vibrating Sample Magnetometer. *Rev. Sci. Instrum.*, **27**(7):548-548 (1956).

[101] S. Foner. Versatile and Sensitive Vibrating - Sample Magnetometer. *Rev. Sci. Instrum.*, **30**(7):548-557 (1959).

[102] J. C. Gallop. *SQUIDs*. Institute of Physics Publishing, Bristol (1991).

[103] J. Clark and A. I. Braginiski, editors. *The SQUID Handbook*. Wiley-VCH, Winheim (2004).

[104] S. K. H. Lam, Wenrong Yang, H T R Wiogo, and C P Foley. Attachment of Magnetic Molecules on a Nanosquid. *Nanotechnology*, **19**(28):285303 (2008).

[105] D. Rugar, R. Budakian, H. J. Mamin, and B. W. Chui. Single Spin Detection by Magnetic Resonance Force Microscopy. *Nature*, **430**(6997):329-332 (2004).

[106] U. Kaiser, A. Schwarz, and R. Wiesendanger. Magnetic Exchange Force Microscopy with Atomic Resolution. *Nature*, **446**(7135):522-525 (2007).

[107] R. Schmidt, C. Lazo, H. Hölscher, U. H. Pi, V. Caciuc, A. Schwarz, R. Wiesendanger, and S. Heinze. Probing the Magnetic Exchange Forces of Iron on the Atomic Scale. *Nano Letters*, **9**(1):200-204 (2009).

[108] Y. Manassen, R. J. Hamers, J. E. Demuth, and A. J. Castellano Jr. Direct Observation of the Precession of Individual Paramagnetic Spins on Oxidized Silicon Surfaces. *Phys. Rev. Lett.*, **62**(21):2531-2534 (1989).

[109] C. Durkan and M. E. Welland. Electronic Spin Detection in Molecules Using Scanning-Tunneling- Microscopy-Assisted Electron-Spin Resonance. *Appl. Phys. Lett.*, **80**(3):458 (2002).

[110] H. J. Lee, W. Ho, and M. Persson. Spin Splitting of s and p States in Single Atoms and Magnetic Coupling in Dimers on a Surface. *Phys. Rev. Lett.*, **92**(18):186802 (2004).

[111] D. Kitchen, A. Richardella, J.-M. Tang, M. E. Flatté, and A. Yazdani. Atom-by-Atom Substitution of Mn in GaAs and Visualization of Their Hole-Mediated Interactions. *Nature*, **442**(7101):436 (2006).

[112] O. Pietzsch, A. Kubetzka, M. Bode, and R. Wiesendanger. Observation of Magnetic Hysteresis at the Nano-Scale by Spin Polarized Scanning Tunneling Spectroscopy. *Science*, **292**(5524):2053-2056 (2001).

[113] R. L. White. The Physical Boundaries to High-Density Magnetic Recording. *J. Magn. Magn. Mater.*, **209**(1-3):1-5 (2000).

[114] A. A. Khajetoorians, S. Lounis, B. Chilian, A. T. Costa, L. Zhou, D. L. Mills, J. Wiebe, and R. Wiesendanger. Itinerant Nature of Atom-Magnetization Excitation by Tunneling Electrons. *Phys. Rev. Lett.*, **106**(3): 037205 (2011).

[115] S. Loth, M. Etzkorn, C. P. Lutz, D. M. Eigler, and A. J. Heinrich. Measurement of Fast Electron Spin Relaxation Times with Atomic Rresolution. *Science*, **329**(5999):1628-1630 (2010).

[116] S. Krause, L. Berbil-Bautista, G. Herzog, M. Bode, and R. Wiesendanger. Current-Induced Magnetization Switching with a Spin-Polarized Scanning Tunneling Microscope. *Science*, **317**(5844):1537-1540 (2007).

[117] M. A. Ruderman and C. Kittel. Indirect Exchange Coupling of Nuclear Magnetic Moments by Conduction Electrons. *Phys. Rev.*, **96**(1):99-102 (1954).

[118] T. Kasuya. A Theory of Metallic Ferro- and Antiferromagnetism on Zener's Model. *Prog. Theor. Phys.*, **16**(1):45-57 (1956).

[119] K. Yosida. Magnetic Properties of Cu-Mn Alloys. *Phys. Rev.*, **106**(5):893-898 (1957).

[120] L. D. Graham and D. S. Schreiber. Conduction-Electron Polarization in the Paramagnetic State of a "Giant-Moment" Dilute Alloy. *Phys. Rev. Lett.*, **17**(12):650-652 (1966).

[121] M. N. Baibich, J. M. Broto, A. Fert, F. Nguyen Van Dau, F. Petroff, P. Etienne, G. Creuzet, A. Friederich, and J. Chazelas. Giant Magnetoresistance of (001)Fe/(001)Cr Magnetic Superlattices. *Phys. Rev. Lett.*, **61**(21):2472-2475 (1988).

[122] G. Binasch, P. Grünberg, F. Saurenbach, and W. Zinn. Enhanced Magnetoresistance in Layered Magnetic Structures with Antiferromagnetic Interlayer Exchange. *Phys. Rev. B*, **39**(7):4828-4830 (1989).

[123] I. D. Hughes, M. Däne, A. Ernst, W. Hergert, M. Lüders, J. Poulter, J. B. Staunton, A. Svane, Z. Szotek, and W. M. Temmerman. Lanthanide Contraction and Magnetism in the Heavy Rare Earth Elements. *Nature*, **446**(7136):650-653 (2007).

[124] T. Dietl, H. Ohno, F. Matsukura, J. Cibert, and D. Ferrand. Zener Model Description of Ferromagnetism in Zinc-Blende Magnetic Semiconductors. *Science*, **287**(5455):1019-1022 (2000).

[125] A. C. Hewson. *The Kondo Problem to Heavy Fermions*. Cambridge University Press (1997).

[126] C. F. Majkrzak, J. W. Cable, J. Kwo, M. Hong, D. B. McWhan, Y. Yafet, J. V. Waszczak, and C. Vettier. Observation of a Magnetic Antiphase Domain Structure with Long-Range Order in a Synthetic Gd-Y Superlattice. *Phys. Rev. Lett.*, **56**(25):2700-2703 (1986).

[127] P. Grünberg, R. Schreiber, Y. Pang, M. B. Brodsky, and H. Sowers. Layered Magnetic Structures: Evidence for Antiferromagnetic Coupling of Fe Layers across Cr Interlayers. *Phys. Rev. Lett.*, **57**(19):2442-2445 (1986).

[128] S. S. P. Parkin, N. More, and K. P. Roche. Oscillations in Exchange Coupling and Magnetoresistance in Metallic Superlattice Structures: Co/Ru, Co/Cr, and Fe/Cr. *Phys. Rev. Lett.*, **64**(19):2304-2307 (1990).

[129] S. S. P. Parkin and D. Mauri. Spin Engineering: Direct Determination of the Ruderman-Kittel-Kasuya-Yosida Far-Field Range Function in Ruthenium. *Phys. Rev. B*, **44**(13):7131-7134 (1991).

[130] C. Kittel. *Solid State Physics*. Academic, New York (1968).

[131] B. Fischer and M. W. Klein. Magnetic and Nonmagnetic Impurities in Two-Dimensional Metals. *Phys. Rev. B*, **11**(5):2025-2029 (1975).

[132] Y. Yafet. Ruderman-Kittel-Kasuya-Yosida Range Function of a One-Dimensional Free-Electron Gas. *Phys. Rev. B*, **36**(7):3948-3949 (1987).

[133] P. Bruno and C. Chappert. Ruderman-Kittel Theory of Oscillatory Interlayer Exchange Coupling. *Phys. Rev. B*, **46**(1):261-270 (1992).

[134] L. M. Roth, H. J. Zeiger, and T. A. Kaplan. Generalization of the Ruderman-Kittel-Kasuya-Yosida Interaction for Nonspherical Fermi Surfaces. *Phys. Rev.*, **149**(2):519-525 (1966).

[135] E. Simon, B. Lazarovits, L. Szunyogh, and B. Újfalussy. Ab-Initio Investigation of RKKY Interactions on Metallic Surfaces. *Phil. Mag.*, **88**(18):2667-2672 (2008).

[136] D. S. Inosov, D.V. Evtushinsky, A. Koitzsch, V. B. Zabolotnyy, S.V. Borisenko, A. A. Kordyuk, M. Frontzek, M. Loewenhaupt, W. Löser, I. Mazilu, H. Bitterlich, G. Behr, J.-U. Hoffmann, R. Follath, and B. Büchner. Electronic Structure and Nesting-Driven Enhancement of the RKKY Interaction at the Magnetic Ordering Propagation Vector in Gd_2PdSi_3 and Tb_2PdSi_3. *Phys. Rev. Lett.*, **102**(4):046401 (2009).

[137] N. Papanikolaou, R. Zeller, and P. H. Dederichs. Conceptual Improvements of the KKR Method. *J. Phys.: Condens. Matter*, **14**(1):2799-2823 (2002).

[138] http://olymp.cup.uni-muenchen.de/ak/ebert/SPR-TB-KKR.

[139] S. Bandyopadhyay, B. Das, and A. E. Miller. Supercomputing with Spin-Polarized Single Electrons in a Quantum Coupled Architecture. *Nanotechnology*, **5**(2):113-133 (1994).

[140] S. Blügel, M. Weinert, and P. H. Dederichs. Ferromagnetism and Antiferromagnetism of 3d-Metal Overlayers on Metals. *Phys. Rev. Lett.*, **60**(11):1077-1080 (1988).

[141] J. P. Pierce, M. A. Torija, Z. Gai, Junren Shi, T. C. Schulthess, G. A. Farnan, J. F. Wendelken, E. W. Plummer, and J. Shen. Ferromagnetic Stability in Fe Nanodot Assemblies on Cu(111) Induced by Indirect Coupling through the Substrate. *Phys. Rev. Lett.*, **92**(23):237201 (2004).

[142] L. Yin, D. Xiao, Z. Gai, T. Z. Ward, N. Widjaja, G. M. Stocks, Z. Cheng, E. W. Plummer, Z. Zhang, and J. Shen. Tuning the Ferromagnetic Coupling of Fe Nanodots on Cu(111) via Dimensionality Variation of the Mediating Electrons. *Phys. Rev. Lett.*, **104**(16):167202 (2010).

[143] J Crangle. Ferromagnetism in Pd-Rich Palladium-Iron Alloys. *Philosophical Magazine*, **5**(52):335-342 (1960).

[144] R. Skomski, J. Zhang, V. Sessi, J. Honolka, K. Kern, and A. Enders. Substrate-Controlled Growth and Magnetism of Nanosize Fe Clusters on Pt. *J. Appl. Phys*, **103**(7):07D519 (2008).

[145] A. Oswald, R. Zeller, and P. H. Dederichs. Giant Moments in Palladium. *Phys. Rev. Lett.*, **56**(13):1419-1422 (1986).

[146] K. Le Dang, P. Veillet, C. Chappert, R. F. C. Farrow, R. F. Marks, D. Weller, and A. Cebollada. Antiferromagnetic Coupling in (111)-Oriented Co/Pt Superlattices. *Phys. Rev. B*, **50**(1):200-204 (1994).

[147] J. Moritz, F. Garcia, J. C. Toussaint, B. Dieny, and J. P. Noziéres. Orange Peel Coupling in Multilayers with Perpendicular Magnetic Anisotropy: Application to (Co/Pt)-Based Exchange-Biased Spin-Valves. *Europhys. Lett.*, **65**(1):123 (2004).

[148] X. Li, J. Bao, L. Lu, X. Xu, and Y. Jiang. Oscillatory Antiferromagnetic Interlayer Coupling in Co/Pt Multilayer with Perpendicular Anisotropy. *Solid State Communications*, **148**(5-6):209-212 (2008).

[149] J. W. Knepper and F. Y. Yang. Oscillatory Interlayer Coupling in Co/Pt Multilayers with Perpendicular Anisotropy. *Phys. Rev. B*, **71**(22):224403 (2005).

[150] N. Quaas, M. Wenderoth, A. Weismann, R. G. Ulbrich, and K. Schönhammer. Kondo Resonance of Single Co Atoms Embedded in Cu(111). *Phys. Rev. B*, **69**(20):201103 (2004).

[151] A. Mosca Conte, S. Fabris, and S. Baroni. Properties of Pt-Supported Co Nanomagnets from Relativistic Density Functional Theory Calculations. *Phys. Rev. B*, **78**(1):014416 (2008).

[152] S. Baud, Ch. Ramseyer, G. Bihlmayer, and S. Blügel. Relaxation Effects on the Magnetism of Decorated Step Edges: Co/Pt(664). *Phys. Rev. B*, **73**(10):104427 (2006).

[153] R.K. Das, R. Misra, S. Tongay, R. Rairigh, and A.F. Hebard. Finite Size Effects with Variable Range Exchange Coupling in Thin-Film Pd/Fe/Pd Trilayers. *J. Magn. Magn. Mater.*, **322**(17):2618-2621 (2010).

[154] P. W. Anderson. Localized Magnetic States in Metals. *Phys. Rev.*, **124**(1):41-53 (1961).

[155] S. D. Kevan. Evidence for a New Broadening Mechanism in Angle-Resolved Photoemission from Cu(111). *Phys. Rev. Lett.*, **50**(7):526-529 (1983).

[156] M. F. Crommie, C. P. Lutz, and D. M. Eigler. Imaging Standing Waves in a Two-Dimensional Electron Gas. *Nature*, **363**(6429):524-527 (1993).

[157] N. Memmel. Monitoring and Modifying Properties of Metal Surfaces by Electronic Surface States. *Surf. Sci. Rep.*, **32**:91-163 (1998).

[158] F. E. Olsson, M. Persson, A. G. Borisov, J.-P. Gauyacq, J. Lagoute, and S. Fölsch. Localization of the Cu(111) Surface State by Single Cu Adatoms. *Phys. Rev. Lett.*, **93**(20):206803 (2004).

[159] L. Limot, E. Pehlke, J. Kröger, and R. Berndt. Surface-State Localization at Adatoms. *Phys. Rev. Lett.*, **94**(3):036805 (2005).

[160] E. J. Heller, M. F. Crommie, C. P. Lutz, and D. M. Eigler. Scattering and Absorption of Surface Electron Waves in Quantum Corrals. *Nature*, **369**(6470):464-466 (1994).

[161] B. Lazarovits, L. Szunyogh, and P. Weinberger. Spin-Polarized Surface States Close to Adatoms on Cu(111). *Phys. Rev. B*, **73**(4):045430 (2006).

[162] S. Lounis, P. Mavropoulos, P. H. Dederichs, and S. Blügel. Surface-State Scattering by Adatoms on Noble Metals: Ab Initio Calculations Using the Korringa-Kohn-Rostoker Green Function Method. *Phys. Rev. B*, **73**(19):195421 (2006).

[163] A. Bergman, L. Nordström, A. Burlamaqui Klautau, S. Frota-Pessôa, and O. Eriksson. Magnetic Structures of Small Fe, Mn, and Cr Clusters Supported on Cu(111): Noncollinear First-Principles Calculations. *Phys. Rev. B*, **75**(22):224425 (2007).

[164] P. A. Ignatiev, N. N. Negulyaev, A. S. Smirnov, L. Niebergall, A. M. Saletsky, and V. S. Stepanyuk. Magnetic Ordering of Nanocluster Ensembles Promoted by Electronic Substrate-Mediated Interaction: Ab Initio and Kinetic Monte Carlo Studies. *Phys. Rev. B*, **80**(16):165408 (2009).

[165] P. Mavropoulos, S. Lounis, and S. Blügel. Exchange Coupling in Transition-Metal Nanoclusters on Cu(001) and Cu(111) Surfaces. *physica status Solidi (b)*, **247**(5):1187-1196 (2010).

[166] V. S. Stepanyuk, L. Niebergall, R. C. Longo, W. Hergert, and P. Bruno. Magnetic Nanostructures Stabilized by Surface-State Electrons. *Phys. Rev. B*, **70**(7):075414 (2004).

[167] V. S. Stepanyuk, L. Niebergall, W. Hergert, and P. Bruno. Ab Initio Study of Mirages and Magnetic Interactions in Quantum Corrals. *Phys. Rev. Lett.*, **94**(18):187201 (2005).

[168] V S Stepanyuk, N N Negulyaev, L Niebergall, and P Bruno. Effect of Quantum Confinement of Surface Electrons on Adatom-Adatom Interactions. *New Journal of Physics*, **9**:388 (2007).

[169] J. Hu, B. Teng, F. Wu, and Y. Fang. Fe Nanostructures Stabilized by Long-Range Interactions on Cu(111): Kinetic Monte Carlo Simulations. *New Journal of Physics*, **10**:023033 (2008).

[170] O. O. Brovko, V. S. Stepanyuk, and P. Bruno. Effect of Exchange Interaction on the Spin-Polarized Bound States on Metal Surfaces: Ab Initio Study. *Phys. Rev. B*, **78**(16):165413 (2008).

[171] O. O. Brovko, V. S. Stepanyuk, W. Hergert, and P. Bruno. Probing Buried Magnetic Nanostructures by Spin-Resolved Local Density of States at the Surface: A Density Functional Study. *Phys. Rev. B*, **79**(24):245417 (2009).

[172] T. Susaki, T. Komeda, and Maki Kawai. Narrow Photoemission Peak at the Fermi Level in Fe/Cu(111). *Phys. Rev. Lett.*, **88**(18):187602 (2002).

[173] O. Pietzsch, S. Okatov, A. Kubetzka, M. Bode, S. Heinze, A. Lichtenstein, and R. Wiesendanger. Spin-Resolved Electronic Structure of Nanoscale Cobalt Islands on Cu(111). *Phys. Rev. Lett.*, **96**(23):237203 (2006).

[174] M. Sicot, O. Kurnosikov, O. A. O. Adam, H. J. M. Swagten, and B. Koopmans. STM-Induced Desorption of Hydrogen from Co Nanoislands. *Phys. Rev. B*, **77**(3):035417 (2008).

[175] B. Lazarovits, L. Szunyogh, P. Weinberger, and B. Újfalussy. Magnetic Properties of Finite Fe Chains at fcc Cu(001) and Cu(111) Surfaces. *Phys. Rev. B*, **68**(2):024433 (2003).

[176] Y. Terada, S. Yoshida, O. Takeuchi, and H. Shigekawa. Real-Space Imaging of Transient Carrier Dynamics by Nanoscale Pump-Probe Microscopy. *Nature Photonics*, doi: 10.1038/NPHOTON.2010.235 (2010).

[177] J. Brede, N. Atodiresei, S. Kuck, P. Lazić, V. Caciuc, Y. Morikawa, G. Hoffmann, S. Blügel, and R. Wiesendanger. Spin- and Energy-Dependent Tunneling Through a Single Molecule with Intramolecular Spatial Resolution. *Phys. Rev. Lett.*, **105**(4):047204 (2010).

[178] N. Atodiresei, J. Brede, P. Lazić, V. Caciuc, G. Hoffmann, R. Wiesendanger, and S. Blügel. Design of the Local Spin Polarization at the Organic-Ferromagnetic Interface. *Phys. Rev. Lett.*, **105**(6):066601 (2010).

[179] A. M. Yakunin, A. Yu. Silov, P. M. Koenraad, J.-M. Tang, M. E. Flatte, J.-L. Primus, W. Van Roy, J. De Boeck, A. M. Monakhov, K. S. Romanov, I. E. Panaiotti, and N. S. Averkiev. Warping a Single Mn Acceptor Wavefunction by Straining the GaAs Host. *Nature Materials*, **6**(7):512-515 (2007).

[180] Y. Léger, L. Besombes, J. Fernández-Rossier, L. Maingault, and H. Mariette. Electrical Control of a Single Mn Atom in a Quantum Dot. *Phys. Rev. Lett.*, **97**(10):107401 (2006).

[181] A. Kudelski, A. Lemaître, A. Miard, P. Voisin, T. C. M. Graham, R. J. Warburton, and O. Krebs. Optically Probing the Fine Structure of a Single Mn Atom in an InAs Quantum Dot. *Phys. Rev. Lett.*, **99**(24):247209 (2007).

[182] C. Le Gall, L. Besombes, H. Boukari, R. Kolodka, J. Cibert, and H. Mariette. Optical Spin Orientation of a Single Manganese Atom in a Semiconductor Quantum Dot Using Quasiresonant Photoexcitation. *Phys. Rev. Lett.*, **102**(12):127402 (2009).

[183] Q. Liu, C. Liu, C. Xu, X. Qi, and S. Zhang. Magnetic Impurities on the Surface of a Topological Insulator. *Phys. Rev. Lett.*, **102**(15):156603 (2009).

[184] R. Yu, W. Zhang, H. Zhang, S. Zhang, X. Dai, and Z. Fang. Quantized Anomalous Hall Effect in Magnetic Topological Insulators. *Science*, **329**(5987):61-64 (2010).

[185] Y. L. Chen, J.-H. Chu, J. G. Analytis, Z. K. Liu, K. Igarashi, H.-H. Kuo, X. L. Qi, S. K. Mo, R. G. Moore, D. H. Lu, M. Hashimoto, T. Sasagawa, S. C. Zhang, I. R. Fisher, Z. Hussain, and Z. X. Shen. Massive Dirac Fermion on the Surface of a Magnetically Doped Topological Insulator. *Science*, **329**(5992):659-662 (2010).

[186] F. Jelezko, T. Gaebel, I. Popa, M. Domhan, A. Gruber, and J. Wrachtrup. Observation of Coherent Oscillation of a Single Nuclear Spin and Realization of a Two-Qubit Conditional Quantum Gate. *Phys. Rev. Lett.*, **93**(13):130501 (2004).

[187] L. Childress, M. V. Gurudev Dutt, J. M. Taylor, A. S. Zibrov, F. Jelezko, J. Wrachtrup, P. R. Hemmer, and M. D. Lukin. Coherent Dynamics of Coupled Electron and Nuclear Spin Qubits in Diamond. *Science*, **314**(5797):281-285 (2006).

[188] R. Hanson, V. V. Dobrovitski, A. E. Feiguin, O. Gywat, and D. D. Awschalom. Coherent Dynamics of a Single Spin Interacting with an Adjustable Spin Bath. *Science*, **320**(5874):352-355 (2008).

[189] P. Neumann, N. Mizuochi, F. Rempp, P. Hemmer, H. Watanabe, S. Yamasaki, V. Jacques, T. Gaebel, F. Jelezko, and J. Wrachtrup. Multipartite Entanglement among Single Spins in Diamond. *Science*, **320**(5881):1326-1329 (2008).

[190] P. Neumann, R. Kolesov, B. Naydenov, J. Beck, F. Rempp, M. Steiner, V. Jacques, G. Balasubramanian, M. L. Markham, D. J. Twitchen, S. Pezzagna, J. Meijer, J. Twamley, F. Jelezko, and J. Wrachtrup. Quantum Register Based on Coupled Electron Spins in a Room-Temperature Solid. *Nature Physics*, **6**(4):249-253 (2010).

[191] B. E. Kane. A Silicon-Based Nuclear Spin Quantum Computer. *Nature*, **393**(6681):133-137 (1998).

[192] Martin Fuechsle, S. Mahapatra, F. A. Zwanenburg, Mark Friesen, M. A. Eriksson, and Michelle Y. Simmons. Spectroscopy of Few-Electron Single-Crystal Silicon Quantum Dots. *Nature Nanotechnology*, **5**(7):502-505, (2010).

Publications

Articles:

F. Meier, **L. Zhou**, J. Wiebe and R. Wiesendanger: *Revealing Magnetic Interactions from Single-Atom Magnetization Curves*. Science **320**, 82 (2008).

L. Zhou, J. Wiebe, S. Lounis, E. Vedmedenko, F. Meier, S. Blügel, P. H. Dederichs and R. Wiesendanger: *Strength and Directionality of Surface Ruderman-Kittel-Kasuya-Yosida Interaction Mapped on the Atomic Scale*. Nature Physics **6**, 187 (2010).

L. Zhou, F. Meier, J. Wiebe and R. Wiesendanger: *Inversion of Spin Polarization above Magnetic Adatoms*. Phys. Rev. B **82**, 012409 (2010).

F. Meier, S. Lounis, J. Wiebe, **L. Zhou**, S. Heers, P. Mavropoulos, P. H. Dederichs, S. Blügel and R. Wiesendanger: *Spin-Polarization of Platinum* (1 1 1) *Induced by the Proximity to Cobalt Nanostripes*. Phys. Rev. B. **83**, 075407 (2011)

A. A. Khajetoorians, S. Lounis, B. Chilian, A. T. Costa, **L. Zhou**, D. L. Mills, J. Wiebe and R. Wiesendanger: *Itinerant Nature of Atom-Magnetization Excitation by Tunneling Electrons*. Phys. Rev. Lett. **106**, 037205 (2011)

Talks and conferences:

L. Zhou, F. Meier, J. Wiebe, and R. Wiesendanger: *Spin-Polarized Scanning Tunneling Microscopy and Spectroscopy*. 1st International Summer School of the GrK "Physics of Functional Micro- and Nanostructures", Hamburg, Germany, 20-21. 09. 2007 (Poster).

L. Zhou: *Spin-Polarized Scanning Tunneling Spectroscopy on Individual Magnetic Adatoms*. 1st Graduate-Class Workshop of the Graduietenkolleg 1286, Reinbek, Germany, 10. 12. 2007 (Talk).

L. Zhou, F. Meier, J. Wiebe, and R. Wiesendanger: *Spin-Polarized Scanning Tunneling Spectroscopy on Individual Magnetic Adatoms*. 72nd Spring Conference, Deutsche Physikalische Gesellschaft, Berlin, Germany, 25. 02. 2008 (Talk).

L. Zhou, F. Meier, J. Wiebe, and R. Wiesendanger: *Oscillatory Magnetic Exchange Coupling at the Atomic Level Revealed from Single-Atom Magnetization Curves*. 25th International Conference on Low Temperature Physics, Amsterdam, the Netherlands, 12. 08. 2008 (Invited talk).

G. Herzog, **L. Zhou**, S. Krause, F. Meier, J. Wiebe, and R. Wiesendanger: *Spin-Polarized Scanning Tunneling Microscopy and Spectroscopy*. 2nd International Summer School of the GrK "Physics of Functional Micro- and Nanostructures", Hamburg, Germany, 11. 09. 2008 (Poster shared with G. Herzog).

L. Zhou, F. Meier, J. Wiebe, R. Wiesendanger, *Revealing Magnetic Interactions from Single-Atom Magnetization Curves*. Joint European Magnetic Symposia (JEMS), Dublin, Ireland, 18. 09. 2008 (Talk).

L. Zhou: *Revealing Magnetic Interactions from Single-Atom Magnetization Curves*. 2nd Graduate-Class Workshop of the Graduietenkolleg 1286, Husum, Germany, 30. 10. 2008 (Talk).

L. Zhou, F. Meier, J. Wiebe, and R. Wiesendanger: *Oscillatory Magnetic Exchange Coupling at the Atomic Level: a Direct Real-Space Study by a Subkelvin Spin-Polarized STM*. 53rd Annual Conference on Magnetism and Magnetic Materials, Austin, Texas, USA, 11. 11. 2008 (Invited talk).

L. Zhou, F. Meier, J. Wiebe, and R. Wiesendanger: *Oscillatory Magnetic Exchange Coupling at the Atomic Level: a Direct Real-Space Study by a Subkelvin Spin-Polarized STM*. the Nano Electronic Materials Research Group, the University of Texas at Austin, Austin, Texas, USA, 12. 11. 2008 (Invited seminar talk).

G. Herzog, **L. Zhou**, S. Krause, F. Meier, J. Wiebe, and R. Wiesendanger: *Spin-Polarized Scanning Tunneling Microscopy and Spectroscopy*. 3rd International Summer School of the GrK "Physics of Functional Micro- and Nanostructures", Hamburg, Germany, 17-18. 09. 2009 (Poster shared with G. Herzog).

L. Zhou: *Strength and Directionality of Surface RKKY-Interaction Mapped on the Atomic Scale*. 3rd Graduate-Class Workshop of the Graduietenkolleg 1286, Schwerin, Germany, 30. 10. 2009 (Talk).

L. Zhou: *Using Single-Atom Magnetization Curves to Study Magnetic Interac-*

tion. LEXI-Workshop "'NANOSPINTRONICS"', Hamburg, Germany, 04. 03. 2010 (Talk).

L. Zhou, F. Meier, J. Wiebe, and R. Wiesendanger: *Inversion of Spin Polarization above Magnetic Adatoms*. 74th Spring Conference, Deutsche Physikalische Gesellschaft, Regensburg, Germany, 25. 03. 2010 (Talk).

L. Zhou: *Mapping Single-Atom Magnetism by Spin-Polarized STM*. State Key Laboratory of Functional Materials for Informatics, Shanghai Institute of Microsystem and Information Technology, Chinese Academy of Sciences, Shanghai, China, 09. 04. 2010 (Invited seminar talk).

L. Zhou: *Mapping Single-Atom Magnetism by Spin-Polarized STM*. Magnetic Ultrathin Film Group, Physics Department, Fudan University, Shanghai, China, 12. 04. 2010 (Invited seminar talk).

Acknowledgements

Many sincere thanks to Prof. Dr. Roland Wiesendanger for giving me the chance to do research in his group, the supervision and the steady support of my work.

I thank Prof. Dr. Ulrich Merkt for all the support via Graduiertenkolleg 1286.

In particular I would like to thank Dr. Jens Wiebe for the supervision, help and for the meticulous reading of this thesis. In all respects he has been an excellent supervisor.

I also thank my LAB006-mates Dr. Focko Meier and Dr. Alexander Khajetoorians, the collaboration with whom was very enjoyful. They supported me a lot. Especially Focko's help with experimental problems was very important to me for the start of my PhD research. I also thank Dr. Felix Marczinowski and Bruno Chilian, who helped me a lot with many technical problems.

The DFT calculations concerning the pairwise RKKY interaction of Co and the spin polarization of Pt were carried out by Dr. Samir Lounis, Prof. Dr. Peter H. Dederichs and Prof. Dr. Stefan Blügel at the Forschungszentrum Jülich. The simulations concerning the magnetization curves of Co pairs were performed by Dr. Elena Vedmedenko in the Institute of Applied Physics of the University of Hamburg. There were also a lot of fruitful discussions with Dr. Paolo Ferriani and Prof. Dr. Stefan Heinze. I would like to thank all of them for the great help and collaboration.

I also thank each member of *Group R*. They were always friendly and helpful in all aspects.

Finally, very special thanks to my parents and my brother as well as to Mei and my coming baby son for their great love. They are the source of my joy and happiness. This makes all the efforts worthwhile.